

**Development and Characterization of a Drug-loaded Smart
Injectable Hydrogel as a Drug Delivery System for the
Treatment of Rheumatoid Arthritis**

By
Prakash Haloi
LIFE11201704003

**National Institute of Science Education and Research (NISER) -
Bhubaneswar**

*A thesis submitted to the
Board of Studies in Life Sciences
In partial fulfillment of requirements
for the Degree of*

DOCTOR OF PHILOSOPHY
of
HOMI BHABHA NATIONAL INSTITUTE

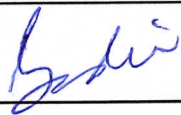
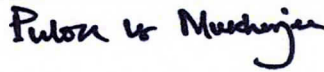
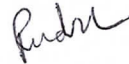


April, 2023

Homi Bhabha National Institute¹

Recommendations of the Viva Voce Committee

As members of the Viva Voce Committee, we certify that we have read the dissertation prepared by Mr. Prakash Haloi entitled "Development and Characterization of a Drug-loaded Smart Injectable Hydrogel as a Drug Delivery Systems for the Treatment of Rheumatoid Arthritis" and recommend that it may be accepted as fulfilling the thesis requirement for the award of Degree of Doctor of Philosophy.

Chairman - Dr. Praful S Singru		09-08-2023
Guide / Convener - Dr. V. Badireenath Konkimalla		09-08-2023
Co-guide – N/A		
Examiner - Prof. Pulok K Mukherjee		09-08-2023
Member 1- Dr. Rudresh Acharya		09-08-2023
Member 2- Dr. Subhadip Ghosh		09-08-2023
Member 3- Dr. Shantibhusan Senapati		09-08-2023

Final approval and acceptance of this thesis is contingent upon the candidate's submission of the final copies of the thesis to HBNI.

I/We hereby certify that I/we have read this thesis prepared under my/our direction and recommend that it may be accepted as fulfilling the thesis requirement.

Date: 09-08-2023

Place: NISER, Bhubaneswar


Signature

Guide

¹ This page is to be included only for final submission after successful completion of viva voce.

STATEMENT BY AUTHOR

This dissertation has been submitted in partial fulfillment of the requirements for an advanced degree at Homi Bhabha National Institute (HBNI). It is deposited in the library to be made available to borrowers under the rules of the HBNI.

Brief quotations from this dissertation are allowable without special permission, provided that accurate acknowledgment of the source is made. Requests for permission for extended quotation from or reproduction of this manuscript in whole or in part may be granted by the Competent Authority of HBNI when, in his or her judgment, the proposed use of the material is in the interests of scholarship. In all other instances, however, permission must be obtained from the author.

Prakash Haloi
(Prakash Haloi)

DECLARATION

I hereby declare that the investigation presented in the thesis has been carried out by me. The work is original and has not been submitted earlier as a whole or in part for a degree/diploma at this or any other Institution / University.

Prakash Haloi

(Prakash Haloi)

CERTIFICATE

This is to certify that the thesis entitled “*Development and Characterization of a Drug-loaded Smart Injectable Hydrogel as a Drug Delivery Systems for the Treatment of Rheumatoid Arthritis,*” which is being submitted by Mr. Prakash Haloi in partial fulfillment of the degree of Doctor of Philosophy (Ph.D.) in Life Sciences of Homi Bhabha National Institute (HBNI) is a record of his research work carried by him. He has researched the thesis subject matter for the last six years under my supervision at the National Institute of Science Education and Research (NISER), Bhubaneswar.

To the best of our knowledge, the matter embodied in this thesis has not been submitted for the award of any other degree.



Signature of the Candidate

Prakash Haloi
School of Biological Sciences,
National Institute of Science Education
and Research (NISER), Jatni, Odisha
752050



Signature of the Supervisor

Dr. V Badireenath Konkimalla
Associate Professor
School of Biological Sciences,
National Institute of Science Education
and Research (NISER), Jatni, Odisha
752050

List of Publications from the thesis

Journal

1. Thermosensitive smart hydrogel of PEITC ameliorates the therapeutic efficacy in rheumatoid arthritis. **Haloi P**, Chawla S, Konkimalla VB. *Eur J Pharm Sci.* **2023**; 181:106367. doi: [10.1016/j.ejps.2022.106367](https://doi.org/10.1016/j.ejps.2022.106367).
2. Formulation of a dual drug-loaded nanoparticulate co-delivery hydrogel system and its validation in rheumatoid arthritis animal model. **Haloi P**, Lokesh BS, Chawla S, Konkimalla VB. *Drug Deliv.* **2023**; 30(1):2184307. doi:[10.1080/10717544.2023.2184307](https://doi.org/10.1080/10717544.2023.2184307).
3. Dual-drug nanoparticulate loaded smart hydrogel as a co-delivery system regulates fibroblast-like synoviocytes-mediated apoptosis, inflammation, and bone destruction. **Haloi P**, Choudhary R, Lokesh BS, Konkimalla VB. **2023**. (*Communicated*).

Other Publications

Journal

4. Quaternary ammonium substituted pullulan accelerates wound healing and disinfects *Staphylococcus aureus* infected wounds in mice through an atypical 'non-pore forming' pathway of bacterial membrane disruption. Roy S, Kumari M, **Haloi P**, Chawla S, Konkimalla VB, Kumar A, Kashyap HK, Jaiswal A. *Biomater Sci.* **2022**; 10(2):581-601. doi [10.1039/d1bm01542g](https://doi.org/10.1039/d1bm01542g).
5. Fabrication and optimization of BSA-PEG-loaded phenethyl isothiocyanate (PEITC) nanoparticles using box-Behnken design for potential application in subcutaneous infection conditions. Lokesh BS, **Haloi P**, Konkimalla VB. *J Drug Deliv Sci Technol.* **2023**; 80:104101. doi.org/[10.1016/j.jddst.2022.104101](https://doi.org/10.1016/j.jddst.2022.104101)
6. Quaternary Pullulan functionalized 2D MoS₂ glycosheets: A potent bactericidal nanoplatfroms promoting safe and efficient wound disinfection and healing. Roy S, **Haloi P**,[#] Choudhary R, Chawla S, Kumari M, Konkimalla VB, Jaiswal A. *ACS Appl Mater Interfaces.* **2023**; 15:24209-24227. doi:[10.1021/acsami.3c04390](https://doi.org/10.1021/acsami.3c04390).

[#]Equal Contribution

7. Palladium Nanocapsules for Photothermal Therapy in the NIR-II Biological Window. Singh P, # **Haloi P**,# Singh K, Roy S, Sarkar A, B SL, Choudhary R, Mohite C, Chawla S, Konkimalla VB, Sanpui P, Jaiswal A. *ACS Appl Mater Interfaces*. **2023**; 15:39081-39098. doi:10.1021/acsami.3c06186. # *Equal Contribution*
8. Biocompatible Quaternary Pullulan functionalized 2D MoS₂ Glycosheet-based Non-leaching & Infection-resistant Coatings for Indwelling Medical Implants. Roy S, # **Haloi P**,# Lokesh BS, Chawla S, Konkimalla VB, Jaiswal A. **2023**. (*Communicated*). # *Equal Contribution*

Conferences

1. *Oral Talks: International*

An injectable phenethyl isothiocyanate (PEITC)-loaded thermosensitive hydrogel for localized and sustained drug delivery in managing rheumatoid arthritis. **Haloi P**,* Konkimalla VB. ICNB 2021, 2nd-5th Feb **2022** (*Online Mode*).

2. *Oral Talks: National*

Preparation, characterization, and studies of phenethyl isothiocyanate (PEITC)-loaded Thermosensitive injectable hydrogel in a rheumatic disease condition. **Haloi P**,* Konkimalla VB. Bioengineering-2019; 06th-07th December **2019**; NIT Rourkela (*Offline Mode*).

Workshops and Symposiums

1. Symposium organized by GATC on "The application of Next Generation Sequencing in health and diseases" at NISER, Bhubaneswar, on 8th-9th September **2017**.
2. Workshop on High-End Widefield Confocal & SR Imaging at NISER Bhubaneswar organized by Carl Zeiss India Pvt. Ltd. Between 30th November to 1st December **2017**.
3. Workshop on Microtomy/Ultra-microtomy, Staining, and Imaging Techniques organized by ILS, Bhubaneswar, on 12-13th April **2018**.

4. Workshop on Interpretation of Instrumental Methods (WIIM-2020) organized by Department of Chemistry, & International Research Centre Sathyabama Institute of Science and Technology (Deemed to be University) & In Association with CSIR-NML, Madras Centre, Chennai, 6th-10th January 2020.

Others

Awards

An injectable phenethyl isothiocyanate (PEITC)-loaded thermosensitive hydrogel for localized and sustained drug delivery in managing rheumatoid arthritis. **Haloj P,**[#] Konkimalla VB. ICNB 2021, 2nd-5th Feb 2022 (Online Mode).

[#] Awarded with Best Presentation Award (1st Position).

Prakash Haloj
(Prakash Haloj)

Dedication

**I dedicate this thesis to
my beloved Dad and Mom,
my family members, friends, and
teachers who helped me throughout
my journey.**

ACKNOWLEDGEMENTS

I want to express my deepest gratitude to my Ph.D. mentor, Dr. V. Badireenath Konkimalla, for his supervision and support. He has helped me in improving my writing and communication skills a lot. His constant encouragement helped me accomplish this task.

I want to thank my doctoral committee members, Dr. Praful Singru, Dr. Rudresh Acharya, Dr. Shantibhusan Senapati, and Dr. Subhadip Ghosh, for their critical evaluations, suggestions, and constant support. I thank the timely support from Dr. Amit Jaiswal, School of Biosciences and Bioengineering, Indian Institute of Technology (IIT) Mandi, India, for the timely help and collaboration. I thank the SEM imaging facility of the Centre for Interdisciplinary Sciences (CIS), NISER, and the central library, NISER, for their support.

I thank all the faculties and staff at SBS, NISER, for their help and guidance whenever required. I thank Dr. Saurabh Chawla and his team at NISER Animal House for their help and support in the animal-related experiments. I sincerely thank Dr. Saurabh Chawla for his constant support during my Ph.D. tenure and for helping me accomplish the *in vivo* experiments.

I would like to acknowledge the support extended by Mr. Kuna Mahara and Ms. Suchismita Mohanty (Animal house facility, NISER) during the animal experiments, especially in animal requirements and histopathological studies. I am thankful to all the animal house staff for their friendly behavior. I am grateful to Dr. Raj Ganesh J., Application Support Manager, TA Instruments Division, Waters (India) Pvt. Ltd, Bangalore, India, for conducting the rheological studies.

Financial assistance from NISER and the Department of Atomic Energy is gratefully acknowledged.

I am indebted to my lab members, Ms. Soma Mondal, Mr. B. Siva Lokesh, Mr. Rajat Choudhury, and Mr. Ashish Kumar Sahoo, for their guidance, suggestions, and motivation. I thank all my batchmates for their moral support during my Ph.D. journey. I am grateful to Mr. Tathagata Mukherjee for his constant help and support in FACS analysis.

I thank my respected seniors and dear juniors, especially Dr. Pranjal Mahanta, Dr. Omprakash Singh, Dr. Pragyesh Dixit, Dr. P. Sanjai Kumar, Dr. Durga Prasad Biswal, Dr. Dinesh Kumar, Mr. Naresh Kumar G, Mr. Saket Awadhesbhai Patel, and Mr. Abhinav Srivastava for being there by my side whenever required.

I thank all the acquainted and unacquainted persons who ensured the supply of the reagents as and when possible.

My parents, uncles, elder brother, sisters, and close friends have been a constant source of motivation and encouragement- I love you and thank you for believing in me. I am thankful for all their continuous financial support in my tough times.

Prakash Haloi
(Prakash Haloi)

CONTENTS

	Page No.
SUMMARY	i-ii
LIST OF FIGURES	iii-v
LIST OF TABLES	vi
LIST OF ABBREVIATIONS USED	vii-xi
Chapter 1: Introduction	1-45
1.1. Anatomy and physiology of joints	2-4
1.2. Rheumatoid arthritis (RA)	4-6
1.3. Epidemiology	6-7
<i>1.3.1. Global prevalence</i>	6-7
1.4. Risk factors	7-11
<i>1.4.1. Genetics</i>	8-9
<i>1.4.2. Epigenetics</i>	9-10
<i>1.4.3. Gender</i>	10
<i>1.4.4. Smoking</i>	10
<i>1.4.5. Dust inhalation</i>	11
<i>1.4.6. Microbiota</i>	11
1.5. Mechanisms of RA	11-12
<i>1.5.1. Preclinical RA</i>	11-12
<i>1.5.2. Early and established RA</i>	12
1.6. Pathogenesis of RA	12-16
<i>1.6.1. The synovium</i>	13
<i>1.6.2. Joint damage</i>	13-16
1.7. Therapeutics for treating RA	16-20
1.8. Roadmap to key possible therapeutic intervention strategies for treating RA	21-22
1.9. Limitation of traditional RA therapy and role of Nanomedicines in treating RA	22-24
1.10. Natural isothiocyanates as a therapeutic agent in RA therapy	24-32
<i>1.10.1. Phenethyl isothiocyanate (PEITC)</i>	27

1.10.2. Nanodelivery of natural isothiocyanates (ITCs)	27-29
1.10.3. Nanodelivery of PEITC	29-30
1.10.4. Therapeutic advantages of nano delivery systems of natural isothiocyanates (ITCs)	30-32
1.11. Disease-modifying anti-rheumatic drugs (DMARDs), a gold standard therapy for RA	32-35
1.11.1. Methotrexate (MTX)	32-34
1.11.2. Rationale of using MTX-loaded nano delivery system	34-35
1.12. Natural polysaccharide-based stimuli-responsive hydrogels	36-37
1.13. Injectable hydrogels in drug carriers for the RA treatment	37-39
1.14. IA route is an alternative approach to reducing the multiple-dose regimens and maximizing drug concentration in the RA joint	39-41
1.15. Animal models of RA	41-43
1.15.1. Adjuvant-induced arthritis (AIA)	41-42
1.15.2. Collagen-induced arthritis (CIA)	42
1.15.3. Antigen-induced arthritis	42-43
1.15.4. Pristane-induced arthritis (PIA)	43
1.15.5. Genetic animal models of RA	43
1.16. Specific objectives of this study	44-45
Chapter 2: Fabrication, characterization, and assessment of the biosafety and therapeutic efficacy of PEITC-loaded thermosensitive <i>in situ</i> injectable hydrogel system in healthy and RA conditions	46-87
2.1. Fabrication of PEITC-loaded CS/PF-127 hydrogel and assessment of various physicochemical parameters	47-59
2.1.1. Preparation and physicochemical characterization of PEITC-loaded hydrogel	47-51
2.1.2. Characterization of PEITC-loaded hydrogel using FTIR and FESEM	51-53
2.1.3. Swelling and degradation profile of PEITC-loaded hydrogel <i>in vitro</i>	53-55
2.1.4. <i>In vitro</i> release profile of PEITC-loaded hydrogel	55-58

2.1.5. <i>In vitro</i> hemolytic activity of PEITC-loaded hydrogel	58-59
2.2. <i>In vivo</i> evaluation of PEITC-loaded hydrogel formulations	59-69
2.2.1. <i>In vivo</i> gel formation and skin biocompatibility studies	60-51
2.2.2. <i>In vivo</i> pharmacokinetics and tissue biodistribution studies of PEITC-loaded hydrogel	62-65
2.2.3. <i>In vivo</i> toxicity and safety evaluation of PEITC-loaded hydrogel in healthy rats	65-69
2.3. Development of adjuvant-induced advanced arthritis animal model (12-day) in rats	70-72
2.4. Cytotoxicity and biocompatibility of PEITC-loaded hydrogel <i>in vitro</i>	72-74
2.5. Evaluation of therapeutic efficacy of PEITC-loaded hydrogel in RA condition in the rat model	74-86
2.5.1. <i>Effect of the PEITC-loaded hydrogel on the various arthritis parameters</i>	74-78
2.5.2. <i>Effect of the PEITC-loaded hydrogel on the oxidative stress and antioxidant markers in RA</i>	78-80
2.5.3. <i>Effect of the PEITC-loaded hydrogel on the cytokines profiles in RA</i>	80-83
2.5.4. <i>Assessment of biosafety and histological analysis of the PEITC-loaded hydrogel in RA</i>	83-86
2.6. Summary of the chapter	87
Chapter 3: Design of a dual nano-particulate drug (MTX and PEITC)-loaded smart hydrogel as a co-delivery system to enhance its synergistic activity in RA conditions	88-141
3.1. Preparation of MTX NP	91-92
3.2. Preparation and optimization of PEITC NE	92-93
3.3. Characterization of drug-loaded nanoparticle formulation	94-95
3.4. Fabrication of dual-drug nanoparticles loaded hydrogel	96
3.5. Characterization of dual-drug nanoparticles loaded hydrogel	96-109
3.5.1. <i>FTIR and FESEM studies</i>	96-99
3.5.2. <i>Drug content</i>	99

3.5.3. <i>Solubility studies</i>	99-101
3.5.4. <i>Sol-gel phase transition studies</i>	101-103
3.5.5. <i>In-vitro degradation studies</i>	104-105
3.5.6. <i>Injectability studies</i>	105
3.5.7. <i>Rheological characteristics</i>	106-109
3.6. <i>In-vitro drug release studies</i>	109-111
3.7. <i>In-vitro drug release kinetics</i>	111-113
3.8. <i>Stability studies for different hydrogel formulations</i>	113-114
3.9. <i>Cell-based studies</i>	114-123
3.9.1. <i>Cytotoxicity and biocompatibility of dual-drug nanoparticles loaded hydrogel in vitro</i>	114-116
3.9.2. <i>Effect of dual-drug nanoparticles loaded hydrogel in cell apoptosis</i>	116-118
3.9.3. <i>In vitro evaluation of anti-inflammatory efficacy of dual-drug nanoparticles loaded hydrogel</i>	118-120
3.9.4. <i>Effect of dual-drug nanoparticles loaded hydrogel on the mRNA expression level</i>	120-123
3.10. <i>Anti-arthritis effects of the dual-drug nanoparticles loaded hydrogel</i>	123-139
3.10.1. <i>Effects of dual-drug nanoparticles loaded hydrogel on arthritis parameters in FCA-induced arthritic rats</i>	123-127
3.10.2. <i>Effect of dual-drug nanoparticles loaded hydrogel on oxidative stress biomarkers in FCA-induced arthritic rats</i>	127-131
3.10.3. <i>Effect of dual-drug nanoparticles loaded hydrogel on serum cytokines level in FCA-induced arthritic rats</i>	131-134
3.10.4. <i>Toxicity assessment of dual-drug nanoparticles loaded hydrogel in the FCA-induced arthritic rats</i>	134-136
3.10.5. <i>Histological analysis of dual-drug nanoparticles loaded hydrogel in the FCA-induced arthritic rats</i>	136-139
3.11. <i>Summary of the chapter</i>	140-141
Chapter 4: Conclusion	142-146
4.1. <i>Conclusion and future work</i>	143-146

Chapter 5: Materials and methods	147-181
5.1. Materials	148-151
5.1.1. Chemicals and reagents used	148-150
5.1.2. Cell lines and primary cells	150
5.1.3. Kits	150-151
5.1.4. Monoclonal antibodies	151
5.1.5. Animals	151
5.2. Methods	151-181
5.2.1. Preparation and characterization of PEITC-loaded hydrogels	152-167
5.2.1.1. Preparation of the PF-127/CS hydrogel	152
5.2.1.2. Incorporation of PEITC into PF-127/CS hydrogel	152-153
5.2.1.3. Physicochemical characterization	153-157
5.2.1.3.1. <i>Sol-gel-sol phase transition measurements ($T_{sol-gel}$) in PEITC-loaded hydrogels</i>	153-154
5.2.1.3.2. <i>Injectability of hydrogels</i>	154
5.2.1.3.3. <i>FTIR characterization</i>	154-155
5.2.1.3.4. <i>Morphological characterization of the hydrogels</i>	155
5.2.2.3.5. <i>Evaluation of pH-responsiveness of hydrogel (swelling ratio)</i>	155
5.2.2.3.6. <i>In vitro hydrogel degradation studies</i>	155-156
5.2.2.3.7. <i>In vitro drug release studies</i>	156-157
5.2.2.3.8. <i>Determination of PEITC using BDT assay</i>	157
5.2.1.4. Hemocompatibility assessment	158
5.2.1.5. <i>In vivo</i> gel formation and degradation studies	158-159
5.2.1.6. Biocompatibility assessment	159
5.2.1.7. Sample preparation and conditions for HPLC	159-160
5.2.1.8. Pharmacokinetic analysis using HPLC	160
5.2.1.9. <i>In vivo</i> biodistribution studies	161
5.2.1.10. <i>In vivo</i> safety studies	161-162
5.2.1.11. Development of an advanced AIA rat model	162
5.2.1.12. <i>In vitro</i> biocompatibility of PEITC-loaded hydrogel on isolated primary cells	162-164

5.2.1.12.1. <i>Isolation and primary culture of FLS cells</i>	162-163
5.2.1.12.2. <i>In vitro cytotoxicity test (MTT assay)</i>	163-164
5.2.1.13. <i>In vivo therapeutic efficacy of PEITC-loaded hydrogel</i>	164-167
5.2.1.13.1. <i>Induction of AIA in SD rats</i>	164
5.2.1.13.2. <i>Assessment of arthritis progression upon FCA administration</i>	164-165
5.2.1.13.3. <i>Blood collection and serum separation</i>	165-166
5.2.1.13.4. <i>Determination of thymus and spleen index</i>	165-166
5.2.1.13.5. <i>Evaluation of oxidative stress</i>	166-167
5.2.1.13.6. <i>Evaluation of cytokines levels in the serum</i>	167
5.2.1.13.7. <i>Biochemical test to assess liver and kidney function</i>	167
5.2.2. <i>Preparation and therapeutic evaluation of dual-drug nanoparticles loaded hydrogel</i>	168-181
5.2.2.1. <i>Fabrication and characterization of drug-loaded nanosystems</i>	168-170
5.2.2.1.1. <i>Fabrication of blank NP and MTX NP</i>	168
5.2.2.1.2. <i>Preparation of PEITC NE</i>	168-169
5.2.2.1.3. <i>Determination of % EE and % DL of MTX NP</i>	169-170
5.2.2.1.4. <i>Drug content for the optimized PEITC NE</i>	170
5.2.3.1.5. <i>PS, PDI, and ZP</i>	170
5.2.2.2. <i>Preparation and characterization of dual-drug nanoparticles loaded hydrogel</i>	170-175
5.2.2.2.1. <i>Fabrication of dual-drug nanoparticles loaded hydrogel</i>	170-172
5.2.2.2.2. <i>FTIR study</i>	172
5.2.2.2.3. <i>Determination of drug content</i>	172
5.2.2.2.4. <i>Solubility studies</i>	172-173
5.2.2.2.5. <i>Determination of gelation time</i>	173
5.2.2.2.6. <i>In vitro degradation studies</i>	173
5.2.2.2.7. <i>Injectability of hydrogels</i>	174
5.2.2.2.8. <i>Morphological characterization of the dual-drug nanoparticles loaded hydrogel</i>	174
5.2.2.2.9. <i>Rheological properties of the dual-drug nanoparticles loaded hydrogel</i>	174

5.2.2.2.10. <i>In-vitro drug release and kinetics studies</i>	174-175
5.2.2.2.11. <i>Stability studies</i>	175
5.2.3.3. Cell-based studies	175-178
5.2.3.3.1. <i>In vitro cytotoxicity test (MTT assay)</i>	175
5.2.3.3.2. <i>Apoptosis detection assay</i>	175-176
5.2.2.3.3. <i>ELISA assay</i>	176-177
5.2.2.3.4. <i>Quantitative RT-PCR analysis</i>	177-178
5.2.3.4. <i>In vivo therapeutic efficacy of dual-drug nanoparticles loaded hydrogel</i>	179-181
5.2.3.4.1. <i>AIA induction and monitoring</i>	179
5.2.3.4.2. <i>Assessment of arthritis progression upon FCA administration</i>	179-180
5.2.3.4.3. <i>Blood collection and serum separation</i>	180
5.2.3.3.4. <i>Determination of thymus and spleen index</i>	180
5.2.3.3.5. <i>Evaluation of oxidative stress</i>	180
5.2.3.3.6. <i>Evaluation of cytokines levels in the serum</i>	180
5.2.3.3.7. <i>Biochemical test to assess liver and kidney function</i>	181
5.2.3.3.8. <i>Histopathological assessment</i>	181
5.2.3.5. Statistical analysis	181
Chapter 6: Bibliography	182-224

SUMMARY

Rheumatoid arthritis (RA) is an autoimmune condition that accompanies chronic inflammation of joints with limited therapeutic options. This disease dramatically affects patients' quality of life, as no single treatment can completely halt the disease's progression. In my Ph.D. thesis, I attempted to treat RA holistically and synergistically by co-delivering Methotrexate (MTX), a standard slow-acting anti-rheumatic drug, and Phenethyl isothiocyanate (PEITC), a poorly bioactive phytochemical, using *in situ* hydrogel formulation. As a first step, a thermosensitive hydrogel-based carrier system was prepared to incorporate PEITC, which showed improved efficacy. An exhaustive study *in vitro* and animals (healthy and disease) was conducted at different stages that simulated the physiological conditions. PEITC-loaded hydrogel possessed desired properties such as superior mechanical strength, thermosensitivity, injectability, biocompatibility, and biosafety that sustainedly released PEITC from the target site. The *in vivo* arthritis study showed significant suppression of inflammation following PEITC-loaded hydrogel (PH50) administration into the knee joint.

As RA is a multifactorial systemic autoimmune disease with few treatment options, my next attempt was to develop a hydrogel as a combinational drug delivery system that can be used for the co-delivery of regimens that can alleviate the disease condition *via* diverse mechanisms. Nanodelivery systems are an excellent approach for the prolonged release of drugs, increasing the residence time at inflamed joints. Combining nanotechnology with materials science can result in better therapeutic efficacy of drugs in the joints, ensuring relief in stressful RA conditions. Therefore, this study prepared individual nanoformulations of MTX (as nanoparticle) and PEITC (as nanoemulsion) to mask their pharmaceutical limitation. The MTX and PEITC NPs were optimized for desired particle size characteristics. The dual-drug nanoparticles loaded

hydrogel (DD NP HG), when injected intra-articularly (IA) into the FCA-induced animals, showed marked amelioration of chronic inflammation and assisted in restoring bone morphology in RA rats.

The *in vitro* cell viability studies on the primary fibroblast-like synoviocytes (FLS) (healthy and RA conditions) showed that both the hydrogel formulations (PH50 and DD NP HG) were biocompatible in normal FLS but showed an inhibitory effect on RA-FLS.

Overall, the thesis confirmed that the site-specific injection of the hydrogel was biocompatible in healthy animals and prolonged the anti-inflammatory activity of PEITC in arthritic conditions. Further, combinational hydrogel-based localized therapy has been shown to enhance the anti-inflammatory efficacy and reverse cartilage disruption through a synergistic effect between two nanoparticulate forms of MTX and PEITC, which can effectively improve the drawbacks of free forms of both drugs. From the thesis work, I successfully optimized and fabricated a novel smart hydrogel-based delivery system for poorly soluble drugs to either deliver them singly or in combination to attain greater efficacy. Such nano-delivery systems have significant applications in diseases that require chronic or multi-drug treatment.

Keywords: Thermosensitive hydrogel; Phenethyl isothiocyanate; Rheumatoid arthritis; Methotrexate; Intra-articular; Adjuvant induced arthritis.

LIST OF FIGURES

Figure No	Figure legend
Figure 1	Structure of a typical healthy synovial joint.
Figure 2	Schematic view of a typical joint and its changes in RA
Figure 3	The global prevalence of RA
Figure 4	Mechanisms involved in the initiation and progression of RA
Figure 5	A schematic roadmap to key possible existing and developing treatment strategies for treating RA.
Figure 6	Various nano-based drug delivery systems in treating RA with administration routes
Figure 7	Nanomedicine strategies for the treatment of RA
Figure 8	Natural isothiocyanates (ITCs)
Figure 9	The main biological activities of ITCs
Figure 10	Molecular structure and cellular function on various cell types of MTX in RA condition.
Figure 11	Schematic representation of the IA administration of an <i>in situ</i> gelling drug formulation into RA joint and changes after treatment (healthy cartilage)
Scheme 1	Schematic overview of the preparation of BH and PEITC-loaded hydrogel
Figure 12	Preparation and characterization of the PEITC-loaded hydrogel
Figure 13	Characterization of PEITC-loaded hydrogel using FTIR and FESEM
Figure 14	The swelling and degradation properties of PEITC-loaded hydrogel <i>in vitro</i>
Figure 15	The drug release properties of PEITC-loaded hydrogel <i>in vitro</i>
Figure 16	Hemolytic activity of PEITC-loaded hydrogel
Figure 17	<i>In vivo</i> biodegradation and biocompatibility of PEITC-loaded hydrogel
Figure 18	<i>In vivo</i> pharmacokinetics and tissue biodistribution of PEITC-loaded hydrogel
Figure 19	<i>In vivo</i> toxicity and safety evaluation in healthy rats
Figure 20	<i>In vivo</i> toxicity and safety evaluation in healthy rats
Figure 21	Development of advanced arthritis animal model (12-day model)
Figure 22	Cytotoxicity and biocompatibility assay of PEITC-loaded hydrogel <i>in vitro</i>
Figure 23	<i>In vivo</i> therapeutic effect of the PEITC-loaded hydrogel in FCA-induced rats

Figure 24	Estimation of oxidative stress, antioxidant, and neutrophil infiltration markers in RA
Figure 25	Quantitative estimation of pro-inflammatory, anti-inflammatory, and bone erosion markers in RA
Figure 26	Biosafety and histological analysis in RA
Scheme 2	A schematic illustration of the preparation and a detailed combinatorial treatment schedule for treating RA using dual-drug nanoparticles loaded hydrogel
Figure 27	Observation of creaming and phase separation in preparing different PEITC NE batches.
Figure 28	Characterization of NP and NE
Figure 29	Characterization of dual-drug nanoparticles loaded hydrogel
Figure 30	% Solubility studies
Figure 31	Sol-gel phase transition characteristics and determination of gelation time
Figure 32	<i>In vitro</i> degradation properties of dual-drug nanoparticles loaded hydrogel
Figure 33	Injectable performance of the different hydrogel formulations
Figure 34	The rheological properties of BD NP HG and DD NP HG
Figure 35	The drug release properties of dual-drug nanoparticles loaded hydrogel <i>in vitro</i>
Figure 36	The drug release kinetics of dual-drug nanoparticles loaded hydrogel <i>in vitro</i>
Figure 37	Cytotoxicity and biocompatibility assay of dual-drug nanoparticles loaded hydrogel <i>in vitro</i>
Figure 38	Effects of dual-drug nanoparticles loaded hydrogel on apoptosis in RA-FLS cells
Figure 39	Effect of dual-drug nanoparticles loaded hydrogel on pro-inflammatory cytokines in LPS-stimulated RA-FLS cells
Figure 40	Effect of dual-drug nanoparticles loaded hydrogel against bone destruction in LPS-stimulated RA-FLS.
Figure 41	<i>In vivo</i> anti-arthritic effect of the dual-drug nanoparticles loaded hydrogel in FCA-induced RA rats.
Figure 42	Evaluation of oxidative stress, antioxidant, and neutrophil infiltration markers in FCA-induced RA rats
Figure 43	Estimating pro-inflammatory, anti-inflammatory, and bone erosion markers in FCA-induced RA rats.

- Figure 44 Toxicity assessment in FCA-induced RA rats.
- Figure 45 Histopathological assessment of dual-drug nanoparticles loaded hydrogel in bone destruction and cartilage damage in RA model
- Figure 46 The probable mechanism of combinational hydrogel (DD NP HG) in treating RA

LIST OF TABLES

Table No.	Table Legend
Table 1	Overview of the different classes of drugs currently approved for RA treatments and under investigation.
Table 2	Pharmacokinetic parameters of Free PEITC (oral and SC) and PEITC-loaded hydrogel in rats' blood.
Table 3	Different polymer compositions with other % EE and % DL
Table 4	Different surfactant concentrations for the preparation of NE
Table 5	Particle size characterization of PEITC NE and MTX NP formulations.
Table 6	Different compositions of SA and PF-127 for the preparation of <i>in-situ</i> hydrogels
Table 7	Drug content (%) of different hydrogel formulations
Table 8	Release kinetic models and their R ² values of different hydrogel formulations
Table 9	Stability studies at 4 °C for different hydrogel formulations for 60 days.
Table 10	Comparison of anti-inflammatory and anti-rheumatic activity of different PEITC and MTX based formulation
Table 11	List of chemicals and reagents used
Table 12	List of cell lines and primary cells
Table 13	List of kits
Table 14	List of monoclonal antibodies
Table 15	Name and description of hydrogel preparations related to methods section –Part A
Table 16	Different polymer compositions for the preparation of MTX NP
Table 17	Different surfactant concentrations for the preparation of PEITC NE
Table 18	Different compositions of SA and PF-127 for the preparation of <i>in-situ</i> hydrogels
Table 19	Name and description of hydrogel preparations related to methods section –Part B
Table 20	Sequences of the primers used for real-time PCR

LIST OF ABBREVIATIONS USED

ACPA	Autoantibodies against citrullinated peptides
AIA	Adjuvant-induced arthritis
ALT	Alanine transaminase
AST	Aspartate transaminase
BD NP HG	Blank dual nanoparticles loaded hydrogel.
BDT	1, 2 Benzenedithiol
BH	Blank hydrogel
BUN	Blood urea nitrogen
CRE	Creatinine
CS	Chitosan
DD NP HG	Dual-drug nanoparticles loaded with hydrogel.
DL	Drug loading
DLS	Dynamic light scattering
DMARDs	Disease-modifying anti-rheumatic drugs
DMSO	Dimethyl sulfoxide
EDTA	Ethylenediaminetetraacetic acid
ELISA	Enzyme-linked immunoassay
FCA	Freund's Complete Adjuvant
FESEM	Field emission scanning electron microscopy
FLSs	Fibroblast-like synoviocytes
FTIR	Fourier transform infrared spectroscopy.
GM-CSF	Granulocyte-macrophage colony-stimulating factor
GSH	Reduced glutathione
H & E	Hematoxylin and eosin
HLB	Hydrophilic–lipophilic balance
HPLC	High-Performance Liquid Chromatography.
IA	Intra-articular
IL-10	Interleukin-10
IL-1 β	Interleukin- 1 beta

IL-6	Interleukin 6
ITCs	Natural isothiocyanates
MDA	Malondialdehyde
MHC	Major histocompatibility complex
MMP	Matrix metalloproteinase
MPO	Myeloperoxidase
MTT	Methyl-thiazolyl diphenyl-tetrazolium bromide
MTX	Methotrexate
MTX NP	MTX-loaded PLGA nanoparticles
MTX NP HG	MTX-PLGA nanoparticle-loaded hydrogel
NE	Nanoemulsion
N-FLS	Normal- Fibroblast-like synoviocytes
NO	Nitric oxide
NP	Nanoparticles
Nrf2	Nuclear factor erythroid 2-related factor-2
NSAIDs	Non-steroidal anti-inflammatory drugs
OA	Osteoarthritis
PBS	Phosphate-buffered saline
PDI	Polydispersity index
PEITC	Phenethyl isothiocyanate
PEITC NE	PEITC nanoemulsion
PEITC NE HG	PEITC nanoemulsion-loaded hydrogel
PEITC20	Free PEITC at conc. 20 mg/mL
PEITC50	Free PEITC at conc. 50 mg/mL
PEITC60	Free PEITC at conc. 60 mg/mL
PF-127	Pluronic F-127
PS	Particle size
PH20	PEITC-loaded hydrogel at conc. 20 mg/mL
PH40	PEITC-loaded hydrogel at conc. 40 mg/mL
PH50	PEITC-loaded hydrogel at conc. 50 mg/mL
PH60	PEITC-loaded hydrogel at conc. 60 mg/mL

PLGA	Poly lactic-co-glycolic acid
PTPN22	Protein tyrosine phosphatase non-receptor 22
RA	Rheumatoid arthritis
RA-FLS	Rheumatoid arthritis- Fibroblast-like synoviocytes
RANKL	Receptor activator of nuclear factor- κ b ligand
RF	Rheumatoid factor
RT	Room temperature
SA	Sodium alginate
SC	Subcutaneous
SO-FG	Safranin O-fast green
T&B	Toluidine blue
TNF - α	Tumor necrosis factor-alpha
ZP	Zeta potential

Chapter 1

Introduction

1.1. Anatomy and physiology of joints

The skeletal system provides vital mechanical support to the body and its internal organs. It also smoothly coordinates with the skeletal muscles for harmonious body movement. Joints are the connecting regions between the two bones that enable this movement. Based on the degree of movement, joints are classified as diarthrosis (movable joints), amphiarthrosis (partially movable joints), and synarthrosis (immovable joints), otherwise as fibrous, cartilaginous and synovial joints depending on the nature of connecting tissues. In the body, most joints are diarthrosis, and all are synovial. The primary function of the synovial joints is to facilitate limited movement and transfer forces from one bone to another. Small joints of the hand, elbow, shoulder, hip, and knee are all synovial (Sawhney and Aggarwal, 2016). The structure of a typical healthy synovial joint with its different components is shown in **Figure 1**.

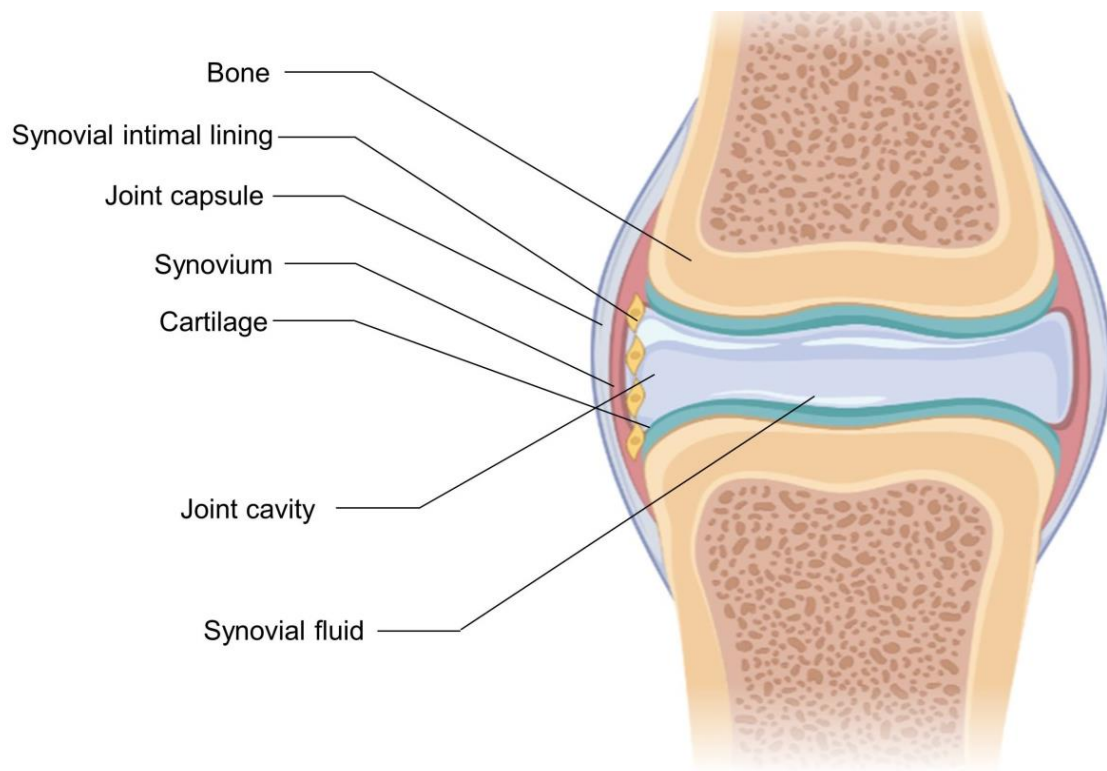


Figure 1. Structure of a typical healthy synovial joint.

A synovial joint comprises different musculoskeletal tissues such as articular cartilage, tensile tissues, synovium, synovial fluid, bone, ligament, and tendon attached at the entheses. A layer of hyaline cartilage covering the articulating bones in the synovial joint acts as a shock absorber to reduce friction during movement. The presence of a joint capsule (synovial cavity) surrounding the joint and the existence of synovial fluid in the joint capsule is the distinguishing primary anatomic property of the synovial joint from others. The synovium or synovial membrane is a soft tissue lining around the synovial surfaces comprising the subintima (outer layer) and intima (inner layer). Various fat cells, connective tissue cells, and blood and lymphatic vessels contain the subintima, and the intima consists of a thin sheet of synovial intimal cells (synoviocytes). The synovial intimal cells are composed of two morphologically different types of cells (Bartok and Firestein, 2010; Edwards, 1994; Nygaard and Firestein, 2020).:

- Type A cells (Macrophages) - non-fixed cells with antigen-presenting abilities essential for removing cell debris and wastes in the joint cavity.
- Type B cells (Fibroblast-like synovial cells also known as synovial fibroblasts) – cells that produce specialized matrix components (hyaluronan, fibronectin, and collagens)

Synovial fluid, or synovia, is a thin fluid secreted by the synovium into the joint cavity with two primary functions. (1) act as a transport medium for nutrients to nourish articular cartilage and (2) protect and lubricate the articulating surfaces for promoting the mechanical function of the joints. As a plasma dialysate, the synovial fluid contains all the plasma proteins, including fibrinogen, alpha-2, and beta-2 macroglobulin (Lillian A. Mundt, Kristy Shanahan, 2011).

Hyaluronate, a mucopolysaccharide synthesized by the synovium, is mixed with this plasma dialysate to produce the synovial fluid. In addition, a typical synovial fluid contains glucose, uric acid, a wide range of cells (monocytes, neutrophils, lymphocytes), and numerous enzymes (alkaline phosphatase, lactic dehydrogenase, acid phosphatase). In a healthy joint, a high concentration of hyaluronic acid in the synovial fluid is maintained to provide exceptional viscoelasticity and lubricating properties, especially during high shear conditions; however, hyaluronic acid alone cannot offer boundary lubrication (the ability of synovial fluid to lower friction between opposing and pressured cartilaginous surfaces irrespective of viscosity). Lubricin is another abundant component of synovial fluid responsible for the boundary lubrication of articular cartilage that dissipates strain energy within the synovial fluid (Jay, 1992; Jay et al., 2007; Swann et al., 1977). Lubricin is a mucinous glycoprotein with globular amino- and carboxyl-terminal domains and a central region whose side chains are substantially modified with O-linked oligosaccharide.

1.2. Rheumatoid arthritis (RA)

RA is a prevalent form of inflammatory arthritis and one of the leading causes of disability (Firestein, 2003). The term "*rheumatoid*" refers to "any defluxion of thin humor" and is derived from the Greek words "*rheuma*," which means that which flows, and "*oid*," which means like or in the form of. The term "*arthritis*" comes from the Greek "*arthrosis*," which means joint and denotes inflammation (Parish, 1963). RA is a chronic autoimmune condition that predominantly affects the lining of the synovial joints and results in significant swelling, tenderness, and destruction of synovial joints, leading to severe disability. It has affected 1% of the world's population (especially women) in all age groups, leading to progressive disability, premature mortality, and socioeconomic burdens. There are three stages of RA progression:

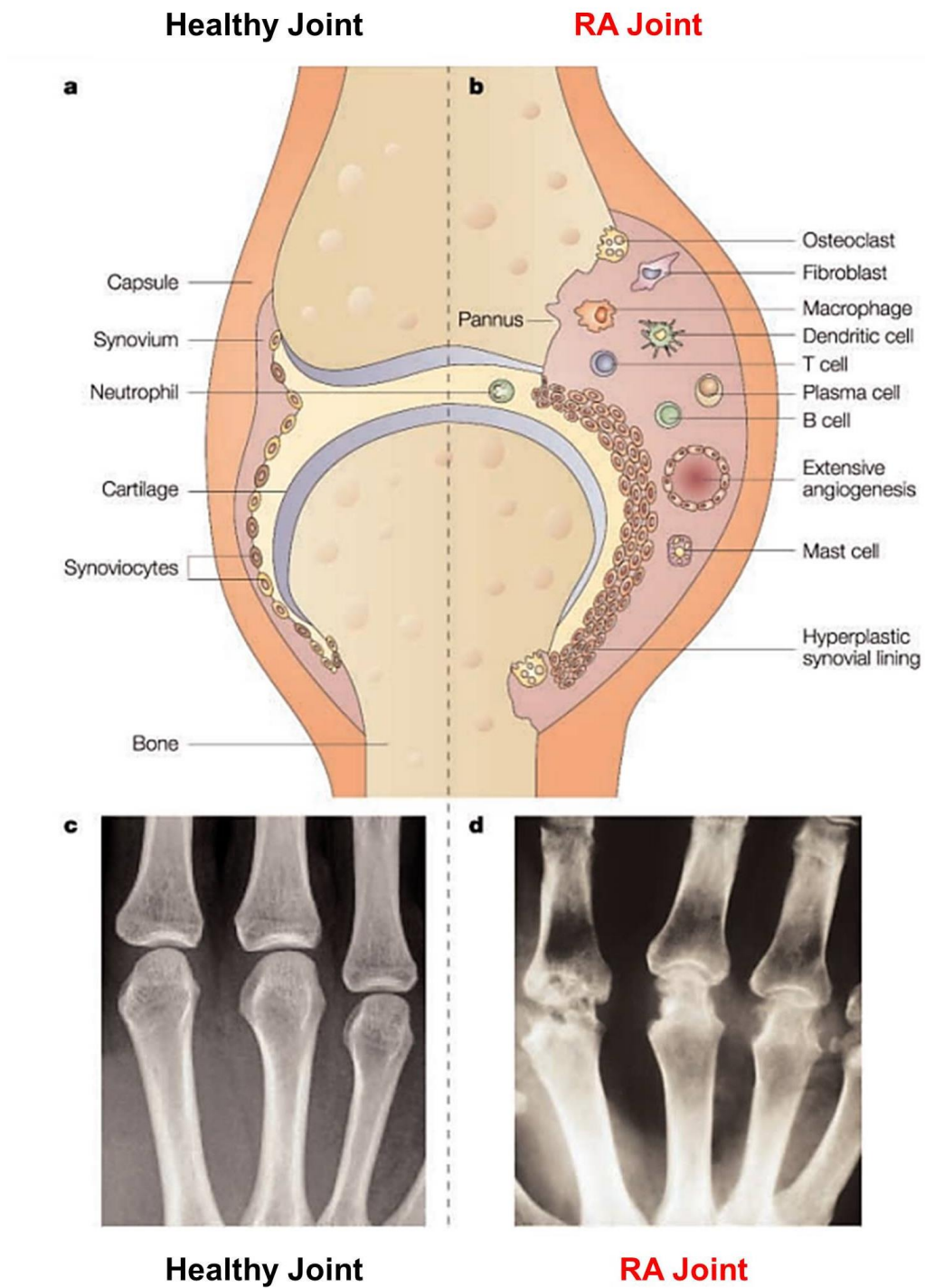


Figure 2. Schematic view of a typical joint and its changes in RA. (a). Healthy synovial joint. (b). RA joint. Radiographic images of joint space of (c). Healthy, and (d). RA patient has three metacarpophalangeal joints from a hand. Figure courtesy (Smolen and Steiner, 2003)

Stage 1: Enlargement of the synovial line that characterizes the initial stage, with discomfort, warmth, stiffness, redness, and swelling surrounding the joint.

Stage 2: thickening of the synovium due to pannus formation (i.e., rapid division and expansion of cells).

Stage 3: secretion of enzymes by the inflamed cells that degrade bone and cartilage, frequently resulting in the affected joint losing its shape and alignment, increased pain, and loss of movement.

Although RA is a chronic condition, spontaneous remissions do not happen often. Instead, RA symptoms continue, waxing and waning in intensity, and the joint structures gradually deteriorate, resulting in deformities and disability (Guo et al., 2018; McInnes and Schett, 2017).

A typical joint and its changes in RA are schematically shown in **Figure 2a-b**, where major distinguishing features between a regular joint and an RA joint are presented. **Figures 2c-d** are sample radiographs of a healthy metacarpophalangeal joint and a joint with established RA (Smolen and Steiner, 2003). Here, bone destruction is the hallmark of RA joints where the joint spaces are narrowed or disappeared as a sign of cartilage degradation and destruction of the adjacent bone (also termed 'bone erosion'). On the other hand, in a healthy joint, the metacarpophalangeal minute anatomic joint space showed no sign of bone erosion and cartilage destruction (as seen in **Figure 2c**).

1.3. Epidemiology

1.3.1. Global prevalence

Globally, there is regional variation in the prevalence of RA, where a higher frequency of occurrence is noted in industrialized nations. This may be due to exposure to environmental risk factors, genetic variables, and diverse demography, as well as exposure to environmental risk

factors. Strong trends in the severity of RA have likely decreased over the past three decades due to improved disease management and changes in therapy paradigms. The prevalence of RA is also on the rise. Frequent risk factors for RA include non-modifiable characteristics, such as genetics and sex, and modifiable lifestyle-associated variables. According to the 2017 Global Burden of Disease (GBD) study (**Figure 3**), between 1990 and 2017, the number of years worldwide with a disability related to RA increased from 0.24 % to 0.31 % (Finckh et al., 2022). India is estimated to have 10 million persons with RA, putting the prevalence at 0.7 %. (Dar et al., 2022).

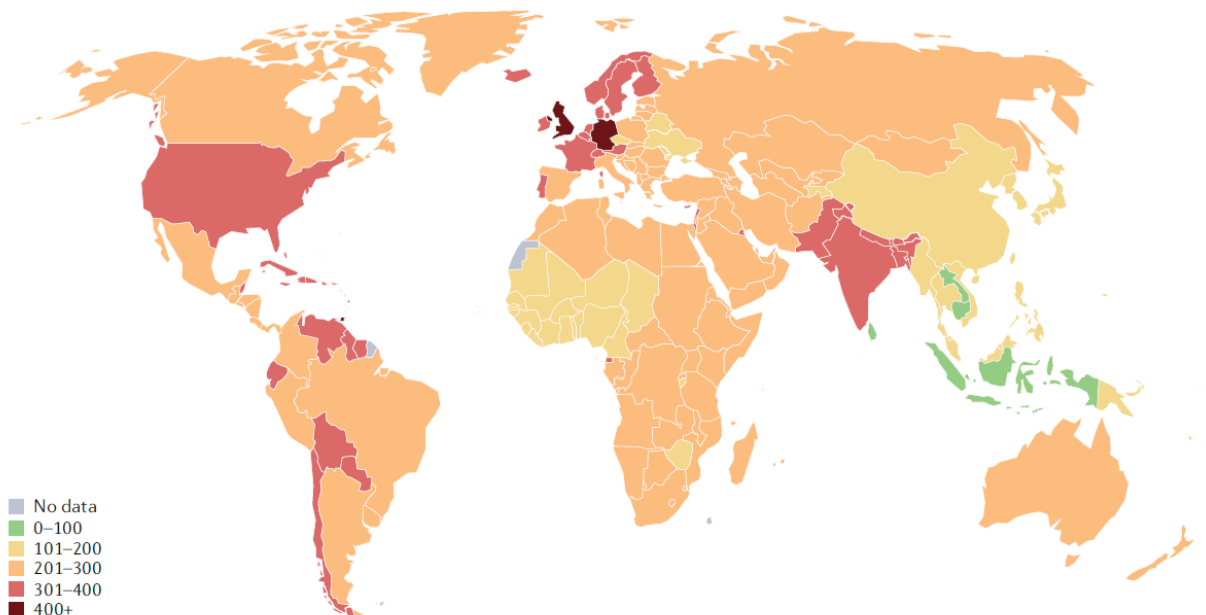


Figure 3. The global prevalence of RA. The key in the figure indicates the reported RA prevalence ranges by country (per 100,000 of the population). Figure courtesy (Finckh et al., 2022).

1.4. Risk factors

Risk factors such as heredity, gender, and environmental factors impact RA development. Smoking, exposure to silica, vitamin D deficiency, microbiota alterations, and obesity are

commonly reported environmental risk factors; however, studies on some of these are controversial.

1.4.1. Genetics

For more than three decades, it has been understood that genetic factors influence the occurrence and severity of RA. Compared to the general population, first-degree relatives of patients are 2–10 times more likely to be diagnosed with RA. The extent to which genetics contributes to RA pathogenesis is still debatable. Twin studies suggest that genetic factors may account for up to 60 % of the occurrence of RA, while the more common estimate is 10 % to 25 %. As a result of gene-environment interactions, the estimated genetic contribution may differ between researchers (MacGregor et al., 2000). The major histocompatibility complex (MHC) contains the alleles recognized as RA's most significant risk factors. According to estimates, one-third of the genetic risk for RA is believed to be located in this region. Most, but probably not all, of this risk is caused by allelic variation in the HLA-DRB1 gene, which codes for the MHC II - chain protein (Gregersen et al., 1987). The shared epitope, located in the 3rd hypervariable region of the HLA-DR-chain at amino acid positions 70 to 74, is shared by the disease-associated HLA-DRB1 alleles. The development of anti-CCP antibodies and worse disease prognosis is linked to carriers of the shared epitope alleles (Gregersen et al., 1987).

Genome-wide association studies (GWAS) identified numerous non-MHC-related genes influencing RA susceptibility. One of the most notable instances of a non-MHC gene controlling the risk of RA is the protein tyrosine phosphatase non-receptor 22 (PTPN22) genes. Patients from various parts of Europe have varying frequencies of this gene (e.g., 3–10 %), whereas patients with East Asian ancestry have shown absence (Viante et al., 2016, 2012). The lymphoid tyrosine phosphatase protein, which is encoded by PTPN22, regulates the activity of T and B

cells. The gain-of-function in the protein caused by inheriting the PTPN22 risk allele is thought to cause aberrant thymic selection of autoreactive T and B cells and is believed to be predominantly linked to anti-CCP-positive disease (Stahl et al., 2010). Other genetic loci probably have less significant functional effects, which may be mediated alone or in combination, for instance, by altered co-stimulatory pathways (such as CD28 and CD40), cytokine signaling, and innate immune activation (Barra et al., 2011; Nell-Duxneuner et al., 2010).

Patients with the shared epitope are more likely to have a higher risk of developing RA. Autoantibodies against citrullinated peptides (ACPAs) and IgG (rheumatoid factor, RF) are well documented to be associated with the seropositivity of RA pathogenesis. At the time of diagnosis, 50–70% of patients had these recognizable autoantibodies for rheumatoid arthritis, and they were remarkably stable throughout the disease (Lenz et al., 2015; Viatte et al., 2015).

1.4.2. Epigenetics

Epigenetics is vital in RA pathogenesis, most likely by combining environmental and genetic variables. An epigenome-wide association study identified ten differentially methylated sites that genetically increase the chances of developing RA. The biology of synovial fibroblasts and leucocytes can also be controlled by altered histone acetylation and DNA methylation. A DNA methylation study from unrelated RA individuals reported an exciting result wherein nine clusters exhibiting distinct HLA region methylation patterns were obtained compared to healthy controls. This shows that altered DNA methylation partially mediates the genetic impact of HLA risk variations (Liu et al., 2013). DNA methylation provides an avenue by which environmental factors can affect cellular activity changes. For instance, ACPA-positive RA smokers who carried the HLA DRB1 risk allele had higher levels of methylation than those who did not; this

difference in methylation was not seen in non-smokers (Smolen et al., 2018). It is interesting to note from the two studies that different DNA methylation and transcription patterns exist in fibroblast-like synoviocytes (FLS) from the joints of RA patients. This finding may better explain a mechanism as to why RA tends to be symmetrical and affects some joints more severely than others (Frank-Bertoncelj et al., 2017).

1.4.3. Gender

Women are two to three times more likely to develop RA than men, where the cumulative lifetime risk for developing adult-onset RA in men is estimated at 1.7 % and 3.6 % in women. The greater prevalence of RA in women is partially linked to the immune system-stimulating properties of estrogen. This area of research to investigate the role of hormonal variables in RA development is still in progress. Although disease remission is usually associated with pregnancy, and disease flare-ups are common postpartum, nulliparity frequently increases the risk of RA in women. Women typically have symptoms of RA around middle age or during menopause. Men who developed the disease later tested positive for RF and had higher ACPA titers (Alpizar-Rodríguez et al., 2017; Crowson et al., 2011; Ngo et al., 2014).

1.4.4. Smoking

A gradual increase in tobacco usage increases the risk of RA. The association between RA and smoking is more pronounced or is restricted to ACPA-positive individuals harboring even one copy of the common epitope. The current smoking status is linked to greater levels of pro-inflammatory cytokines and more advanced RA conditions. Smoking strongly correlates with hypomethylation in particular DNA sequences, indicating that epigenetic modifications may be the mechanism through which smoking increases the risk of RA Pathogenesis (Sokolove et al., 2016; Sugiyama et al., 2010; Svendsen et al., 2016; Vesperini et al., 2013).

1.4.5. Dust inhalation

Exposure to silica is a potential environmental risk factor for RA. A study on firefighters and other emergency responders exposed to dust at the 2001 World Trade Center collapse site in New York, USA, reported a significantly high number of patients with systemic autoimmune illnesses, including RA. A group of Malaysian women was also shown to have a considerably higher chance of developing RA after exposure to textile dust at work (Stolt et al., 2005; Too et al., 2016; Webber et al., 2015).

1.4.6. Microbiota

A higher risk of RA is also linked to periodontal disease. Interestingly, *Porphyromonas gingivalis* and *Aggregatibacter actinomycetemcomitans* are two oral microbiota species hypothesized to play a role in the relationship between RA and periodontal disease. The gut microbiota, in addition to periodontal microbiota, may also be relevant in RA condition, where the biodiversity of the gut microbiota is reduced in RA patients (Chen et al., 2016; Hajishengallis, 2015; Kharlamova et al., 2016; Konig et al., 2016).

1.5. Mechanisms of RA

1.5.1. Preclinical RA

RA's pathophysiology begins in most individuals' years before the clinical disease becomes apparent, while an early onset indicating a rapid immunological disturbance is still conceivable (Masi, 1983). Preclinical RA is believed to occur before articular inflammation (early RA) develops. RA is seen as a continuum that begins with a high-risk or susceptibility stage based on hereditary factors. A pre-disposing genotype regulates the onset of RA, followed by environmental and genetic factors acting upon producing the inflammatory and destructive response in the synovium. It is still not entirely understood how environmental risk factors

promote disease. Citrullination, (also known as deamination, involves the modification of arginine to citrulline) that occurs in mucosal areas as a result of the stimulation of peptidyl arginine deiminases in response to stressors, such as cigarette smoke (Makrygiannakis et al., 2008). Citrullination and other post-translational modifications, such as acetylation or carbamylation, increase the probability of the modified peptides binding with MHC protein heterodimers, particularly if they share the same epitope. This results in T-cells presenting antigens, which then stimulates B-cells to create a variety of antibodies that recognize self-proteins, including RF (targeting IgGs) and ACPAs (targeting citrullinated proteins) (Holers, 2013; Muller and Radic, 2015). RF and ACPAs can be used as prognostic and diagnostic indicators since they are linked to a more aggressive disease progression (Laurent et al., 2015; Sokolove et al., 2014).

1.5.2. Early and established RA

Synovial inflammation due to mononuclear cell infiltration, predominantly constituted of CD4⁺ T-cells and macrophages, and early stromal cell activation are the hallmarks of early RA. The synovial intimal lining of synovial biopsy samples collected within a week of the onset of RA symptoms showed elevated levels of matrix-degrading enzymes, such as matrix metalloproteinases (MMPs). Additional autoantibodies that recognize immunoglobulins (RF), type 2 collagen (particularly in oxidized form), proteoglycans, glucose-6-phosphate isomerase, nuclear antigens, and other joint autoantigens expand the pathways by which autoantibodies are expected to contribute to pathogenesis in addition to ACPAs (Steiner, 2007).

1.6. Pathogenesis

RA pathogenesis is mainly regulated by a predisposing genotype in which environmental and genetic factors are vital in promoting the inflammatory and destructive synovial response

(Figure 4). However, the post-translational modification of proteins, i.e., citrullination in the mucosal sites, further enables ACPA generation. Following citrullination or other post-translational modifications (such as acetylation or carbamylation), the altered peptides bind to MHC protein heterodimers with the shared epitope. This causes antigen presentation to T cells, which in turn prompts B cells to produce a variety of antibodies that recognize self-proteins, such as RF (targeting IgGs) and ACPAs (targeting citrullinated proteins). Finally, the presence of circulating ACPAs, RF, pro-inflammatory cytokines, and chemokines, together with an additional hit (like the formation of an immune complex, activation of the complement), promotes synovitis characterized by increased vascular permeability and an influx of inflammatory cells into the synovium.

1.6.1. The synovium

Although RA is a systemic disorder, the synovium plays a central role in regulating the various immunological activities outside the joint at primary lymphoid tissues and mucosal surfaces (**Figure 4a-b**); the synovium is a key player (**Figure 4c**). The synovium performs two essential functions to maintain homeostasis: it produces lubricants that allow cartilage surfaces to move in a low-friction environment and supplies the cartilage with nutrients. In RA, the synovium exhibits two significant pathogenetic changes that lead to synovial inflammation. Firstly, the synovial lining is greatly expanded due to the synoviocytes (fibroblast and macrophage), a significant source of cytokines and proteases (Alivernini et al., 2011). Second, RA-related change is Adaptive immune cell infiltration into the synovial sublining (Ziff, 1974).

1.6.2. Joint damage

Joint swelling in RA is attributed to immune activation-related synovial membrane inflammation and is characterized by inflammatory cell infiltration into the generally thinly

populated synovial compartment (**Figure 4d**). Innate immune cells (e.g., monocytes, dendritic cells, and mast cells), adaptive immune cells (e.g., T-helper-1 and T-helper-17 cells, B cells, plasmablasts, and plasma cells) and synoviocytes (fibroblast and macrophage) are the key cellular components in RA. An intensive tissue-specific response accelerated by synovial fibroblasts produces an aggressive inflammatory, matrix regulatory, and invasive phenotype that together increases chondrocyte catabolism and synovial osteoclastogenesis, promoting articular degradation (Smolen et al., 2007).

A complex network of cytokines and chemokines governs the inflammatory environment in the synovial compartment; clinical treatments have shown that tumor necrosis factor- α (TNF- α), interleukin 6 (IL-6), and maybe granulocyte-monocyte colony-stimulating factor (GM-CSF) are critical players in the process (Marc Feldmann and Maini, 2008). Cytokines and chemokines contribute to the initiation or progression of the inflammatory response by stimulating endothelial cells and recruiting immune cells into the synovial compartment. Activated synovial fibroblasts, together with activated T- and B-cells, monocytes, and macrophages, gradually trigger osteoclast formation *via* the receptor activator of nuclear factor- κ B ligand (RANKL), which is expressed on T-cells, B-cells, and fibroblasts (Pettit et al., 2001; Redlich et al., 2002).

The development and activation of osteoclasts play a significant role in bone erosions. Osteoclasts can break down the calcified bone matrix by producing proteases, notably cathepsin K, in a specialized acidified local tissue *milieu* (Redlich and Smolen, 2012). Moreover, it has been hypothesized that ACPAs cause the maturation and activation of osteoclasts by interacting with citrullinated peptides expressed by osteoclasts and osteoclast precursors, such as citrullinated vimentin (Krishnamurthy et al., 2016).

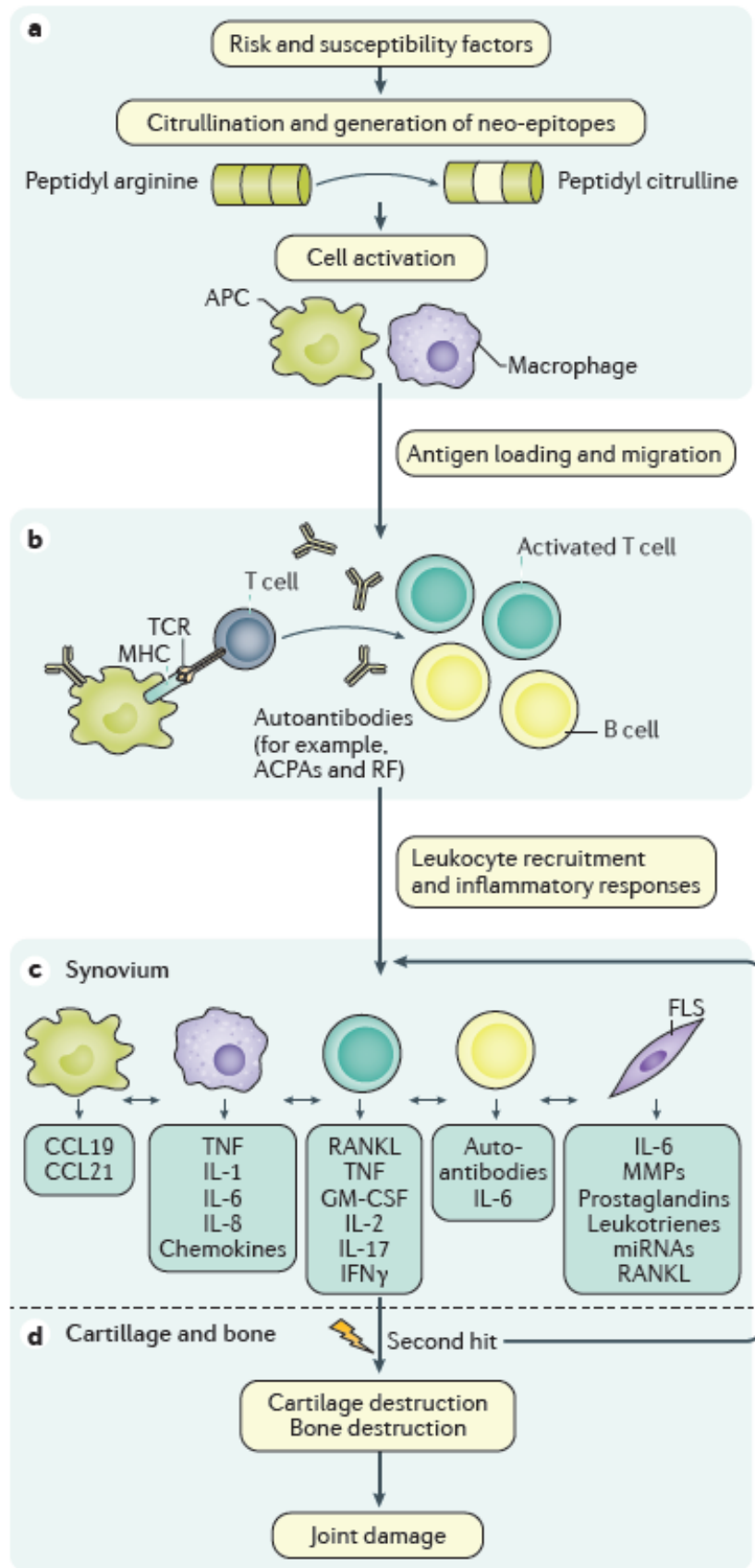
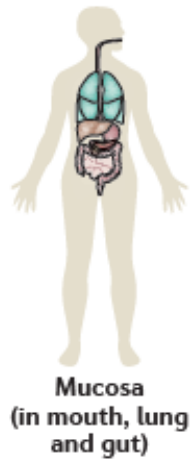


Figure 4. Mechanisms involved in initiation and progression of RA. (a). Post-translational modifications. (b). Autoantibody production is induced by activating the adaptive immune response in lymphoid tissues by antigen-presenting cells (APCs) (c). Locally activated stromal cells, including FLS, APCs, and macrophages, can release various inflammatory factors that cause synovial inflammation by boosting cytokine production (d). Cytokines' paracrine and autocrine effects ultimately result in the degeneration of bone and cartilage. CCL19: CC-chemokine ligand 19; CCL21: CC-chemokine ligand 21; miRNA: MicroRNA; RF: Rheumatoid factor; TCR: T cell receptor; Figure courtesy (Smolen et al., 2018)

Catabolic effects in chondrocytes result in cartilage degradation due to the activation of matrix metalloproteinases (MMPs) and other enzymes (Martel-Pelletier et al., 2001). Synovial cells produce cytokines that bind to corresponding receptors to initiate different intracellular signal transduction events, which operate as a bridge between extracellular activities and the activation of a variety of genes that cause or exacerbate inflammation and joint degradation.

1.7. Therapeutics for treating RA

RA is a multifactorial autoimmune condition. Its diagnosis at a preclinical stage, thorough knowledge and understanding of disease manifestation and mechanisms of RA development, and new possible therapeutic approaches can pave the path for future RA prevention (Deane, 2013). The major classes of anti-rheumatic drugs range significantly in their properties, mechanisms of action, and clinical outcomes. Current RA drug therapies are developed mainly based on the following two approaches: (1) symptomatic treatment with non-steroidal anti-inflammatory drugs (NSAIDs) and (2) disease-modifying anti-rheumatic drugs (DMARDs), i.e., conventional and biologics. NSAIDs do not affect the underlying immunoinflammatory events or delay joint degeneration; instead, they only affect a small portion of the

inflammatory cascade, specifically prostaglandin production by cyclooxygenases (COXs). In contrast, DMARDs "modify" the course of the disease in all these aspects, and once they start working, no more symptomatic treatments are required (Smolen and Steiner, 2003). The biological DMARDs are the RA drugs that have recently been developed. These drugs have been demonstrated to significantly improve RA signs and symptoms and delay the progression of articular cartilage degradation.

Moreover, oral corticosteroids are potent and efficient anti-inflammatory drugs that may assist in modifying disease conditions (Cohen and Emery, 2010). Daily symptomatic management and exercise are pivotal in improving joint flexibility and function while quitting smoking significantly negates its adverse effects on antibody development (Ben Mrid et al., 2022; Guo et al., 2018). **Table 1** summarizes the approved drugs for treating RA with side effects.

Table 1. Overview of the different classes of drugs currently approved for RA treatments and under investigation. The data are taken from (Ben Mrid et al., 2022; Guo et al., 2018; Huang et al., 2021)

Generic name of the drug	Mechanism of action	Shared side effects	Phases
Non-steroidal anti-inflammatory drugs (NSAIDs)			
Naproxen, Aspirin, Flurbiprofen, Ibuprofen	Inhibition of COX enzymes (COX-1 and COX-2) promoting the production of the chemical mediators, prostaglandins.	Gastrointestinal problems, nausea, abdominal discomfort, kidney impairment, cardiovascular effects, rash	Approved
Corticosteroids: Dexamethasone Methylprednisolone Prednisone Triamcinolone	Modulate gene expression by binding to glucocorticoid receptors exert immunosuppressive, anti-inflammatory, vasoconstrictive properties.	Immunosuppression, steroid-induced diabetes and osteoporosis, muscle weakness, thin skin, easy bruising, hypertension, edema, and hypokalemia	Approved
Conventional synthetic DMARDs			
Methotrexate	Folate-dependent processes; Adenosine signaling; Methyl-donor production; Reactive oxygen species; Adhesion-molecule expression; Cytokine profiles Eicosanoids and MMPs.	Gastrointestinal disorders, hepatic dysregulations, pneumonitis, hematologic disorders, infections, nephrotoxicity	Approved
Leflunomide/Teriflunomide	Inhibit the metabolism of pyrimidines, Leading to a reduction of Th1 inflammatory responses	Hypertension, diarrhea, nausea, hepatotoxicity	Approved
Sulfasalazine	Increases adenosine synthesis at the site of inflammation, inhibit TNF- α expression, and suppress B-cell function.	Gastrointestinal, central nervous system and hematologic adverse effects	Approved

Contd.

Generic name of the drug	Mechanism of action	Shared side effects	Phases
Chloroquine /Hydroxychloroquine	Blocks the interaction between antigen-presenting macrophages and T helper cells leading to a decrease in the overall inflammatory response	Gastrointestinal disorders, dermatological disorders retinal toxicity	Approved
Biological DMARDs			
TNF-α targeted therapy			
Infliximab Adalimumab Etanercept Golimumab Certolizumab pegol	TNF- α inhibitor	Infection (pneumonia and atypical tuberculosis) injection-site reaction, Hypertension, severe /anaphylactoid transfusion reaction.	Approved
B-cell targeted therapy			
Rituximab Ofatumumab Belimumab Atacicept Tabalumab	B cell depleting Inhibitors of B cell function	Infection, hypertension, viral reactivation Severe/anaphylactoid transfusion Reaction	Approved
T-cell targeted therapy			
Abatacept Belatacept	Autoantigen recognition: Immune cell infiltrate; T cell activation	Infection, malignancy	Approved
Interleukin targeted therapy			
Tocilizumab Secukinumab	IL-6 inhibition IL-17 inhibition	Infections and infestations, high blood pressure, skin rashes, neutropenia, malignancy	Approved
Growth and differentiation factors			
Denosumab	RANKL inhibitor	Low Ca ²⁺ and phosphate in the blood, muscle cramps, and cellulitis.	Approved

Contd.

Generic name of the drug	Mechanism of action	Shared side effects	Phases
Small molecule targets			
JAK pathway			
Tofacitinib	JAK1 and JAK3 inhibitor	Heart attack or stroke	Approved
Baricitinib	JAK1 and JAK2 inhibitor	Zoster infection	Approved
Filgotinib	JAK1 inhibitor	Urinary tract infection	Approved
Upadacitinib	JAK1 inhibitor	Urinary tract infection	Approved
Peficitinib	Pan-inhibitor of JAKs kinase	Neutropenia	Approved
Itacitinib	JAK1 inhibitor	Thrombocytopenia	Phase 3
p38 MAPK Pathway			
RO4402257	MAP kinase inhibitor	Skin rash, dizziness	Phase 2
IRAK-4			
PF-06650833	IRAK-4 inhibitor	GIT problems	Phase 2
BAY1834845	IRAK-4 inhibitor	Abdominal pain, ulcer	Phase 1
BAY1830839	IRAK-4 inhibitor	Nausea, abdominal pain	Phase 1
CD20			
Ofatumumab	Inhibition of CD-20	Chest pain, fever, rash, dizziness	Phase 3
BTK			
M2951	Inhibitor of BTK	Nasopharyngitis	Phase 2
GS-4059	Selective BTK inhibitor	Neutropenia, rash, vomiting	Phase 1
IL-6			
Olokizumab	Inhibitor of IL-6 receptor	Diarrhea, headache	Phase 3
DNA methylation			
Decitabine	Nucleoside metabolic inhibitor	Pale skin, dizziness	Animal study
Histone modification			
GSK-J4	Histone lysine demethylase inhibitor		Animal study
I-BET151	Bromodomain protein inhibitor		Animal study
CKD-506	HDAC6 inhibitor		Animal study

1.8. Roadmap to key possible therapeutic intervention strategies for treating RA

A schematic roadmap to develop RA and key possible existing and in-development therapeutic intervention strategies was displayed in **Figure 5**.

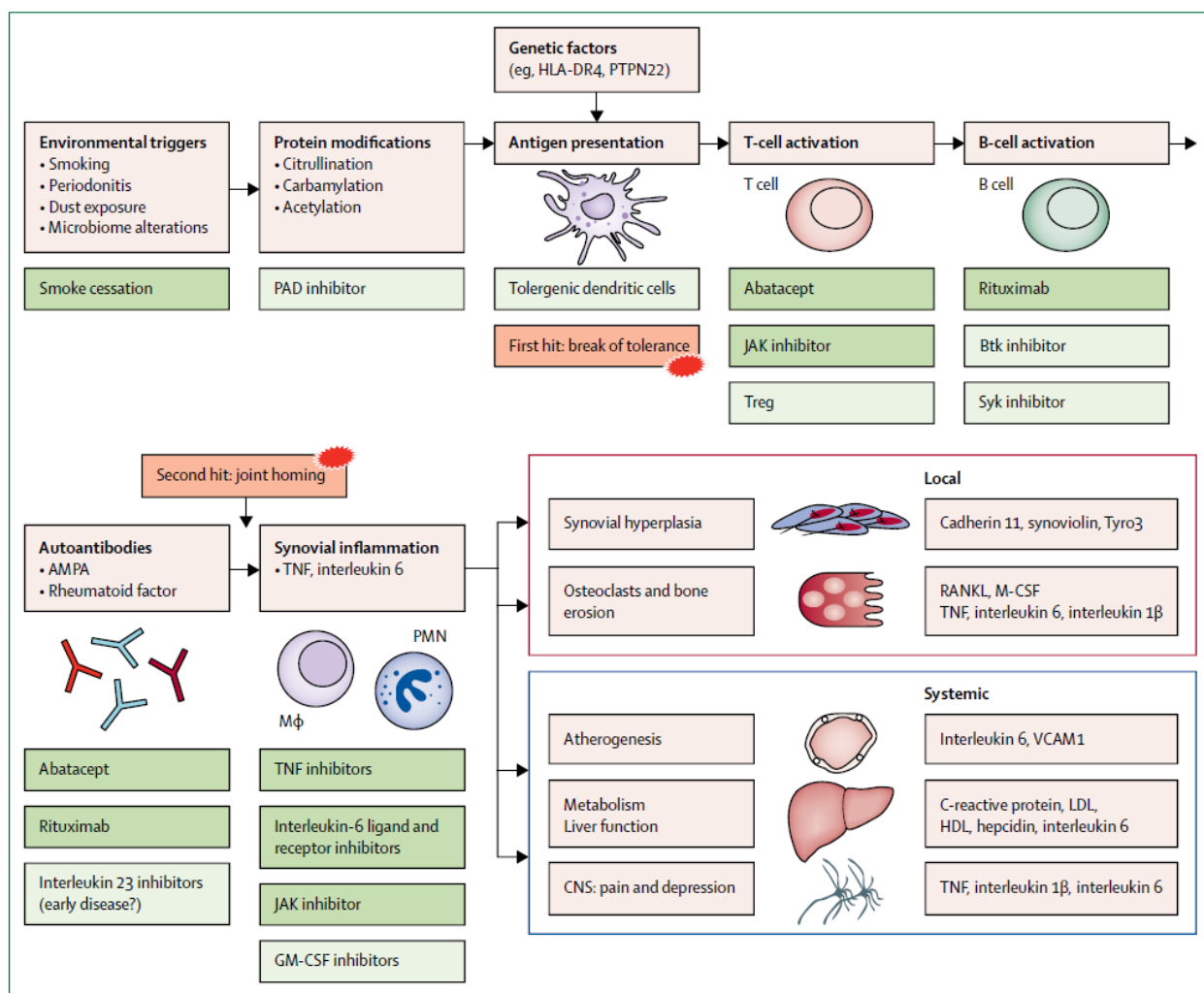


Figure 5. A schematic roadmap to key possible existing and developing treatment strategies for treating RA. *Brown color-* RA development steps, *dark green color-* existing therapeutic intervention, and *light green color* - therapeutic interventions in development strategies for RA. PAD: Protein arginine deiminases; JAK: Janus kinase; Treg: Regulatory T cell, Btk: Bruton’s tyrosine kinase; Syk: Spleen tyrosine kinase; Mφ: Macrophage; PMN: Polymorphonuclear

leukocytes; M-CSF: Macrophage colony-stimulating factor; VCAM1: Vascular cell adhesion molecule 1. Figure courtesy (McInnes and Schett, 2017)

1.9. Limitation of traditional RA therapy and role of Nanomedicines in treating RA

The key challenges with the conventional therapy of RA were poor patient compliance, a short half-life, poor bioavailability, and insufficient solubility; these drawbacks might be addressed by finding new treatment strategies (Movahedi et al., 2015).

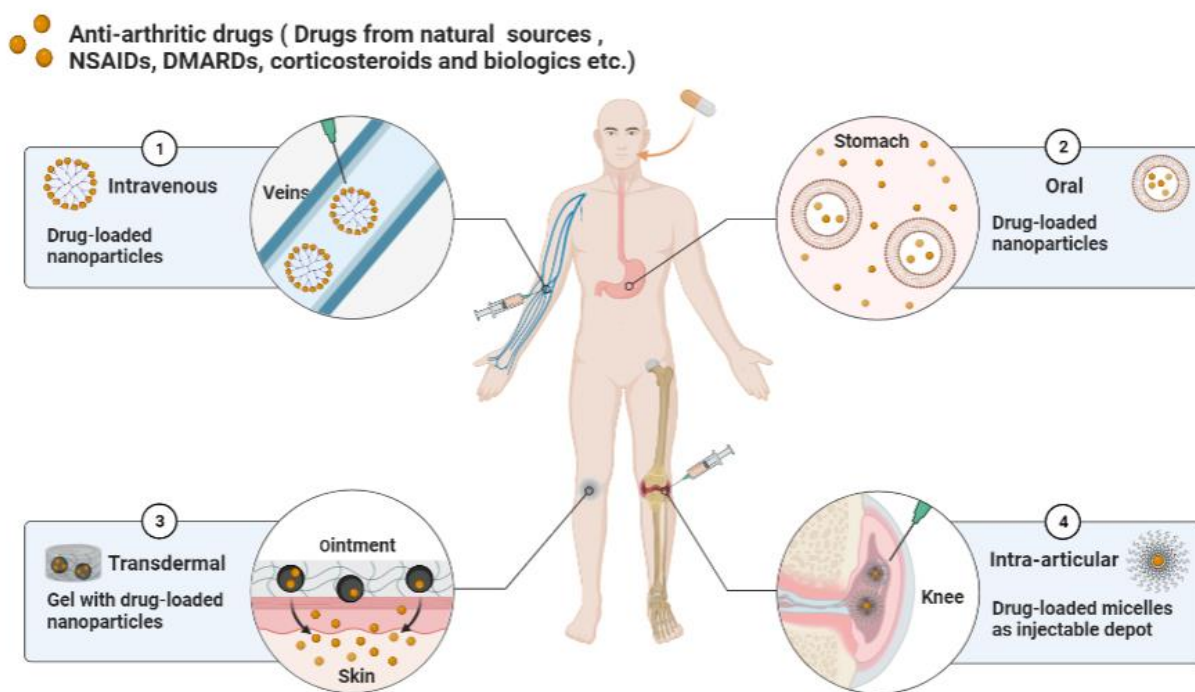


Figure 6. Various nano-based drug delivery systems in treating RA with administration routes.

Recently, nanomedicine has been extensively employed as an innovative therapeutic approach to develop highly efficient drug delivery systems for treating various diseases (including cancer and RA). The utilization of nanomedicine in RA is greatly sought due to the efficient accumulation of nanoparticles in the inflammatory microenvironments of arthritic

joints. To address the issues with current traditional RA therapies, the nanoscale drug delivery systems emerged as a new promising potential therapeutic approach (**Figure 6**). It has been demonstrated that nanocarriers can enhance the solubility of drugs, extend their residence time in the systemic circulation, limit drug clearance, and deliver medicines effectively to the target sites (Jeong and Park, 2021).

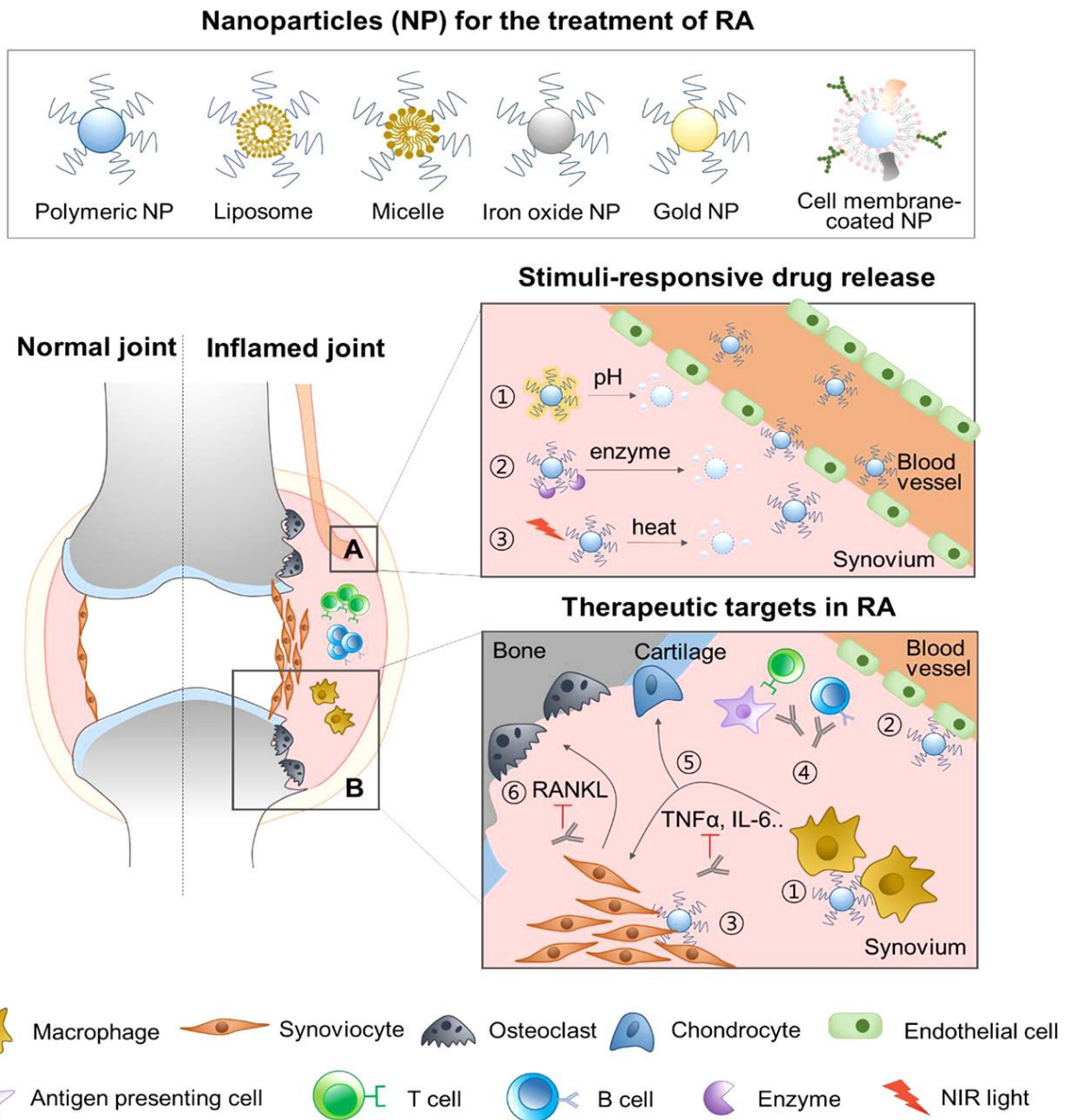


Figure 7. Nanomedicine strategies for the treatment of RA. Nanoparticles with various

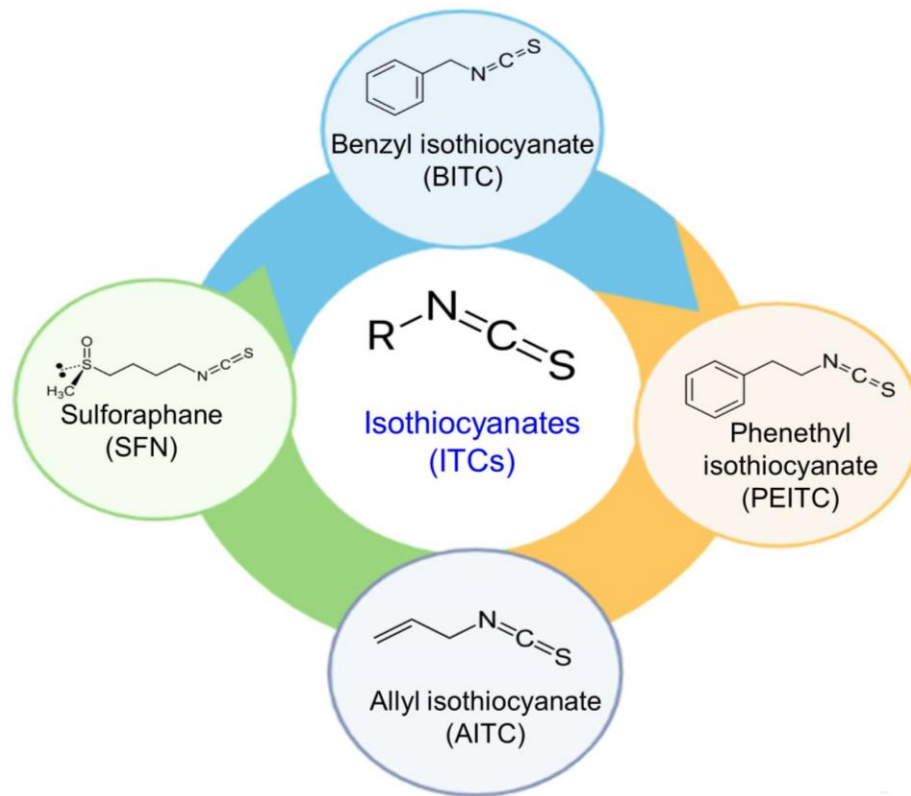
functions were developed to enhance therapeutic effects in inflamed joints. Nanoparticles with multiple functions were designed to boost therapeutic effects in inflamed joints. (A). Nanoparticles selectively release the encapsulated drug in response to (1). Low pH (2). An enzyme that targets inflammation, and (3). Externally delivered NIR light. (B). Nanoparticles target disease-related cells like (1). Macrophages (2). Angiogenic endothelial cells, and (3). FLS. (4). FDA-approved biologics target immune cells like B and APC. (5). Pro-inflammatory chemicals such cytokines, ROS, and (6). Nanoparticles mask osteoclast differentiation factors. Figure courtesy (Jeong and Park, 2021)

These systems can increase therapeutic efficacy by delivering the drug at a higher concentration to the targeted region. **Figure 7** highlights the different strategies employed in nanomedicine with various functional capacities to enhance the therapeutic effects in inflamed joints for the treatment of RA.

1.10. Natural isothiocyanates as a therapeutic agent in RA therapy

Natural isothiocyanates (ITCs) are biologically active hydrolysis (breakdown) products of glucosinolates. They are widely present in many cruciferous vegetables, including broccoli, watercress, cauliflower, Brussels sprouts, mustard, cabbage, kale, wasabi, etc. (**Figure 8B**) (Wang and Bao, 2021). As shown in **Figure 8A**, the chemical structures of ITCs consist of an isothiocyanate group ($N=C=S$) in common with various side chains. Sulforaphane (SFN), phenethyl isothiocyanate (PEITC), allyl isothiocyanate (AITC), and benzyl isothiocyanate (BITC) are among the extensively studied ITCs that used their strong therapeutic effects. ITCs possess various biological functions via the direct reaction with a functional group, i.e., an isothiocyanate group with multiple proteins.

A



B



Figure 8. Natural isothiocyanates (ITCs). (A). The basic structure and main types of ITCs. (B). Sources of ITCs.

The biological activities of ITCs and their mechanisms are summarized in **Figure 9** (Wang and Bao, 2021). This class of phytochemicals has been widely researched for cancer prevention and treatment in various study models (Haloi et al., 2023).

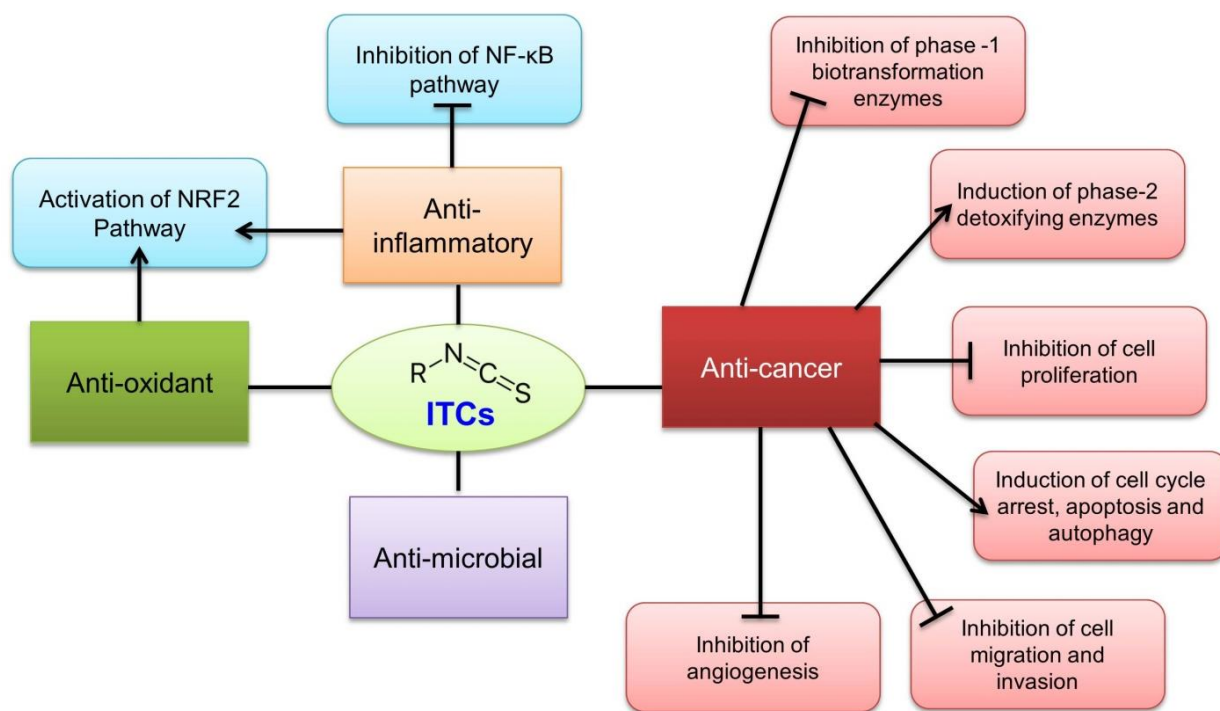


Figure 9. The main biological activities of ITCs. Figure adapted from (Wang and Bao, 2021)

However, later studies have shown the profound chemopreventive, antioxidant, and anti-inflammatory effects of ITCs. The Nrf-2 and its downstream effector pathway are reported to be predominantly associated with these effects elicited by ITCs. The Nrf2/ARE (nuclear factor erythroid 2-related factor-2/antioxidant response element) pathway is a major pathway that is well-studied to be involved in acute and chronic inflammation as any perturbation in the pathway leads to inflammatory diseases such as RA, asthma, emphysema, gastritis, colitis, and atherosclerosis (Kumar et al., 2014). Natural ITCs are active inducers of the Nrf2/ARE pathway, activating phase II detoxification enzymes in response to reactive species and redox potentials at

the transcriptional level. Two natural ITCs, sulforaphane (SFN) and phenethyl isothiocyanate (PEITC), have been studied *in vitro* and *in vivo* for their capacity to stimulate phase II gene expression (Dayalan Naidu et al., 2018; Gan et al., 2010; Yang et al., 2020).

1.10.1. Phenethyl isothiocyanate (PEITC)

PEITC, a member of the natural isothiocyanate family, found in many cruciferous vegetables, has aroused much interest as a health-promoting molecule due to its anti-cancer and chemopreventive properties (Cang et al., 2014; Hu et al., 2007). In various cell-based studies, PEITC has also been demonstrated to have antioxidant, anti-inflammatory, and anti-proliferative properties and can trigger apoptosis (Shoaib et al., 2021). Apart from PEITC's numerous biological functions, a few recent studies have highlighted the involvement of PEITCs in osteoclastogenesis regulation, a critical event in bone and joint disorders such as osteoporosis and RA (Murakami et al., 2007). Only a few *in vivo* studies of PEITC were reported in the treatment of RA (Choudhary et al., 2020). Its poor solubility, low bioavailability, instability, oily nature, and daily administration of PEITC limit this further clinical utilization (Mohanty et al., 2020; Wang and Bao, 2021). Researchers have recently developed various drug and nano-delivery systems to overcome these limitations. Using a nanotechnology approach, different nanomaterials were employed as transport modules to carry ITCs and/or other therapeutic agents to obtain a synergistic effect (Wang and Bao, 2021).

1.10.2. Nanodelivery of natural isothiocyanates (ITCs)

The absorption, metabolism, distribution, and excretion of ITCs inside the human body are essential in their bioactivity. Various cellular and animal models demonstrate the effectiveness of several ITCs against cancer, RA, and other disorders. Although, their therapeutic

application is constrained due to their limited solubility, stability, bioavailability, and the "biphasic dose-response"(Wang and Bao, 2021). Scientists have recently developed nano-delivery technology to overcome these limitations. For this purpose, various kinds of nano-delivery systems have been constructed. These nano-delivery systems are simple to construct and target specific cells rather than healthy ones. The most popular nano-delivery techniques are liposomes, dendrimers, polymeric nanoparticles, carbon nanotubes, quantum dots, magnetic nanoparticles, micelles, and gold nanoparticles (Wang and Bao, 2021).

However, in treating inflammatory conditions such as RA and OA, only a few studies have been reported where nanotechnology significantly improved the pharmaceutical drawbacks of ITCs in the free form. Previously from our lab, *Mohanty et al. 2020* reported a combination of nano-based approaches of nutraceuticals such as naringin (NAR), SFN, and PEITC to treat RA. According to the physicochemical findings, the liposomal preparations had a zeta potential of -47.3 to -53.3 mV, an average size between 140.5 and 165.6 nm, and were monodisperse (PDI 0.062–0.248) in water. The optimized liposomal formulation showed significantly reduced level of pro-inflammatory cytokines (TNF- α , IL-6, and IFN- γ), lowered immune cell infiltration, decreased pannus formation, and improved joint and cartilage destruction in FCA-induced RA animal model (Mohanty et al., 2020).

Ko et al. 2013 reported an SFN-based drug delivery system for the IA treatment of osteoarthritis. The protein and mRNA expression of COX-2, ADAMTS-5, and MMP-2 in LPS-stimulated articular chondrocytes was significantly reduced by SFN-PLGA microsphere treatment. In the surgically-induced OA animal model, the local administration (IA route) of SFN-PLGA microspheres markedly reduced the disease progression. This study demonstrated

that SFN-PLGA microspheres can be a functional injectable delivery system for treating OA (Ko et al., 2013).

In another study, *Monteiro do Nascimento et al. 2021* demonstrated that an ITC-loaded hydrogel carrier system, i.e., SFN-loaded hyaluronic acid-poloxamer hybrid hydrogel (PL407-PL338-HA-SFN) enriches cartilage protection in *ex vivo* OA models. The hybrid hydrogel did not show noticeable cytotoxic effects on either osteoblast or chondrosarcoma cell lines. Both *in vitro* and *ex vivo*, treatment with the hybrid hydrogel significantly down-regulated the NF- κ B and COX-2 expression, up-regulated the expression of type II collagen, and restored the proteoglycan depletion. This study emphasizes the safety and therapeutic effectiveness of SFN-loaded PL-HA hybrid hydrogel as a local drug delivery system for treating OA (Monteiro do Nascimento et al., 2021).

1.10.3. Nanodelivery of PEITC

PEITC has been of particular interest in recent years due to its distinct *in vitro* and *in vivo* anti-cancer, anti-proliferative, anti-inflammatory, and antimicrobial properties. Due to its potent electrophilic nature, PEITC can easily interact with nucleophiles in physiological conditions like other ITCs. Additionally, it is strongly volatile, poorly soluble, and has a distinctive pungent odor. Such characteristics limit its effectiveness as a cancer-preventative agent, and the scientific community is still searching for a suitable delivery system to address its drawbacks. Using nanoencapsulation techniques might boost PEITC activity, stability, and absorption while lowering excretion from the circulatory system. Additionally, such nano delivery methods might increase the therapeutic performance of PEITC, lower toxicity, make it easier to handle, and extend shelf life.

Pulliero et al. 2014 examined the ability of the liposomal drug delivery system to alter the pharmacological properties of PEITC. A simple ethanol injection approach was used to synthesize the nanoliposomes, which had an average size of 70 nm, using 1,2-di-O-octadecenyl-3-trimethylammonium propane (DOTMA), cholesterol, and D-alpha-tocopheryl polyethylene glycol succinate (TPGS). Their findings indicated that PEITC NPs considerably improved PEITC's capacity to prevent DNA damage on cigarette smoke condensate and to trigger protective apoptosis in bronchial epithelial cells both *in vitro* and *ex vivo* (Pulliero et al., 2014).

In a recent study, *Wu et al. 2019* developed an innovative dual drug delivery system based on black phosphorus nanosheet (BPN) for the concurrent delivery of DOX and PEITC. The therapeutic effectiveness of BPNs-based drug delivery systems in preventing drug resistance in tumors with minimal adverse effects has been demonstrated in both *in vitro* and *in vivo* studies. For the treatment of MDR breast cancer, this novel synergistic nano-delivery method offers significant application potential (Wu et al., 2019).

Based on the previously reported literature showed that the therapeutic efficacy of PEITC in treating inflammatory illnesses like RA and OA has not yet been thoroughly investigated. A detailed investigation is needed to further PEITC, which can be used as an anti-inflammatory agent. Additionally, implementing nano-delivery techniques will improve PEITC's solubility, bioavailability, and anti-inflammatory effectiveness.

1.10.4. Therapeutic advantages of nano delivery systems of natural isothiocyanates (ITCs)

A successful nano-delivery system can be determined by its high drug-loading and encapsulation efficiency, prolonged drug release, extended self-life, and increased therapeutic

effectiveness with minimal adverse effects. Several featured nano-delivery systems were developed to deliver natural ITCs to improve their physicochemical drawbacks.

Increase solubility and bioavailability.

Oil-in-water nanoemulsion increased the solubility and bioavailability of AITC and BITC with a droplet size of 10–250 nm and 99% encapsulation efficiency using this nano delivery method. The liposomal formulation, a highly versatile nano-delivery technique, significantly improved PEITC's solubility and bioavailability (Wang and Bao, 2021).

Enhanced stability

Enhancing the stability of therapeutic drugs susceptible to factors like light, temperature, or pH is another crucial benefit that nanotechnology offers. According to reports, ITC nano-delivery systems exhibit minimal polydispersity and excellent colloidal stability that lasts for several weeks. For instance, AITC NPs can endure three freeze-thawing cycles and are stable at 110⁰ C. In a physiological condition and a pH range of (4.7-8.0), BITC NPs demonstrated good long-term stability. Notably, most ITC NPs are stable at physiological conditions (pH 7.4) (Wang and Bao, 2021).

Improved therapeutic targeting

Most lipid nano delivery systems designed for ITCs, such as polymeric NP, micelle, and liposome, vary in size from 100 nm to 200 nm and have greater tumor accumulation. This leads to dramatically better anti-cancer efficacy with minimal side effects, for example, SFN-loaded PLGA NP (Wang and Bao, 2021)

Combinational therapy

The term "co-delivery system" refers to the simultaneous administration of various therapeutic agents to the same target locations. Recent advances in nanotechnology make it simple to implement such co-delivery systems. An efficient multifunctional nano-delivery system can be formed by including extra components, such as targeting motifs and imaging probes. For example, encapsulating SFN and DOX in nanoliposomes resulted in high synergistic activity toward triple-negative breast cancer cells (Wang and Bao, 2021).

1.11. Disease-modifying anti-rheumatic drugs (DMARDs), gold standard therapy for RA

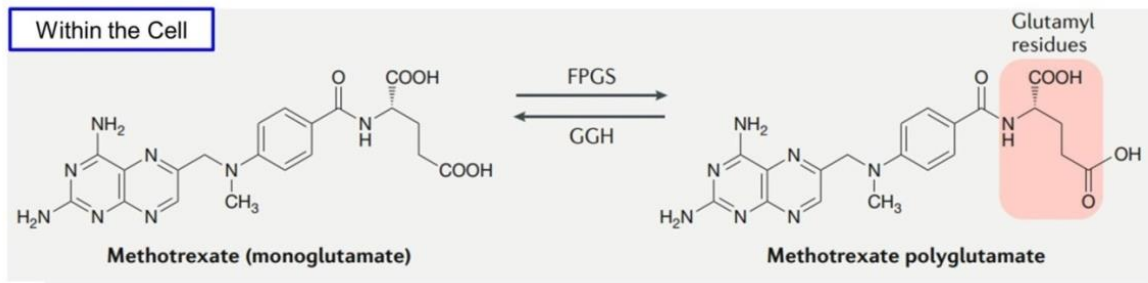
1.11.1. Methotrexate (MTX)

MTX is the first-line DMARDs for RA therapy as well as other forms of inflammatory arthritis, which also improves the therapeutic effects of the majority of biological agents used to treat RA (Cronstein and Aune, 2020). MTX initially appeared as a "pro-drug," accumulating in tissue as a polyglutamated form. The MTX native form, i.e., MTX mono glutamate, is now known to undergo recurrent polyglutamation within cells with varying additions of glutamic acid. MTX polyglutamate can be detected in tissues for several weeks (**Figure 10A**). MTX regulates nearly all inflammatory cell types, both directly and indirectly, including neutrophils, monocytes, T cells, B cells, endothelial cells, and FLS (**Figure 10B**) (Cronstein and Aune, 2020).

It is well established that MTX exhibits potent anti-angiogenic, anti-inflammatory, and analgesic activity; however, its poor aqueous solubility, pharmacokinetics, and narrow therapeutic window, with non-specific tissue distribution are of significant concern (Lyu et al., 2021; Wu et al., 2021) These lead to a substantial risk of severe adverse effects, including

hepatotoxicity, bone marrow suppression, nephrotoxicity, and severe neutropenia that significantly limits its therapeutic applications (Li et al., 2022).

A



B

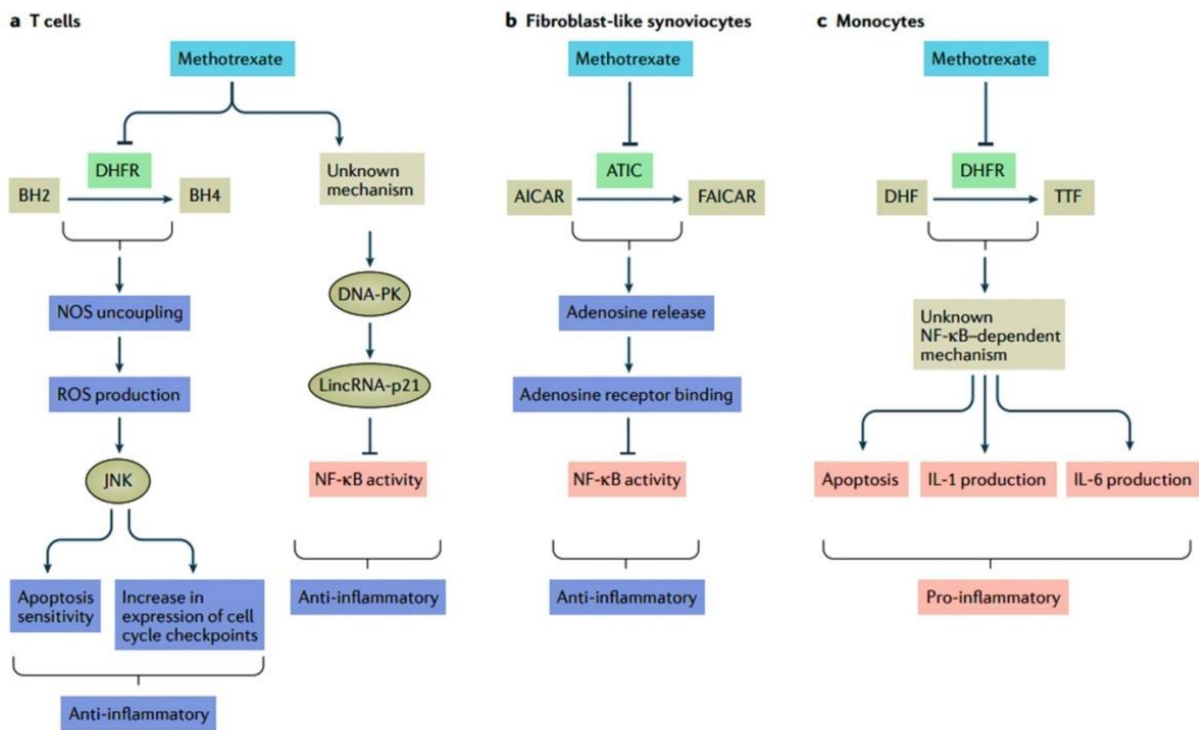


Figure 10. Molecular structure and cellular function on various cell types of MTX in RA condition. (A). Within cells, methotrexate mono glutamate undergoes serial polyglutamation to form methotrexate polyglutamate, the active form of MTX. (B). Cell-specific mechanisms of MTX in RA: (a). T cells and (b). FLS - anti-inflammatory, (c). Monocytes - pro-inflammatory.

DHFR: Dihydrofolate reductase, BH₂: Dihydrobiopterin, BH₄: Tetrahydrobiopterin, NOS: Nitric oxide synthase, ROS: Reactive oxygen species, JNK: JUN N-terminal kinase, DNA-PK: DNA-dependent protein kinase, LincRNA-p21: Long intergenic noncoding RNA p21, AICAR: 5-aminoimidazole-4-carboxamide ribonucleotide,ATIC: 5-aminoimidazole-4-carboxamide ribonucleotide formyltransferase/ inosine monophosphate cyclohydrolase, FAICAR: Formyl AICAR, DHF: Dihydrofolate and TTF: Tetrahydrofolate. Figure courtesy (Cronstein and Aune, 2020)

Recently, NPs have gained significant interest in developing more suitable MTX formulations, broadening their scope of application. A wide range of NPs have been designed to deliver MTX, including polymer-based, carbon-based, lipid-based, and inorganic. *Qindeel et al.* 2020 synthesized polycaprolactone-polyethylene glycol-polycaprolactone (PCL-PEG-PCL) triblock copolymer by ring-opening copolymerization reaction and used it as a carrier for the fabrication of MTX-loaded nano micelle. NPs are loaded into a hydrogel with eucalyptus oil as a skin penetrant to avoid the first-pass effect, improve patient compliance, and reduce liver toxicity. When NP is applied in the RA mouse model, compared with free MTX, a significant aggregation in the inflamed joints, reduced expression of inflammatory factors, and restoration in the behavioral response ability of mice was observed (Qindeel et al., 2020).

1.11.2. Rationale of using MTX-loaded nano delivery system

MTX is a drug with significant therapeutic potential for various ailments, including cancer and auto-immune disorders (RA and OA); the suboptimal pharmacological response of MTX limits its use. The therapeutic potential of conventional drug delivery strategies is constrained because of MTX's poor pharmacokinetics, drug resistance, low bioavailability, and

dose-dependent side effects. MTX's most often reported side effects are diarrhea, anemia, dermatitis, bruises, hepatitis, pulmonary fibrosis, and bone marrow depression. (Yu et al., 2020).

In this regard, using alternative delivery technologies has offered a significant chance to overcome these limitations of MTX. *In vitro* studies and *in vivo* animal models have demonstrated the importance of drug delivery platforms based on NPs, such as polymer and lipid-based NPs and inorganic nanostructures, for increasing the biological availability of MTX at the site of activity (Yu et al., 2020). Consequently, a simple and efficient method for synthesizing targeted NPs may be used to reduce the adverse effects of the drug on healthy tissues. Before constructing nanomaterial-based MTX formulations as anti-RA medication, key considerations must include high drug loading, encapsulation efficiency, and controlled MTX release at the targeted location.

In another strategy, the co-delivery of MTX and other therapeutic agents might be an innovative approach to mitigate the side effects of their free-form used for longer periods. Co-delivery might decrease drug resistance, particularly in long-term and frequent applications. This approach reduces adverse effects without increasing the initial dose, making it clinically applicable.

In this scenario, a hydrogel system would be ideal as it can help overcome the limitations of PEITC and MTX when injected with a required dose. It can exert a pharmacological response without any adverse effects. This approach can be employed as an injectable depot formulation with the integration of nanotechnology that can release and maintain the drug(s) concentrations for extended periods in articular joints.

1.12. Natural polysaccharide-based stimuli-responsive hydrogels

Stimuli-responsive hydrogels with versatile properties garnered substantial attention in various drug delivery applications (Haloi et al., 2023). Drug-loaded hydrogels have broadened different drugs' scope in tissue engineering and delivery applications (Li et al., 2021). Thermosensitive hydrogels are the most extensively studied smart hydrogels, as many polymers have the property to undergo a temperature-responsive phase transition. Upon injection, the mixture (with the encapsulated drug) in a solution state at a lower temperature transforms into a gel (at body temperature) with mechanical properties that provide structural support, enabling the diffusion of the drug through the porous structures (Xiao et al., 2021). Various applications have been developed using biodegradable polymers that can trigger drug release depending on the stimuli present in the physiological/pathological microenvironment (e.g., pH, redox, enzymes, metabolite, temperature, etc.) (El-Husseiny et al., 2022; Sikdar et al., 2021). These thermosensitive hydrogels can be instilled in different body parts. Therefore, it is extensively used as a drug delivery carrier for applications where minimal invasiveness, sustained release, high local drug concentration, and low systemic toxicities are desired (Xiao et al., 2021).

Natural polysaccharide hydrogels, especially chitosan (CS) and sodium alginate (SA)-based hydrogels are much explored as drug carriers as they are biocompatible, amenable, and mimic the extracellular matrix (ECM) (Haloi et al., 2023; Liu et al., 2020). The thermo-gelation property (stimuli response) of polysaccharides-based hydrogels is achieved by optimally balancing the driving forces (hydrophobic interactions) at a temperature transition (from room temperature to physiological body temperature) between the neutral chitosan molecules and micelle packing (Sarwan et al., 2020).

Pluronic-based *in-situ* gelling systems as injectable have shown promising potential as drug delivery platforms in different tissue engineering applications (such as chondrogenesis and bone regeneration) (Abdeltawab et al., 2020; Liu et al., 2020). Pluronic F-127 (PF-127, also known as poloxamer 407) possesses good thermo-responsive sol-to-gel transition behavior and is a safe polymeric material for preparing thermosensitive hydrogels. Further, the amphiphilic structure of pluronic F-127 allows the encapsulation of both hydrophilic and hydrophobic drugs, thus offering a broad scope for incorporating different types of drugs (Zarrintaj et al., 2020). However, it needs better mechanical strength and high porosity (leading to rapid gel erosion and drug diffusion), significantly limiting its application in sustained drug delivery applications. This drawback is mitigated substantially by blending pluronic with other biomacromolecules (chitosan, dextran, and alginate) as composite hydrogels (Haloi et al., 2023; Ur-Rehman et al., 2011).

1.13. Injectable hydrogels in drug carriers for the RA treatment

In RA research, Injectable hydrogels, i.e., thermosensitive hydrogels, have gained much attention among the hydrogel-based carrier systems since they have shown improved drug characteristics (solubility, stability, and drug bioavailability) and can be injected directly into inflamed joints (Yin et al., 2020a). The following are recently reported studies where hydrogel-based carrier systems are widely used as an injectable depot for the sustained release of therapeutic agents/biomolecules into the RA joints.

Yin et al., 2020b reported an injectable hydrogel depot system (D/siRNA-NGel) where the combination of the non-steroidal anti-inflammatory drug indomethacin (IND) and the slow-acting anti-rheumatic drug MTX successfully installed and studies for the treatment of inflammatory arthritis, i.e., RA. Intra-articular (IA) administration of D/siRNA-NGel hydrogel

can effectively reduce the expression of inflammatory cytokines and delay the progression of bone erosion, significantly inhibiting the inflammatory response (Yin et al., 2020b).

In another study, *Yeo et al., 2019* developed an innovative nitric oxide-scavenging nanogel (NO-Scv gel) as a therapeutic material for treating RA. The results demonstrated that the nanosized NO-Scv gel effectively removed NO *in vitro* by decomposing NO-cleavable cross-linker (NOCCL) and exerting anti-inflammatory effects against activated macrophages. Furthermore, the NO-Scv gel effectively alleviated bone resorption and cartilage destruction compared to the commercial drug dexamethasone. The study indicated that the local application of NO-Scv gel has the potential as a therapeutic material for various inflammatory diseases like RA (Yeo et al., 2019).

In a recent study, *Ma et al., 2022* synthesized different self-assembled supramolecular polypeptide hydrogels to deliver MTX intra-articularly (IA) into the inflamed joints and minimize systemic side effects. The MTX was initially conjugated with a supramolecular self-assembling hydrogel composed of D-amino acids with the sequence GDFDFDY. Comparing the results obtained from MTX-GDFDFDY and MTX-GFFY hydrogels, it was inferred that MTX-GDFDFDY hydrogels were more stable with prolonged drug-releasing behavior. More importantly, MTX-GDFDFDY hydrogels were non-toxic to the normal cells and effectively inhibited the invasion of RA-FLS and inflammatory M1 macrophage polarization. In addition, MTX-GDFDFDY hydrogels significantly suppressed the RA-related symptoms (joint destruction, swelling, and fever) and might hold great potential for applications in RA therapy. (Ma et al., 2022).

Ren et al., 2021 demonstrated that acupoint nanocomposite hydrogel composed of triptolide (TP)-Human serum albumin nanoparticles (TP@HSA NPs) and 2-chloro-N (6)-

cyclopentyl adenosine (CCPA) could effectively treat RA. The results showed that treatment with TP@HSA NPs nanocomposite hydrogel markedly improved the analgesic effects at the acupoint compared with non-acupoint. *In vivo*, RA studies suggested that acupoint and nanocomposite hydrogel combination synergistically exerted its influence, significantly suppressing inflammation and bone erosion and reducing systemic toxicity. Furthermore, the Th17/Treg balance was restored by regulating the inflammatory factors. This novel therapeutic approach with acupoint nanocomposite hydrogel bridges acupuncture and chemotherapy and opens an avenue for exploring multimodal systems combining traditional and modern medicine (Ren et al., 2021).

Currently, two hydrogel formulations, namely polyvinyl alcohol (PVA) hydrogel (NCT04693104) and hydroxyethyl cellulose hydrogel (PROMGEL-OA, NCT04061733), are undergoing clinical trials for the treatment of knee OA patients. An adjunctive adrenocorticotrophic hormone (ACTH) gel (NCT02030028) is now undergoing clinical trials for RA treatment.

1.14. IA route is an alternative approach to reducing the multiple-dose regimens and maximizing drug concentration in the RA joint

IA drug administration has numerous benefits over systemic drug administration, including minimal adverse effects, lower costs, reduced systemic exposure, and greater local concentration (bioavailability). The delivery of therapeutic molecules through the IA approach is a well-established clinical procedure for treating inflammatory arthritis, including RA and osteoarthritis (OA). However, certain drawbacks of the drug, such as rapid clearance from the joint due to lymphatic drainage and/or the short half-life, limit its therapeutic effectiveness (Diaz-Rodriguez et al., 2021). As a result, boosting the therapeutic efficacy of medications while

limiting side effects is a difficult task in RA treatment. Co-administration of two or more pills, as combination drug therapy, has become more prevalent in recent years to harness the RA severity owing to the uncertainty of RA's pathophysiology and the difficulty in treating the same.

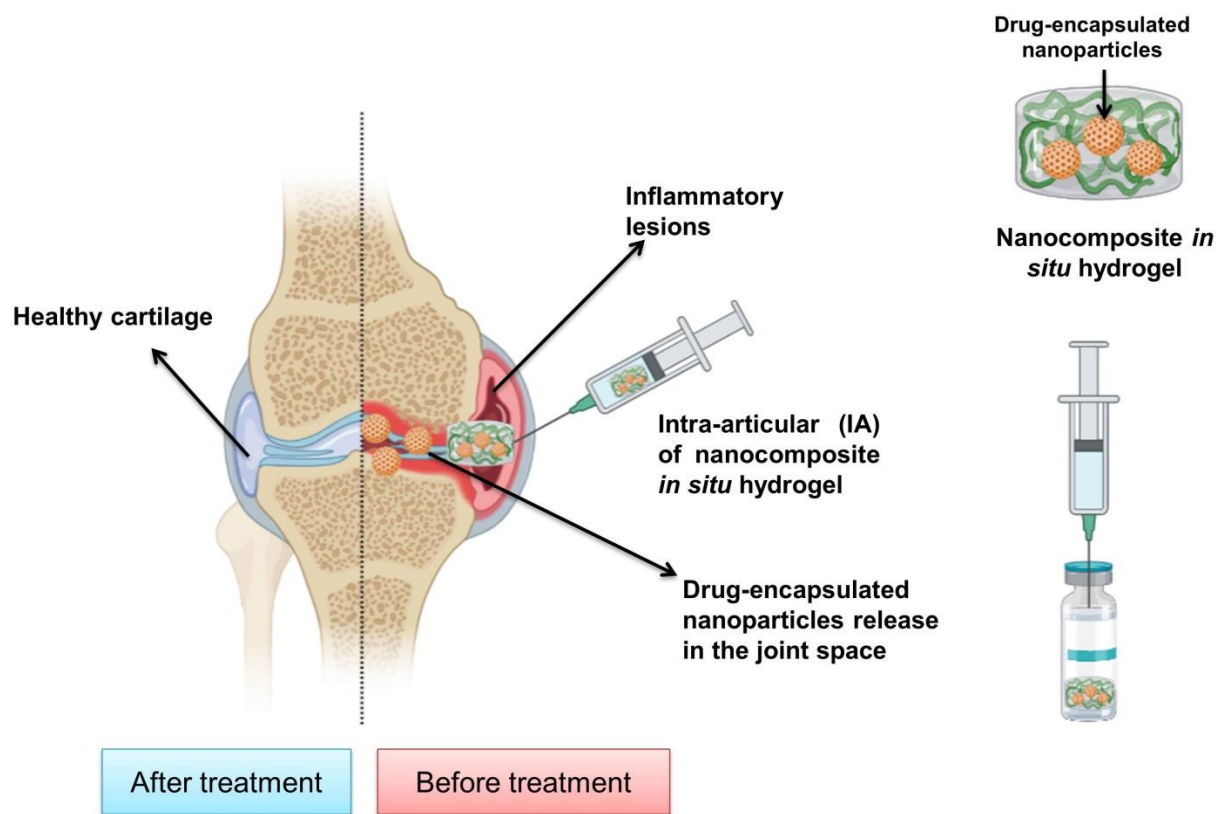


Figure 11. Schematic representation of the IA administration of an *in situ* gelling drug formulation into RA joint and changes after treatment (healthy cartilage).

Several studies have reported the synergistic effect of combining multiple drugs through the IA route, enhancing the anti-inflammatory activity and therapeutic effectiveness (Reum Son et al., 2015). Recently, IA administration of hydrogels incorporated with the drug has drawn substantial attention in RA therapy. The viscous nature of the matrix allows retention of the drug at the joint site, releasing the incorporated drug sustainedly into the surrounding tissues, thereby

providing much-needed prolonged pharmacological effects. The high water content in the hydrogel lubricates and soothes the inflamed tissues, mimicking the soft tissues within the synovium (Ren et al., 2017). *In situ* forming hydrogels are particularly relevant for IA administration of gels by altering their composition to form a gel *in situ* depending on the physiological conditions like a change in pH, temperature, or ionic composition (Koland et al., 2022).

1.15. Animal models of RA

The application of RA animal models has significantly improved our understanding of the mechanisms/mediators involved in developing inflammation, cartilage loss, and bone resorption, thus considerably improving therapeutic intervention for this disease. RA animal models are widely utilized in studies on the pathogenesis of inflammatory arthritis and in the pharmaceutical sector to screen new anti-arthritic drugs. The capacity to predict an agent's therapeutic effectiveness in humans, the model's ease of performance, the data's reproducibility, the appropriate duration of the study period, and a model's relevance to the pathology and pathogenesis of the human disease are all crucial factors in the selection of a model (A.M. Bendele, 2001).

1.15.1. Adjuvant-induced arthritis (AIA)

AIA is a gold-standard experimental model of polyarthritis that has been extensively utilized for preclinical testing of various anti-arthritic medicines that are either under preclinical or clinical development and are currently employed as treatments for this disease. The features of this model are reliable development and progression of a polyarticular inflammation that is robust, easily measurable, and characterized by significant bone resorption and cartilage

destruction. The pathophysiology and causes of adjuvant arthritis developed after the injection of atherogenic substances, i.e., Freund's Adjuvant, Complete cell suspension (FCA) supplemented with heat-killed *Mycobacterium tuberculosis* at the base of the tail or in one of the foot pads of the healthy animals, i.e., rats and mice (Choudhary et al., 2018).

1.15.2. Collagen-induced arthritis (CIA)

CIA is researched more extensively as an RA preclinical animal model as it shares several immunological and pathological characteristics with human RA. A joint antigen (collagen type II) is the target of an immunological response in CIA. The CIA model's two key traits are the breach of tolerance and the production of autoantibodies against collagen and self. This model is T helper cell-mediated, in which both T helper (Th1) and (Th17) responses are induced in CIA, but Th17 cells appear to play the dominant pathological role. This model is T helper cell-mediated, in which both T helper (Th1) and (Th17) responses are induced in CIA, but Th17 cells appear to play the dominant pathological role. The first CIA animal model was established in rats by immunization with type II collagen. The CIA model was later reproduced in mice and monkeys (Choudhary et al., 2018).

1.15.3. Antigen-induced arthritis

In the antigen-induced arthritis model, the animal is immunized using subcutaneous or intradermal injections of the multiple antigens, which is often a cationic material like methylation bovine serum albumin (m-BSA), which will attach to negatively charged cartilage and remain in the joint. An injection of the antigen causes acute inflammation in one or both joints, rapidly progressing to joint destruction. The pathophysiology involves an arthus response on the articular cartilage, as antibodies to the positively charged antigen that are injected form

complexes that activate complement locally and cause cartilage degradation. The effectiveness of biological treatments and the function of specific cytokines in the different phases of disease pathogenesis have been extensively studied using mouse models of antigen arthritis (Choudhary et al., 2018).

1.15.4. Pristane-induced arthritis (PIA)

PIA is a novel RA experimental murine disease model induced by administering well-defined synthetic adjuvant oil, pristane. Severe and chronic arthritis developed within two weeks after a single intradermal injection of 150 μ l of pristane in rats. The inflammation mainly contributed to joint-specific pannus development, MHC class II expression, and T lymphocyte infiltration (Choudhary et al., 2018).

1.15.5. Genetic animal models of RA

In contrast to the induced-arthritis models (AIA, CIA, PIA), the development of arthritis occurs spontaneously in some genetically modified animals, especially in mice. Most of these mouse models are transgenic or knockout for a particular gene of interest. These models provide information regarding the role of various genes in the inflammation process and serve as a research tool to study the effect of multiple therapeutics for RA drug development. K/BxN mice, SKG mice, and human tumor necrosis factor gene (HTNFG) mice are commonly used transgenic RA mouse models (Choudhary et al., 2018).

1.16. Specific objectives of this study

The main focus of this thesis was to develop a drug-loaded smart injectable hydrogel as a drug delivery system for the treatment of RA, which can deliver therapeutic agents in tandem to allow for enhanced targeting and improve treatment therapy. My first step was to prepare an optimal PEITC-loaded hydrogel as a smart injectable and assess its efficacy in Freund's complete adjuvant (FCA)-induced arthritis conditions. This is a comprehensive study where different parameters related to the formulation, release kinetics (*in vitro* and *in vivo*), toxicity (drug and polymer) in major organs, and the efficacy of the hydrogel in a RA condition are being assessed to deliver a safe and reliable thermosensitive injectable formulation loaded with PEITC.

Since RA is a multifactorial autoimmune condition; next, I attempted to treat RA holistically and synergistically by co-delivering MTX, a standard slow-acting anti-rheumatic drug, and PEITC using a SA-PF-127 *in situ* hydrogel formulation. This was an improvisation of the result obtained from the first step of the study. Despite exhibiting good anti-arthritic activity, the drawbacks of MTX and PEITC, such as poor solubility, low bioavailability, and several side effects, are undesirable properties that limit their usage. Co-delivering MTX and PEITC in their nano-particulate form can enhance stability and solubility and further facilitate greater penetration in the target arthritic tissues.

The specific research objectives for the present study include

- 1) To formulate and characterize a thermosensitive injectable hydrogel loaded with a natural isothiocyanate, i.e., PEITC.
- 2) To assess the biodegradability and biocompatibility of PEITC-loaded thermosensitive injectable hydrogels *in vitro* and *in vivo*.

- 3) To determine the therapeutic efficacy of PEITC-loaded thermosensitive injectable hydrogel system in animal models of arthritis.
- 4) To construct dual-drug nanoparticles loaded smart hydrogel (MTX and PEITC) as a safe and biocompatible co-delivery system to enhance its synergistic activity in RA conditions.

Chapter 2

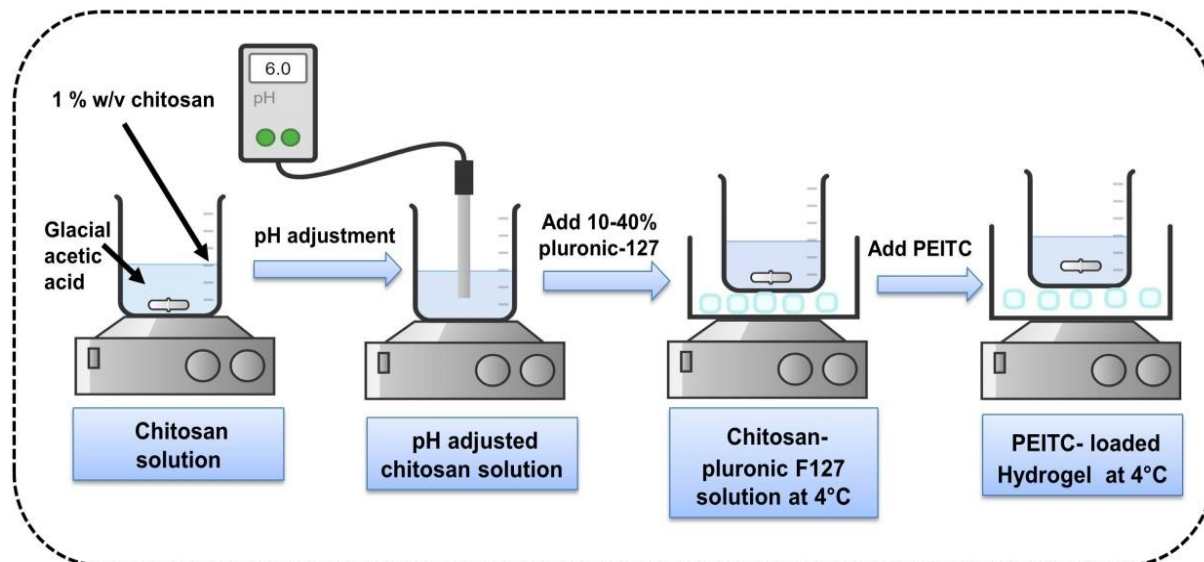
**Fabrication, characterization, and
assessment of the biosafety and
therapeutic efficacy of PEITC-loaded
thermosensitive *in situ* injectable hydrogel
system in healthy and RA conditions**

RA is an autoimmune condition that accompanies chronic inflammation of joints with limited therapeutic options. Among natural ITCs, PEITC is commonly used for treating various diseases, including cancer and RA. This bioactive phytochemical exerts its chemopreventive, antioxidant, and anti-inflammatory activity via the Nrf-2 pathway. However, limited water solubility, short half-life, and instability are reasons for the low bioavailability of PEITC that hampers clinical application. Considering the above pharmaceutical drawbacks, my first step was to prepare an optimal PEITC-loaded hydrogel as a smart injectable and assess its efficacy in Freund's complete adjuvant (FCA)-induced arthritis conditions. This is a comprehensive study where different parameters related to the formulation, release kinetics (*in vitro* and *in vivo*), toxicity (drug and polymer) in major organs, and the efficacy of the hydrogel in a RA condition are being assessed to deliver a safe and reliable thermosensitive injectable formulation loaded with PEITC.

2.1. Fabrication of PEITC-loaded CS/PF-127 hydrogel and assessment of various physicochemical parameters

2.1.1. Preparation and physicochemical characterization of PEITC-loaded hydrogel

The CS/PF-127 hydrogel or Blank hydrogel (BH) are expected to remain in solution at room temperature and gelate at physiological conditions (37 °C and pH 7.4) for proper depot formation *in vivo*. The gelation behavior and nature of the CS/PF-127 hydrogels mainly depend on temperature and PF-127 concentrations and can be suitably altered to cater to different clinical requirements (Chang et al., 2002; Chung et al., 2020). Therefore, other CS/PF-127 hydrogels with varying concentrations of PF-127 (10-40 %) were initially prepared by a physical mixing cold method (**described in the M&M section, Chapter 5**), as illustrated in **Scheme 1**.



Scheme 1: Schematic overview of the preparation of BH and PEITC-loaded hydrogel.

Sol-gel transition studies were performed at 25 °C and 37 °C to determine the time for gel formation at different temperatures by tube tilting. As shown in **Figure 12A**, gel formation was only observable at more than 18 % w/v of PF-127 mixed with CS. A substantial difference in gelation time of 396 ± 15 s (at 25 °C) and 61 ± 4 s (at 37 °C) was observed when 20 % w/v PF-127 was added. The time differences were relatively small in other mixtures. For ease of application, minimal gelation at 25 °C and a more extended sol-to-gel transition period are preferred. This enables proper solution dispensing into the syringe that can be smoothly injected into the body (**Figure 12A**). Therefore, a 1:20 ratio of CS: PF-127 was selected for the preparation of three PEITC hydrogels loaded with 20 mg (PH20), 40 mg (PH40), and 60 mg (PH60) PEITC.

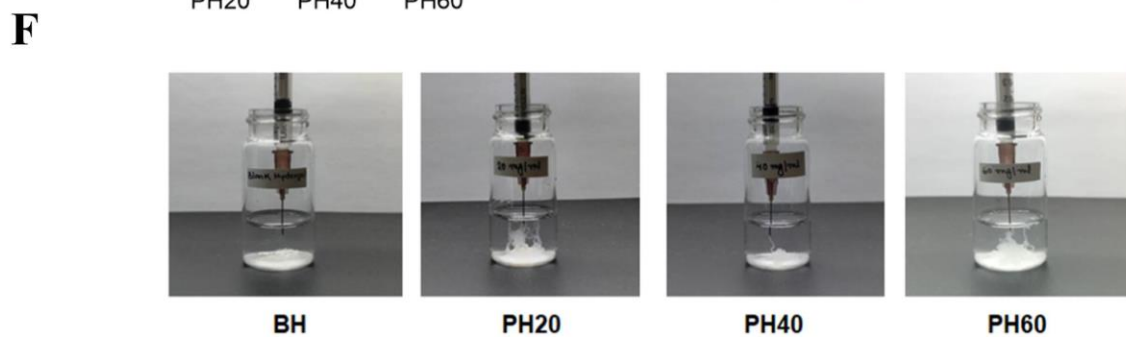
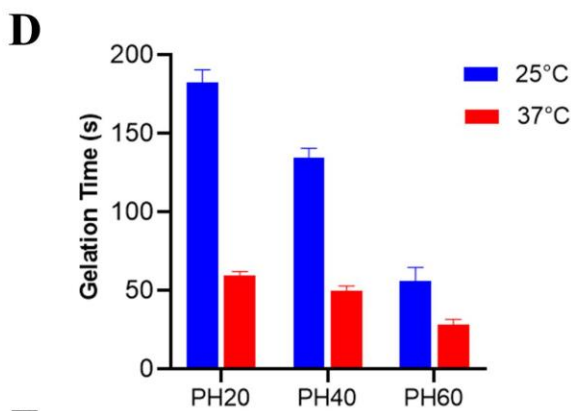
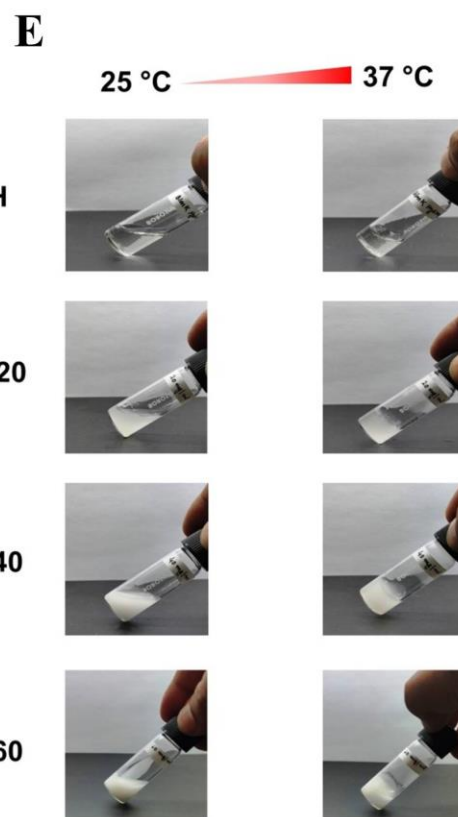
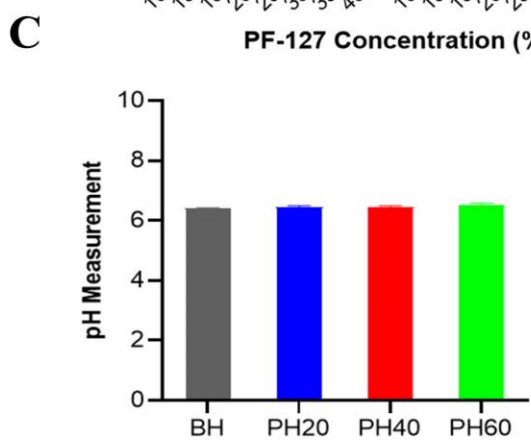
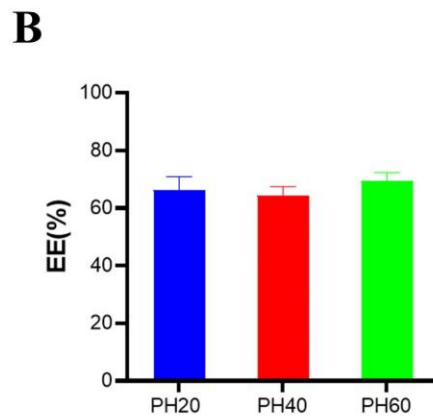
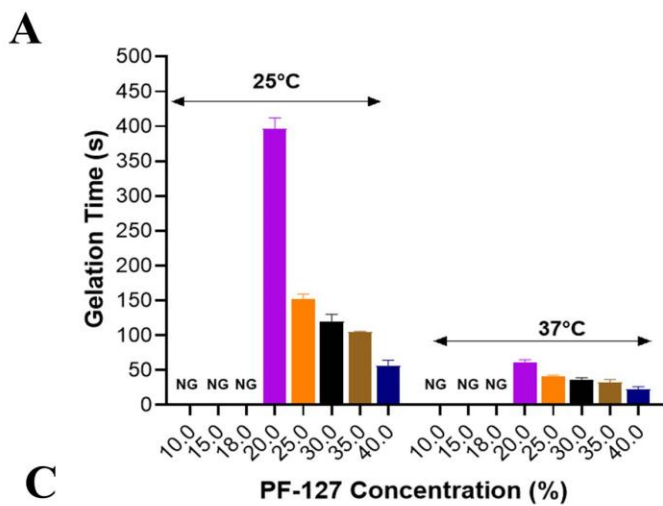


Figure 12. Preparation and characterization of the PEITC-loaded hydrogel (A). Gelation time at 25 °C and 37 °C of hydrogels of varying concentrations PF-127. NG: No gelation. (B). The encapsulation efficiency (EE) (%) of PEITC-loaded hydrogels (PH20, PH40, PH60). The values are expressed in mean \pm SD (n = 3). (C). The pH of the final hydrogels. Results are presented as mean \pm SD (n=3). (D). The gelation time of the different concentrations of PEITC-loaded hydrogels (PH20, PH40, PH60) was at 25 °C and 37 °C. (E). Representative image of the sol-gel phase transition characteristics of BH and PEITC-loaded hydrogels (PH20, PH40, PH60). Phase changes with a temperature increase. (F). The injectability of the different hydrogels was studied under physiological conditions (37 °C and pH- 7.4).

The mixing of PEITC (a water-immiscible oily molecule) in the CS/PF-127 solution (clear aqueous phase) resulted in a white opaque hydrogel emulsion. The white color and gel consistency intensity increased with PEITC with a % drug entrapment for the PH20, PH40, and PH60 formulations to be 66 ± 4.56 , 64 ± 3.22 , and 69 ± 2.82 , respectively (**Figure 12B**). No noticeable variation in pH value was observed before and after drug incorporation into the BH. The final pH of all the PEITC-loaded hydrogel formulations (PH20, PH40, and PH60) was 6.40-6.53 (**Figure 12C**).

The increased loading of PEITC into the BH did affect the gelation time. From the gelation studies for sol-gel transition time, an increase in the PEITC amounts in BH solution gradually decreased the gelation time (at 37 °C), i.e., 59.3 s, 49.6 s, and 28.0 s for 20 mg/mL, 40 mg/mL and 60 mg/mL of PEITC respectively (**Figure 12D**). A relatively quick gel was formed in the case of PH60 gel (56 s at 25 °C and 28 s at 37 °C) compared to the time taken by PH20 and PH40 gels.

The different hydrogel formulations (BH, PH20, PH40, and PH60) remained homogenous and stable at room temperature and formed a gel-like structure at physiological temperature (37 °C) (**Figure 12E**). Its performance as an injectable was verified by injecting the hydrogel solution into phosphate buffer saline (PBS) (at 37 °C). At this stage, the solution flows freely into the syringe and can be injected smoothly, forming a continuous thread-like soft gel without any phase separation or aggregates (**Figure 12F**).

2.1.2. Characterization of PEITC-loaded hydrogel using FTIR and FESEM

Fourier transform infrared spectroscopy (FTIR) was used to confirm the possible interactions between PEITC and the polymeric matrix (PF-127 and CS) by comparing peak shifts in the wavenumber (cm^{-1}) (Lieber et al., 1959). The infrared spectra of Free PEITC at conc. 60 mg/mL (PEITC60), BH, and PH60 samples are shown in **Figure 13A**. The FTIR spectra of the PH60 sample were compared with the peaks of PEITC60 and BH to confirm PEITC incorporation and for any chemical modifications. The following similar functional characteristic peaks of the polymer were observed in BH and PH60 gel, respectively: (i) The –OH group stretching vibration was observed at 3416 cm^{-1} (BH) and 3395 cm^{-1} (PH60). (ii) The –CH group was stretching vibration at 2885 cm^{-1} (BH) and 2883 cm^{-1} (PH60). In the case of PEITC, the functional peaks of (-N=C=S) characteristic for isothiocyanates (ITCs) were previously reported either at 2140 cm^{-1} or between 2060 cm^{-1} and 2105 cm^{-1} (Lieber et al., 1959; Mohanty et al., 2020). From the samples of PEITC60 and PH60, functional characteristic peaks were observed at 2188 cm^{-1} ; 2115 cm^{-1} , and 2182 cm^{-1} ; 2110 cm^{-1} , respectively. These results confirm the incorporation of PEITC into the hydrogel and further validate the non-covalent interaction of PEITC with the hydrogel components. At the same time, it remains encapsulated in the polymer matrix.

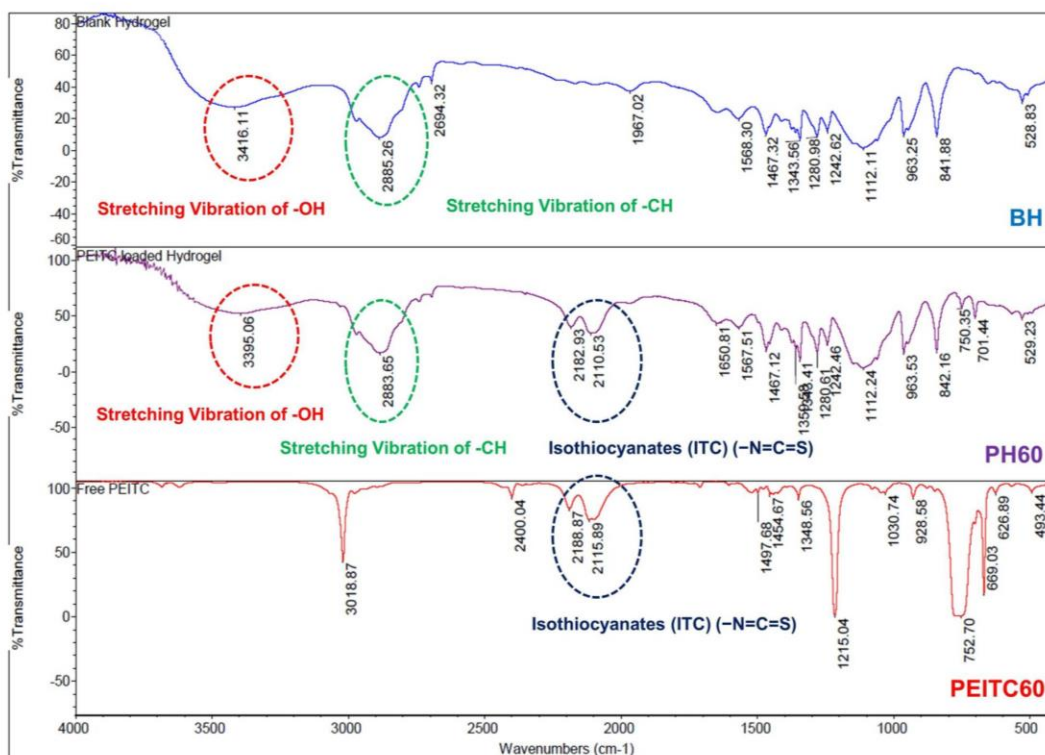
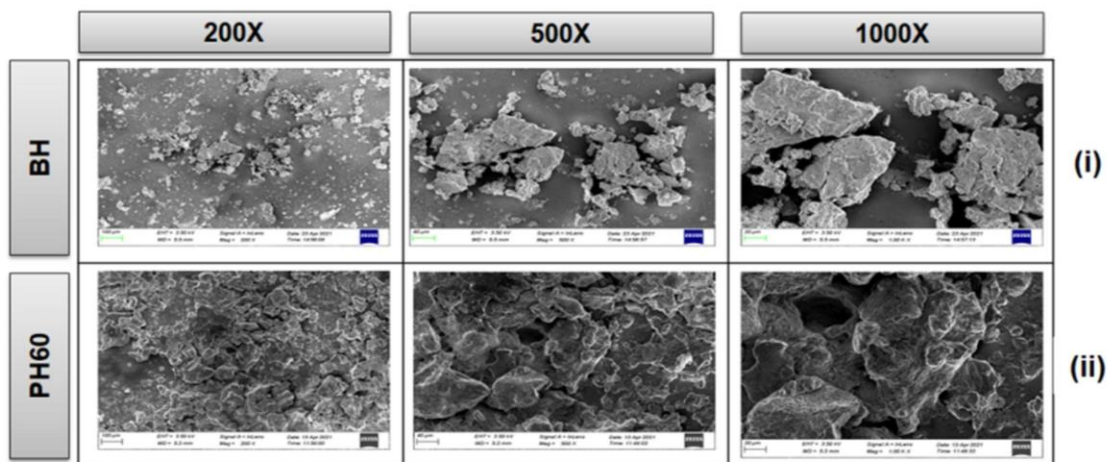
A**B**

Figure 13. Characterization of the PEITC-loaded hydrogel using FTIR and FESEM. (A). FTIR spectra of BH, PH60, and PEITC60. (B). FESEM images of (i). BH and (ii). PH60 at 200 \times , 500 \times , and 1000 \times magnification. FTIR: Fourier transform infrared spectroscopy, FESEM:

Field emission scanning electron microscope.

The present FTIR study aimed to determine whether any drug-excipient interaction could result in a chemical change in the PEITC when combined with the hydrogel. Meanwhile, no peak shift was seen from the PH60 and BH excipients; PEITC has not undergone any chemical alteration.

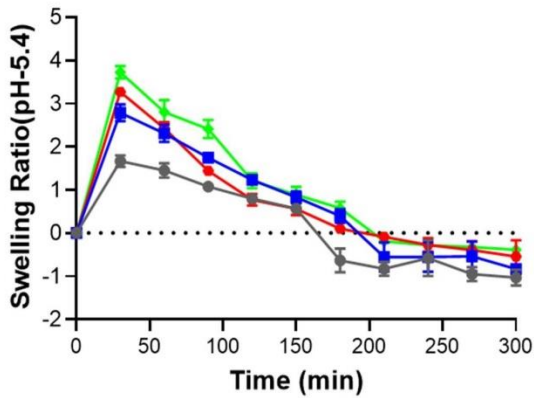
A field emission scanning electron microscopy (FESEM) study was performed to further analyze the structural and morphological features of lyophilized BH and PH60 before and after PEITC incorporation (Leyva-Gómez et al., 2017). The FESEM images showed several porous structures in BH and PH60 samples at higher magnifications due to the hydrophobic interaction between CS molecules and PF-127 (Chung et al., 2020; Park et al., 2009). A smooth surface with well-defined edges was observed in the BH images (see **Figure 13B, (i)**). In the case of PH60, the PEITC incorporation into the hydrogel resulted in an irregular surface with a three-dimensional (3D) porous network structure (**Figure 13B, (ii)**). The porous structure provides higher drug-loading and sustained release properties to the PEITC-loaded hydrogel (Turabee et al., 2019; Wang et al., 2016).

2.1.3. Swelling and degradation profile of PEITC-loaded hydrogel in vitro

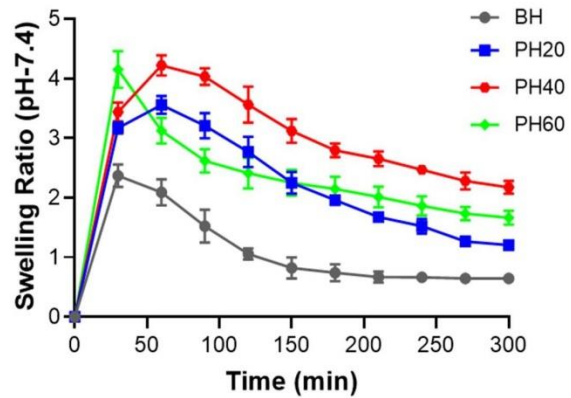
The swelling property of the hydrogel is a critical factor for drug release, as it dramatically affects the release of the drug from the hydrogel matrix (Carbinatto et al., 2014). The accessibility of the hydrogel to water molecules and its stability as a gel is mainly dependent on polymer crosslinking efficiency and gelation at a given pH and temperature. The swelling behavior of the hydrogels (BH, PH20, PH40, and PH60) was studied at pH 7.4 and pH 5.4 at 37 °C. At pH 7.4, all hydrogels remained swollen until 5 h, as shown in **Figure 14A, (ii)**.

A

(i) at pH - 5.4



(ii) at pH - 7.4



B

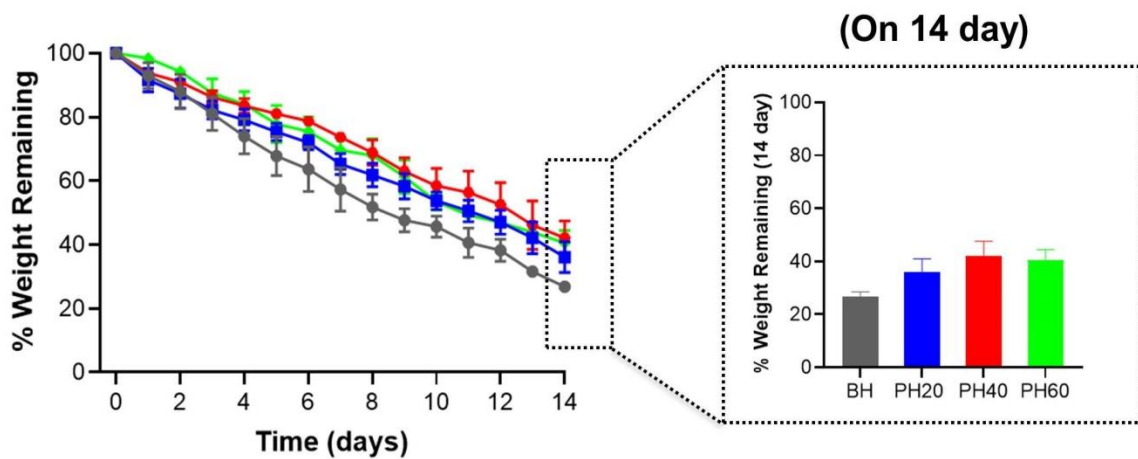


Figure 14. The swelling and degradation properties of PEITC-loaded hydrogel *in vitro*. (A). The swelling behavior of hydrogels was studied in two different pH conditions (i). pH 5.4 and (ii). pH 7.4 at 37 °C. (B). The degradation rate of the hydrogels at 37°C was studied by calculating the % amount of remaining hydrogels at different time points until 14 days. The bar graph shows the weight of the non-degraded fraction of the gel on the final day (14th day) for

other hydrogels. All the data are presented as mean \pm SD (n = 3).

In pH 5.4 conditions, the hydrogels could endure their swollen state only until 30 min, followed by complete dissolution into the medium after 150 min (**Figure 14A, (i)**). Here, the dissolution at pH 5.4 may be due to the protonation of its amine groups in CS polymer, resulting in a strong electrostatic repulsion among the ionized amine groups affecting the crosslinks (Szymańska & Winnicka, 2015). In addition, the increased hydrophilicity of PF-127 in an acidic environment might have resulted in the faster dissolution of the gel structure (Chatterjee et al., 2019; Klouda and Mikos, 2008). This study validates the hydrogel matrix CS: PF-127 (1:20) as a promising drug carrier system for the encapsulation of PEITC that can be delivered in different *in vivo* pH conditions.

Following a gradual release of the drug, slow degradation of the hydrogel matrix is desirable for its different biomedical applications (especially in the case of injectable hydrogels) to negate the need for any additional surgical intervention to remove the matrix (Pankongadisak and Suwantong, 2019; Ren et al., 2017). From an *in vitro* degradation study under physiological conditions for 14 days (pH 7.4 and 37 °C), the % remaining mass of PH20, PH40, and PH60 was determined to be 36.07 %, 42.18 %, and 40.50 %, respectively, while the BH showed higher degradation (remaining of 26.81 %) (**Figure 14B**).

2.1.4. In vitro release profile of PEITC-loaded hydrogel

The different parameters that play a critical role in the release kinetics of the drug include the physicochemical property of the loaded drug, its amount, and the pH of the *in vivo* microenvironment (where the hydrogel will be placed). These parameters significantly affect the

crosslinks in the matrix, affecting its release. Therefore, drug-loaded hydrogel intended for different microenvironments requires utmost care and optimization.

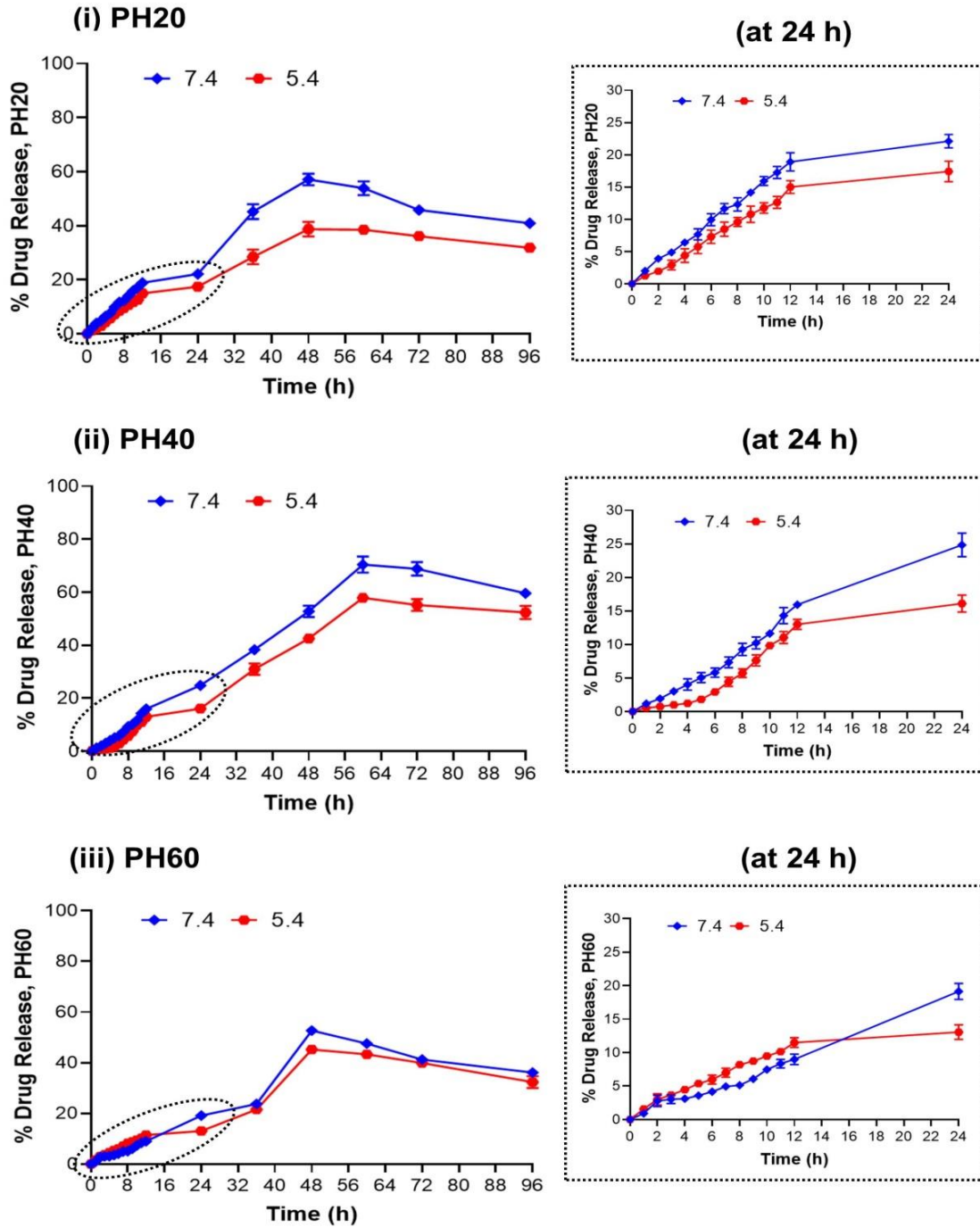


Figure 15. The drug release properties of PEITC-loaded hydrogel *in vitro*. % PEITC release from the hydrogel vs. time (h) at pH 7.4 and 5.4 at 37 °C with different PEITC concentrations (i). 20 mg/mL (PH20) (ii). 40 mg/mL (PH40) and (iii). 60 mg/mL (PH60) was measured at 365 nm. *Blue* color: pH = 7.4, and *red*: pH = 5.4. All the data were presented as mean \pm SD (n = 3).

Prior to the *in vivo* assessment in animals, the effect of pH on the release of PEITC from the differently loaded hydrogels (PH20, PH40, and PH60) was studied in pH 7.4 (neutral) and pH 5.4 (acidic) conditions at 37 °C *in vitro* (Turabee et al., 2019). The PEITC concentration in the respective samples (at different time points) was determined by BDT assay (**M&M section chapter 5**). Overall, a sustained release of PEITC from all hydrogel preparations in both pH conditions (**Figure 15, (i-iii)**). However, in pH 7.4 conditions, a pH-responsive release profile was observed where the % cumulative PEITC release from the hydrogel was higher than PEITC release in pH 5.4. At 48 h (in pH 7.4), the % cumulative release of PEITC from its hydrogel (PH20, PH40, PH60) was found to be 57.13 %, 52.80 %, and 52.71 %, respectively, while the samples from pH 5.4 showed lower PEITC releases (38.71 %, 42.53 %, and 45.22 % respectively). The lower release rate of PEITC at pH 5.4 from the hydrogels suggests that most of the PEITC molecules were inside the hydrophobic core of micelles, and the PEITC molecules on the outer layers were released initially (Turabee et al., 2019).

A higher release profile of PEITC from equally loaded hydrogels at pH 7.4 was observed, possibly due to the porous structure in the hydrogels, as evidenced by the FESEM study. At physiological pH conditions (pH 7.4), both polymers PF-127 and CS were previously reported to remain less soluble, retaining the 3D structure of the hydrogel with high porosity (Turabee et al., 2019). This way, PEITC (with low molecular weight = 163.24 g/mol) has a higher chance of diffusing out more rapidly from hydrophobic core micelle at a neutral pH than in an acidic

environment. Taking the results together, it is clear that incorporating PEITC into the hydrogel matrix facilitated the formation of a well-interconnected 3D structure of the latter, thereby increasing its mechanical stability.

2.1.5. *In vitro* hemolytic activity of PEITC-loaded hydrogel

The hemolytic activity of the drug-loaded hydrogel was performed *in vitro* to establish its biosafety and effectiveness as the released components from the injected site enter the systemic circulation from the injected site and first come in contact with the blood.

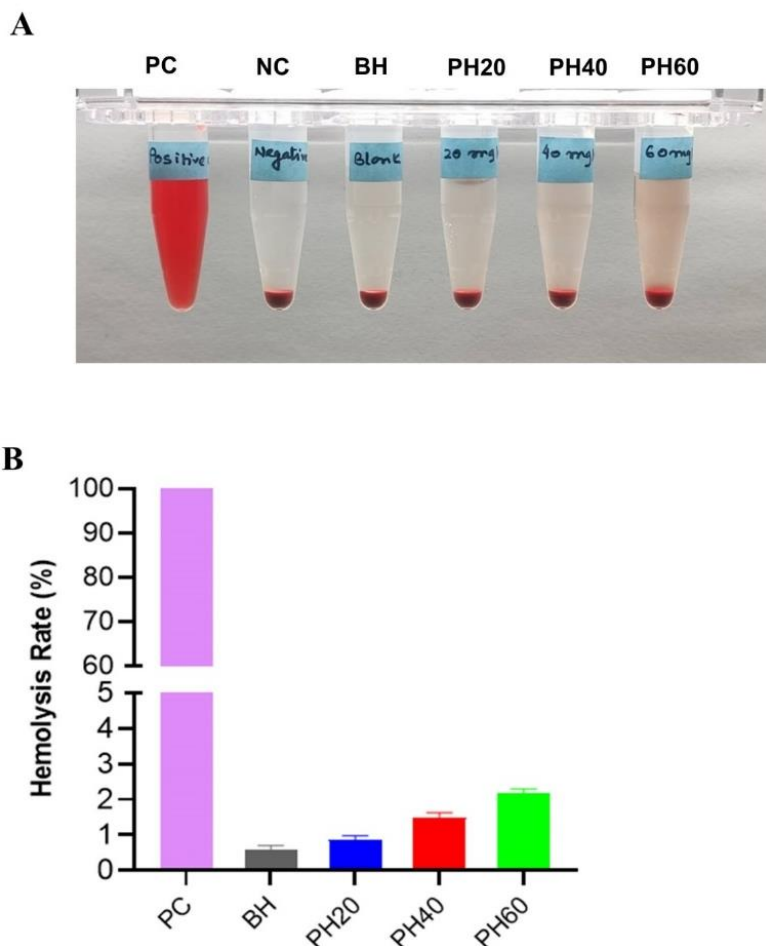


Figure 16. Hemolytic activity of PEITC-loaded hydrogel. The hemolysis assay determined the

hemolytic activity of the hydrogels and PEITC. (A). Representative image of erythrocytes treated with BH, different PEITC-loaded hydrogels (PH20, PH40, PH60) and compared with the positive control (erythrocyte incubated with 1 % Triton X-100, 100 % lysis) and negative control (erythrocyte incubated with PBS, 0 % lysis). (B). Bar graphs represent the hemolysis rate (%). The data are expressed as mean \pm SD (n = 3). PC - Positive control, NC - Negative control.

The hemolysis assay results in **Figure 16A-B** show that the BH had 0.60 % hemolytic activity. In the case of PEITC-loaded hydrogels, the maximal hemolysis (%) was 2.15 % (for PH60), followed by 1.49 % and 0.87 % for PH40 and PH20, respectively. Although the % hemolysis increased with an increase in drug concentration, it was much lower than 5 %, confirming hydrogel's non-hemotoxic and biocompatible nature (Shi et al., 2016). Overall, the *in vitro* studies concluded that PEITC-loaded hydrogel up to 60 mg/mL is non-hemolytic and can be safely injected into animals for further *in vivo* studies.

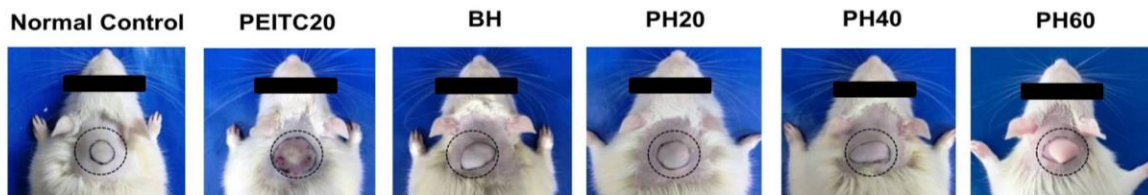
2.2. *In vivo* evaluation of PEITC-loaded hydrogel formulations

An ideal gel system must be biocompatible and synergize the tissue regeneration process. Further, the polymer materials must biodegrade gradually within the system without adversely affecting any major organs or their functioning. Upon optimizing and evaluating the required PEITC-loaded formulation for *in vitro* conditions, the biocompatibility and biosafety of the loaded drug and hydrogel carrier were assessed in whole animals (rats). Here, *in vivo*, parameters for biocompatibility and distribution, such as skin compatibility, hemocompatibility, the pharmacokinetics of the drug from hydrogel, its distribution, and accumulation in major organs, were studied to establish the safety of the optimal dose *in vivo*.

2.2.1. *In vivo* gel formation and skin compatibility studies

The *in vivo* gel formation and degradation of BH and PEITC-loaded hydrogels (PH20, PH40, PH60) were evaluated following a single subcutaneous (SC) injection of hydrogel solution into the SD rats. The hydrogel formed an easily noticeable globular protuberance (Xu et al., 2019). After thirty minutes, the skin around the protuberance was excised to see the fully-formed hydrogels, indicating successful *in situ* gelation (**Figure 17A-B, row 1**).

A



B

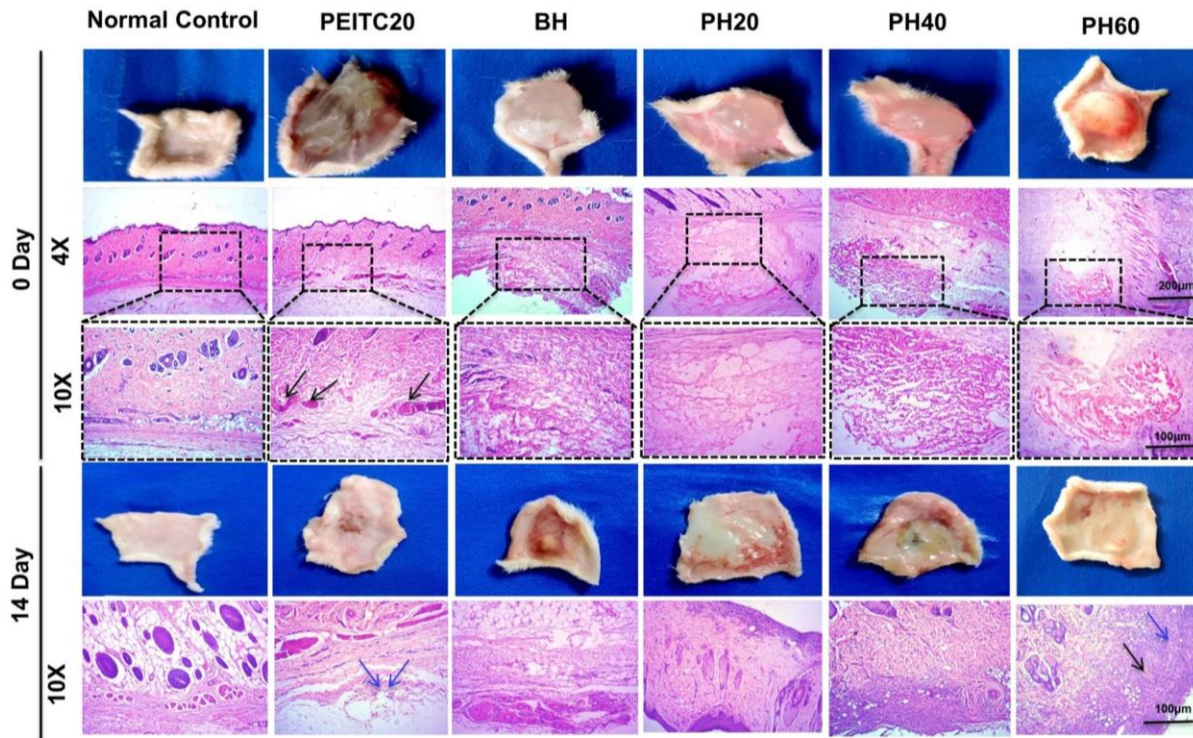


Figure 17. *In vivo* biodegradation and biocompatibility of PEITC-loaded hydrogel. (A). *In situ* gel formation and *in vivo* gel maintenance of the BH and PEITC-loaded hydrogels (PH20, PH40, PH60) were performed following SC injection in the back of rats. Images around the implants (marked as a black-dotted circle) were taken at 30 min (0 days) to indicate the formation of the hydrogels. (B). *In vivo*, degradation was recorded from the images of the excised skin around the implanted site at 0 days and 14 days after the injection. Histological images of the SC tissues (H&E stained) surrounding the hydrogels. Scale bar = 200 μm (4x) and 100 μm (10x). *Black* arrow – focal areas of angiotelectasis/ dilation of blood vessels, *blue* arrow – inflammatory cells with necrotic tissue. H&E: Hematoxylin and eosin.

Over time, all *in situ* hydrogels degraded gradually and disappeared completely within 14 days (**Figure 17B, row 4**). In contrast to the degradation *in vitro*, the hydrogels displayed a faster degradation rate *in vivo* (Xu et al., 2019).

Histological studies on the skin tissues excised around the hydrogel injected site (in the SC layer) were H&E stained and examined under a microscope to confirm the *in vivo* biocompatibility of the PEITC-loaded hydrogels (Xu et al., 2019). The PEITC20 group showed enhanced inflammatory cells and angiotelectasis, indicating progressive acute inflammation through 0 and 14 days post-injection (**Figure 17B**). However, on day 14, with the complete degradation of the hydrogels, surrounding tissue was similar to normal tissue in the hydrogels (BH, PH20 & PH40) treated groups. Toxic symptoms were observed in the PH60 injected skin sections on day 14; skin samples injected with the highest PEITC concentration showed persistent inflammation with inflammatory cells and angiotelectasis.

2.2.2 *In vivo pharmacokinetics and tissue biodistribution studies of PEITC-loaded hydrogel*

The pharmacokinetic study using high-performance liquid chromatography (HPLC) was performed following a single SC injection of PH20 in healthy rats and compared with Free PEITC (PEITC20) injected animals as control groups (SC and oral). As mentioned earlier, PEITC is poorly soluble, highly unstable, and is metabolized and eliminated rapidly with a shorter plasma half-life, thereby limiting its therapeutic activity *in vivo*. The pharmacokinetic profile of PEITC, when administered in free form and as a drug-loaded hydrogel, was evaluated and compared based on different parameters (mainly T_{max} , AUC, and plasma half-life) to study its accumulation, release, and elimination. The plasma concentration profile of the PEITC20 (oral), PEITC20 (SC), and PH20 are shown in **Figure 18A**.

Following 12 h of PEITC administration by oral or SC route, only a negligible amount of PEITC was detected in the blood plasma. However, a reasonably well-detectable amount ($1.40 \pm 0.23 \mu\text{g/mL}$) of PEITC released from the hydrogel (PH20) was present in blood plasma simultaneously. Trace amounts ($0.085 \pm 0.092 \mu\text{g/mL}$) of PEITC from PH20 were detectable till 48 h. The results from different pharmacokinetic parameters showed that the AUC_{0-t} of PH20 was **8.5-** and **3.0-fold** higher than the PEITC20 (SC) and PEITC20 (oral), respectively. The plasma half-life ($t_{1/2}$) of PEITC from PH20 was determined to be **4.45** and **2.07-fold** higher than PEITC20 (SC) and PEITC20 (oral), respectively. The PH20 had **5.3** and **3.43-fold** higher mean residence time than the PEITC20 (SC) and the PEITC20 (oral), confirming the presence of PEITC released from the hydrogel in the systemic circulation for an extended period. These results ensured that the half-life of PEITC in the plasma can be well-prolonged when incorporated into the CS/PF-127 hydrogel as a carrier system. The sustained release pattern of PEITC from the hydrogel showed a similar release profile as obtained from the *in vitro* studies.

The other pharmacokinetic parameters related to PEITC20 (oral), PEITC20 (SC), and PH20 are shown in **Table 2**.

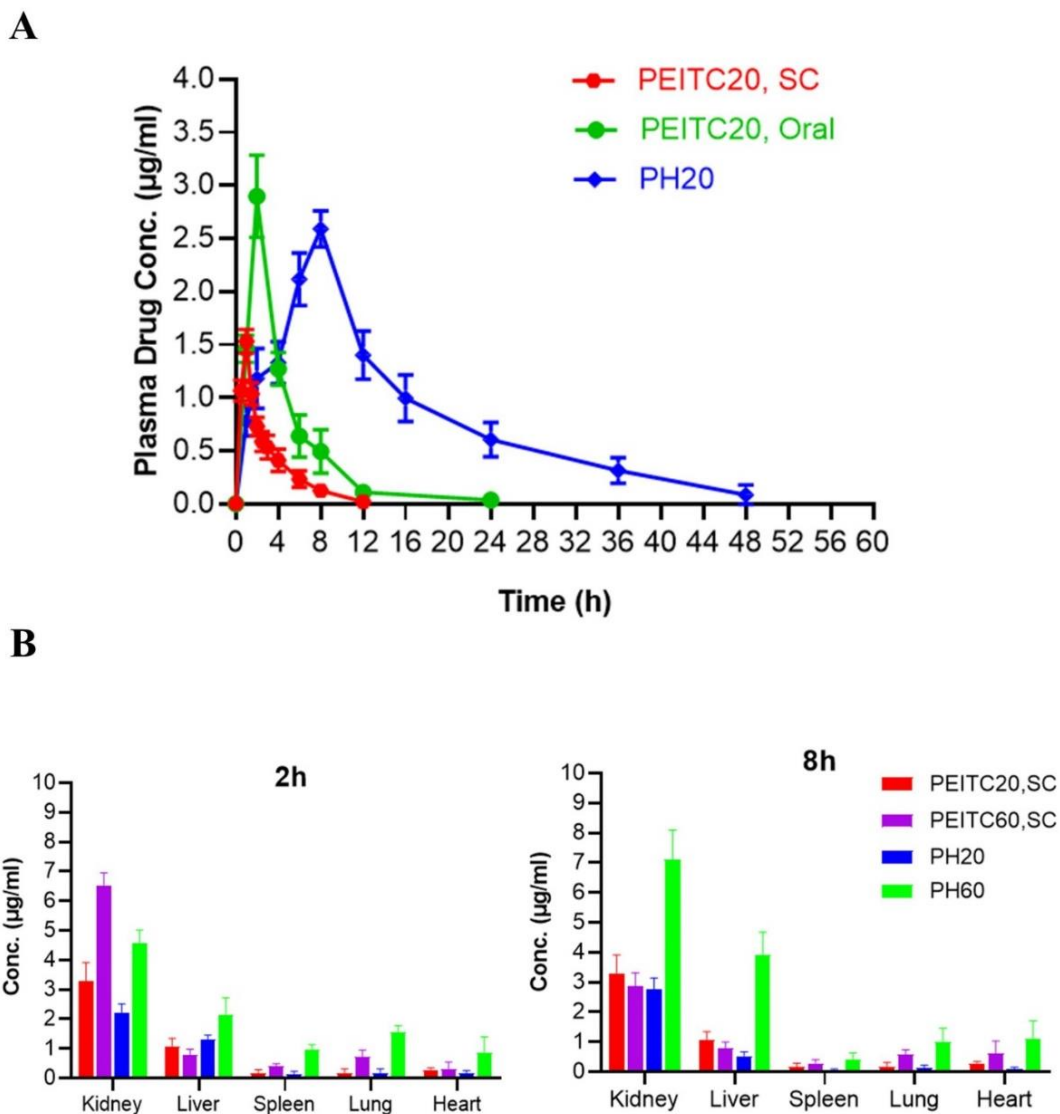


Figure 18. *In vivo* pharmacokinetics and tissue biodistribution of PEITC-loaded hydrogel. The rats were injected with either the hydrogel or in the free form *via* the SC route and sacrificed at various times. PEITC accumulation in major organs (heart, liver, spleen, lung, and kidney) of the rats after 2 h and 8 h were analyzed by HPLC. (A). Plasma concentration

vs. time profiles of PEITC following single SC administration of PEITC20 (oral), PEITC20 (SC), and PH20 in healthy rats analyzed by HPLC. *Blue* color - Plasma concentration vs. time profile of PH20, *Green* color - Plasma concentration vs. time profile of PEITC20 (oral), *Red* color - Plasma concentration vs. time profile of PEITC20 (SC). (B). *In vivo* biodistribution of free PEITC (PEITC20, PEITC60) and PEITC-loaded hydrogels (PH20, PH60) in healthy rats. Each data point is plotted as mean \pm SD of duplicate measurements. HPLC: High-performance liquid chromatography.

Table 2. Pharmacokinetic parameters of Free PEITC (oral and SC) and PEITC-loaded hydrogel in rats' blood after SC administration of PEITC20 (oral), PEITC20 (SC), and PH20. Each data point is plotted as mean \pm SD of duplicate measurements.

Pharmacokinetics Parameters	Treated Samples		
	PEITC20,Oral	PEITC20,SC	PH20
C_{\max} ($\mu\text{g/mL}$)	2.89 ± 0.38	1.53 ± 0.11	2.60 ± 0.17
T_{\max} (h)	2.00 ± 0.00	1.00 ± 0.00	8.00 ± 0.00
C_0 ($\mu\text{g/mL}$)	1.46 ± 0.12	1.06 ± 0.09	0.78 ± 0.14
AUC_{0-t} ($\mu\text{g/mL} \cdot \text{h}$)	12.93 ± 2.87	4.64 ± 0.35	39.51 ± 4.62
AUMC ($\mu\text{g/mL} \cdot \text{h}^2$)	61.94 ± 29.28	14.06 ± 2.74	645.52 ± 175.94
Mean residence time (h)	4.58 ± 1.14	2.98 ± 0.33	15.71 ± 1.95
Half-life, $t_{1/2}$ (h)	3.63 ± 1.20	1.69 ± 0.70	7.52 ± 4.06
K_{el} (1/h)	0.205 ± 0.064	0.45 ± 0.18	0.109 ± 0.058
Clearance ($\text{mg}/(\mu\text{g/mL})/\text{h}$)	1.57 ± 0.37	4.28 ± 0.37	0.49 ± 0.078

An *in vivo* biodistribution study was performed in healthy rats to evaluate the retention of the hydrogel formulations in different organs. Following a single SC administration of the

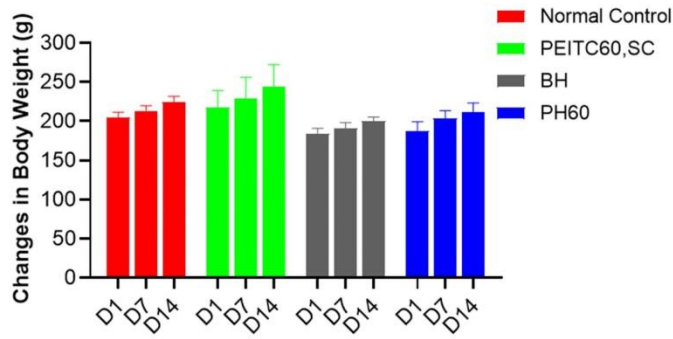
different formulations, the animals were sacrificed at different time points (2 h and 8 h) to determine the PEITC accumulation in the major organs (kidney, liver, spleen, lung, and heart) (Jin et al., 2020). The results show that Free PEITC (PEITC20 and PEITC60, SC) was rapidly distributed and retained more PEITC in the highly vascularized tissues (kidney and liver) as compared to PEITC-loaded hydrogels (PH20 and PH60) (**Figure 18B**). This shows that the organ's blood flow (and perfusion rate) critically affects the distribution of PEITC (Kim et al., 2015). A minor quantity of PEITC accumulated in other organs (especially for PH60) indicates that dose optimization is required to avoid untoward effects.

2.2.3. In vivo toxicity and safety evaluation of PEITC-loaded hydrogel in healthy rats.

There is a broad consensus that *in vivo* toxicity evaluation is vital from the safety perspective of systemic drug delivery systems (Song et al., 2018). Therefore, an *in vivo* safety study of PEITC-loaded hydrogel (PH60) was performed for 14 days to assess whether accumulated PEITC leads to systemic toxicity and/or toxicity to any major organs. Observing changes in body weight is a crucial parameter for understanding the toxicity of any biomaterials (Zhang et al., 2018). Throughout the study period (14 days), as shown in (**Figure 19A**), no significant change was seen in the weight of animals in both of the groups (healthy standard control and treated). Animals in both groups showed increased body weight on day 7 and day 14 compared to day 1 with no signs of abnormal behavior.

The hematopoietic system is the standard and sensitive target for toxic biomaterials and an essential indicator of the body's overall physiological and pathological status (Sundaram et al., 2021).

A



B

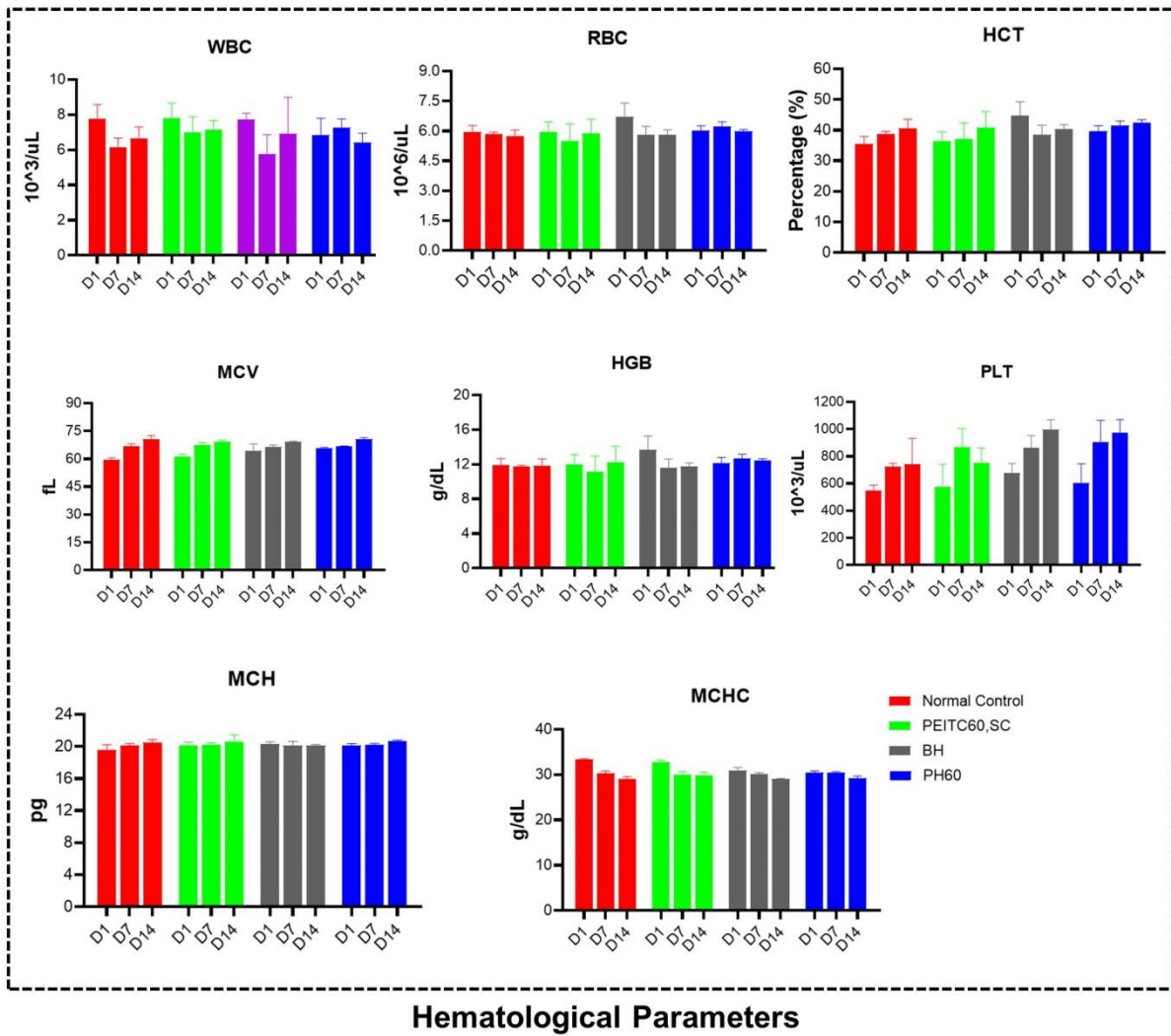


Figure 19. *In vivo* toxicity and safety evaluation in healthy rats. Biosafety evaluation of PEITC-loaded hydrogel (PH60) was performed in the healthy rat following a single SC injection, and the blood samples were collected on days 1, 7, and 14 (D1, D7 & D14). (A). Changes in body weight (in g) on days 1, 7, and 14. (B). Standard hematological parameters assessed in whole blood samples include White blood cells (WBC), Red blood cells (RBC), Hematocrit (HCT), Mean corpuscular volume (MCV), Hemoglobin (HGB), Platelets (PLT), Mean corpuscular hemoglobin (MCH) and Mean corpuscular hemoglobin concentration (MCHC). The data are represented as the mean \pm SD (n = 3).

Following SC injection, the different components of the hydrogel can directly/indirectly alter the hematology factors (such as white blood cells), thereby affecting the immune system (Chen et al., 2013). Hence, observing the effect of the hydrogel on the different hematological parameters provides valuable information on the hemocompatibility properties of the hydrogel and its initial acceptance when present in the bloodstream. From assessing the hematological parameters following a hydrogel administration, two important indicators, the WBC and RBC, showed no profound changes on day 1, day 7, and day 14 (**Figure 19B**). Other parameters, HCT, MCV, HGB, PLT, MCH, and MCHC, were in the normal range compared to the standard control group (He et al., 2017; Xu et al., 2018).

Alongside PEITC release, the degraded hydrogel components that enter the bloodstream can accumulate in the major internal organs (e.g., the heart, liver, spleen, and kidney) (Chen et al., 2013). Therefore, assessing whether this leads to organ toxicity is equally essential. For this purpose, different safety biomarkers for liver and kidney function were evaluated from the serum samples on 1, 7, and 14 days of hydrogel administration (Ko et al., 2019; Xu et al., 2018).

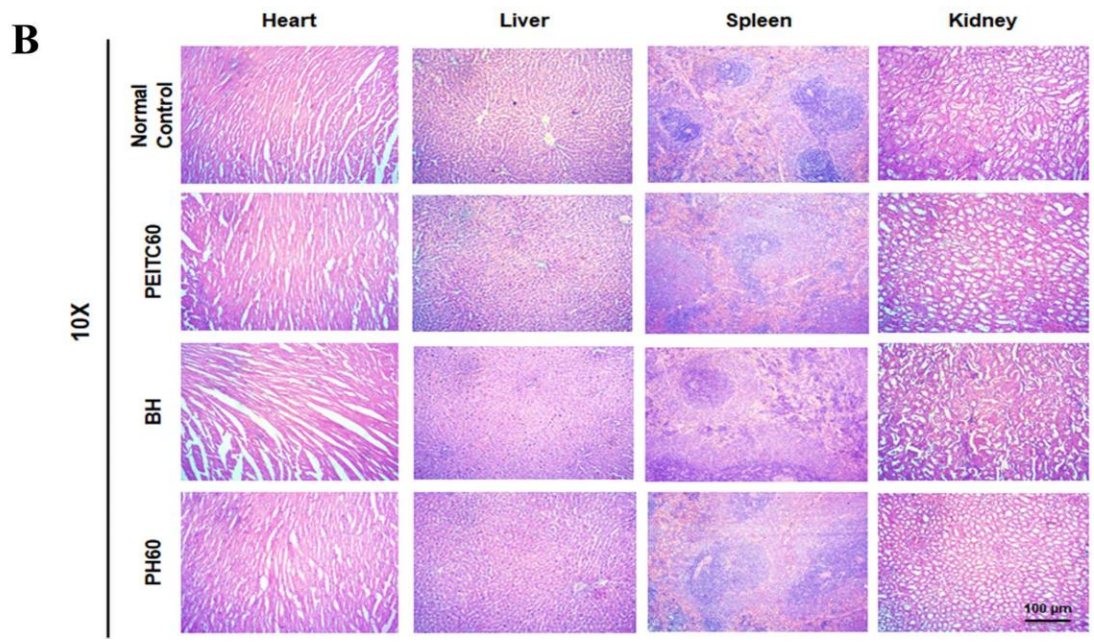
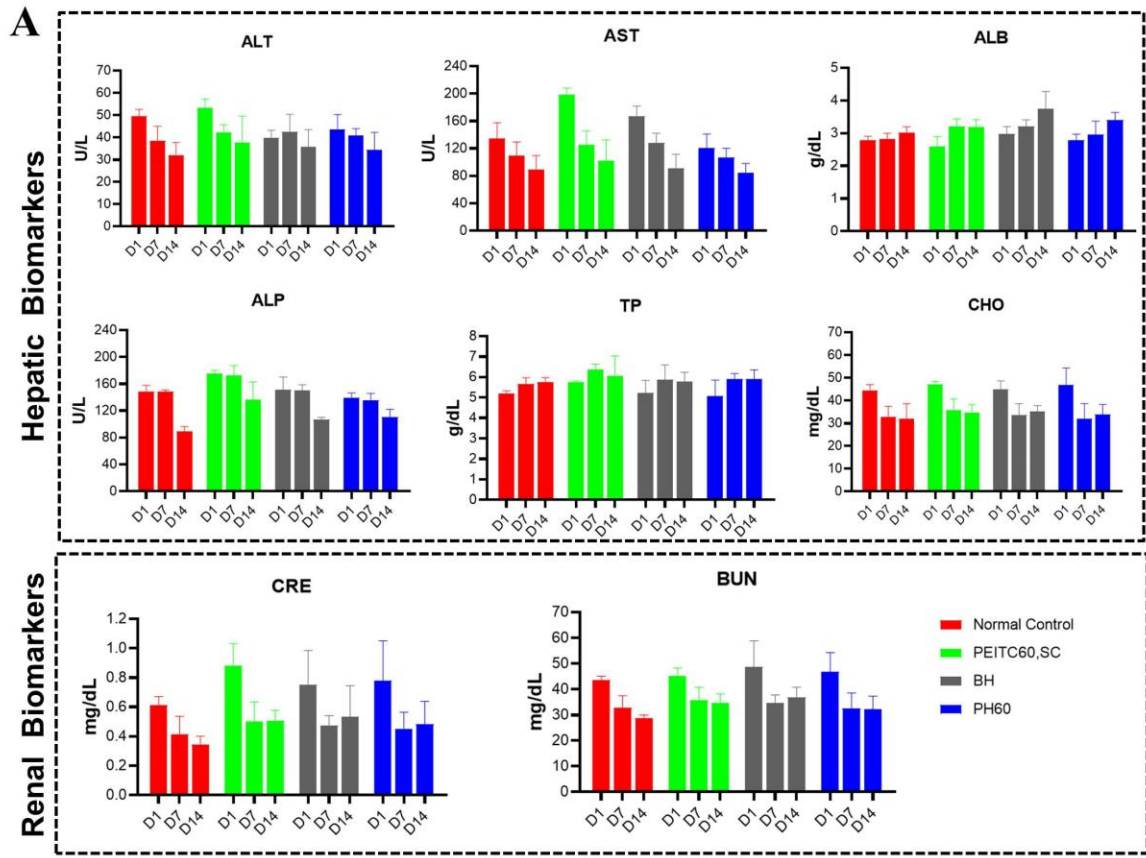


Figure 20. *In vivo* toxicity and safety evaluation in healthy rats. Biosafety evaluation of PEITC-loaded hydrogel (PH60) was performed in the healthy rat following a single SC injection, and the blood samples were collected on days 1, 7, and 14 (D1, D7 & D14 (A)). The serum samples were studied for different biochemical parameters. Alanine transaminase (ALT), Aspartate transaminase (AST), Albumin (ALB), Alkaline phosphatase (ALP), Total protein (TP), Cholesterol (CHO), Creatinine (CRE), and Blood urea nitrogen (BUN). The data are represented as the mean \pm SD (n = 3). (B). Histopathological assessment (H & E stained sections) of primary organs from day 14 animals observed under 100(10x) μ m. H & E: Hematoxylin and eosin.

The serum concentrations of AST, ALT, ALP, TP, ALB, CHO, CRE, and BUN in treated animals were within their normal ranges as in the healthy regular control group shown in **Figure 20A**. Macroscopic examination of the major organs showed no gross morphological alternations after 14 days of administration of the free drug at 60 mg/mL (PEITC60, SC) and BH and PH60 groups, compared to the major organs of the standard control group.

Further, the biosafety of the PEITC-hydrogel treatment group was ensured by microscopically examining the H&E stained sections of the major internal organs (**Figure 20B**). Under different magnifications, No clear areas of atrophy, hyperplasia, necrosis, or inflammation were observed in all the groups (Bailly et al., 2019; Zheng et al., 2017). The results further validate that the PEITC-loaded hydrogel formulation at 60 mg/mL concentration had no toxicity to major body organs.

2.3. Development of adjuvant-induced advanced arthritis animal model (12-day) in rats

A robust 12-day adjuvant-induced advanced arthritis rat model was successfully established using FCA immunization given to healthy rats through intradermal injection into the left hind paw. The redness and swelling were observed after 4 days of FCA immunization. To assess the progression of the disease, various arthritic parameters, including paw volume, arthritis index, changes in body weight, and estimation pro-inflammatory and bone erosion markers (TNF- α , IL-17A, and RANKL) were examined.

Compared to the healthy animals (standard control, without FCA immunization), the FCA-immunized animals (arthritic control) showed a significant increase in paw volume and arthritis score. In this period, the mean body weight in the arthritic control was markedly reduced compared to the standard control. Estimating important pro-inflammatory cytokines (TNF- and IL-17A) and a bone erosion marker (RANKL) in paw tissues and blood using an ELISA kit further established the disease's molecular progression. As shown in **Figure 21F-G**, the paw tissue and serum concentrations of the RANKL, IL-17A, and TNF- α were significantly up-regulated in arthritic control rats compared to respective samples in normal control rats. This study indicates that the FCA-induced rat model represents both pathologic and physiologic features of active RA. So, in further *in vivo* RA studies, the 12-day immunization period will be referred to as “*advanced arthritis*.”

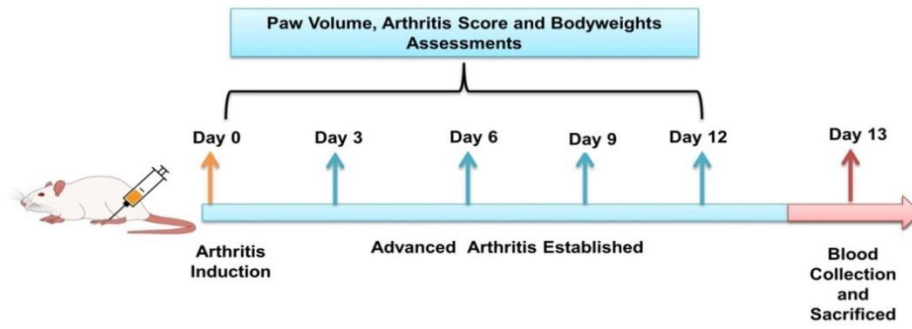
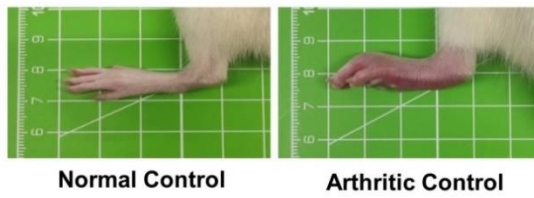
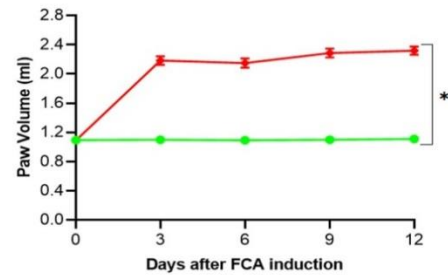
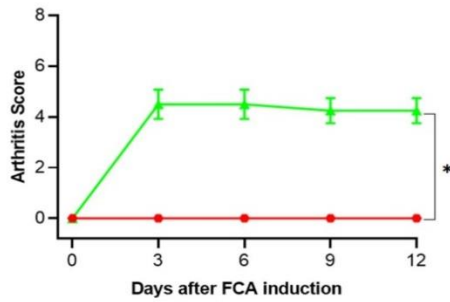
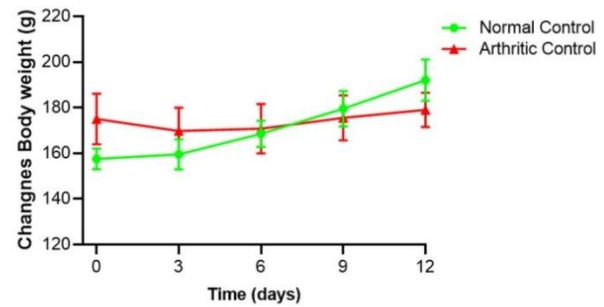
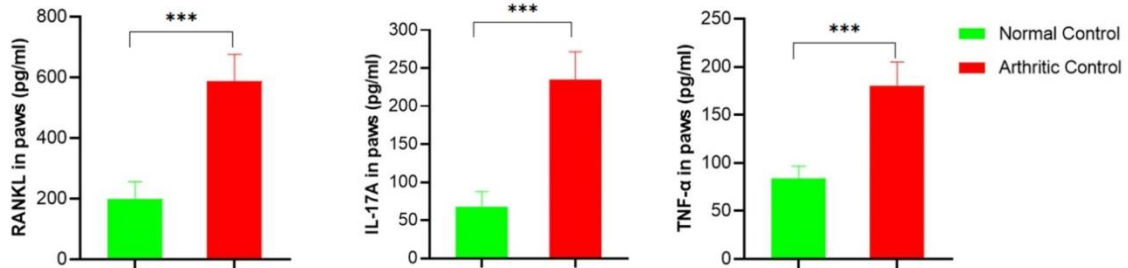
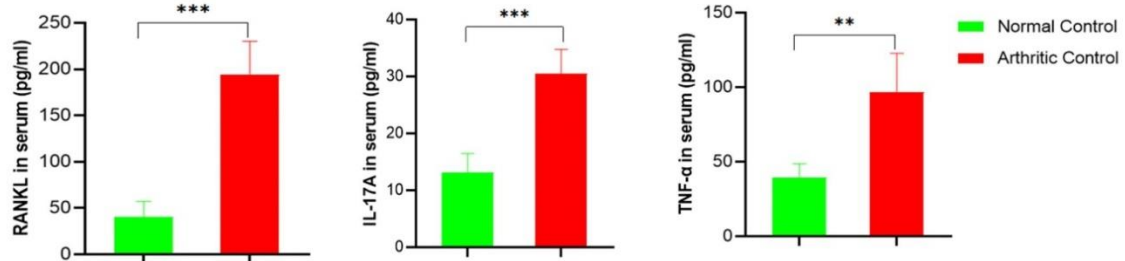
A**B****C****D****E****F****G**

Figure 21. Development of advanced arthritis animal model (12-day model). (A). The schematic illustration of the establishment of advanced arthritis animal. (B). Representative paw images of standard control and arthritic control animals at the endpoint (day 12). (C). Changes in paw volume (D). Arthritis score. According to the standard scoring method, the average arthritis score was assessed by blind testing (scale of 0-4). (E). Changes in body weight. The pro-inflammatory cytokine levels TNF- α , IL-17A, and RANKL (bone erosion marker) in the (F). Paw tissue, (G). Serum cytokine level in the rat (on day 13) was estimated by ELISA. All the values are expressed in Mean \pm SD (n=4). A two-tailed paired Student's t-test was used to compare the differences. The difference with p values: * p < 0.05, ** p < 0.01, *** p < 0.001 was considered statistically significant. ELISA: Enzyme-linked immunoassay, TNF- α : Tumor Necrosis Factor-alpha, IL-17A: Interleukin 17A, RANKL: Receptor activator of nuclear factor-kappa-B ligand.

2.4. Cytotoxicity and biocompatibility of PEITC-loaded hydrogel *in vitro*

The biocompatibility and toxicity of PEITC-loaded hydrogel on the FLS of RA (RA-FLS) and healthy-FLS (N-FLS) were studied *in vitro* by assessing the % cell viability using methyl-thiazolyl diphenyl-tetrazolium bromide (MTT) assay. Initially, the cytotoxicity of PEITC-loaded hydrogel on N-FLS was studied to ensure that the normal functioning of the FLS was not perturbed. The N-FLS is essential for maintaining healthy joint function since it promotes joint lubrication, regulates synovial fluid formation, plays a part in joint repair, and prevents joint damage (Yu et al., 2022).

As shown in **Figure 22B**, no toxicity of BH and different concentrations of PEITC-loaded hydrogel ranging from 5 μ M to 100 μ M were observed for N-FLS, where 97–85 % of

cells were viable at all-time points (24 h and 48 h). In the case of RA-FLS, these are the most prevalent cell type at the pannus-cartilage junction that contributes to joint degeneration by producing pathogenic mediators, such as cytokines and inflammatory proteases, which causes RA to develop and persist (Nygaard and Firestein, 2020). In this study, I also investigated how PEITC-loaded hydrogel affected the viability of RA-FLS cells. These cells demonstrated a mild inhibitory effect only when exposed to higher concentrations of PEITC-loaded hydrogel (100 μM), with a percentage of cell viability of 72 % and 69 % at 24 and 48 h, respectively (**Figure 22B**).

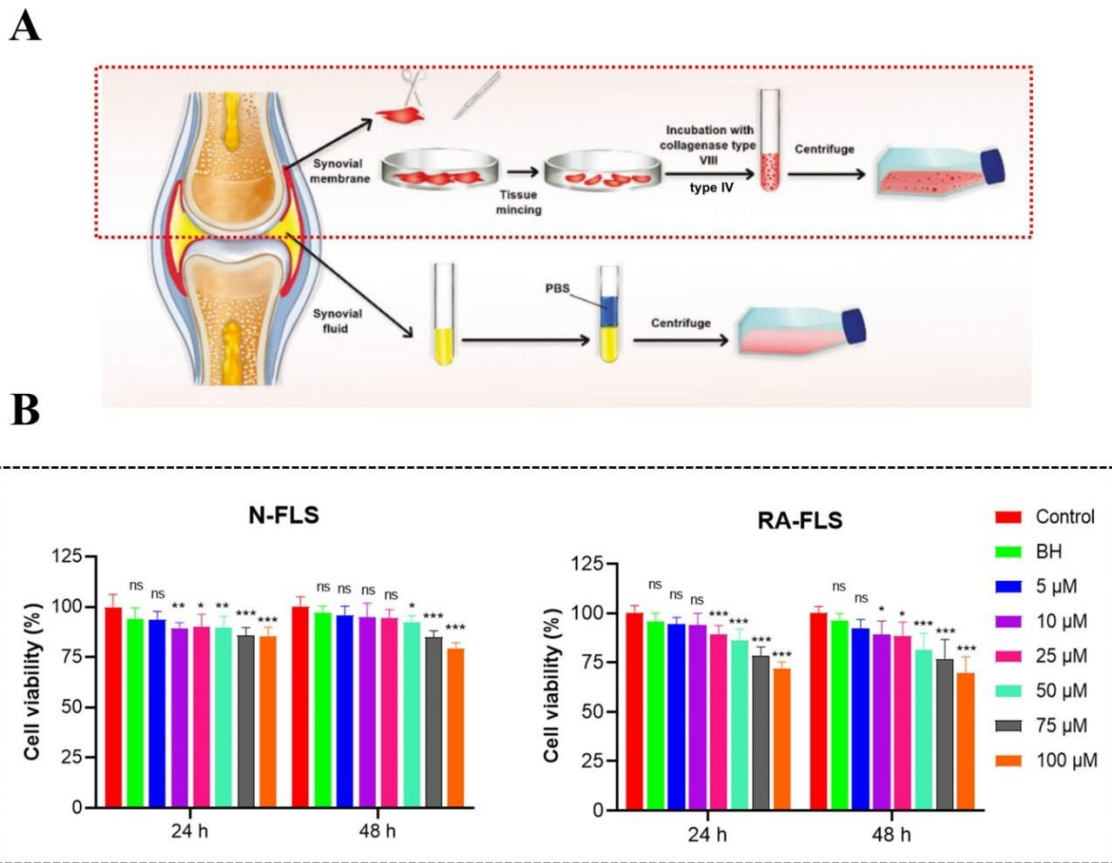


Figure 22. Cytotoxicity and biocompatibility assay of PEITC-loaded hydrogel *in vitro*. (A). Schematic representation of the isolation and culture of FLS from healthy and RA knee joints.

The red box indicates the current adopted isolation protocol. (B). Cytotoxicity of N-FLS and RA-FLS cells with various treatments at 24 h and 48 h. The data are represented as mean \pm SD (n = 6). The values were statistically examined using a one-way ANOVA test. Statistical significance: *p < 0.05, **p < 0.01, ***p < 0.001, and ns- non-significant.

Taking together the results from N-FLS and RA-FLS, I validated that the PEITC-loaded hydrogel had a high level of biosafety for N-FLS cells and a modest inhibitory effect on RA-FLS at higher concentrations. The above results comply with a study that earlier reported a methodology for assessing *in vitro* toxicity of biomaterials concerning the biocompatibility of hydrogel formulations (Joshi et al., 2018).

2.5. Evaluation of therapeutic efficacy of PEITC-loaded hydrogel in RA condition in the rat model

Upon establishing the biosafety and biocompatibility of the PEITC-loaded hydrogel in healthy rats. The PH50 (optimized thermo-sensitive PEITC-loaded hydrogel) as an injectable was finally studied for its therapeutic activity in RA conditions induced in rats. Different parameters for assessing inflammation and arthritis were examined to establish the efficacy of PEITC-loaded hydrogel as a suitable drug delivery system in chronic inflammatory conditions.

2.5.1. Effect of the PEITC-loaded hydrogel on the various arthritis parameters

The therapeutic effect of PH50 was studied in the FCA-induced rat model for RA. After immunization, the rats were randomly divided into different study groups and sacrificed on day 37 (**Figure 23A**). **Figure 23B** (*red bar*) shows a noticeable paw swelling in model rats from day 14 to 35 after FCA immunization. While during this period, a significant inhibition in the paw

swelling was observed in the PH50 (*blue* bar) compared to the *model* group. The PEITC50 and BH failed to improve paw swelling in adjuvant-induced *model* rats. On day 35, the PH50 group showed a marked reduction in paw volume (1.58 ± 0.072) compared to the *model* group (2.43 ± 0.077). In contrast, the paw volume for Free PEITC (PEITC50, 1.89 ± 0.048) and BH (1.96 ± 0.158) did not differ significantly. The difference in paw volume indicated the efficacy of PH50 in improving the *model* rats' paw edema and inflammation. In contrast, only a slight decrease in paw edema and inflammation was observed in other treatment groups.

The arthritis score is a critical parameter for assessing the severity and progression of the disease. On day 12, following FCA administration, fully developed arthritis was confirmed in the *model* group after observing noticeable swelling, tenderness, deformity, and ankylosis in the arthritis-induced paws sustained until the endpoint (**day 35, 4.0 ± 0.0**). In the PH50, the arthritis score peaked on day 14 (4.75 ± 0.5) and markedly decreased to 1.75 ± 0.5 by day 35 (**Figure 23C**). Similar to the earlier observation for paw volume, a slight decrease in arthritis scores was observed in PEITC50 (3.50 ± 0.58) and BH (3.25 ± 0.5).

Observation of changes in body weight in disease or drug-treated conditions is a critical parameter to knowing the pathological state or recovery of the animal condition. As shown in **Figure 23D**, a single dose of FCA injection in the rats led to a significant loss of body weight within the first 12 days that gradually increased over the study period (up to 36 days) with symptoms of inflammation. At the endpoint (day 36), the FCA-immunized rats treated with PH50 recorded a body weight of 237.00 ± 15.98 g, while the body weight of rats in the *model* group was 216.50 ± 8.43 g. This marked rise in body weight change and decreased paw volume compared to *model* rats is regarded as progress in the recovery.

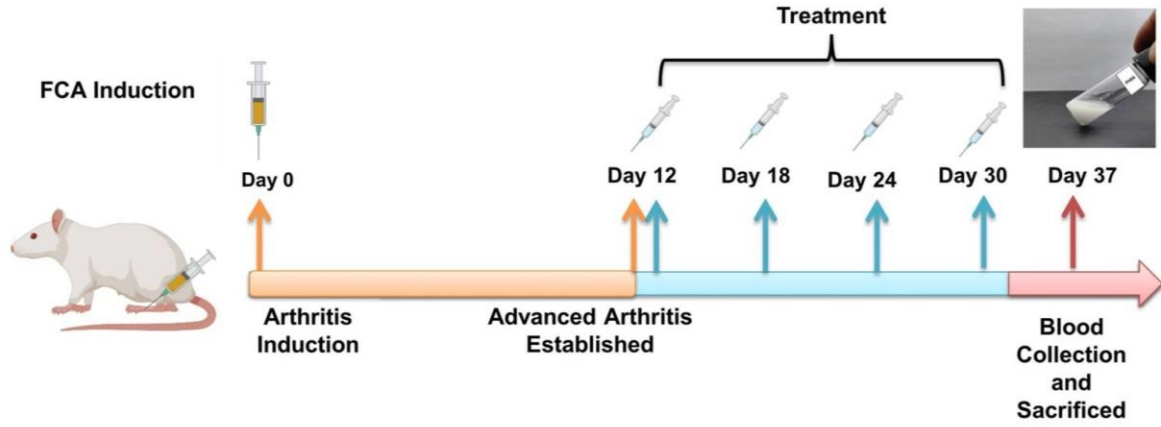
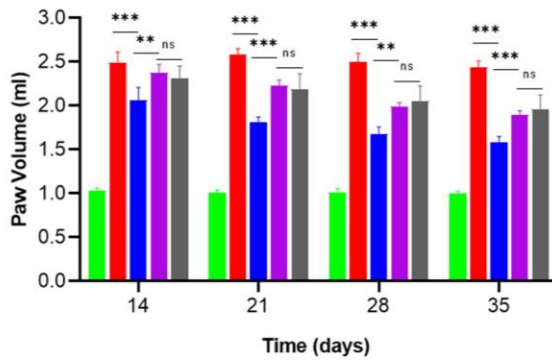
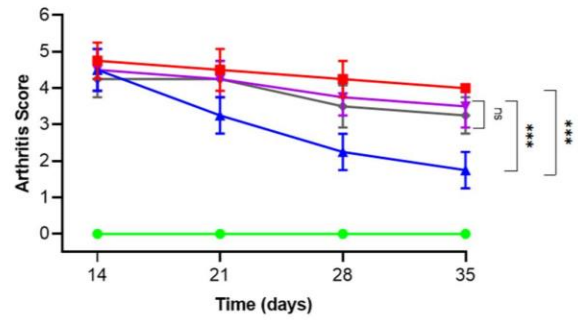
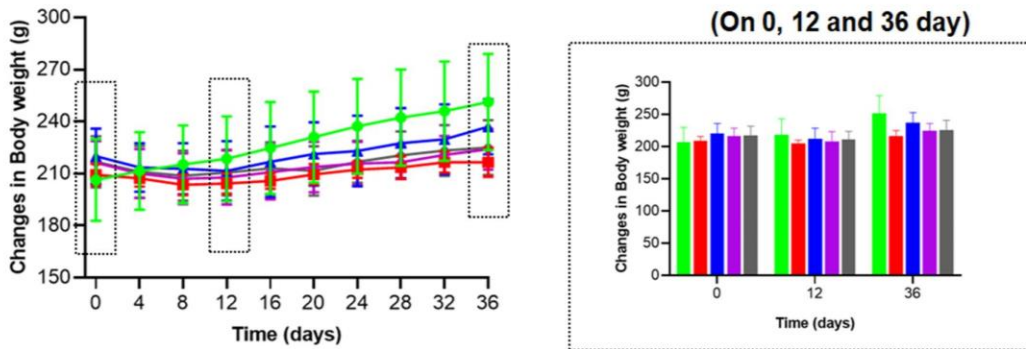
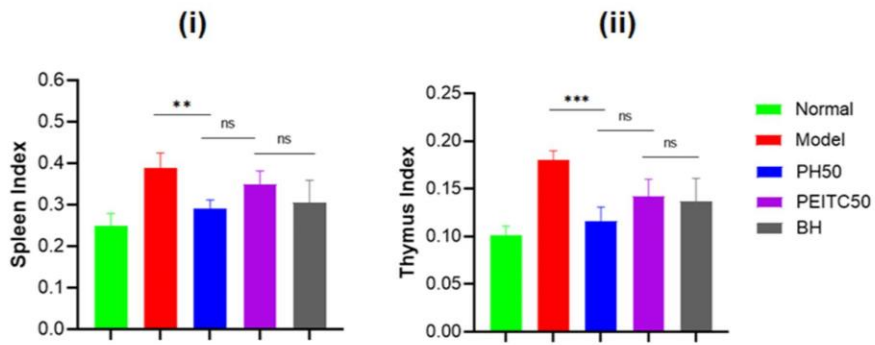
A**B****C****D****E**

Figure 23. *In vivo* therapeutic effect of the PEITC-loaded hydrogel in FCA-induced rats.

(A). Timeline for the PEITC-loaded hydrogel treatment in RA model rat (FCA-induced) with different treatment groups. Adjuvant (FCA)-induced arthritis (AIA) model: Healthy normal rat without FCA immunization (Normal control), FCA-immunized rat with PBS (*model*), FCA-immunized rat with PH50, FCA-immunized RA rat with PEITC50, and FCA-immunized RA rat with BH were studied. (B). Changes in paw volume over time in the different treatment groups. (C). Arthritis score for RA in rats on day 35 following treatment with different formulations. According to the standard scoring method, the average arthritis score was assessed by blind testing (scale of 0-4). (D). Changes in body weight in the FCA-immunized rats after 36 days of treatment. (E). The index of (i). Spleen and (ii). Thymus on day 37 in different treatment groups of FCA-immunized rats. The index of the thymus and spleen were expressed as the ratio (mg/g) of thymus and spleen wet weight versus body weight, respectively. The data are represented as mean \pm SD (n = 4). The values were statistically examined using a one-way ANOVA test. Statistical significance: *p < 0.05, **p < 0.01, ***p < 0.001, and ns- non-significant. FCA: Freund's complete adjuvant.

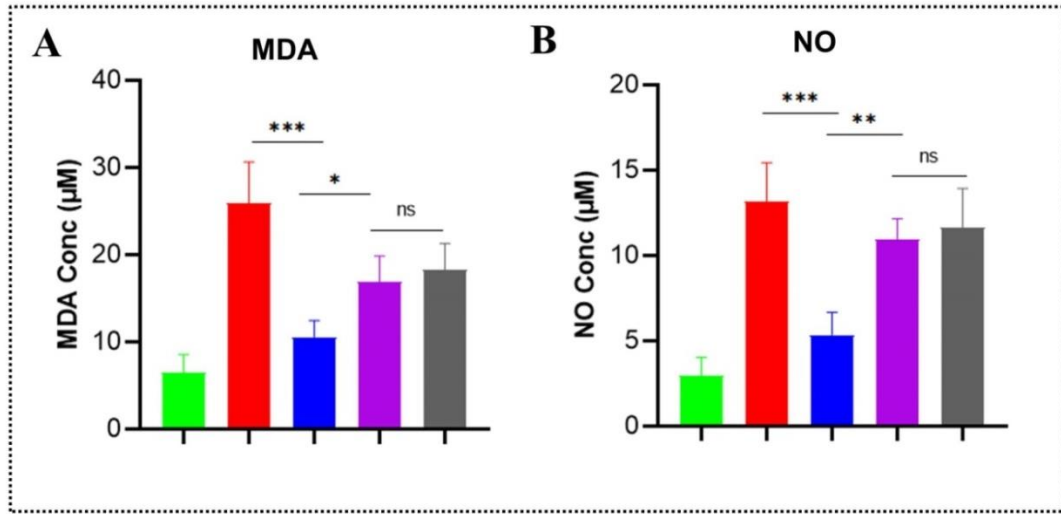
The weight increase of Free PEITC (PEITC50) (**224.00 \pm 11.83**) and BH (**225.00 \pm 15.88**) treatment groups was similar to that of *model* rats. Overall, the results show that PH50 positively impacts the recovery of the FCA-immunized rats.

As major immune organs, the thymus and spleen are associated with diverse immunological functions, where the thymus functions as a central immune organ and the spleen as a peripheral immune organ (Wang et al., 2021). Alterations in the thymus and spleen indices are considered overall improper immune system functioning. Therefore, their relative weights are commonly used as preliminary indicators to evaluate the immune-regulatory activity of tested

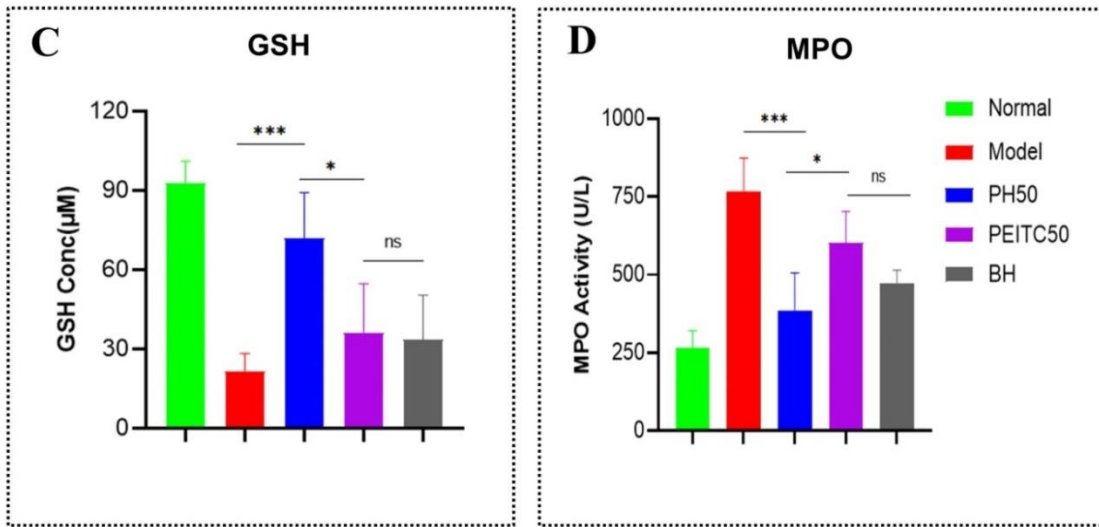
substrates used for treating RA (Rao et al., 2018). As seen in **Figure 23E (i-ii)**, a marked increase in the weights of the thymus and spleen was observed in the *model* group rats as a hyper-immune response to FCA injection. In contrast, the PH50 treatment negated this immune response. The treatments with PEITC50 and BH decreased the spleen or thymus index compared to the *model* group, but not effectively. The results confirm that immune regulation due to the treatment of PH50 played an essential role in the anti-arthritic activity of PEITC.

2.5.2. Effect of the PEITC-loaded hydrogel on the oxidative stress and antioxidant markers in RA

Oxidative stress is an essential marker for understanding RA's pathogenesis and progression. During chronic inflammation in rheumatoid arthritis, oxidative stress as a secondary messenger in cellular immune response leads to joint dysfunction, further aggravating the condition. The exposure of free radicals to T-cells induces an abnormal immune response that can directly affect the joint cartilage or indirectly damage the protein/enzyme function, forming a complex glycated end product (Abdel Jaleel et al., 2021). Reactive oxygen species (ROS) activate the osteoclast activity and up-regulate the expression of matrix metalloproteinases, e.g., MMP-9 (Phillips et al., 2010). The ROS activity was measured using different biochemical markers. Malondialdehyde (MDA) and nitric oxide (NO) are markers to evaluate oxidative damage (Abdel Jaleel et al., 2021). The reduced glutathione (GSH) levels are required to determine antioxidant activity (Kalinina et al., 2014), while myeloperoxidase (MPO) is a well-known neutrophil infiltration marker, and its increased levels in RA contribute to oxidative stress (Stamp et al., 2012).



Oxidative Stress Markers



Antioxidant Marker

Neutrophil Infiltration Marker

Figure 24. Estimation of oxidative stress, antioxidant, and neutrophil infiltration markers in RA. Effect of PEITC-loaded hydrogel on serum concentration of (A). MDA (B). NO (C). GSH and (D). MPO. On day 37, the serum of the different treatment groups was collected and quantified. The data are represented as mean \pm SD (n = 4). The values were statistically examined using a one-way ANOVA test. Statistical significance: *p < 0.05, **p < 0.01, ***p <

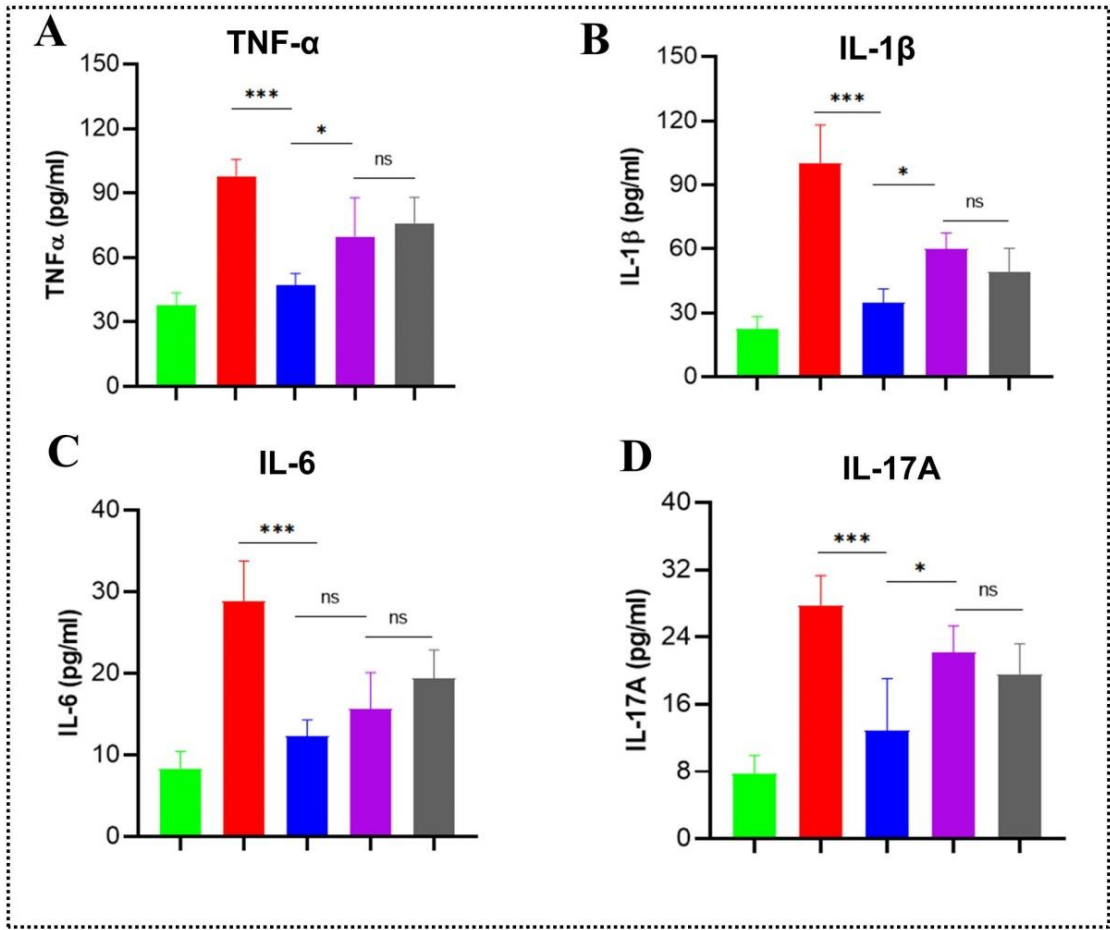
0.001 and ns-non significant. MDA: Malondialdehyde, NO: Nitric oxide, GSH: Reduced glutathione, and MPO: Myeloperoxidase.

The serum samples of FCA-injected rats showed a **4-fold** increase in MDA and a **4.5-fold** increase in NO levels compared to the standard control. A treatment with PH50 significantly reduced the increased levels of both oxidative stress parameters (MDA= **2.45-fold** and NO = **2.45-fold**) compared to *model* rats. In the case of PEITC50 and BH treatments, no substantial change in the serum concentration of MDA (**Figure 24A**) and NO (**Figure 24B**) levels was induced. While a **4.24-fold** decrease in serum GSH was observed in *model* rats concerning the normal control rats, the PH50 showed a significant increase in the serum GSH to **3.33-fold** (**Figure 24C**).

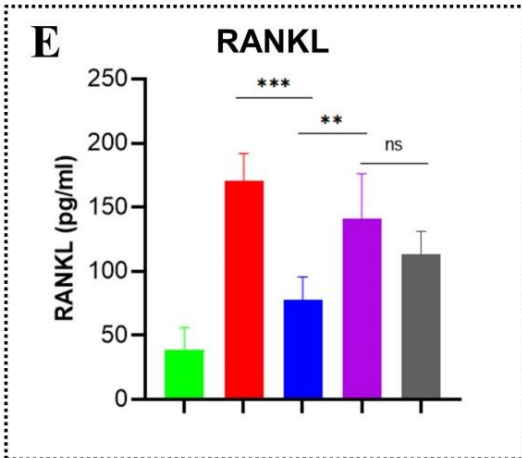
In the *model* group, the serum MPO level increased by **2.9-fold** to reach the standard control, while it noticeably decreased up to **2.0-fold** following treatment with the PH50. Interestingly, the PEITC50 and BH treatment did not significantly change serum MPO levels (**Figure 24D**). The results suggested that PEITC-loaded hydrogel (PH50) markedly improved the serum GSH levels and restored the abnormal changes of serum MDA, NO, and MPO, indicating prolonged contact of PEITC at sub-toxic concentration was able to balance the oxidative stress induced by FCA.

2.5.3. Effect of the PEITC-loaded hydrogel on the cytokines profiles in RA

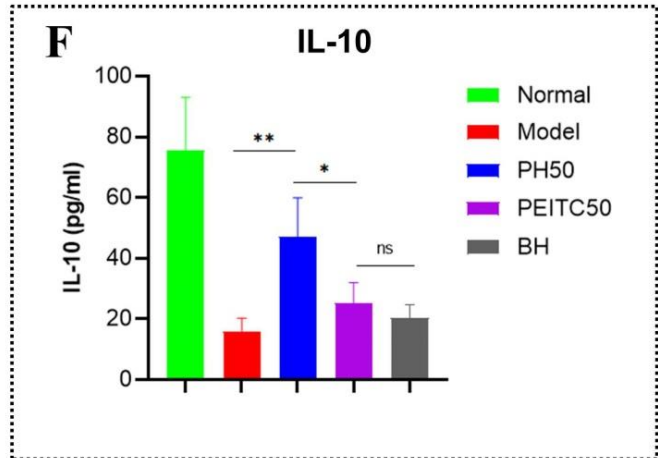
Since the pathogenesis of RA still being unclear, the immediate goal of the current therapeutic approaches is to, by all means, restore homeostasis in the joint by setting a balance between inflammation and pain. In my study, the PEITC-loaded hydrogel-based treatment group significantly improved RA symptoms compared to the *model group*.



Pro-inflammatory Markers



Bone Erosion Marker



Anti-inflammatory Marker

Figure 25. Quantitative estimation of pro-inflammatory, anti-inflammatory, and bone erosion markers in RA. Effect of PEITC-loaded hydrogel on serum pro-inflammatory cytokine levels (A). TNF- α , (B). IL-1 β , (C). IL-6 and (D). IL-17A. (E). RANKL (bone erosion marker) (F). IL-10 (anti-inflammatory cytokine). The serum cytokine level in the rat (on day 37) was estimated by ELISA. The data are represented as mean \pm SD (n = 4). The values were statistically examined using a one-way ANOVA test. Statistical significance: *p < 0.05, **p < 0.01, ***p < 0.001, and ns- non-significant. TNF- α : Tumor Necrosis Factor-alpha, IL-1 β : Interleukin 1 beta, IL-6: Interleukin 6, IL-17A: Interleukin 17A, RANKL: Receptor activator of nuclear factor-kappa-B ligand and IL-10: Interleukin-10, ELISA: Enzyme-linked immunoassay.

Also, the pro-inflammatory cytokines and their levels in the *milieu* are critical mediators of the progression of rheumatoid arthritis. This can shed light on the possible mode of anti-inflammatory activity of PEITC. Therefore, the cytokine levels as an index of therapeutic efficacy were measured in arthritic mice treated with different formulations (Li et al., 2017).

The serum samples from the endpoint were assayed to determine the levels of key pro-inflammatory cytokines (TNF- α , IL-1 β , IL-6, and IL-17A) using specific ELISA kits. As shown in **Figure 25A-D**, the serum concentration of the TNF- α , IL-17A, IL-6, and IL-1 β was significantly up-regulated in *model* rats compared to respective samples in normal control rats. The PH50-treated rats showed a substantially lower concentration of pro-inflammatory cytokines than the *model* rats and other groups. On the other hand, the serum concentration of TNF- α , IL-1 β , IL-6, and IL-17A was not much affected following the treatment with PEITC50 and BH compared to normal control rats. These data demonstrated that PEITC-loaded hydrogel-based therapy could suppress the production of pro-inflammatory cytokines in RA conditions (**Figure**

25A-D).

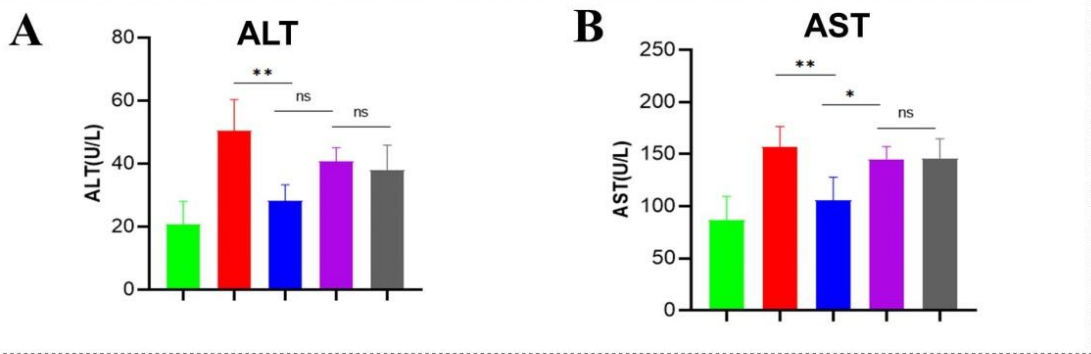
Further, since bone erosion is a critical consequence of RA, assessing the anti-arthritis effect of the PH50 is vital. To examine the possible mechanism of action, the serum levels of RANKL were determined to grade osteoclastogenesis (Stolina et al., 2005). As shown in **Figure 25E**, interestingly, the level of RANKL was significantly increased in the *model group* (PBS-treated adjuvant-induced rats group) compared to the healthy regular control group. A treatment with PH50 noticeably decreased the RANKL levels compared to the *model group*, indicating that PEITC-loaded hydrogel can potentially reduce bone erosion by affecting the RANKL levels in RA conditions. A marked decrease in the serum levels of IL-10 (anti-inflammatory cytokine) in the *model group* rats was observed compared to the standard control group (**Figure 25F**). Treatment with PH50 significantly improved the reduced levels of IL-10 in the serum of arthritic control rats.

2.5.4. Assessment of biosafety and histological analysis of the PEITC-loaded hydrogel in RA

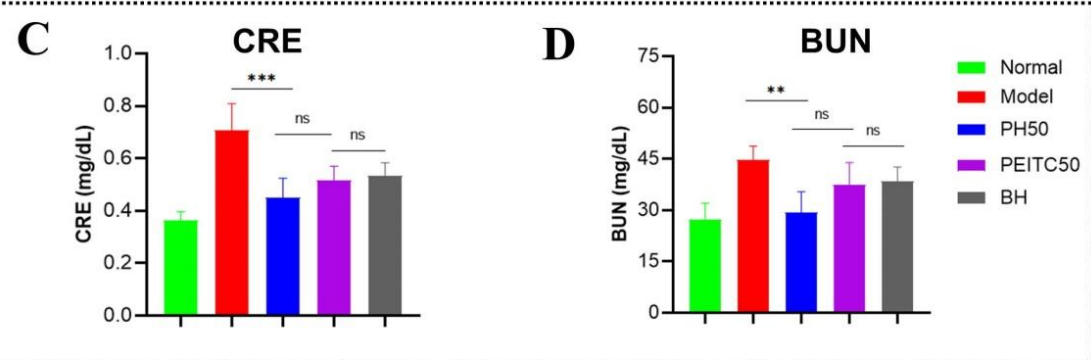
Considering the significance and importance of the biocompatibility of material for biological and clinical applications, an assessment was performed on liver and kidney function following treatment (Yin et al., 2020). FCA-induced arthritic rats exhibited a considerable rise in liver function and kidney function enzymes such as ALT, AST, CRE, and BUN compared to normal healthy control rats (**Figure 26A-D**). After treatment with PH50, the enzyme levels significantly decreased compared to *model* rats. It was observed that the elevated biochemical parameters tend to return to average values in all the treatment groups.

The pathological state of the RA condition is associated with persistent synovitis, progressive cartilage, and bone destruction (Chen et al., 2020).

Hepatic Biomarkers



Renal Biomarkers



E

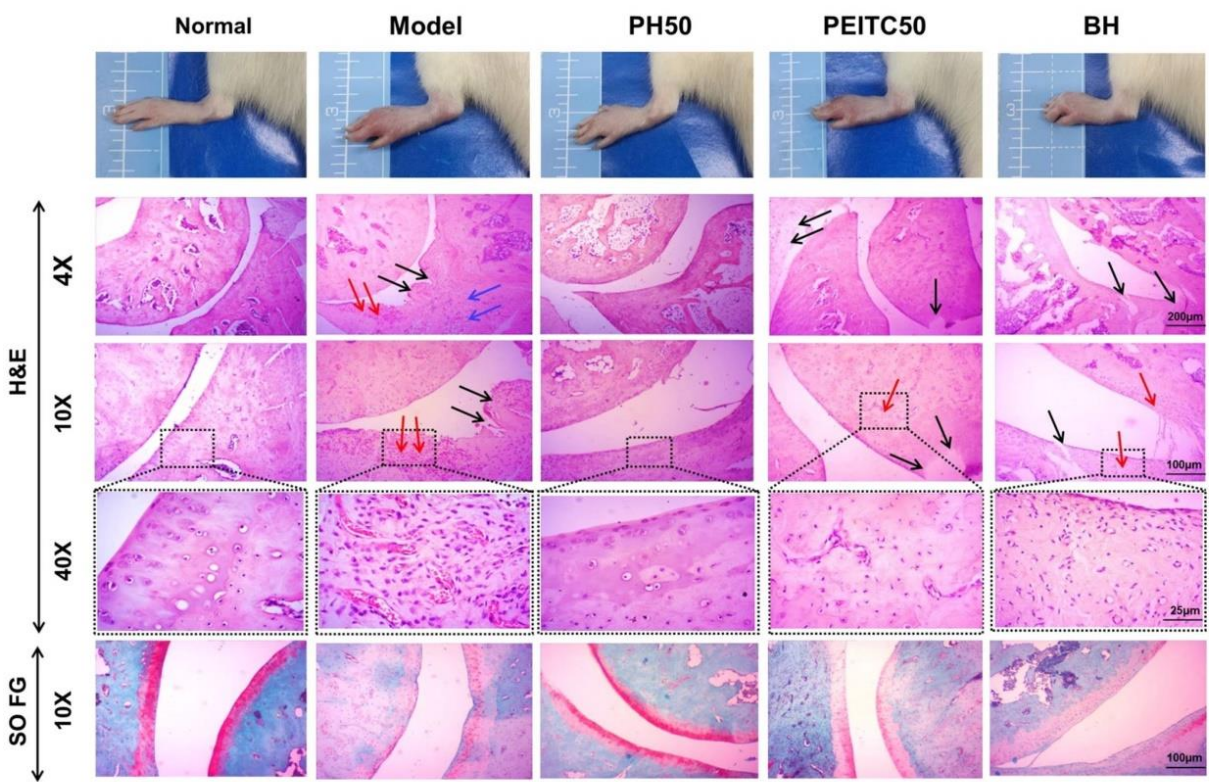


Figure 26. Biosafety and histological analysis in RA. Effects of PEITC-loaded hydrogel on hepatic and renal function. (A and B) hepatic biomarkers (ALT and AST) and (C and D) renal biomarkers (CRE and BUN). The values were statistically examined using a one-way ANOVA test. Statistical significance: * $p < 0.05$, ** $p < 0.01$, *** $p < 0.001$, and ns- non-significant. (E). Histopathology examination was performed on H&E and SO-FG stained sections of ankle joints. *Blue* arrow- synovitis, *red* arrow- inflammatory cellular infiltration, *black* arrow -bone erosion and cartilage degradation. The scale bar is 25 (40x), 100(10x) and 200(4x) μm . ALT: Alanine transaminase, AST: Aspartate transaminase, CRE: Creatinine, BUN: Blood urea nitrogen (BUN), H & E: Hematoxylin and eosin, and SO-FG: Safranin O-fast green.

The progression or recovery of the RA in the animal model following PH50 administration was confirmed by assessing the status of bone, cartilage, and synovium from the final day of the study (day 37). Histological analysis of H&E and Safranin O-fast green (SO-FG) stained ankle joint sections of the rat was examined to assess the extent of bone erosion and cartilage loss and its regeneration.

Smooth cartilage was observed from H&E-stained sections of the standard control groups (**Figure 26E**) without cartilage loss and bone erosion. Whereas, from the sections in the *model* group, the RA condition was evident as the indicator of chronic inflammation, such as severe distortion of ankle joint structure with hyperplastic synovial tissue, the influx of infiltrated inflammatory cells, and proliferation of mononuclear cells, and bone erosion were observed. Similarly, the ankle joints treated with PEITC50 and BH showed visible cartilage loss and synovial inflammation. However, the treatment with PH50 effectively ameliorated or slowed the progression of the disease. Overall, the architecture of the ankle joint was more well-preserved

than the *model* group. The extent of bone or cartilage erosion and inflammation was much less than in other treatment groups, and the joint anatomy was restored to normal compared to that of a healthy control joint.

Furthermore, SO-FG staining was performed on all five groups. SO-FG staining is a well-established technique to stain cartilage tissues mainly composed of proteoglycans (Jang et al., 2020). The intensity of SO-FG staining (red staining) is proportional to the proteoglycan content in the chondrogenesis area. In the *model* group, noticeable proteoglycan loss was found (the red color almost faded), indicating severe damage to the cartilage. In the following intervention with PH50, the intensity of the red color increase was much higher than in the other three treatment groups. This validates the protective role of PH50 in cartilage preservation compared to the standard healthy control group (**Figure 26E, last row**). The histopathology result demonstrates the therapeutic effect of PH50 in counteracting inflammation and delaying disease progression in the RA condition.

2.6. Summary of the chapter

In this chapter, I successfully developed an intelligent hydrogel of CS/PF-127 as a carrier system loaded with PEITC as an injectable depot for potential application to treat chronic inflammatory joint diseases (like RA). According to the *in vitro* and *in vivo* findings, the PEITC-loaded hydrogel displayed the desired features, including high mechanical strength, thermosensitivity, injectability, good biocompatibility, and biosafety for prolonged release of PEITC from the targeted area. In addition, cell-based studies indicated that PEITC-loaded hydrogel (at conc. 100 μ M) had a high level of biosafety for healthy FLS cells and a modest inhibitory effect on RA-FLS cells. This will reflect the anti-inflammatory effect of PEITC-

loaded hydrogel at the *in vitro* RA condition. Further *in vivo* arthritis study in a rat model showed a remarkable suppression of inflammation markers by the local administration of PEITC-loaded thermosensitive hydrogel (PH50) into the knee joint. The animal studies in healthy animals suggested that the limitations of PEITC (thermal instability, rapid clearance, and short half-life) in the free form were significantly masked. When incorporated into a hydrogel, the PEITC at sub-toxic concentration was bioavailable, and its therapeutic activity in the microenvironment was exerted for a prolonged time.

Previous reports have shown that the free form of PEITC can act as an anti-rheumatoid agent in an FCA-induced RA rat model where the therapeutic activity was achieved by administering PEITC orally at a dose of 50 mg/kg (Choudhary et al., 2020). Since it was reported that the free form of PEITC has low systemic bioavailability and stability (Wang & Bao, 2021). Our study adopted an innovative approach to encapsulate the PEITC inside an *in situ* polysaccharide-based hydrogel carrier to reduce the dosing interval. The IA injection of PEITC-loaded thermosensitive hydrogel (PH50) helps markedly improve therapeutic efficacy in the FCA-induced RA rat model by reducing a 4-fold dose of PEITC as compared to the free PEITC dose. At the same time, their clinical limitations, including bioavailability and stability, were significantly masked.

In conclusion, our findings suggest that biocompatible and biodegradable polysaccharide-based hydrogel systems are the ideal carriers for delivering natural phytochemicals for autoimmune conditions like RA and OA.

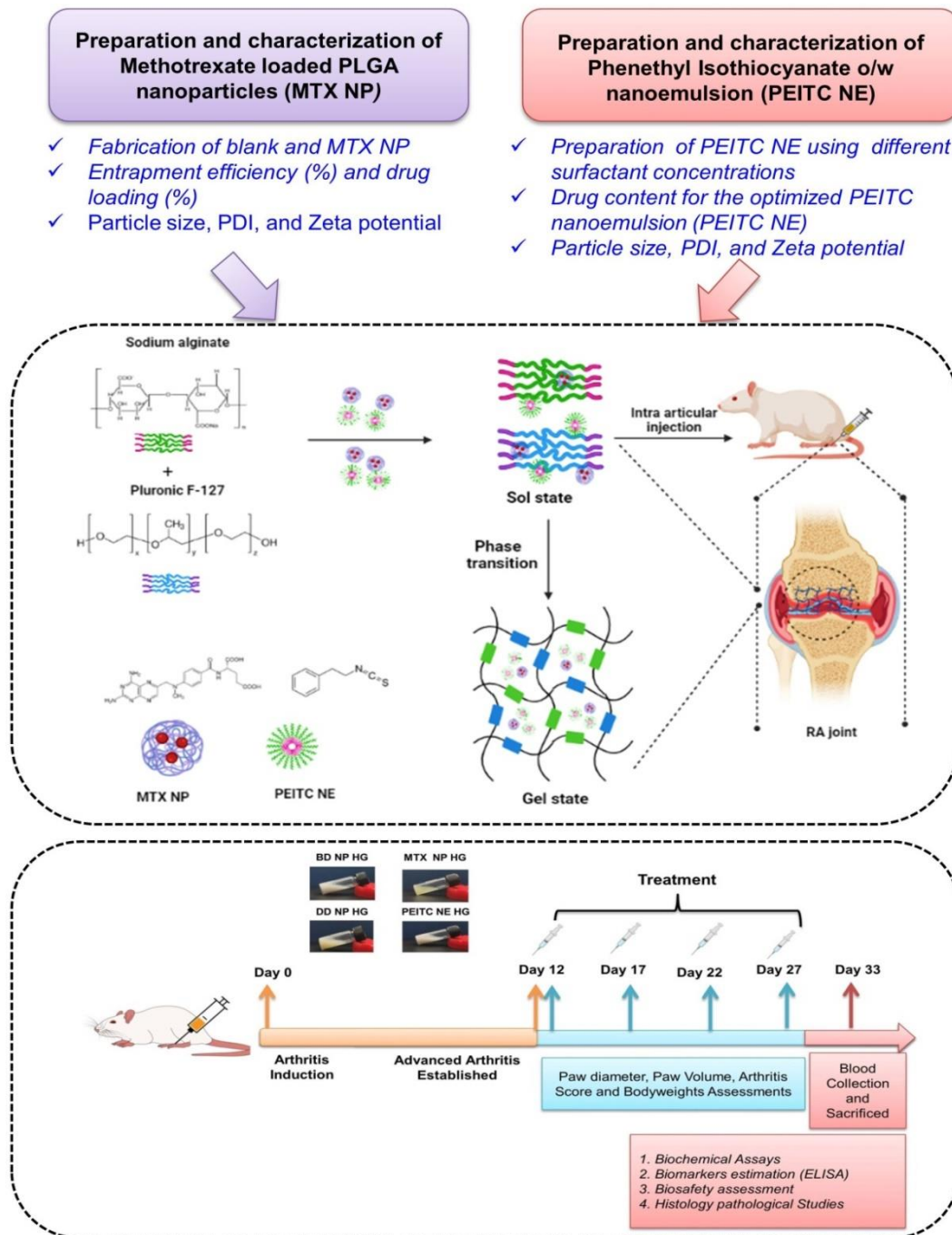
Chapter 3

**Design of a dual nano-particulate drug
(MTX and PEITC)-loaded smart
hydrogel as a co-delivery system to
enhance its synergistic activity in RA
conditions.**

RA is an autoimmune disease with complex disease etiology with limited treatment options. Various drug combinations are standard practices to alleviate RA patients' pain and joint inflammation. Considering the point mentioned earlier, my next step was to develop an injectable hydrogel as a combinational drug delivery system that can be used for the co-delivery of regimens that can alleviate the disease condition via diverse mechanisms. Nanodelivery systems are an excellent approach for the prolonged release of drugs, increasing the residence time at inflamed joints. Combining nanotechnology with materials science can result in better therapeutic efficacy of drugs in the joints, ensuring relief in stressful RA conditions. This was an improvisation of the result obtained from the first step of the study (**objective 2**).

This chapter focuses mainly on the holistic and collaborative approaches to treating RA using co-delivering MTX, a standard slow-acting anti-rheumatic drug, and PEITC, a bioactive phytochemical, using an SA-PF-127 *in situ* hydrogel formulation. Despite exhibiting good anti-arthritic activity, the drawbacks of MTX and PEITC, such as poor solubility, low bioavailability, and several side effects, are undesirable properties that limit their usage. Therefore, a nanotechnology approach was employed to overcome a few limitations. MTX-poly(lactic-co-glycolic acid) (PLGA) loaded nanoparticles (MTX NP) were fabricated using a nanoprecipitation method. On the other hand, PEITC nanoemulsion (PEITC NE) was fabricated through the o/w nanoemulsion method.

Further, the nanoparticles were fabricated *in situ* hydrogels prepared with SA and PF-127 biocompatible polymers (DD NP HG) to check unique qualities such as biocompatibility, biodegradability, high porosity, and prolonged drug release. Finally, the IA injection of DD NP HG into RA joints to evaluate the synergistic therapeutic effectiveness. A schematic illustration of the fabrication of the smart hydrogel co-delivery system is presented in (**Scheme 2**).



Scheme 2. A schematic illustration of the preparation and a detailed combinatorial treatment schedule for treating RA using dual-drug nanoparticles loaded hydrogel. Created with Biorender (biorender.com).

Here, the different steps involved in the preparation and characterization of nano-encapsulated drugs (MTX and PEITC) are shown with a detailed combinatorial treatment schedule for evaluating the therapeutic efficacy of the dual-drug nanoparticles loaded hydrogel (DD NP HG) as an injectable depot for treating RA.

3.1. Preparation of MTX NP

Despite exhibiting good anti-arthritis activity, the drawbacks of MTX, such as poor solubility, low bioavailability, and several side effects, are undesirable properties that limit its usage. Therefore, a nanoprecipitation method using solvent evaporation was employed in this study to overcome a few of the limitations. A well-known biodegradable polymer PLGA was utilized to load the MTX into the polymer matrix. For optimization purposes, three different batches of MTX NPs were prepared using 0.1 % (w/v) PF-127 (as surfactant) with varying concentrations of PLGA (80, 120, 150 mg), yielding an entrapment efficiency of **53.73 ± 4.83 %** (2.79 ± 0.25 mg), **64.60 ± 2.34 %** (3.36 ± 0.12 mg) and **78.45 ± 3.10 %** (4.08 ± 0.16 mg) respectively (**Table 3**).

Here, it was observed that as the concentration of PLGA increased, the % entrapment efficiency (% EE) of the drug also increased due to the increase in viscosity of the organic phase that can hamper the diffusion of the drug from the organic phase to the aqueous phase. Further, the undiffused lipophilic drug may get entrapped in the matrix of alkyl chains of PLGA with weak interactions and released slowly from the polymeric matrix (Ray et al., 2015). Among the prepared formulations, **batch no-III** (PLGA- 150 mg) was found to be optimum, with a greater % EE of the drug (approx. 4 mg), and therefore, further utilized for the fabrication of DD NP HG.

Table 3. Different polymer compositions with different % EE and % DL.

Batch no	PLGA polymer composition (mg)	Amount of drug (mg)	Solvent mixture (Acetone: DMSO)	PF-127 % (w/v)	% EE	% DL
I	80	5.2	9:1	0.1	53.73 ± 4.83	2.66 ± 0.24
II	120	5.2	9:1	0.1	64.60 ± 2.34	2.31 ± 0.08
III	150	5.2	9:1	0.1	78.45 ± 3.08	2.33 ± 0.09

3.2. Preparation and optimization of PEITC NE

An oil-in-water nanoemulsion of PEITC was prepared by dissolving it in olive oil to form the oil phase. Olive oil, a model oil with mild anti-inflammatory activity, may also aid in the potentiation of treatment efficacy. The aqueous phase (72 %) and oil phase (18 %) were kept constant in the current preparation, varying only the surfactant ratios.

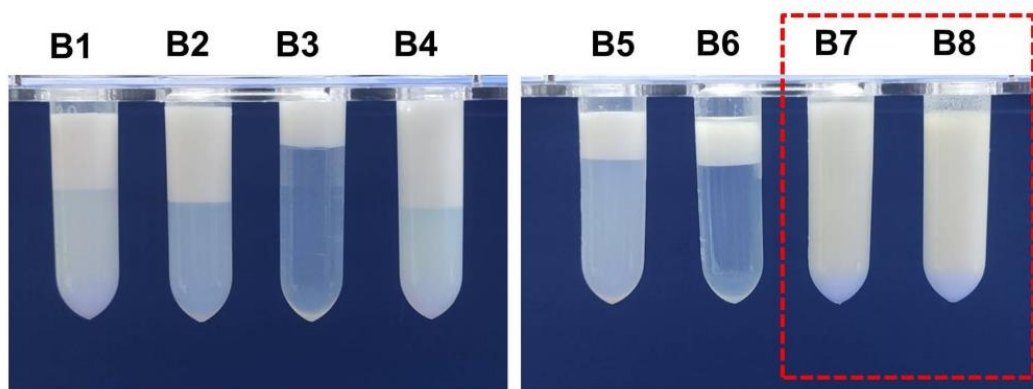


Figure 27. Observation of creaming and phase separation in preparing different PEITC NE batches.

To obtain a stable emulsion, two non-ionic surfactants, span-80 and tween-80, were used as surfactant mixtures (Li et al., 2015). Stirring and probe sonication were employed to reduce the

droplet size to an optimum range. A total of eight different batches were prepared by altering the surfactant concentrations based on the HLB value. The HLB value of the surfactant mixtures between 4 and 5 exhibited higher stability than other batches (**batch-7** HLB of 4.62 and **batch-8** HLB of 4.3), where no creaming or phase separation was observed, as shown in **Figure 27**.

Table 4. Different surfactant concentrations for the preparation of NE

Batch no	Constants	Variables		Creaming/ phase separation	Particle size (PS) (nm)
		Surfactant 1 (% Span 80)	Surfactant 2 (% Tween 80)		
1	Aqueous phase-72% Oil phase-18%	6	4	Observed	Not determined
2		8	2	Observed	Not determined
3		2	8	Observed	Not determined
4		9	1	Observed	Not determined
5		3	7	Observed	Not determined
6		1	9	Observed	Not determined
7		9.7	0.3	Not observed	303.5 ± 5.12
8		10	0	Not observed	240.67 ± 4.75
Batch-8 (optimized PEITC NE) - Drug content = 83.16 ± 10.87 % (33.4 ± 4.35 mg).					

Therefore, these two batches (**7&8**) were selected and, with further optimization, yielded an improved (lower) particle size of 240.67 ± 4.75 nm (**batch-8**) and 303.5 ± 5.12 nm (**batch-7**), as shown in **Table 3**. This may be due to increased lipophilic surfactant (Span-80) that might help uniformly distribute highly lipophilic PEITC into the aqueous phase. The drug content in the finally optimized formulation of PEITC NE (**batch-8**) was found to be **83.16 ± 10.87 %** (33.4 ± 4.35 mg) (**Table 4**).

3.3. Characterization of drug-loaded nanoparticle formulation

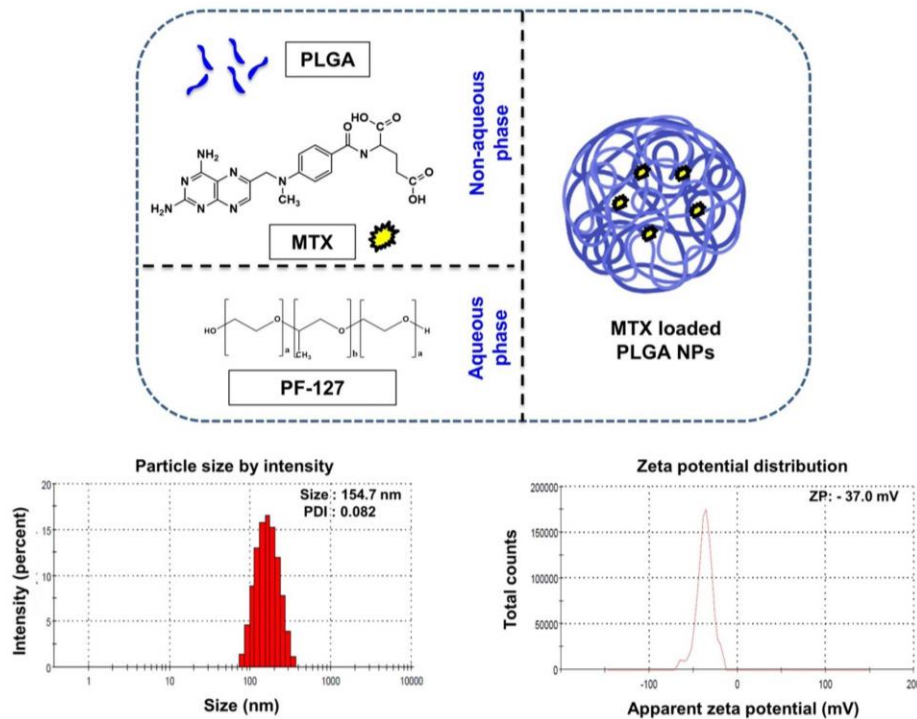
The particle size characterization studies by dynamic light scattering (DLS) from both the formulations (MTX NP and PEITC NE) confirmed monodisperse, nanometer-sized preparation with good zeta potential (**Figure 28A-B**). The optimized MTX NP had a negative surface charge (average ZP of **-34.50 mV**) and a narrow size range with a mean diameter of **151.8 ± 2.65 nm**. On the other hand, PEITC NE had a negatively charged surface (**ZP = -50.73 mV**) with an average size of **240.67 ± 4.75 nm** (**Table 5**).

The primary objective of particle characterization on the nanoformulations is to ensure enhanced nanoparticle permeation, stability, and uniformity (Danaei et al., 2018). Therefore, the designed nanoparticulate system has a particle size < 250 nm, and there, it would principally enable the persistence of modified nanoparticles in the joint cavity. Finally, the optimized uniformly dispersed drug nanoparticles (MTX NP and PEITC NE) were suitably loaded into the SF- PF-127 hydrogel system to prepare as an injectable for IA administration. (Trujillo-Nolasco et al., 2019).

Table 5. Particle size characterization of PEITC NE and MTX NP formulations. PS: Particle size, PDI: Polydispersity index, ZP: Zeta potential

Sl.no.	Name of the formulation	PS (nm)	PDI	ZP (mV)
1	MTX NP	151.8 ± 2.65	0.099 ± 0.015	-34.5 ± 2.29
2	PEITC NE	240.67 ± 4.75	0.351 ± 0.003	-50.73 ± 2.02

A



B

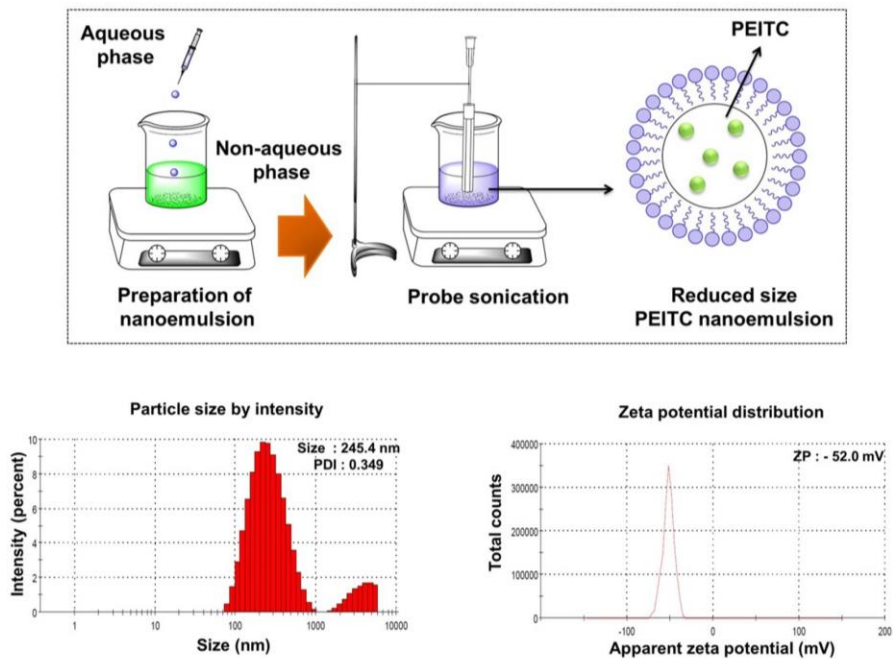


Figure 28. Characterization of NP and NE. The PS, PDI, and ZP of (A). MTX NP and (B). PEITC NE was determined using DLS. DLS: Dynamic light scattering.

3.4. Fabrication of dual-drug nanoparticles loaded hydrogel

Following the optimization studies, two SA-hydrogels single NP-loaded with MTX NP (**MTX NP HG**) or PEITC NE (**PEITC NE HG**) and a dual-drug loaded hydrogel loaded with MTX NP and PEITC NE (**DD NP HG**) were prepared with the composition as given in **Table 6**. The three individual HG formulations were utilized for further studies, as described below.

Table 6. Different compositions of SA and PF-127 for the preparation of *in-situ* hydrogels

Batch no.	Name of the hydrogel	SA composition (%) (w/v)	PF-127 composition (%) (w/v)
I	MTX NP HG	1	19
II	PEITC NE HG	1	12
III	DD NP HG	1	12

3.5. Characterization of dual-drug nanoparticles loaded hydrogel

3.5.1. FTIR and FESEM studies

FTIR studies were performed to observe any peak shifts due to chemical alterations in the drugs (MTX and PEITC) and the polymers/excipients (olive oil, span-80, tween-80, PLGA, SA, and PF-127) utilized in the formulation of nanoparticulate hydrogels. The infrared spectra of Free MTX, Free PEITC, BD NP HG, and DD NP HG samples are shown in **Figure 29A**.

The FTIR spectra of different drug-loaded hydrogels are compared with the peaks of BD NP HG and their respective free drugs to ensure drug incorporation and verify any covalent modifications. The following are the similar functional group characteristic peaks observed between BD NP HG and DD NP HG gel, respectively: i) The –OH group stretching vibration was observed at 3472.46 cm⁻¹ (BD NP HG) and 3420.71 cm⁻¹ (DD NP HG).

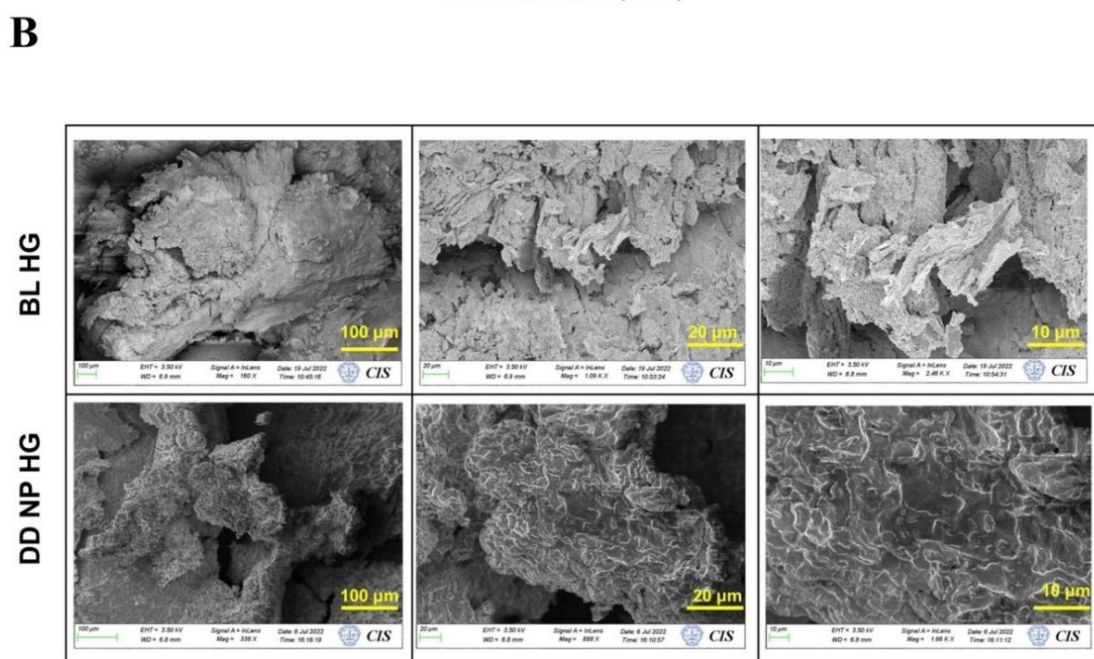
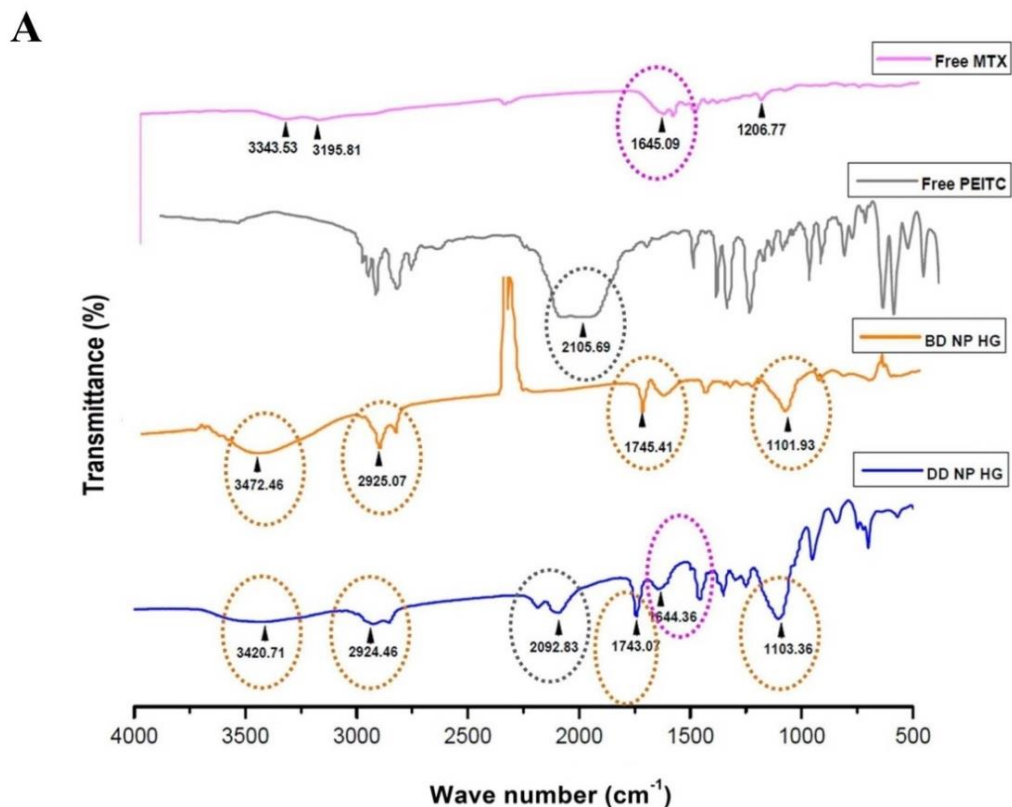


Figure 29. Characterization of dual-drug nanoparticles loaded hydrogel. (A). FTIR spectra of Free MTX, Free PEITC, BD NP HG, and DD NP HG. **(B).** FESEM images represent the morphological structure of BL HG and DD NP HG. Scale bars represent 100, 20, and 10 μm .

FTIR: Fourier transform infrared spectroscopy, FESEM: Field emission scanning electron microscopy.

This peak may be due to the presence of –OH in PLGA polymer (used in the MTX NP formulation) or from alginate (Dalal et al., 2021). ii) The –CH group stretching vibration at 2925.07 cm^{-1} (BD NP HG) and 2924.46 cm^{-1} . This principal absorption peak may be the alginate/pluronic/alkyl chains (Dalal et al., 2021; Karolewicz et al., 2017). iii) The characteristic –C=O (COOH) peak was observed at 1745.41 cm^{-1} (BD NP HG) and 1743.07 cm^{-1} (DD NP HG). This peak may be due to an acidic group in PLGA (Gao et al., 2017) or from the olive oil containing several acids (Wang et al., 2020). iv) The –C-O stretching vibration at 1101.93 cm^{-1} (BD NP HG) and 1103.36 cm^{-1} (DD NP HG). This peak is related to the ether chains of the PF-127 used to formulate the hydrogel (Karolewicz et al., 2017). The principal absorption peaks related to drugs (PEITC and MTX) showed an isothiocyanate (-N=C=S) peak of PEITC at 2105.69 cm^{-1} (Coscueta et al., 2021) and MTX at 3343.53 cm^{-1} confirming the presence of the -OH group and 1645.09 cm^{-1} corresponding to the –C=C group (Jang et al., 2019). A comparison of the FTIR spectra of Free PEITC with DD NP HG FTIR showed a distinctive peak at 2092.83 cm^{-1} , corresponding to the –N=C=S group, and a peak at 1644.36 cm^{-1} for the –C=C group. This data confirmed that PEITC NE and MTX NP are successfully incorporated with weak interactions into the hydrogel matrix.

FESEM studies were performed on the freeze-dried and gold sputter-coated samples of BL HG and DD NP HG hydrogels to investigate the cross-linked structure of the hydrogels. The images for both the hydrogel samples showed a macroporous structure with no apparent differences; however, a more complex 3D microstructure was observed in DD NP HG than in the

BL HG (**Figure 29B**). The representative FESEM images of DD NP HG shown in **Figure 29B** display a better-interconnected network with more distinctive pores than that of BL HG. This result indicates that the fabricated dual-drug loaded nanoparticles inside the hydrogel will be more favorably distributed within the DD NP HG hydrogel structure and could retain a sustained and controlled drug release due to the more interconnected porous system.

3.5.2. Drug content

Following the qualitative validation of the incorporation of both drugs (MTX and PEITC) into the hydrogel, the centrifugation method was used to determine the quantitative amount of each drug content (%) in various hydrogel formulations. **Table 7** showed that the % drug content for different hydrogel formulations ranged between **81 %** and **90 %**.

Table 7. Drug content (%) of different hydrogel formulations.

Batch no	Name of the hydrogel	Drug content (%)	Amount of drug (mg/mL)
I	MTX NP HG	90.87 ± 1.90	3.63 ± 0.076
II	PEITC NE HG	85.63 ± 3.36	34.25 ± 1.35
III	DD NP HG (MTX)	88.24 ± 9.27	3.53 ± 0.37
IV	DD NP HG (PEITC)	81.75 ± 3.50	32.7 ± 1.4

3.5.3. Solubility studies

Solubility studies were performed to determine the efficiency of nanoparticles or emulsions loaded into the hydrogel to solubilize the otherwise poorly soluble drugs. In the current study, both the drugs MTX and PEITC are hydrophobic in nature, which is a major drawback for their clinical utilization. Therefore, increasing their nanoparticulate solubility will help mitigate this drawback. As shown in **Figure 30**, the aqueous solubility (%) of Free MTX

and MTX in DD NP HG was found to be 0.36 ± 0.29 % (1.46 ± 1.17 $\mu\text{g/mL}$) and 72.96 ± 4.88 % (29.18 ± 1.95 $\mu\text{g/mL}$) respectively. On the other hand, PEITC, which is immiscible in water, showed a considerable increase in its aqueous solubility (%) up to 73.13 ± 8.86 % (29.25 ± 3.55 $\mu\text{g/mL}$) in the DD NP HG (PEITC) hydrogel formulation.

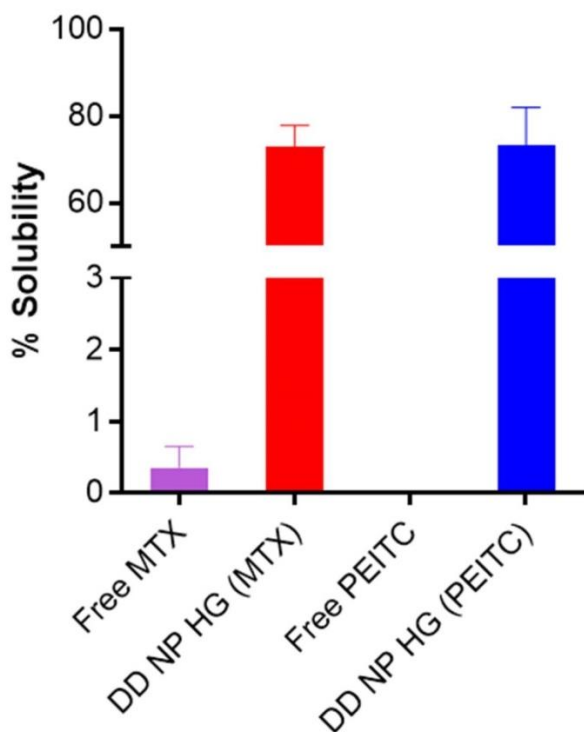


Figure 30. % Solubility studies of MTX and PEITC from DD NP HG and in free forms (Free MTX and Free PEITC). The respective amounts were calculated spectrophotometrically. All the data are represented as mean \pm SD (n = 3).

The solubility studies showed that the nanocomposite hydrogel system considerably improved the solubility of both loaded drugs (MTX and PEITC). This may be attributed to several factors, including highly water-soluble SA and PF-127 coating on the nanoparticles and/or reduced particle size of the loaded MTX NP or PEITC NE. Compared to free form, this

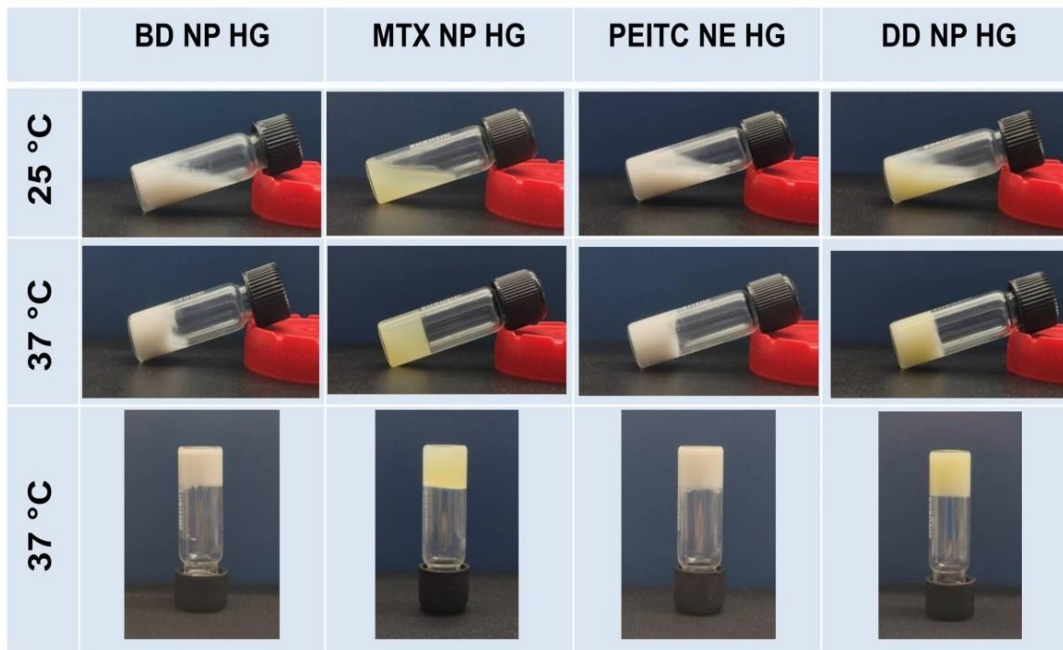
higher solubility may increase the effectiveness in treating arthritic conditions by potentiating the release of both drugs in their nanoparticulate forms.

3.5.4. Sol-gel phase transition studies

Typically, it is anticipated that the thermosensitive hydrogels will continue to exist in the sol state at a temperature between 4 °C to 25 °C before gradually transitioning to a gel state at physiological body temperature (37 °C). To properly construct a depot injectable, it is imperative to consider the sol-gel transition period, which is largely dependent on the temperature, polymer concentration (PF-127), and oil content. In the PF-127 structure (PEO-PPO-PEO), PPO chain forms are responsible for forming temperature-dependent packed micellar microstructure. At optimum concentrations and temperatures, PEO chains often overlap adjacently with the packed micellar structures, giving rise to a thermoreversible gelation property.

In the current study, sol-gel transition studies were carried out at two different temperatures, i.e., 25 °C and 37 °C, respectively, to verify the thermosensitivity of the *in situ* hydrogels. All prepared hydrogels underwent a sol-to-gel transition from 25 °C to 37 °C (**Figure 31A**). The drug-incorporated nanoparticle considerably affected the gelation time at 25 °C and 37 °C. As observed in **Figure 31B**, the time for gelation for BD NP HG was relatively higher (**245 ± 37.7 and 150 ± 30 s**) in comparison to the other hydrogels, MTX NP HG (**140 ± 22.9 s and 55 ± 17.3 s**), PEITC NE HG (**180 ± 30 s and 70 ± 8.7 s**) and DD NP HG (**120 ± 15 s and 45 ± 15 s**) at 25 °C and 37 °C respectively. The time difference in the gelation at 25 °C and 37 °C was found suitable, giving ample time for administration of the formulation into the site and its gelation (**Figure 31B**).

A



B

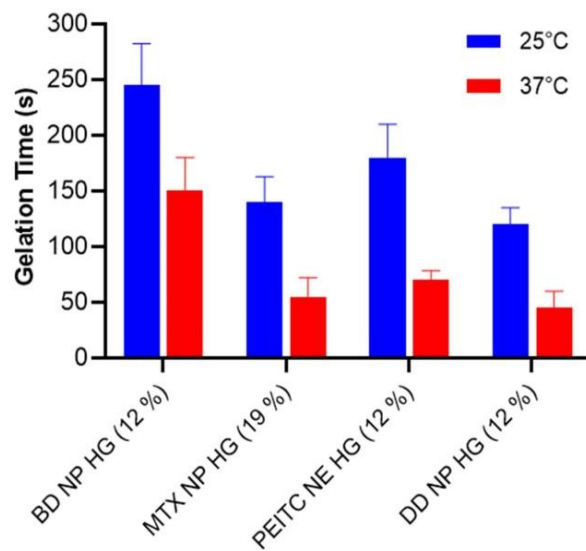


Figure 31. Sol-gel phase transition characteristics and determination of gelation time (A)

Representative image of the sol-gel phase transition characteristics of different hydrogel

formulations (BD NP HG, MTX NP HG, PEITC NE HG, and DD NP HG). Phase transition with an increased temperature. (B). The gelation time of the different hydrogel formulations (BD NP HG, MTX NP HG, PEITC NE HG, and DD NP HG) was measured at 25 °C and 37 °C. Data are shown in mean \pm SD (n=3).

The adsorption of PPO groups of PF-127 at the interface of the oil droplet makes it more hydrophobic, and these highly hydrophobic groups further form mixed micelles responsible for its thermosensitive behavior. Hence, the nanoemulsion-loaded hydrogels exhibit thermoreversible characteristics even at lower concentrations of PF-127 (Hashemnejad et al., 2019). It was observed that with an increase in the PF-127 concentration ($> 12\%$ w/v), a hard gel was formed that prevented the gel from passing through the syringe even at a lower temperature ($< 10\text{ }^{\circ}\text{C}$), resulting in poor injectability. Hydrogel-containing nanoemulsion constructed with 12% (w/v) of PF-127 has a considerable gelation time difference between $25\text{ }^{\circ}\text{C}$ and $37\text{ }^{\circ}\text{C}$. Hence, 12% (w/v) PF-127 concentration is preferred in preparing the hydrogel-containing nanoemulsion (PEITC NE HG and DD NP HG) to ensure good injectability and thermosensitive properties.

In the formulation of DD NP HG, the gelation time was observed to be lowest at both $25\text{ }^{\circ}\text{C}$ and $37\text{ }^{\circ}\text{C}$ (**$120 \pm 15\text{ s}$ at $25\text{ }^{\circ}\text{C}$ and $45 \pm 15\text{ s}$ at $37\text{ }^{\circ}\text{C}$**) in comparison to other hydrogel formulations because the presence of PEITC, PLGA, and oil enhanced the gelation properties. It is followed by MTX NP HG (**$140 \pm 22.9\text{ s}$ at $25\text{ }^{\circ}\text{C}$ and $55 \pm 17.3\text{ s}$**), PEITC NE HG (**$180 \pm 30\text{ s}$ at $25\text{ }^{\circ}\text{C}$ and $70 \pm 8.7\text{ s}$ at $37\text{ }^{\circ}\text{C}$**), and BD NP HG (**$245 \pm 37.7$ at $25\text{ }^{\circ}\text{C}$ and $150 \pm 30\text{ s}$ at $37\text{ }^{\circ}\text{C}$**) (Figure 31B).

3.5.5. *In-vitro* degradation studies

It is a pre-requisite for any biomaterials administered into a living system to be biodegradable and eliminated from the body without causing any adverse systemic toxicity (Pankongadisak and Suwantong, 2019). The degradation kinetics of the hydrogel and its components can be studied *in vitro* for a prolonged period in different physiologically simulated conditions (in PBS medium, pH 7.4) to predict its *in vivo* biodegradability or stability. Here, the *in vitro* degradation study of all the hydrogels *in situ* was carried out as a function of time in PBS (pH 7.4) at 37 °C for 6 days.

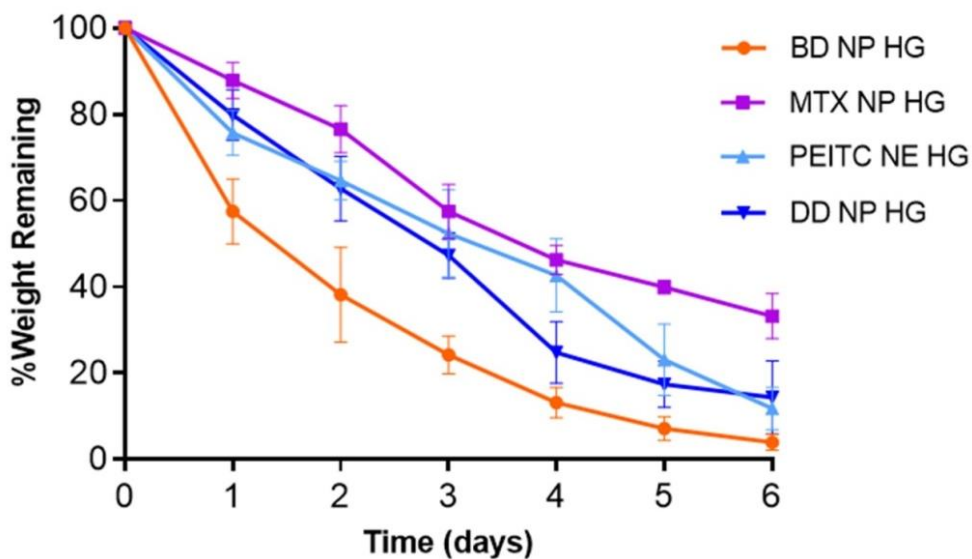


Figure 32. *In vitro* degradation properties of dual-drug nanoparticles loaded hydrogel. The rate of degradation (%) of the hydrogels at 37 °C was investigated by estimating the percent amount of residual hydrogels at various time intervals up to 6 days. All the data are expressed as mean \pm SD (n = 3).

Figure 32 shows the kinetics of degradation of the different hydrogels (MTX NP HG, PEITC NE HG, and DD NP HG) and the % remaining weight after 6 days of the study period. The results showed that all the hydrogels showed more than 67 % degradation for up to 6 days, indicating sustained bio-degradation. The final % weight of remaining hydrogel MTX NP HG, PEITC NE HG, and DD NP HG was determined to be **33.18 %**, **11.78 %**, and **14.32 %**, respectively, while the BD NP HG showed higher degradation (remaining of **3.86 %**).

3.5.6. Injectability studies

The *in vivo* performance of the hydrogel as an injectable can be studied *in vitro* using a physiologically simulated condition (37 °C). The different hydrogel formulations moved freely into the syringe. Upon injection into PBS (at 37 °C), the contents moved smoothly out of the needle, forming an uninterrupted thread-like soft gel settling at the bottom of the vial without any phase separation or clumps, indicating a homogenous and stable preparation suitable as a thermoresponsive injectable (**Figure 33**).

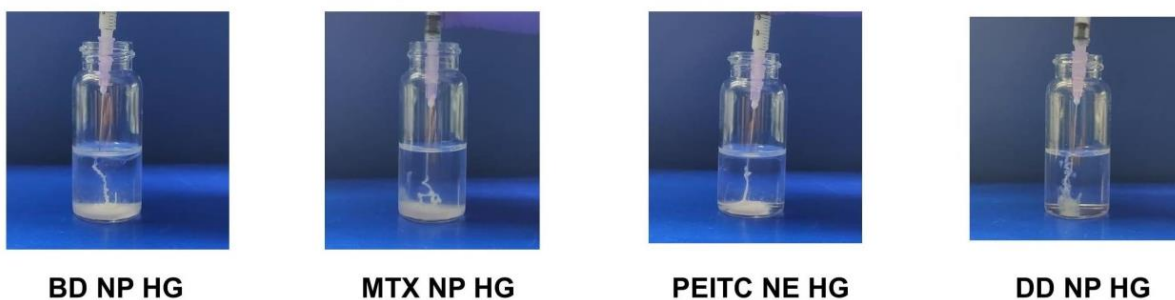


Figure 33. Injectable performance of the different hydrogel formulations studied at body physiological conditions (pH-7.4 and 37 °C).

3.5.7. Rheological characteristics

Determining the rheological characteristics of injectable hydrogels is essential for understanding the behavior of a hydrogel following injection and the structural behavior of the formulation by measuring the viscoelastic property as a function of frequency, temperature, and stress/strain. The most significant visco-elastic rheological parameters considered for its application in the biomedical area are complex viscosity (η^*), storage modulus (G'), and loss modulus (G''). Complex viscosity measures the ability of the gel to resist shearing forces within an injection site during injection. In contrast, storage modulus (G') and loss modulus (G'') differences measure the sol-gel conversion of the injectable hydrogel (Alonso et al., 2021). To calculate the temperature-dependent viscoelastic property of the hydrogel, the temperature sweep test was performed at the constant frequency and strain rate. The rheological parameters of the BD NP HG and DD NP HG, namely G' (storage) and G'' (loss) modulus, have been illustrated as the function of temperature.

As shown in **Figure 34A-B**, all the rheological parameters depend highly on the temperature. From the heating cycle, 25 °C was determined to be the sol-gel transition temperature for both hydrogel formulations. The BD NP HG and DD NP HG show a gel-like behavior at the beginning of the heating cycle (after 25 °C) as the storage modulus is higher than the loss modulus. In the gel state, the storage and loss modulus values of BD NP HG and DD NP HG indicate that both are mechanically stable. The sample DD NP HG shows a sudden increase in the storage modulus value at 37 °C during the heating cycle, whereas the sample BD NP HG shows a gradual increase in the modulus during the heating cycle. Thus, the sample DD NP HG has a higher level of gel structure above 37 °C.

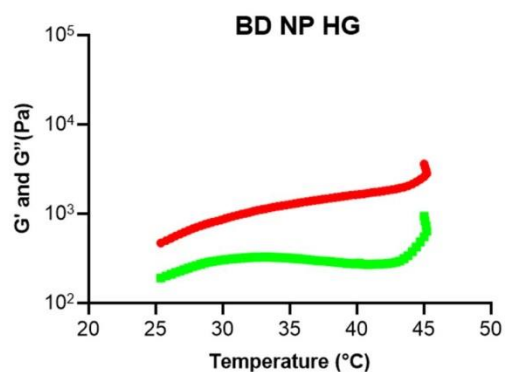
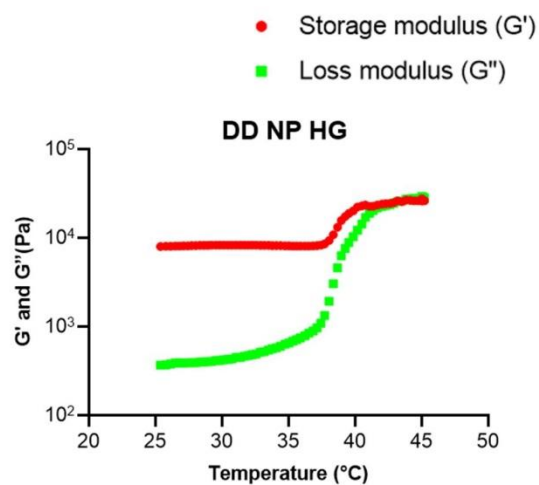
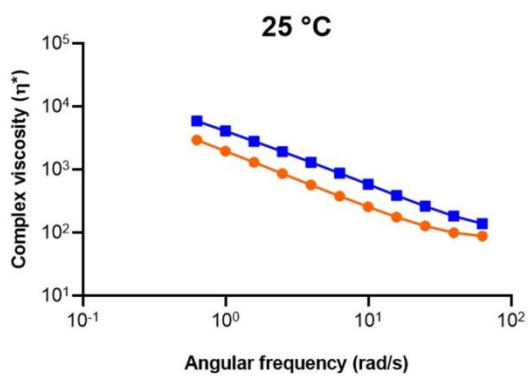
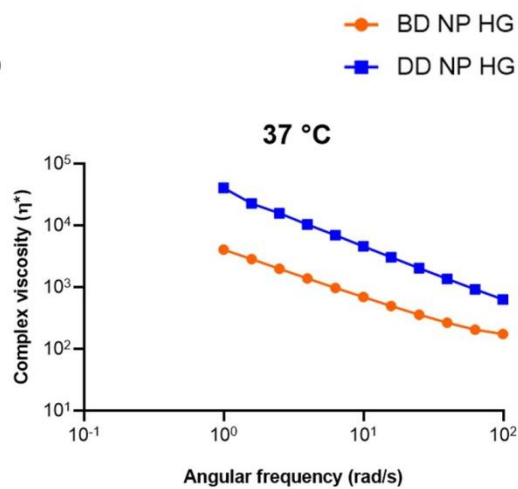
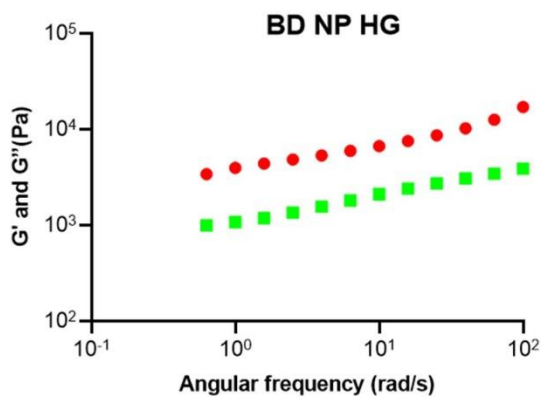
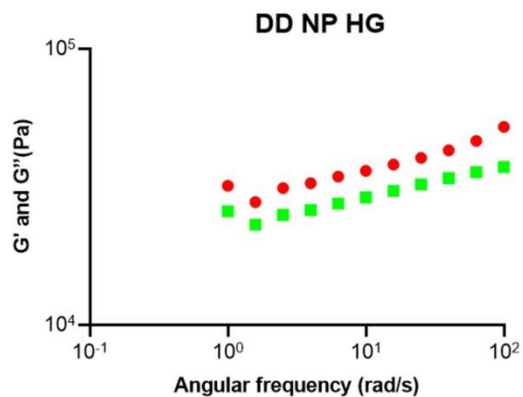
A**B****C****D****E****F**

Figure 34. The rheological properties of (A). BD NP HG and (B). DD NP HG. Complex viscosity versus angular frequency for BD NP HG and DD NP HG at (C). 25 °C and (D). 37 °C. Storage modulus (G') and loss modulus (G'') of the (E). BD NP HG and (F). DD NP HG hydrogels on the angular frequency at 37 °C.

The frequency dependence (and equivalently, the time dependence) of a material's viscoelastic characteristics is commonly measured using frequency sweeps. High and low frequencies, respectively, generally represent short-time and long-time scales. The sinusoidal stress response is used to calculate the dynamic moduli G'' (loss) and G' (storage). The complex viscosity, frequently used in place of the complex modulus, is calculated as the complex modulus divided by the applied frequency. Frequency tests are typically conducted in the linear range (small strain); in this case, the results are independent of the applied strain. **Figure 34C-D** shows the complex viscosity of the gel measured as a function of frequency at 25 °C and 37 °C. The hydrogel shows the shear-thinning behavior as the gel is subject to a high deformation rate, indicating that the complex viscosity (η^*) is decreasing with the increasing deformation rate (i.e., angular frequency). This suggests that the hydrogels were highly shear thinning and suitable as an injectable for the animal *in vivo* studies. The hydrogel DD NP HG shows a higher complex viscosity than the BD NP HG sample at both temperatures.

Hydrogels' storage modulus (G') and loss modulus (G'') changed with angular frequency. From the results in **Figure 34E-F**, G' , and G'' increased obviously at 37 °C, with the angular frequency increasing. By observing data, DD NP HG showed increased levels of both G' and G'' compared to BD NP HG. This indicates that the incorporation of drugs in the hydrogel led to increased hydrogel strength and enhanced mechanical stability. Hence, G' was always greater than G'' , which is a typical gel-like flow behavior when it is subjected to a higher frequency (i.e.,

rate of deformation). The improved rheological parameters of DD NP HG might occur due to strong inter-micellar interactions between the drug-loaded nanoparticulate system inside hydrogels with SA and PF-127 in the hydrogel.

3.6. *In-vitro* drug release studies

In vitro dissolution studies were conducted to evaluate the rate and quantity of drug release, which may substantially impact treating disease, before the *in vivo* assessment studies for a particular drug formulation (dose frequency and assessment). In most studies, it is believed that improved solubility and dissolution with sustained drug release behavior may enhance the treatment efficiency. An additional advantage of the *in vitro* release study is that it helps to decide the dosing frequency in the *in vivo* treatment studies. In the current study, all the hydrogels showed > 68 % drug release sustaining up to 120 h, as shown in **Figure 35B**. Initially, the amount of PEITC release from both the hydrogels was 55 % (DD NP HG) and 54 % (PEITC NE HG) in 24 h, and a sustained release behavior was observed up to 120 h (PEITC NE HG -81 % & DD NP HG – 68 %). In contrast, MTX released from the hydrogel was 48 % in DD NP HG and 26 % in MTX NP HG, respectively, in 24 h; over time, an extended-release was studied up to 120 h in both the hydrogels (MTX NP HG – 69 % & DD NP HG- 79 %). The variable release rate of MTX may be due to the slow erosion or degradation of the rigid hydrogel network surrounding the MTX NP, which is observed in the *in vitro* degradation studies, or another reason may be that the nanoemulsion potentiates the solubility of MTX in the combinational nanogel and further aids in the increased dissolution of the MTX (Hemelryck et al., 2019). Owing the saturation of lipophilic drug in the buffer solution or adsorption of the drug to the dialysis membrane may be an obstacle to preventing 100 % of the drug release. This may be overcome by increasing the sink condition (Ahsan et al., 2020).

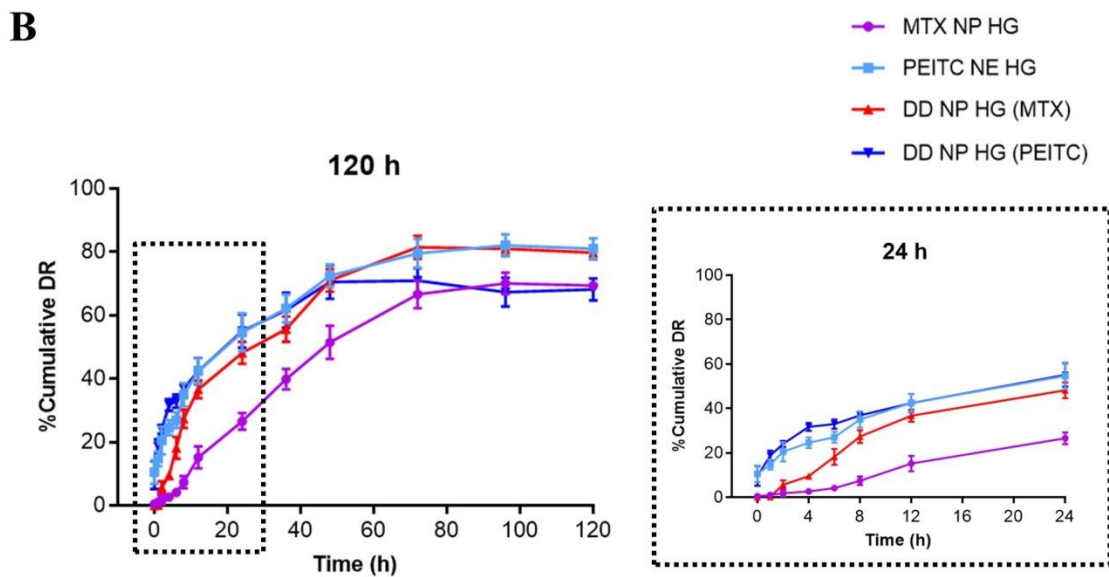
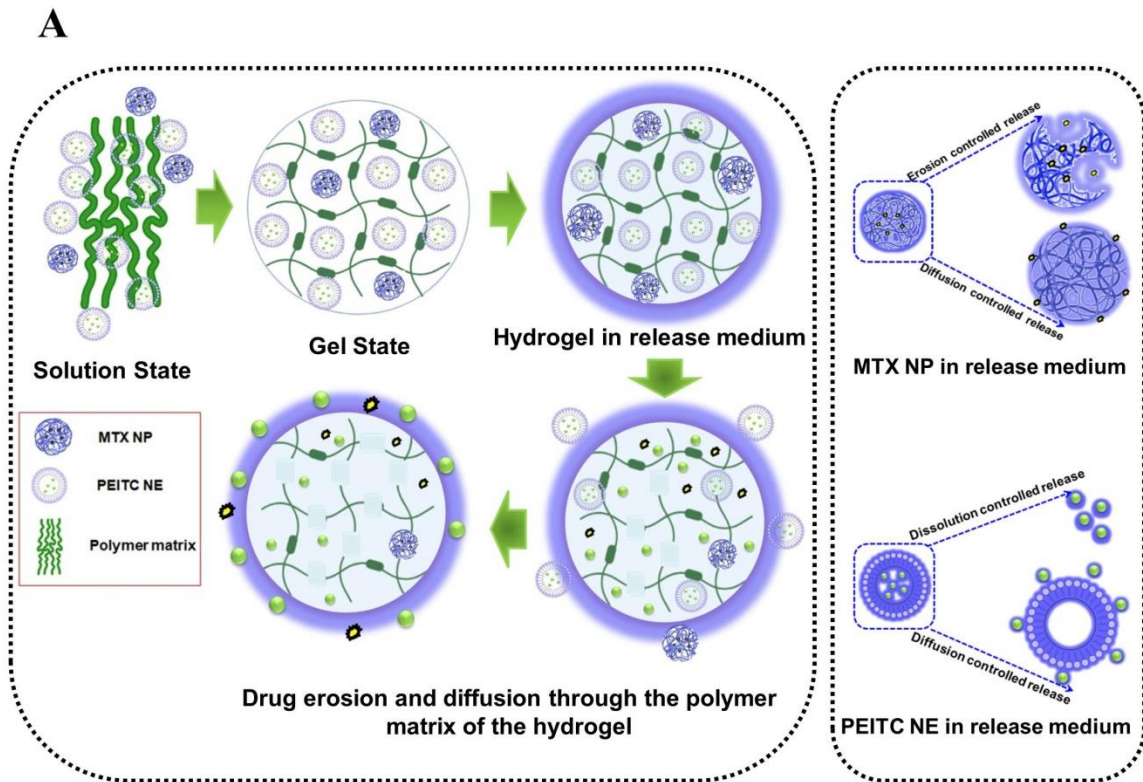


Figure 35. The drug release properties of dual-drug nanoparticles loaded hydrogel *in vitro*.

(A). Schematic representation of drug release mechanism of DD NP HG. (B). % MTX and

PEITC release from the hydrogel vs. time (h) at pH 7.4 at 37 °C at 24 h and 120 h was measured. *purple* color: MTX release rate from MTX NP HG, *light blue* color: PEITC release rate from PEITC NEHG, *red* color: MTX release rate from DD NP HG, and *navy blue* color: PEITC release rate from DD NP HG. Results are presented as mean \pm SD (n = 3). Created with Biorender (biorender.com).

In summary, hydrogels not only increased the solubility and dissolution but also sustained the release of both drugs for 120 h, which is ideal for the delivery of drugs continuously in the inflamed joints for a prolonged period.

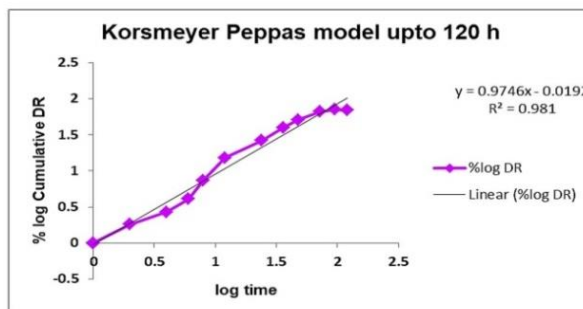
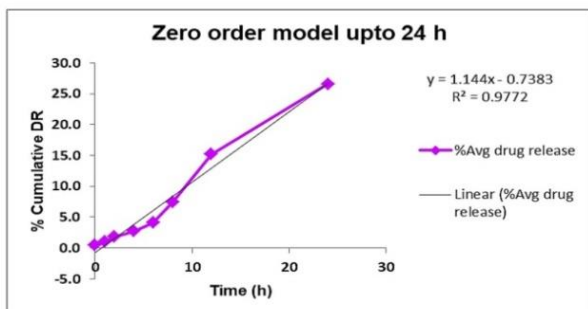
3.7. *In-vitro* drug release kinetics

It was concluded that MTX from DD NP HG followed the Korsmeyer Peppas model for 24 h and later by the Higuchi model. In contrast, MTX NP HG followed zero order initially (for 24 h) and was followed by the Korsmeyer Peppas model. In the case of PEITC, it followed a similar mechanism pattern from both the hydrogels (DD NP HG and PEITC NE HG), initially released by the Korsmeyer Peppas model for 24 h and then continued with the Higuchi model (Figure 36, Table 8).

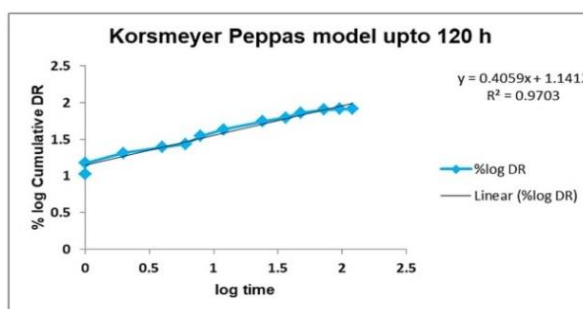
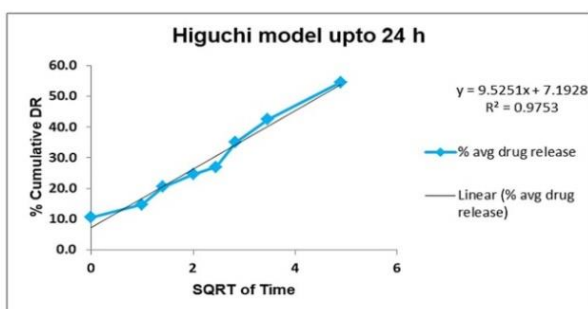
The Higuchi model represents that the drug is embedded inside the hydrogel matrix and slowly diffuses out by the diffusion and erosion mechanisms. Solvent or dissolution media enters the matrix, then dissolves and transfers the drug from inside to outside the membrane by erosion and diffusion-controlled mechanisms.

Korsmeyer model represents anomalous diffusion of the drug from the hydrogel matrix. The zero-order model represents the controlled release of the drug diffusion from the hydrogel matrix.

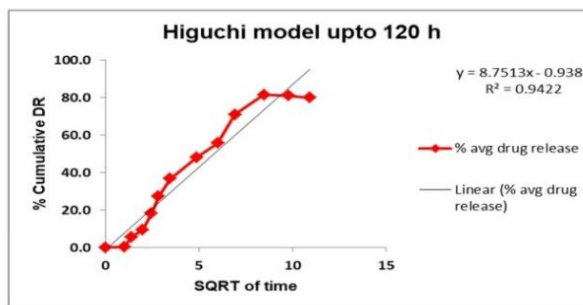
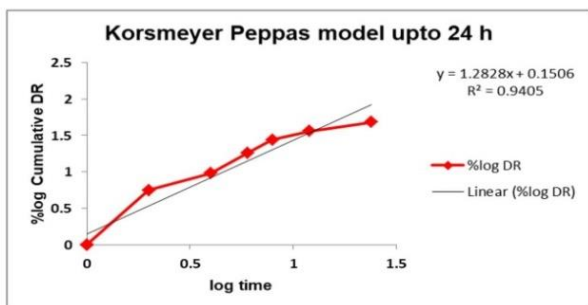
(A) MTX release kinetics from MTX NP HG



(B) PEITC release kinetics from PEITC NE HG



(C) MTX release kinetics from DD NP HG



(D) PEITC release kinetics from DD NP HG

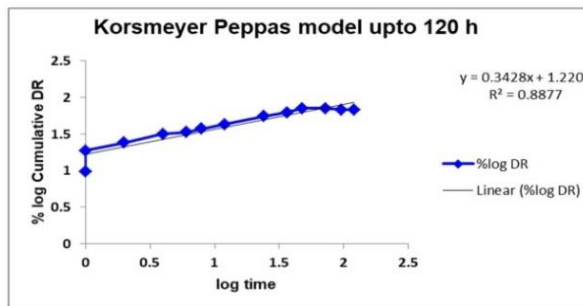
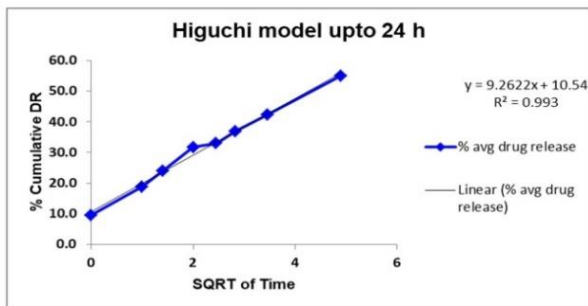


Figure 36. The drug release kinetics of dual-drug nanoparticles loaded hydrogel *in vitro*.

Release kinetics (%) MTX and PEITC release from the hydrogel was calculated using different kinetics models at (A). MTX release kinetics (%) from MTX NP HG at 24 h and 120 h. (B). PEITC release kinetics (%) from PEITC NE HG at 24 h and 120 h (C). MTX release kinetics (%) from DD NP HG at 24 h and 120 h (D). PEITC release kinetics (%) from DD NP HG at 24 h and 120 h. *Purple color*: MTX release rate from MTX NP HG, *light blue color*: PEITC release rate from PEITC NE HG, *red color*: MTX release rate from DD NP HG, and *navy blue color*: PEITC release rate from DD NP HG. All the data are represented as mean \pm SD (n = 3).

Table 8. Release kinetic models and their R² values of different hydrogel formulations

***- indicates the particular formulation following that release model or kinetics

Name of the model	R ² values							
	DD NP HG				MTX NP HG		PEITC NE HG	
	MTX		PEITC		MTX		PEITC	
	24 h	120 h	24 h	120 h	24 h	120 h	24 h	120 h
Zero-order	0.909	0.796	0.863	0.671	0.977***	0.833	0.929	0.804
First order	0.621	0.465	0.633	0.505	0.868	0.616	0.778	0.636
Higuchi	0.934	0.942***	0.993***	0.877	0.837	0.941	0.975***	0.953
Hixon-Crowell	0.936	0.864	0.909	0.710	0.974	0.935	0.957	0.875
Korsmeyer-Peppas	0.940***	0.891	0.853	0.887***	0.968	0.981***	0.955	0.970***

3.8. Stability studies for different hydrogel formulations

The hydrogels exhibited good stability at 4 °C with negligible differences in % drug content (% DC) shown in **Table 9**.

Table 9. Stability studies at 4 °C for different hydrogel formulations for 60 days.

Formulation	Time (days)	DC (%)		Amount of drug (mg)	
MTX NP HG	0	90.9 ± 3.8		3.63 ± 0.07	
	30	86.7 ± 2.7		3.47 ± 0.11	
	60	82.2 ± 4.6		3.29 ± 0.18	
PEITC NE HG	0	85.7 ± 3.7		34.25 ± 1.35	
	30	78.3 ± 4.0		31.32 ± 1.59	
	60	75.6 ± 4.3		30.21 ± 1.72	
DD NP HG		PEITC	MTX	PEITC	MTX
	0	81.8 ± 7.2	88.3 ± 9.3	32.7 ± 1.4	3.53 ± 0.37
	30	75.7 ± 4.0	86.6 ± 9.0	30.26 ± 1.6	3.46 ± 0.36
	60	71.7 ± 5.8	83.7 ± 5.8	28.7 ± 2.32	3.35 ± 0.23

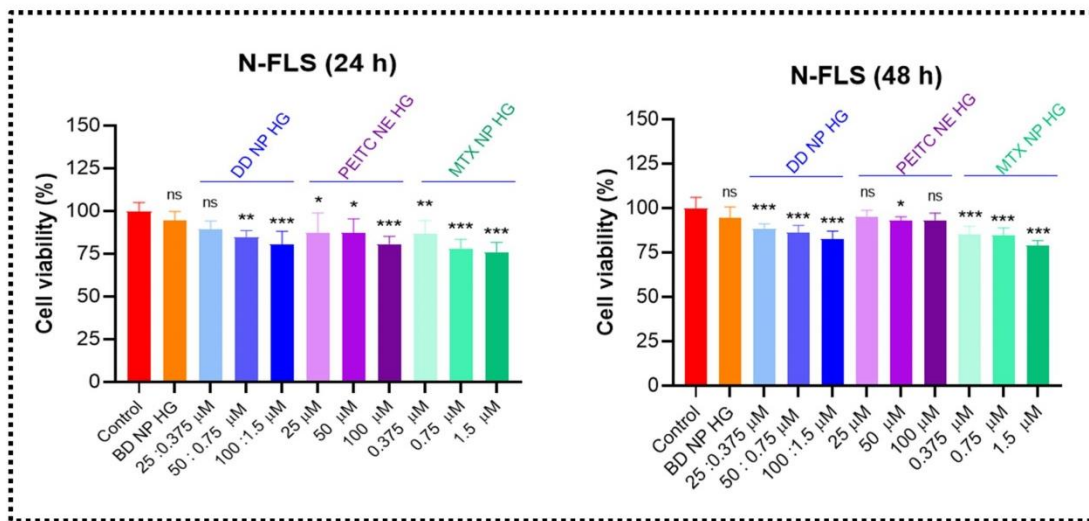
3.9. Cell-based studies

3.9.1. Cytotoxicity and biocompatibility of dual-drug nanoparticles loaded hydrogel *in vitro*

The *in vitro* biocompatibility and toxicity of DD NP HG on the N-FLS and RA-FLS were studied by assessing the percentage cell viability using MTT assay. Initially, the cytotoxicity of DD NP HG on N-FLS was examined to ensure that the normal functioning of the FLS was not impaired. The healthy FLS, i.e., N-FLS, are essential for maintaining normal joint function by promoting joint lubrication, regulating the synovial fluid amount, actively participating in joint repair, and reducing joint inflammation (Yu et al., 2022).

According to **Figure 37A-B**, N-FLS cells did not exhibit any toxicity to DD NP HG and various concentrations of PEITC NE HG, MTX NP HG, and DD NP HG. The percentage of cell viability (%) for all treatment groups was determined to be **94 -76 %** at 24 h and **95 -78 %** at 48 h.

A



Concentration
PEITC : MTX
 25 : 0.375 μM
 50 : 0.75 μM
 100 : 1.5 μM

B

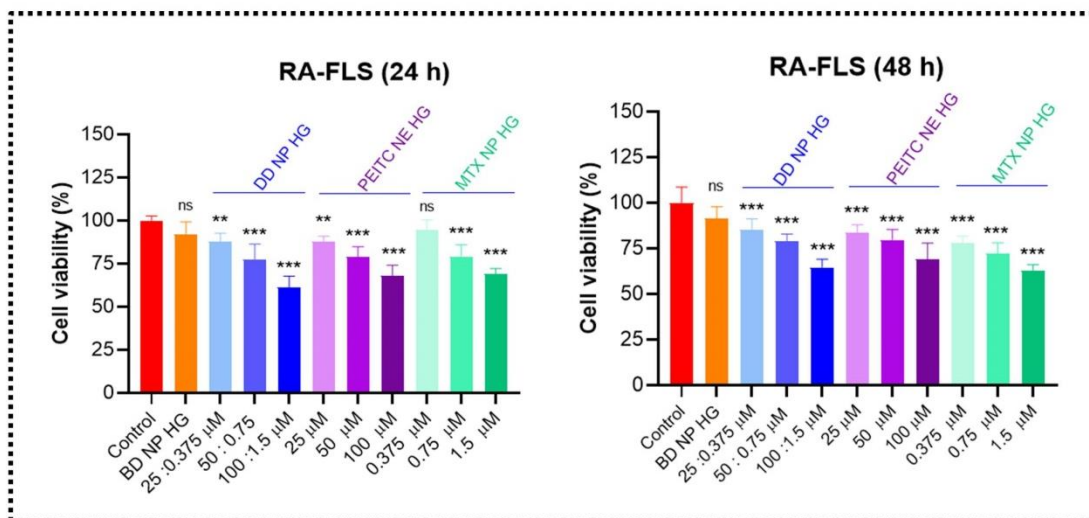


Figure 37. Cytotoxicity and biocompatibility assay of dual-drug nanoparticles loaded hydrogel *in vitro*. Cell viability (%) of (A). N-FLS and (B). RA-FLS cell with various treatments at 24 h and 48 h. The data are represented as mean ± SD (n = 6). The values were statistically examined using a one-way ANOVA test. Statistical significance: *p < 0.05, **p <

0.01, *** $p < 0.001$, and ns- non-significant.

In the context of RA-FLS, these are the most prevalent cell types at the pannus-cartilage junction that contribute to joint degeneration by producing pathogenic mediators, including cytokines and inflammatory proteases, causing the onset and duration of RA (Nygaard and Firestein, 2020). The viability of RA-FLS cells was examined here in relation to the impact of DD NP HG. Following the administration of DD NP HG and varied PEITC NE HG concentrations, MTX NP HG and DD NP HG showed an inhibitory effect at high concentrations. **Figure 37A-B** illustrates the % cell viability for the various treatment groups at higher concentrations: **PEITC NE HG** [100 μ M: **68.01 %** & **69.04 %** (24 h & 48 h)]; **MTX NP HG** [1.5 μ M: **69.22 %** & **63.00 %** (24 h & 48 h)] and **DD NP HG** [PEITC (100 μ M) and MTX (1.5 μ M): **61.16 %** & **64.46 %** (24 h & 48 h)] respectively.

Together, the N-FLS and RA-FLS results validated that the DD NP HG possessed good biosafety for healthy FLS cells and a modest inhibitory effect on RA-FLS at higher concentrations. The findings above are consistent with a study that previously presented a methodology for evaluating the biomaterials' *in vitro* toxicity in relation to their biocompatibility (Joshi et al., 2018).

3.9.2. Effect of dual-drug nanoparticles loaded hydrogel in cell apoptosis

To further illustrate whether DD NP HG treatment could induce cell apoptosis in RA-FLS cells, the Annexin V-FITC/PI apoptosis detection kit was employed, and the apoptosis was detected by flow cytometry.

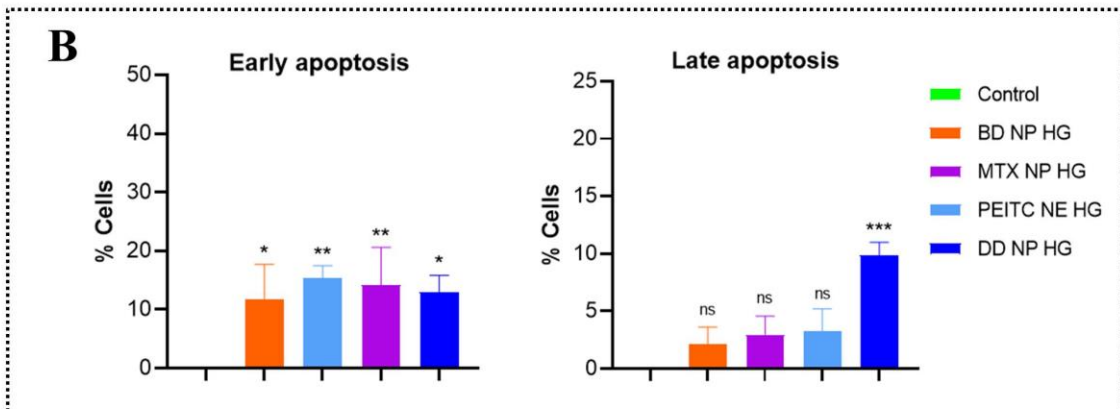
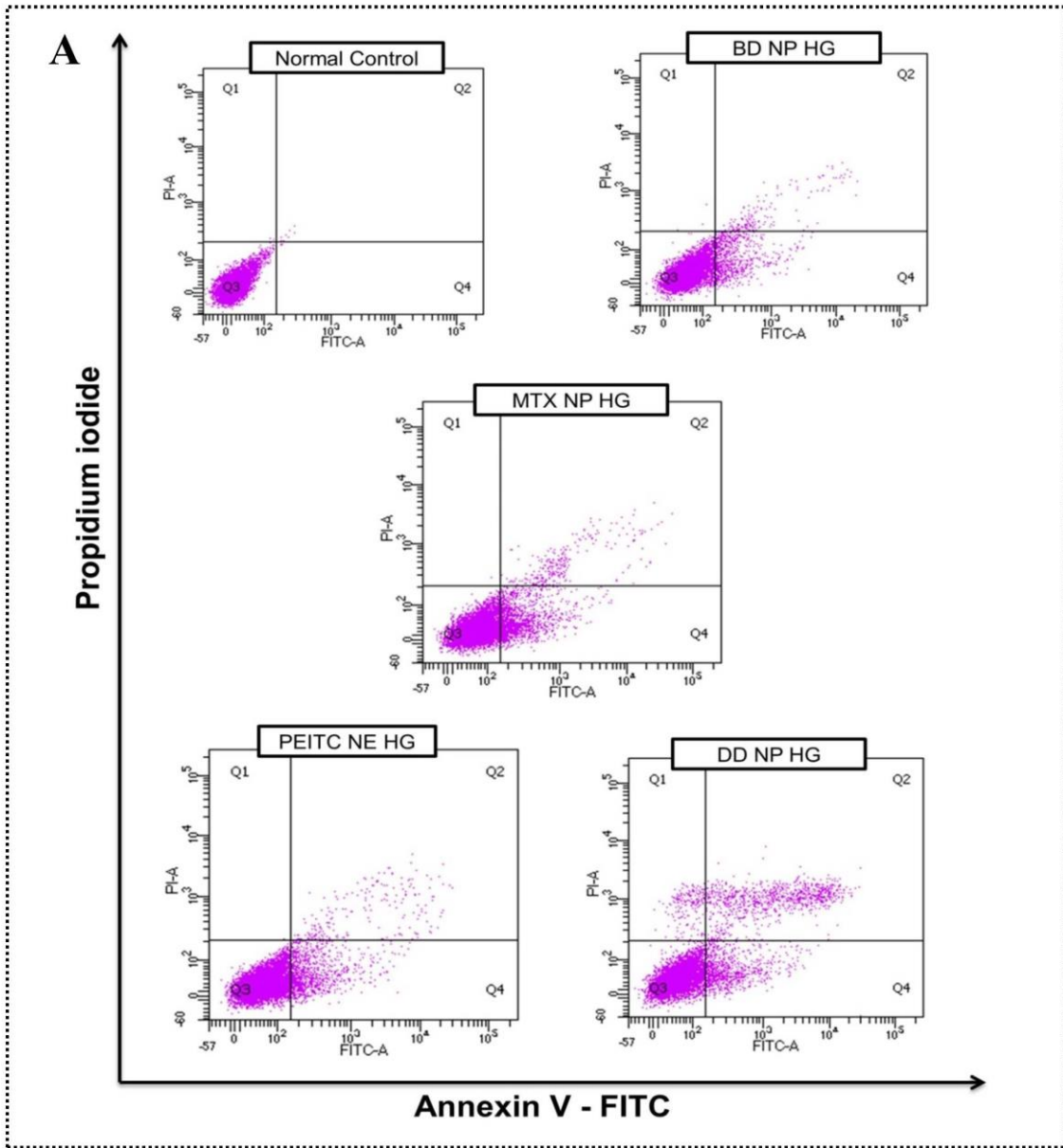


Figure 38. Effects of dual-drug nanoparticles loaded hydrogel on apoptosis in RA-FLS cells. (A). Representative dot plot images and (B). The induction of apoptotic death was calculated as the rate of early and late apoptosis (%) by each treatment in RA-FLS. RA-FLS cells were incubated with various treatments for 24 h and then analyzed by flow cytometry. The values were statistically examined using a one-way ANOVA test. Statistical significance: * $p < 0.05$, ** $p < 0.01$, *** $p < 0.001$ and ns-non significant.

In RA-FLS, the DD NP HG treatment significantly promoted early and late apoptosis (**Figure 38A-B**). However, DD NP HG had a significantly higher late apoptotic rate for 24 h than the other treatment groups. The late apoptosis rate (%) in DD NP HG, MTX NP HG, PEITC NE HG, and BD NP HG was **9.87 %**, **2.97 %**, **3.23 %**, and **2.13 %**, respectively. On the other hand, the early apoptosis rate (%) was found to be **13 %** (DD NP HG), **15.33 %** (MTX NP HG), **14.23 %** (PEITC NE HG), and **11.67 %** (BD NP HG), respectively. The results of the apoptosis detection demonstrated that the combined therapy of MTX NP and PEITC NE, i.e., DD NP HG, significantly increased RA-FLS cell apoptosis induction.

3.9.3. In vitro evaluation of anti-inflammatory efficacy of dual-drug nanoparticles loaded hydrogel

The pathophysiology of RA is significantly influenced by numerous pro-inflammatory cytokines and chemokines released by RA-FLS in the synovial intimal lining, including TNF- α , IL-17A, and IL-6. These cytokines are known to induce the activation of immune cells at the site of the RA joint, resulting in inflammation and joint destruction (Alunno et al., 2017; Nygaard and Firestein, 2020).

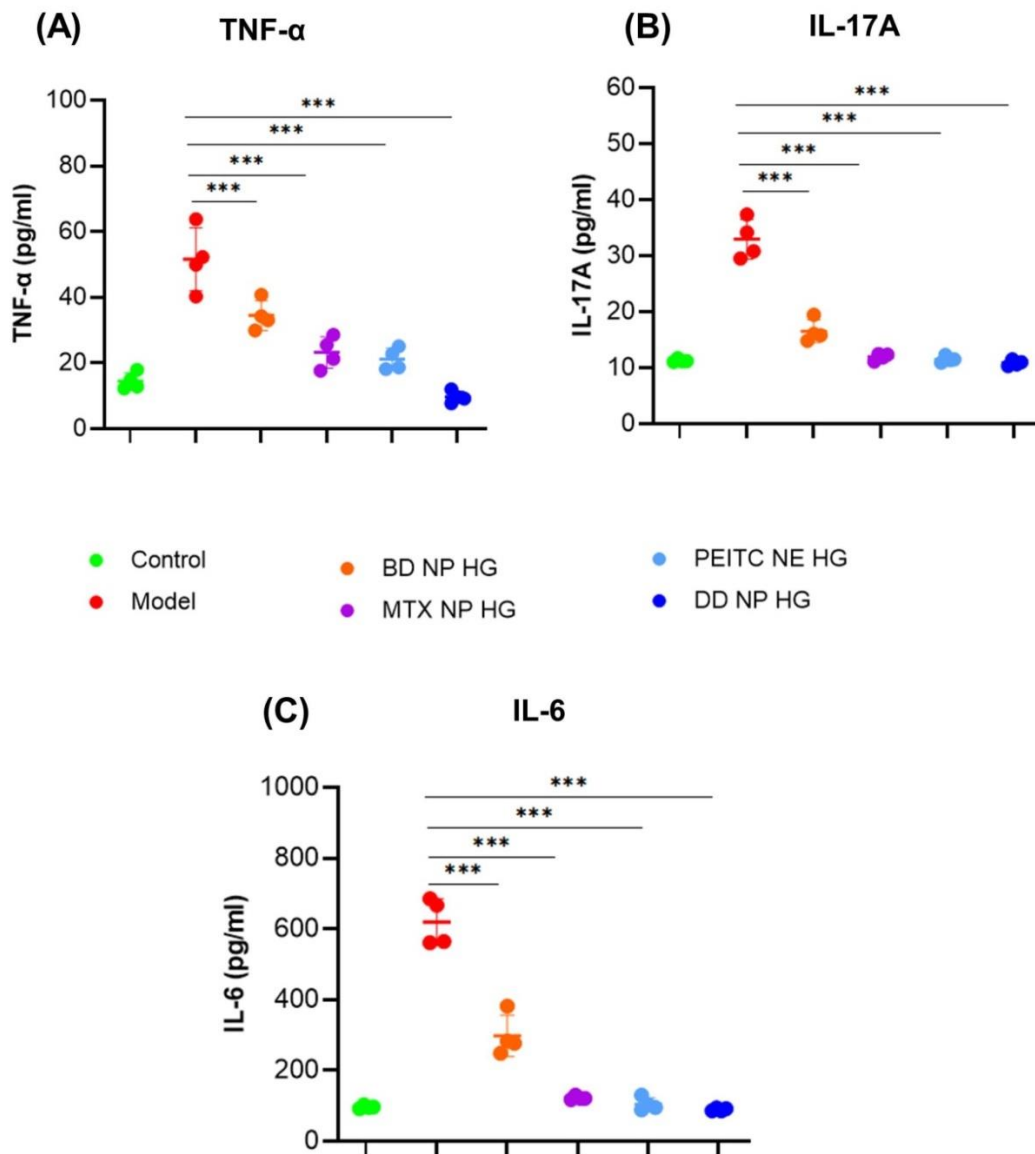


Figure 39. Effect of dual-drug nanoparticles loaded hydrogel on pro-inflammatory cytokines in LPS-stimulated RA-FLS cells. The levels of pro-inflammatory cytokines: (A). TNF- α , (B). IL-17A, and (C). IL-6 was quantified using ELISA kits as per the manufacturer's protocol. The data are represented as mean \pm SD (n = 4). The values were statistically examined using a one-way ANOVA test. Statistical significance: *p < 0.05, **p < 0.01, ***p < 0.001, and ns- non-significant. TNF- α : Tumor Necrosis Factor-alpha, IL-17A: Interleukin 17A, IL-6:

Interleukin 6, LPS: Lipopolysaccharides, ELISA: Enzyme-linked immunoassay.

To investigate the anti-inflammatory efficiency of DD NP HG, RA-FLS cells were pretreated with LPS for 4 hours, followed by a 24-hour treatment with DD NP HG. The ELISA method was then used to measure the levels of inflammatory cytokines in the culture medium. As depicted in **Figure 39A-C**, TNF- α , IL-17A, and IL-6 levels were elevated in LPS-stimulated RA-FLS. Treatment with DD NP HG significantly inhibited the secretion of TNF- α , IL-17A, and IL-6 in the RA-induced synovial cells.

3.9.4. Effect of dual-drug nanoparticles loaded hydrogel on the mRNA expression level

In RA pathogenesis, the inflammatory microenvironment components, such as T-cells and macrophages, contribute to the production of pro-inflammatory cytokines (TNF- α , IL-1 β , IL-6, and IL-17A), chemokines (RANKL, GM-CSF, and MMPs), inflammatory enzymes (iNOS and COX-2) mediate the immune response (Mizoguchi et al., 2018). Here, we further explored whether DD NP HG has any regulatory potential on the gene expression levels of DD NP HG on gene expression in LPS-stimulated RA-FLS cells, the mRNA expression of IL-1 β , RANKL, OPG, NFATc1, and DKK1 performed by qRT-PCR.

As shown in **Figure 40A**, LPS-stimulated RA-FLS, i.e., the *model group*, showed elevated levels of IL-1 β m-RNA expression. Upon DD NP HG treatment, the mRNA expression of IL-1 β was significantly downregulated by **~6 fold**. On the other hand, it was found that the mRNA level of RANKL and OPG was significantly downregulated by **~2.8 fold** and significantly upregulated by **~6.8 fold** in the DD NP HG group when compared with the *model group*, respectively (**Figure 40B-C**).

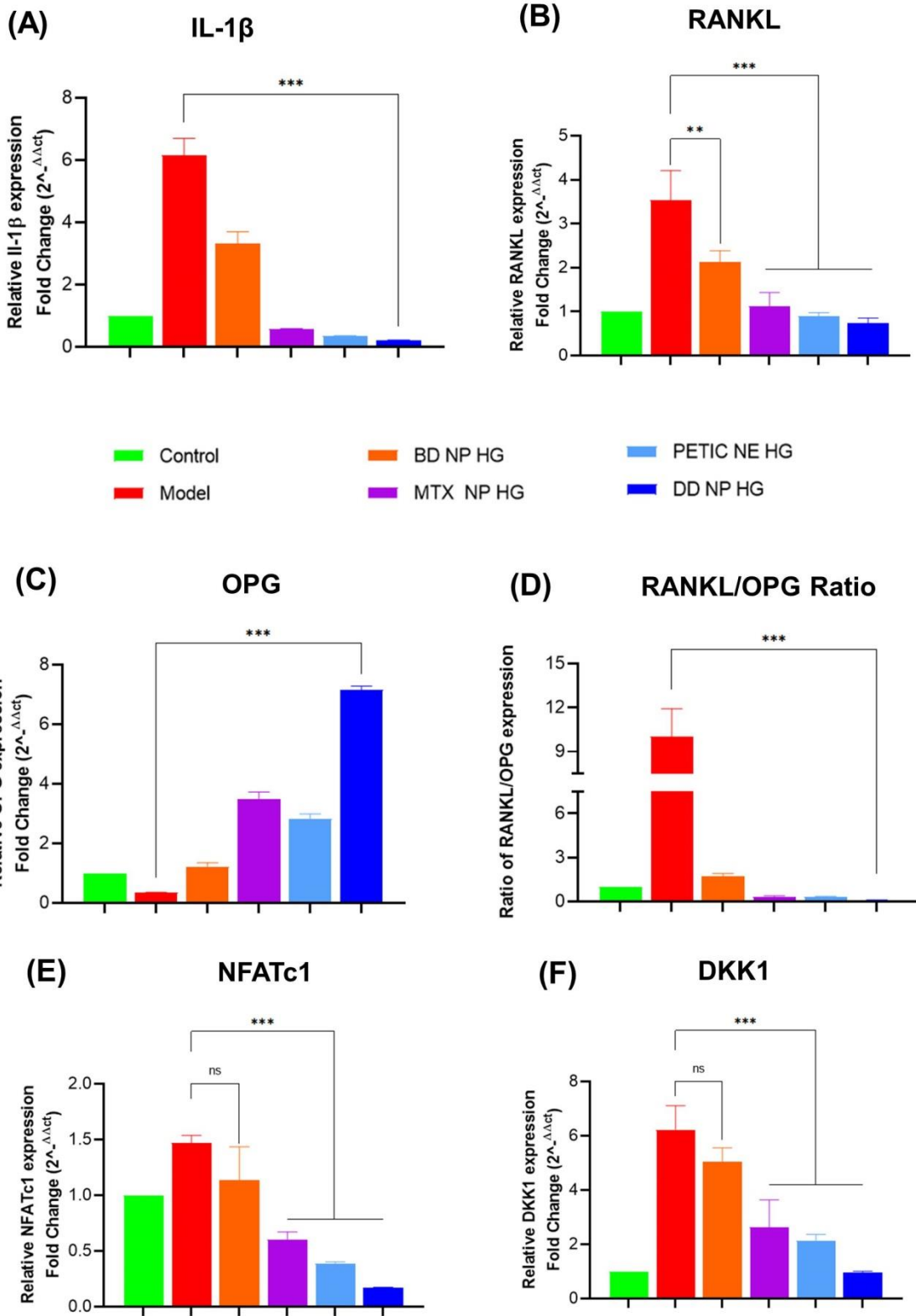


Figure 40. Effect of dual-drug nanoparticles loaded hydrogel against bone destruction in LPS-stimulated RA-FLS. The relative mRNA expression of (A). An inflammatory marker is IL-1 β (B). Osteoclast marker as RANKL, (C). Osteoblast marker as OPG, (D). RANKL/OPG ratio, (E). NFATc1, (F). DKK1. The data are represented as mean \pm SEM (n = 4). The values were statistically examined using a one-way ANOVA test. Statistical significance: *p < 0.05, **p < 0.01, ***p < 0.001, and ns- non-significant. IL-1 β : Interleukin 1 beta, RANKL: Receptor activator of nuclear factor-kappa-B ligand, OPG : Osteoprotegerin, NFATC1 : nuclear factor of activated T cells 1, DKK1 : Dickkopf WNT signaling pathway inhibitor 1, LPS :Lipopolysaccharides

A considerably lower relative ratio of RANKL/OPG is observed in the DD NP HG group compared to the other treatment groups (**Figure 40D**). Thus, the observed mRNA expression and their ratio of RANKL and OPG suggest that osteoclastogenesis is negatively regulated, and osteoblastic activity is promoted by OPG in RA FLS.

Osteoclastogenic master cytokine, RANKL mediates canonical and non-canonical NF- κ B pathways, which further induces positive regulators such as c-Fos and nuclear factor of activated T cells c1 (NFATc1) to drive osteoclast differentiation. Previously, the RANKL-RANK pathway induced NFATc1 expression in bone marrow macrophage and RA synovial cells (Asagiri et al., 2005; Takayanagi et al., 2002; Zhao et al., 2021). As shown in **Figure 40E**, Upon DD-NP HG treatment, the mRNA expression of NFATc1 was significantly downregulated by **~1.5 fold**, compared with the *model* group.

Moreover, Dickkopf-related protein 1 (DKK1), a regulatory molecule of the Wnt pathway, plays a vital role in bone resorption and remodeling (Juarez et al., 2016). Previous

findings suggest that IL-1 β upregulates DKK1 and sclerostin (SOST), which may downregulate the osteoblasts (Redlich and Smolen, 2012). Pro-inflammatory mediators like IL-15 and DKK 1 are produced by FLS, leading to the promotion of joint inflammation and destruction in RA (McHugh, 2020). As shown in **Figure 40F**, the mRNA expression of DKK1 in the DD NP HG treated group exhibited a **~5-fold** downregulation compared to the model group. In contrast, the treatment with MTX NP HG and PEITC NE HG groups showed a significant **~3.5 fold** and **~4 fold** change difference in mRNA expression compared with the model group (**Figure 40F**). These findings ultimately confirmed that the nanoparticulate form of MTX and PEITC, when used as a dual-drug combination (DD NP HG), significantly inhibited osteoclastogenesis and promoted bone remodeling.

3.10. Anti-arthritic effects of the dual-drug nanoparticles loaded hydrogel

3.10.1. Effects of dual-drug nanoparticles loaded hydrogel on arthritis parameters in FCA-induced arthritic rats

The therapeutic efficacy of combinational nanocomposite hydrogel was investigated in a chronic rat model of RA immunized by Freund's Complete Adjuvant (FCA). After FCA immunization, the rats were randomly assigned into various experimental groups on day 12 and continued till day 33 as the end study point (**see Figure 41A**).

The changes in paw volume and thickness were the initial parameters observed to measure inflammation and swelling in AIA rats and the treated groups. Following FCA immunization, on day 12, the different AIA groups of rats received an IA injection of either PBS, Free PEITC + Free MTX, PEITC NE HG, MTX NP HG, BD NP HG, and DD NP HG at an

interval of every four days for up to 27 days where changes in the arthritis score and swelling of the entire paw were observed and recorded (**Figure 41B-C**). Paw volume and paw thickness in the inflamed paws gradually increased in the PBS-treated rat as the disease progressed, while this progression was slower in the animals treated with the PEITC NE HG, MTX NP HG, and DD NP HG. Compared to the PBS-treated group, the PEITC NE HG and the MTX NP HG alleviated the symptoms of arthritis in rats. However, Free PEITC + Free MTX and blank HG loaded with blank NP failed to inhibit the disease progression, as there was no effect on the inflamed paw volume and thickness of the paws in these groups. The treatment with DD NP HG improved the arthritis symptoms (i.e., paw volume and paw thickness) to a greater extent among the groups (**Figure 41B-C**).

Hind paws of RA rats were scored for signs of arthritis (i.e., arthritis score) to monitor the disease severity and assess the prepared formulation's effectiveness in treating RA. A modest amount of erythema and swelling was evident in the current AIA rat model on the 5th day following FCA injection. On the 12th day post-FCA injection, considerable swelling and erythema appeared in the injected hind paws, indicating the full onset of RA. The AIA-rats were then administered with different formulations every four days, initiated on day 12 and ending on day 27. As depicted in **Figure 41D**, after treatment, groups treated with PEITC NE HG, MTX NP HG, or DD NP HG exhibited a reduction in the arthritis scores. At the endpoint, i.e., the 33rd day, the Free PEITC + Free MTX and BD NP HG treated groups showed a cumulative arthritis score of 3.50 ± 0.58 and 3.25 ± 0.50 and the arthritic control group with an arthritis score of 3.75 ± 0.50 . The rat treated with DD NP HG showed a marked reduction in arthritis score (1.25 ± 0.50) than the Free PEITC + Free MTX and BD NP HG treated group and the arthritic control

group. PEITC NE HG and MTX NP HG treated animals had arthritis scores of 1.75 ± 0.50 and 1.50 ± 0.58 , respectively.

In arthritic rat models, reduction in body weight is an essential parameter to measure inflammation. Changes in the body weights were monitored for up to 32 days to measure FCA-induced inflammation and the effectiveness of treatment groups, as presented in **Figure 41E**. Here, the normal healthy control group showed an increased body weight than the arthritic control group. The body weight loss in FCA-induced rats might be attributed to restricted mobility, decreased intestinal absorption, and inflammatory response. After 32 days, compared to the arthritic control group, the DD NP HG treated group showed improvement and significantly gained body weight. These findings imply that DD NP HG has effectively decreased arthritic-induced inflammation.

Assessing the ratio of primary immune organs (such as the spleen and thymus) is a vital indicator in relating an autoimmune condition (like RA) with its disease progression (Wang et al., 2019). As a result, alterations in the spleen and thymus indexes were assessed across all study groups. **Figure 41F (i-ii)** shows that the arthritic control group had a higher spleen and thymus index than the normal healthy control group. The spleen and thymus index in the treatment groups, PEITC NE HG, MTX NP HG, or DD NP HG, decreased significantly compared to the arthritic control group.

Comparing the animals treated with Free PEITC + Free MTX and DD NP HG to the arthritic control group, no discernible differences were seen in the spleen and thymus indexes. Compared to other treatment groups, the group receiving DD NP HG treatment showed the most significant improvement in the spleen index.

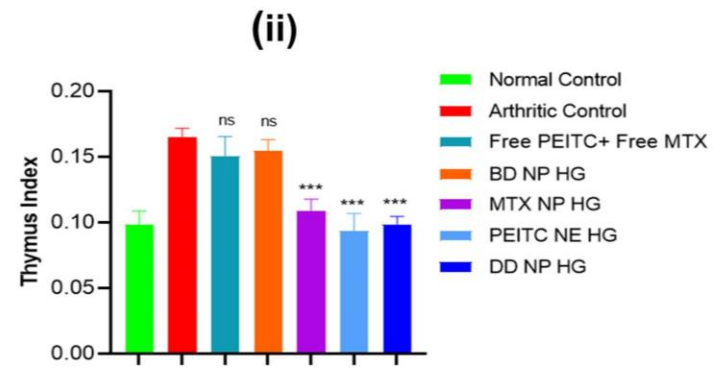
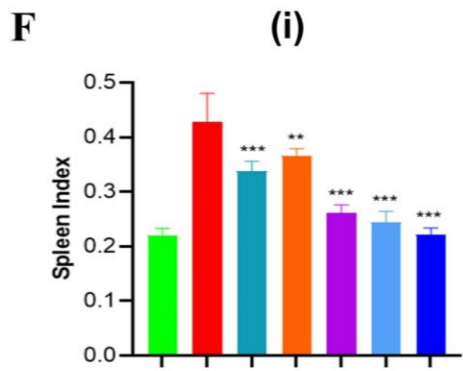
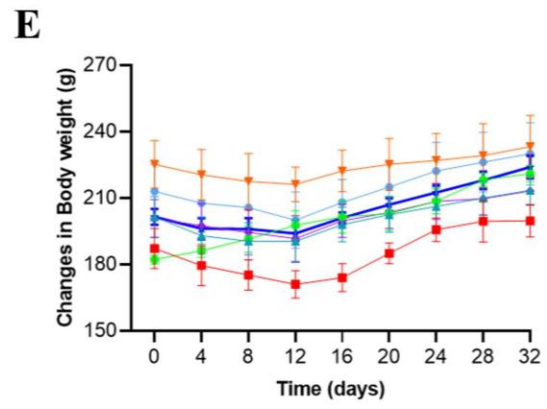
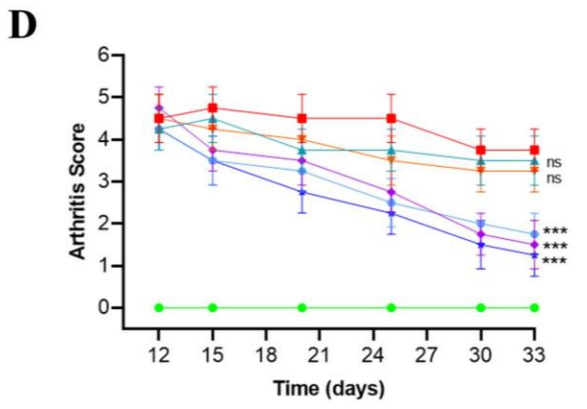
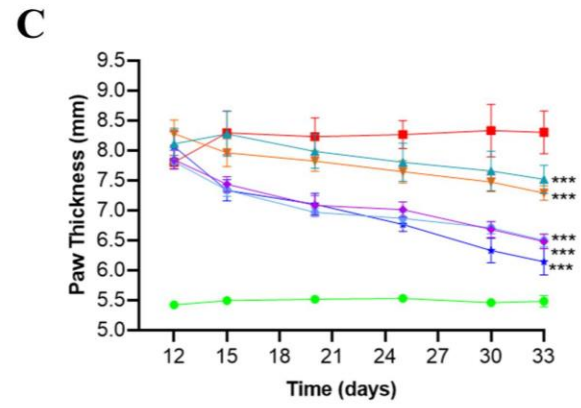
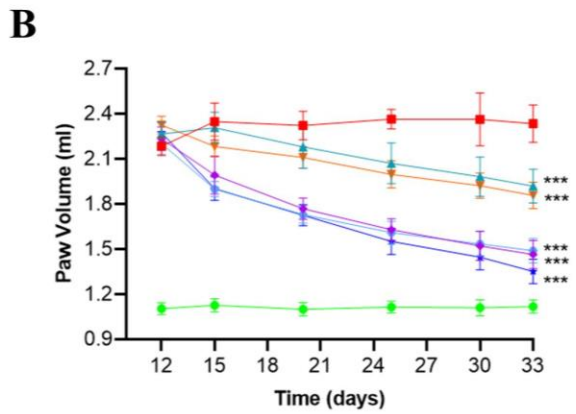
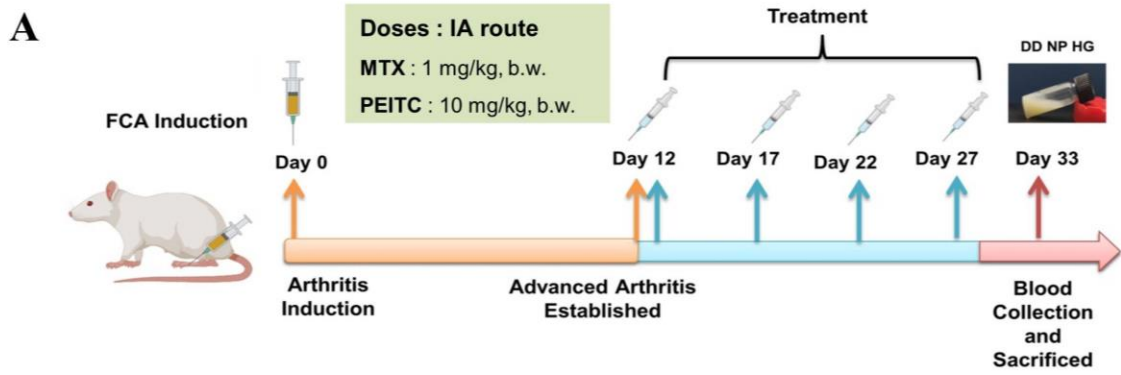


Figure 41. *In vivo* anti-arthritic effect of the dual-drug nanoparticles loaded hydrogel in FCA-induced RA rats. (A). Timeline for the dual-drug nanoparticles loaded hydrogel treatment in RA model rat (FCA-induced) with different treatment groups. (B). Changes in paw volume over time in the different treatment groups. (C). Changes in paw thickness over time in the different treatment groups (D). Arthritis scores for RA in rats on following treatment with different formulations. According to the standard scoring method, the average arthritis score was assessed by blind testing (scale of 0-4). (E). Changes in body weight in the FCA-immunized rats after 32 days of treatment. (F). The index of (i) spleen and (ii) thymus on day 33 in different treatment groups of FCA-immunized rats. The index of the thymus and spleen were expressed as the ratio (mg/g) of thymus and spleen wet weight versus body weight, respectively. The data are represented as mean \pm SD (n = 4). The values were statistically examined using a one-way ANOVA test. Statistical significance: *p < 0.05, **p < 0.01, ***p < 0.001, and ns- non-significant. FCA: Freund's complete adjuvant.

The trend observed comparing the elevated paw volume and cumulative arthritis scores in arthritic rats demonstrates that the DD NP HG group helps to improve arthritis disease conditions more effectively than the PEITC NE HG and MTX NP HG groups, suggesting that the combined therapeutic effect of the two drugs in their nanoparticulate form was more effective than the therapeutic effect of the individual nano form of the drug itself.

3.10.2. Effect of dual-drug nanoparticles loaded hydrogel on oxidative stress biomarkers in FCA-induced arthritic rats

The pathogenesis of RA is greatly influenced by oxidative stress. Reactive oxygen species (ROS), such as NO, H₂O₂, O₂, and HOCl, are produced due to various infiltrating

activated immune cells. Different detoxifying enzymes, such as GSH, naturally shield the tissues from harmful ROS (Wruck et al., 2011). However, as RA progresses, these protective mechanisms gradually become reactive due to increased ROS production, which results in the peroxidation of lipids (formation of MDA), which worsens the inflamed joint tissues and exacerbates the disease (Zimmerman et al., 2017). Simultaneously, neutrophil granule proteins, such as myeloperoxidase (MPO), are also detected in high amounts in the synovial fluid of the RA, which are responsible for joint destruction (Li et al., 2019).

MDA levels were also detected in the serum as an indicator of lipid peroxidation following 33 days of FCA induction (Qindeel et al., 2020). A noticeable increment in the serum MDA levels was observed in rats subjected to AIA compared to normal healthy control groups. **Figure 42A** demonstrates that the arthritic control group displayed a **2.42-fold** increased MDA level than the normal healthy control group. Following treatment with PEITC NE HG, MTX NP HG, and DD NP HG, a substantial decrease in MDA level was noted. However, the levels of MDA formation were decreased by **1.93** and **1.77-fold**, respectively, by PEITC NE HG and MTX NP HG, and this formation was further reduced by **2.20-fold** in the group treated with DD NP HG. Compared to the arthritic control group, the levels of MDA in the Free PEITC + Free MTX and DD NP HG groups decreased by **1.15-fold** and **1.25-fold**, respectively (**Figure 42A**).

The number of total nitrites, which indicates nitrosative stress, increases in many inflammatory disease situations, such as RA (Abdel Jaleel et al., 2021). Serum NO levels were assessed in the seven treatment groups at the study endpoint. As demonstrated in **Figure 42B**, the arthritic control group (immunized with FCA) had a **2.29-fold** greater NO level in the serum compared to the healthy control group. In contrast, the other treatment groups (PEITC NE HG, MTX NP HG, and DD NP HG) had a considerably lower NO increment.

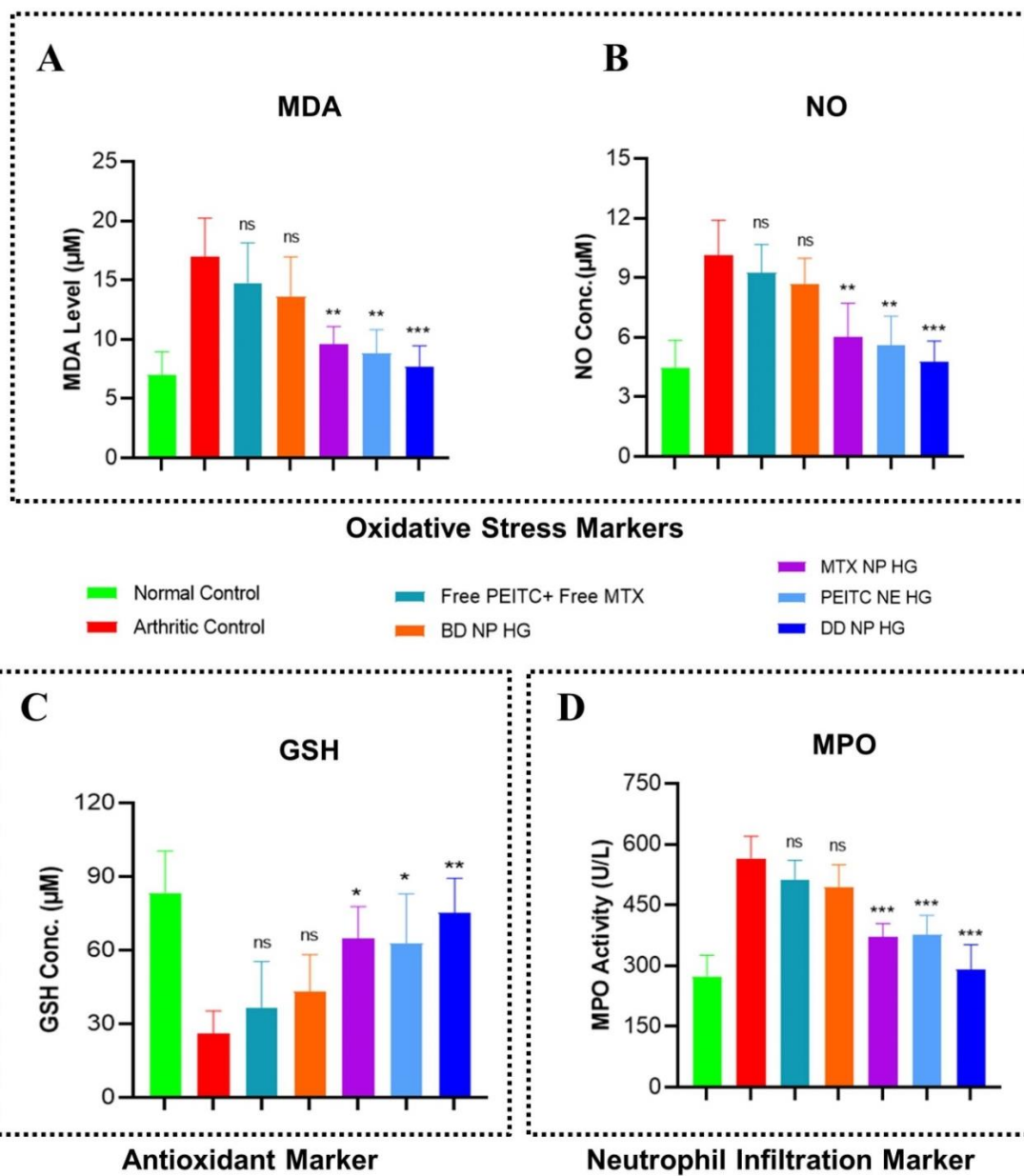


Figure 42. Evaluation of oxidative stress, antioxidant, and neutrophil infiltration markers in FCA-induced RA rats. Effect of dual-drug nanoparticles loaded hydrogel on serum concentration of (A). MDA (B). NO (C). GSH and (D). MPO. On day 33, the serum of the different treatment groups was collected and quantified. The data are represented as mean \pm SD (n = 4). The values were statistically examined using a one-way ANOVA test. Statistical

significance: *p < 0.05, **p < 0.01, ***p < 0.001 and ns-non significant. MDA: Malondialdehyde, NO: Nitric oxide, GSH: Reduced glutathione, and MPO: Myeloperoxidase.

The PEITC NE HG and MTX NP HG treatments significantly reduced the NO level to **1.81-fold** and **1.69-fold** compared to the arthritic control group. The DD NP HG treated group markedly showed a lower NO level up to **2.12-fold** compared to the arthritic control group and displayed the highest degree of defense against oxidation (**Figure 42B**).

Glutathione (GSH, a tripeptide antioxidant enzyme) content in the serum is a valuable indicator for estimating the degree of oxidative stress (Qindeel et al., 2020). Compared to normal control rats, the serum GSH in arthritic control rats was markedly reduced by **3.2-fold** (**Figure 42C**). Treatment with PEITC NE HG and MTX NP HG demonstrated a considerable rise in serum GSH levels to **2.40-fold** and **2.50-fold**, respectively, compared to the arthritic control rats. The DD NP HG treated rat markedly improved the level of oxidative stress across all treatment groups, with a significant increase in serum GSH up to **2.89-fold** (**Figure 42C**).

MPO is a known marker for neutrophil infiltration and plays a significant role in the pathophysiology of RA (Aborehab et al., 2017; Li et al., 2019). Compared to the normal healthy control group, the mean serum level of MPO was considerably higher in the arthritic control group (**2.06-fold**). The PEITC NE HG (**1.50-fold**) and MTX NP HG (**1.53-fold**) treatment groups had significantly lower mean serum levels of MPO than the arthritic control group. The highest decline in the mean serum level of MPO was observed in the DD NP HG (**1.94-fold**) (**Figure 42D**).

According to the results obtained from all the above biochemical parameters, PEITC NE HG and MTX NP HG dramatically reduced oxidative enzymes while improving the level of

protective enzymes compared to Free PEITC + Free MTX and BD NP HG. However, DD NP HG enhances the status of oxidative and protective enzymes to a greater extent than the other treatment groups. The localized and site-specific delivery of MTX and PEITC in the nanoparticulate form in inflamed joints may be the basis of DD NP HG's superior efficacy than Free PEITC and Free MTX.

3.10.3. Effect of dual-drug nanoparticles loaded hydrogel on serum cytokines level in FCA-induced arthritic rats

The underlying etiology of RA is yet unknown. The primary goal of any new treatment approach is to obtain immunological homeostasis in the joint by balancing inflammation and halting the progression of the disease, which has tremendous therapeutic potential. Cytokines and chemokine play essential roles in the advancement and development of RA, whereas suppressing the expression or function of cytokines and chemokine increases the probability of remission of RA and protects bones and cartilage from destruction (Gravallese, 2002; Ren et al., 2021).

In AIA rats, the expression of both pro-inflammatory and anti-inflammatory cytokines was investigated in relation to the effects of various treatment groups by ELISA. Here, the serum levels of important pro-inflammatory cytokines, such as TNF- α , IL-6, IL-1 β , IL-17A, and IL-10, were determined in the different study groups. In PBS-treated arthritic rats, an increased level of IL-6, IL-1 β , IL-17A, and TNF- α with decreased IL-10 was observed as the disease progressed (**Figure 43A-D, 41F**). Compared to the arthritic control group, no substantial difference was observed, although Free PEITC + Free MTX and BD NP HG treatment slightly lowered the level of pro-inflammatory cytokines. Following administration of PEITC NE HG, MTX HG, and DD NP HG, the expression of pro-inflammatory cytokines was markedly reduced, while anti-

inflammatory cytokine levels were increased (**Figure 43A-D, 41F**). This showed that DD NP HG treatment significantly increased the anti-inflammatory cytokine (IL-10) while suppressing the pro-inflammatory cytokines (TNF- α , IL-6, IL-1 β , and IL-17A), demonstrating its therapeutic impact was far superior to that of PEITC NE HG or MTX NP HG alone (**Figure 43A-D, 41F**).

The RANKL/OPG system plays a pivotal role in joint destruction in RA by regulating the differentiation and function of osteoclasts (Pettit et al., 2006). To elucidate the mechanisms responsible for the joint-protective action, the serum level RANKL was measured to signify the grade of osteoclastogenesis (Stolina et al., 2009). As depicted in **Figure 43E**, the serum levels of RANKL in AIA model rats (arthritic control) were significantly up-regulated than the healthy control group.

Treatments with PEITC NE HG, MTX NP HG, and DD NP HG markedly down-regulated the serum concentration of RANKL. Moreover, RANKL levels in the DD NP HG rats showed the highest decline among the other treatment groups, following the trend of the healthy control group. However, the aforementioned results indicated that DD NP HG could considerably improve the production of cytokines (pro-inflammatory anti-inflammatory) and bone erosion markers; hence, DD NP HG had the most significant therapeutic impact on preventing the onset of RA.

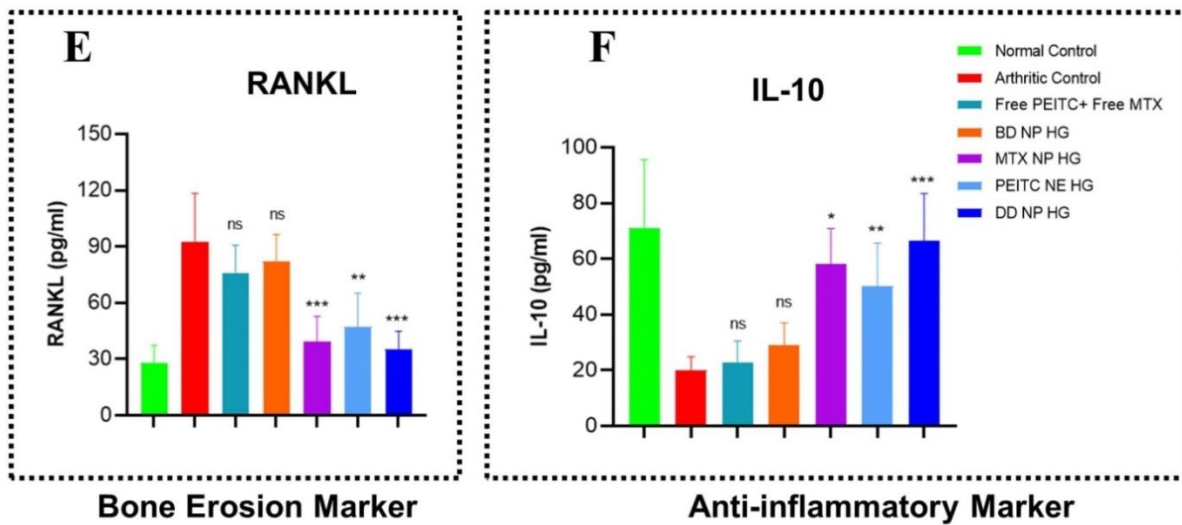
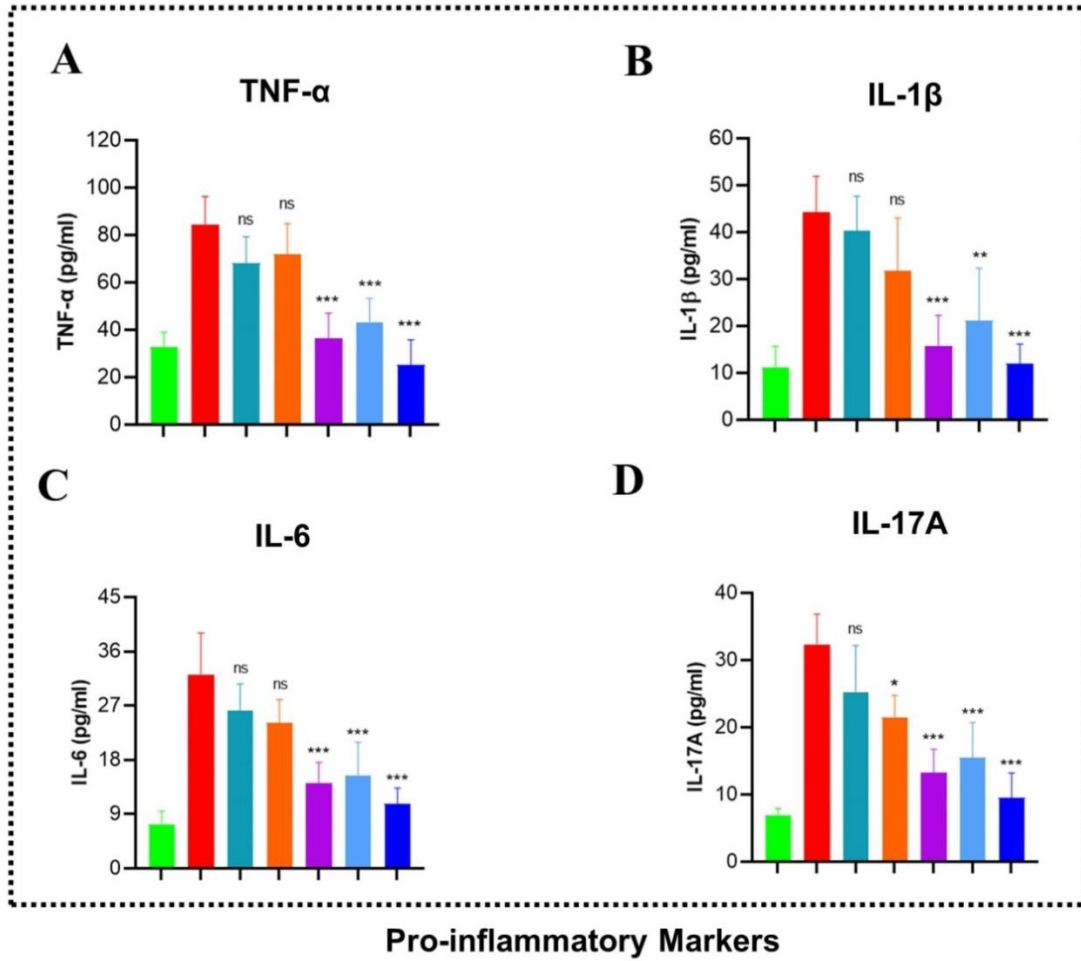


Figure 43. Estimation of pro-inflammatory, anti-inflammatory, and bone erosion markers

in FCA-induced RA rats. Effect of dual-drug nanoparticles loaded hydrogel on serum pro-inflammatory cytokine levels (A). TNF- α , (B). IL-1 β , (C). IL-6 and (D). IL-17A. (E). RANKL (bone erosion marker) (F). IL-10 (anti-inflammatory cytokine). The serum cytokine level in the rat (on day 33) was estimated by ELISA. The data are represented as mean \pm SD (n = 4). The values were statistically examined using a one-way ANOVA test. Statistical significance: *p < 0.05, **p < 0.01, ***p < 0.001, and ns- non-significant. TNF- α : Tumor Necrosis Factor-alpha, IL-1 β : Interleukin 1 beta, IL-6: Interleukin 6, IL-17A: Interleukin 17A, RANKL: Receptor activator of nuclear factor-kappa-B ligand and IL-10: Interleukin-10, ELISA: Enzyme-linked immunoassay.

3.10.4. Toxicity assessment of dual-drug nanoparticles loaded hydrogel in the FCA-induced arthritic rats

The impact of various treatment groups on liver and kidney functions was evaluated to assess the biocompatibility of nanocarriers for their utilization in biological and medical applications (Yin et al., 2020a). As seen in **Figure 44A–D**, arthritic control rats showed a substantial rise in the liver (ALT and AST) and kidney (CRE and BUN) enzyme levels compared to healthy control rats; however, these levels remained within normal ranges. Previously, it was reported that MTX caused liver and kidney function toxicity. Considering the side effects of MTX, I analyzed the impact of MTX-loaded hydrogel treatment groups, i.e., MTX NP HG and DD NP HG, on liver and kidney function. In addition, the blood biochemical analysis demonstrated that the ALT, AST, BUN, and CRE in the groups (MTX NP HG and DD NP HG) were within normal ranges. Hence, these hydrogels were effective and safe for *in vivo* RA therapy as they did not affect the liver and kidney functions.

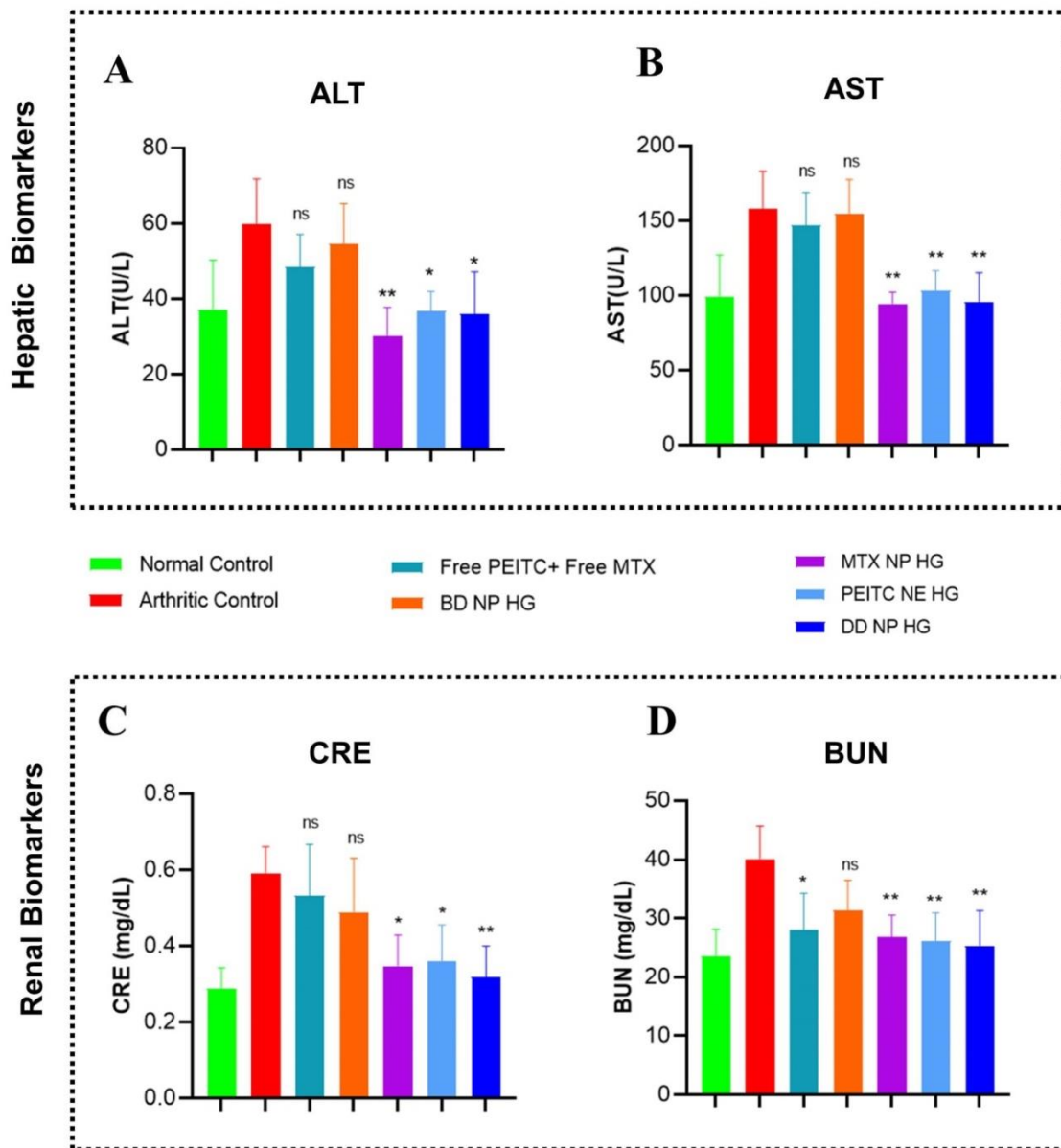


Figure 44. Toxicity assessment in FCA-induced RA rats. Effects of dual-drug nanoparticles loaded hydrogel on hepatic and renal function. (A and B) hepatic biomarkers (ALT and AST) and (C and D) renal biomarkers (CRE and BUN). The data are presented as mean \pm SD (n = 4). The values were statistically examined using a one-way ANOVA test. Statistical significance: *p < 0.05, **p < 0.01, ***p < 0.001, and ns- non-significant. ALT: Alanine transaminase, AST: Aspartate transaminase, CRE: Creatinine, BUN: Blood urea nitrogen (BUN).

By examining the serum biochemical profiles of the other hydrogel treatment groups, BD NP HG and PEITC NE HG, it was determined that all biochemical parameters (ALT, AST, BUN, and CRE) were within the normal ranges, indicating that none of the hydrogel formulations appeared to have a substantially detrimental effect on kidney or liver function (**Figure 44A-D**). These outcomes demonstrated the safety and biocompatibility of the constructed hydrogel-based carrier system *in vivo*.

3.10.5. Histological analysis of dual-drug nanoparticles loaded hydrogel in the FCA-induced arthritic rats

RA is the most prevalent form of autoimmune arthritis, characterized by persistent synovitis, cartilage degradation, and bone destruction (Catrina et al., 2016). FCA-induced adjuvant arthritis (AIA) in the rat is a polyarthritis experimental model extensively utilized for preclinical testing of various anti-arthritic drugs that are either being investigated in preclinical or clinical research or are currently being used as treatments in this disease condition (Pearson, 1956). Furthermore, AIA is a type of T-cell-mediated autoimmune arthritis extensively researched for the immunological aspects of RA and other inflammatory or arthritic disorders in humans (van Eden et al., 1996). The local injection of adjuvant (*Mycobacterium tuberculosis* suspended in mineral oil) into rats produces an immune response that typically entails inflammatory degradation of cartilage and bone in the distal joints with concurrent swelling of surrounding tissues.

The animals from the various treatment groups were sacrificed at the end of the study period (i.e., the 33rd day) using CO₂ asphyxia to verify the therapeutic effectiveness of DD NP HG treatment in FCA-induced arthritic rats. The ankle joints were carefully dissected for gross

and histological analysis. The histological assessment of ankle joints was performed with H&E, SO-FG, and Toluidine blue (T&B) staining to compare synovial inflammation, cartilage destruction, and bone erosion in all groups microscopically.

Healthy normal control showed no apparent signs of inflammation, bone erosion, or cartilage destruction. Their morphologies clearly distinguished the interface between cartilage and bone in healthy rats (**Figure 45B**). The arthritic control group had more pronounced severe infiltration of inflammatory cells (red arrows), bone erosion, and cartilage damage (black arrows), which characteristics features of RA (**as seen from H&E are staining in Figure 45B**) (Zhang et al., 2018). The stained microsections of the ankle joint from the groups treated with the Free MTX + Free PEITC and BD NP HG groups confirmed an intermediary disease state with abundant infiltration of inflammatory cells with considerable bone erosion and cartilage degradation. Treatment with MTX NP HG and PEITC NE HG showed minimal bone erosion and cartilage destruction with nominal cell infiltration in the joint. In addition, the ankle joint sections from DD NP HG-treated rats showed a relatively healthy articular surface with minimal inflammatory cell infiltration. The DD NP HG showed minimal histological alterations compared to other AIA treatment groups and was quite similar to healthy normal control rats without AIA (**Figure 45B**).

SO-FG is a standard staining method to detect the amount and distribution of proteoglycans in cartilage tissues (Jang et al., 2020). Safranin O (SO) works by forming a reddish-orange complex when it binds to acidic proteoglycans in the cartilage tissues, such as chondroitin sulfate or keratan sulfate, with a high affinity. A matrix proteoglycan depletion assessment is made possible by the degree of the color of SO, which represents proteoglycan content indirectly (Yin et al., 2020a). The joint sections of the PBS-treated rat (arthritic control),

Free MTX + Free PEITC, and BD NP HG showed significant proteoglycan loss (the red color almost vanished), indicating severe damage and considerable loss of cartilage and bone (**Figure 45C**). As shown in **Figure 45C**, minimal cartilage destruction in the rat treated with MTX NP HG and PEITC NE HG, evident from the red color's intensity, increased to a different extent. However, the rat treated with DD NP HG had minimal cartilage loss with the highest intensity of red color, quite similar to the healthy normal control without AIA induction (**Figure 45C**).

Another popular method for histologically evaluating differentiated cartilaginous and chondrogenic tissues is T&B staining. T&B is a cationic dye that visualizes proteoglycans in tissue because its high affinity for the sulfate groups in proteoglycans results in blue color (Bergholt et al., 2019). T&B staining showed a significant proteoglycan loss in the arthritic control group, indicating that articular cartilage was severely degraded and damaged (**Figure 45D**). While in the DD NP HG group, the blue color positive areas of T&B staining were more prominent compared to Free MTX + Free PEITC and BD NP HG, demonstrating that cartilage injury was effectively reversed, and it could effectively alleviate synovitis and cartilage damage in AIA rats (**Figure 45D**). The outcomes from the histopathological studies supported the therapeutic potential of combinational nanocomposite hydrogel (DD NP HG) in reducing inflammation and slowing the onset of RA disease.

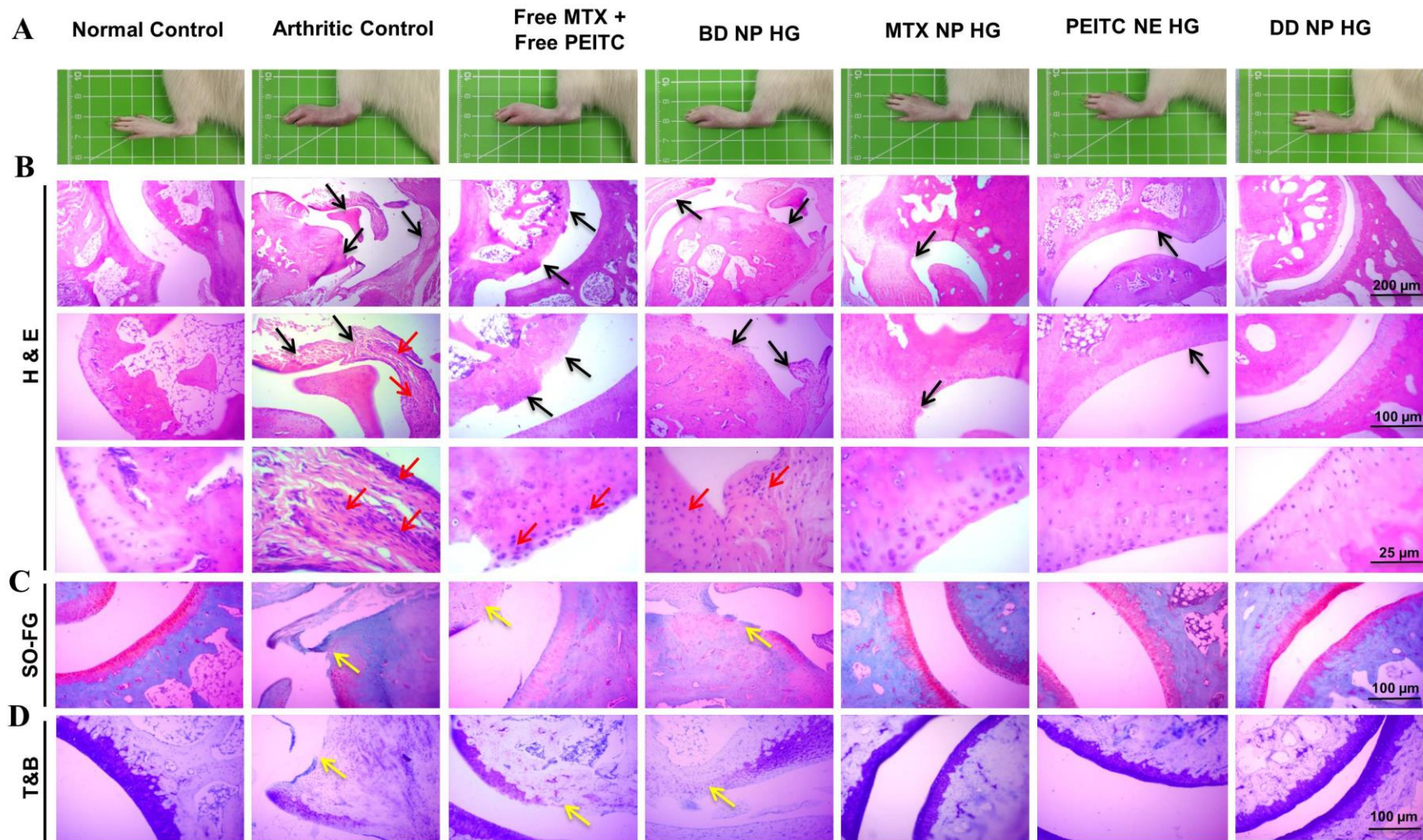


Figure 45. Histopathological assessment of dual-drug nanoparticles loaded hydrogel in bone destruction and cartilage damage in RA model. (A). *In vivo* paw images of the rats from different groups at the endpoint, i.e., 33rd day. Histological sections with (B). H&E, (C). SO-FG and (D). T&B staining of ankle joints in different treatment groups. The red arrow is inflammatory cellular infiltration, and the black arrow is bone erosion and cartilage degradation. Yellow arrows indicate loss of proteoglycan. Scale bar = 200 μm , 100 μm and 25 μm . H&E: Hematoxylin and eosin; SO-FG: Safranin O-fast green; T&B: Toluidine blue.

3.11. Summary of the chapter

In this chapter, a dual-nanoparticulate hydrogel formulation of MTX and PEITC (DD NP HG) was successfully prepared and verified for the therapeutic potential of co-delivering of MTX, a slow-acting anti-rheumatic drug, and PEITC, a bioactive phytochemical with potent anti-inflammatory activity, to inflamed joints for synergistic treatment of treating RA. While both medications are used for treating RA or inflammatory conditions, the expected therapeutic efficacy was never achieved. The *in vitro* data demonstrated that both drugs, in their nanoparticulate form, have the necessary features, such as better mechanical strength, thermosensitivity, injectability, and good biosafety, for prolonged release of MTX and PEITC from the target site, when synthesized as an injectable hydrogel using pluronic and alginate. The cell-based studies showed that DD NP HG had a high biosafety level for healthy FLS cells. On the other hand, DD NP HG treatment could significantly reduce the viability and increase the induction of cell apoptosis in RA-FLS cells. The underlying molecular mechanism study demonstrated that the inhibition of pro-inflammatory cytokines (TNF- α , IL-17A, and IL-6) and improvement in the gene expression of bone destruction (IL-1 β , RANKL, OPG, NFATc1, and DKK1) are potential therapeutic targets of DD NP HG in LPS-stimulated RA-FLS.

From the studies conducted on FCA-induced RA in rats, I could demonstrate that the DD NP HG treatment enhanced the efficacy of combination therapy where the inflammatory response was significantly inhibited, reducing chronic inflammation effectively and delaying bone erosion. In conclusion, the result demonstrates that the anti-RA treatment accelerated by the intra-articular injection of DD NP HG can maximize the therapeutic effects and reduce the dose-related side effects of both drugs' free form (MTX and PEITC). The possible mechanism can be postulated that the sustained release of nanoparticulate forms of MTX and PEITC from the smart

hydrogel resulted in pronounced anti-inflammation over time, eventually leading to amelioration from the RA state.

Essien et al. 2023 recently reported PAMAM dendrimers as a nanocarrier for the co-delivery of SFN and MTX for treating RA. The optimized dual-drug nanoparticle formulation showed potential anti-inflammatory effects against LPS-stimulated murine macrophages while biocompatible with healthy murine macrophages *in vitro*. Further, *in vivo* studies on RA-induced animal models improve arthritis symptoms by a decrease in the arthritic scoring and reduction in knee diameter and exert anti-inflammatory effects by enhancing the serum cytokine levels (Essien et al., 2023).

In another study, *Yin et al., 2020b* developed a temperature-sensitive hydrogel (D-NGel) containing nanoparticles (D-NPs), simultaneously delivering indomethacin (IND) and MTX for the treatment of RA. The hydrogel represents a fluid state at room temperature. *In vivo*, release studies revealed that when the hydrogel is injected into the articular cavity of CIA rats, it quickly changes from a fluid state to a gel *in situ* and releases the drugs continuously for a sustained period of up to 72 h. In conclusion, the D-NGel substantially reduced bone degradation, joint swelling, and inflammatory cytokine expression in joint fluid. This novel approach, which can deliver two kinds of drugs, inspires synergistic therapy (Yin et al., 2020b).

Both of the above studies supported our hypothesis that nanoparticulate forms of MTX and PEITC could be beneficial for treating RA while improving the clinical drawbacks. Integrating material science and nanotechnology was an innovative step in constructing a dual-drug delivery system (DD NP HG). Further, IA administration of DD NP HG significantly ameliorated the RA symptoms by reducing side effects in their free form. This combination approach will be a novel RA therapy in the future, which will exert a synergistic effect.

Chapter 4

Conclusion

4.1. Conclusion and future work

Many combinational therapies are available for arthritis, but the combination of MTX and PEITC still needs to be explored. Both drugs are reported to have good anti-arthritic effects in animal models; nevertheless, both have several limitations. To overcome these limitations, nanoparticle drug delivery may help improve the therapeutic activity. MTX is observed to be more toxic on higher doses, so low doses of MTX were preferred. Further low doses on more prolonged exposure showed drug resistance (decreased therapeutic efficacy). To counteract these challenges, PEITC combined with MTX may potentiate anti-arthritic activity. These prepared nanoparticles are loaded into a biocompatible hydrogel carrier to increase the residence time near the inflamed joints and help in localized therapy.

This thesis described the development of polymer systems for delivering hydrophobic drugs for treating joint diseases, such as RA and OA. By applying a nanotechnology approach, I formulated a smart nano-particulate co-delivery hydrogel system that was extensively assessed *in vitro* and *in vivo*. This approach immensely abrogated the pharmaceutical limitations of the loaded drugs (MTX and PEITC) when prepared as nanoparticles. Further loading these NPs into a hydrogel system enabled co-delivery, sustained release, injectability, and thermoresponsive behavior.

RA is a multifactorial systemic autoimmune disease with few treatment options. As a combinational drug delivery system, a hydrogel co-delivered the regimens that can alleviate the condition by acting *via* diverse mechanisms. A probable mechanism of combinational hydrogel in treating RA is shown in **Figure 46**. When injected into the FCA-induced animals, the DD NP HG showed marked amelioration of chronic inflammation and assisted in restoring bone morphology in RA rats.

Studies on healthy rats confirmed the biocompatibility and safety of the formulation at the injection site and when sustainedly released into the systemic circulation. Further, combinational hydrogel-based localized therapy has been shown to enhance the anti-inflammatory efficacy and reverse cartilage disruption through a synergistic effect between two nano-particulate forms of MTX and PEITC, which can effectively improve the drawbacks of free forms of both drugs. From the thesis work, I successfully optimized and fabricated a novel smart hydrogel-based delivery system for poorly soluble drugs to either deliver them singly or in combination to attain greater efficacy. Such nano-delivery systems have significant applications in diseases that require chronic or multi-drug treatment.

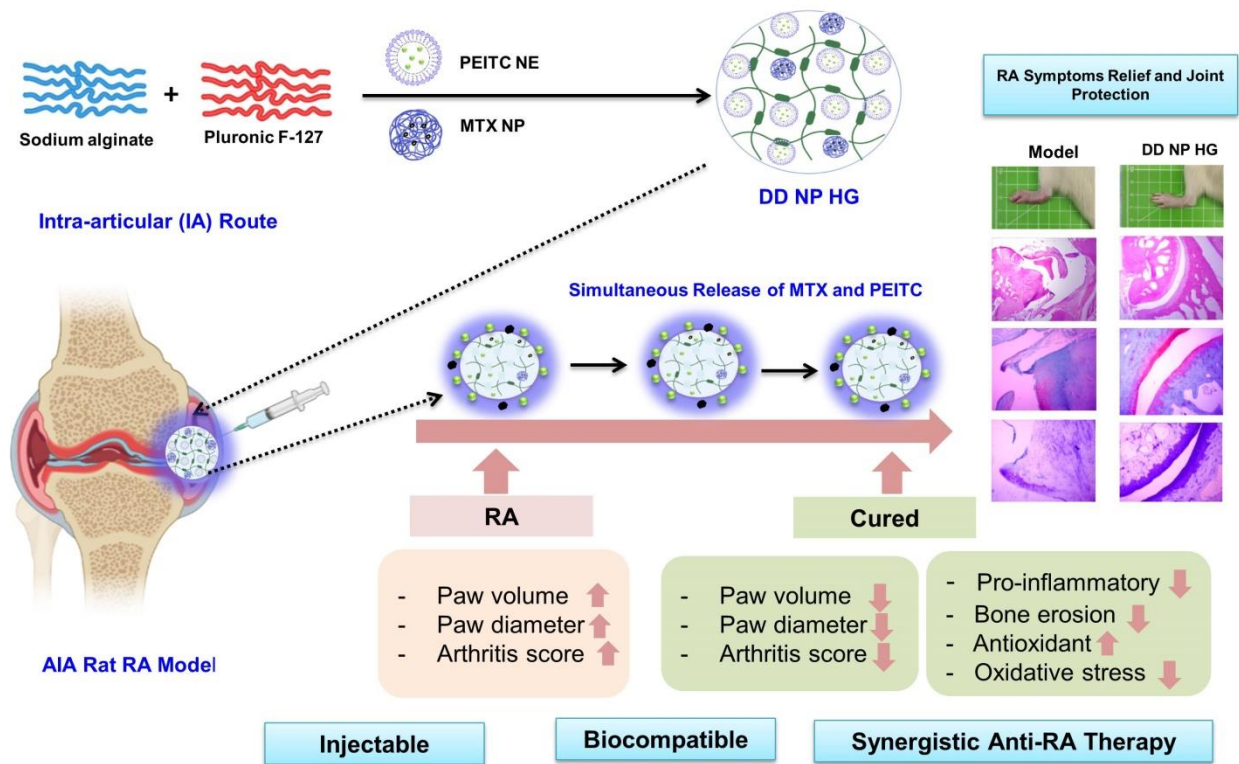


Figure 46. A probable mechanism of combinational hydrogel (DD NP HG) in treating RA.

Table 10: Comparison of anti-inflammatory and anti-rheumatic activity of different PEITC and MTX based formulation

Compound	Formulation	study types	Dose and Route	Duration	Outcomes	Remarks
PEITC	PEITC in CMC	<i>In vivo</i> : CFA-induced RA in the animal model	50 mg/kg, Orally	21 days (21 doses)	Anti-rheumatic activity	Daily dosing is required. Since Free PEITC had low bioavailability. (Choudhary et al., 2020)
MTX	MTX nano micelle-based hydrogel	<i>In vivo</i> : CFA-induced RA in the animal model	0.215 ug/kg, every two days up to 21 days, Transdermal	21 days (10 doses)	Anti-rheumatic activity	Continuous dosing was required to achieve a therapeutic effect <i>in vivo</i> . Cell-based targeted study, especially in RA-FLS and macrophages, was not reported. Combinational-based RA therapy will be more beneficial in this study. (Qindeel et al., 2020)
IND and MTX	IND and MTX nanoparticle-based hydrogel	<i>In vivo</i> : CIA-induced RA in an animal model	IND-0.4 mg/kg MTX -0.2 mg/kg Intra-articular	35 days (8 doses)	Anti-rheumatic activity	This study demonstrated a synergistic anti-RA therapy <i>in vivo</i> . However, the hydrogel was continuously administered to achieve the desired therapeutic effect <i>in vivo</i> . The cell-based targeted study was not studied, especially in RA-FLS and macrophages. (Yin et al., 2020)
PEITC and MTX (Our study)	PEITC and MTX nanoparticle-based hydrogel	<i>In vivo</i> : CFA-induced RA in the animal model <i>In vitro</i> : LPS-stimulated RA-FLS primary cell.	PEITC- 10 mg/kg MTX – 1 mg/kg Intra-articular PEITC – 100 µM MTX – 1.5 µM	33 days (4 doses) 24 h and 48 h	Anti-rheumatic Activity Anti-inflammatory activity	In our study, we tried to limit dosing numbers (4 doses). IA-based therapy was adopted to achieve the synergistic activity. (Haloi et al., 2023) The RA-FLS targeted approach was adopted and validated for the cellular interaction of MTX and PEITC <i>in vitro</i> RA-induced conditions.

Future work should include investigations on drug delivery that can broaden the scope of different low molecular weight hydrophobic phytochemicals with pharmaceutical limitations (low bioavailability, low aqueous solubility, and low stability).

A combination therapy strategy has a promising future for the synergistic treatment of RA and other metabolic bone degenerative conditions and is urgently needed. Future work should include extensive pre-clinical research on larger animals, i.e., monkeys, dogs, and horses, which will provide the applicability of this combinatory therapy in humans.

Although this research focuses on treating symptoms of RA, future work should include this combination therapy strategy that can restore synovial homeostasis in RA by targeting FLSs.

Chapter 5

Materials and methods

5.1. Materials

5.1.1. Chemicals and reagents used

Table 11. List of chemicals and reagents used

Chemicals and reagents used	Source
1,1,3,3-tetramethoxypropane	Sigma-Aldrich
2-thiobarbituric acid (TBA)	Sigma-Aldrich
5,5'-dithiobis(2-nitrobenzoic acid) (DTNB)	Sigma-Aldrich
Acetic acid glacial (ReagentPlus®, ≥ 99 %)	Sigma-Aldrich
Acetone (EMSURE ACS for analysis)	Merck
Acetonitrile (for HPLC)	Spectrochem
Acid alcohol	CDH
Antibiotic solution 100X Liquid	Himedia
Benzene-1, 2-dithiol (BDT, 96 %),	Sigma-Aldrich
Chitosan (degree of deacetylation > 75 %)	Sigma-Aldrich
Collagenase, Type IV	Sigma-Aldrich
D.P.X. Mountant (Liquid)	Himedia
Dialysis membrane -70	Himedia
Diluent for DNA extraction, molecular biology	Himedia
Dimethyl sulfoxide (DMSO for HPLC, ≥ 99.7)	Sigma-Aldrich
Disodium hydrogen phosphate	MP Biomedicals
D-Mannitol	Merck
Dulbecco's modified eagle medium (DMEM), High glucose	Himedia
EDTA disodium salt dihydrate, Hi-AR™	Himedia
Eosin, 2% w/v	Himedia
Ethanol absolute (EMSURE ACS for analysis)	Merck
Fast green FCF, Hi-Cert™	Himedia
Fetal bovine sera, sterile filtered, heat-inactivated, US	Himedia
Formaldehyde, ACS (37 %)	MP Biomedicals

Freund's complete adjuvant (FCA)	Sigma-Aldrich
Haematoxylin (Mayer)	Himedia
Hanks' balanced salt solution, HBSS, 1X, sterile	Himedia
Hematoxylin stain, Hi-Cert™	Himedia
Lipopolysaccharides (LPS)	Sigma-Aldrich
Methanol (EMSURE ACS for analysis)	Merck
Methotrexate (MTX)	MP Biomedicals
Methyl-thiazolyl diphenyl-tetrazolium bromide (MTT)	Himedia
Olive oil	Himedia
Phenethyl isothiocyanate (PEITC, 99 %)	Sigma-Aldrich
Phosphate buffered saline (PBS, pH 7.2)	Sigma-Aldrich
Picric acid (saturated, aqueous)	Himedia
Pluronic F-127 powder	Sigma-Aldrich
Poly lactic-co-glycolic acid (PLGA)	Sigma-Aldrich
Poly-L-lysine solution (0.1 % w/v in water)	Sigma-Aldrich
Polysorbate-80	Himedia
Potassium bromide (KBr, FTIR Grade, ≥ 99 %)	Sigma-Aldrich
Potassium chloride	Sigma-Aldrich
Potassium dihydrogen phosphate	MP Biomedicals
Reduced glutathione	MP Biomedicals
Safranine (Safranin O), Hi-Cert™	Himedia
Sodium acetate anhydrous (molecular biology grade)	Merck
Sodium alginate	Sigma-Aldrich
Sodium chloride	Sigma-Aldrich
Sodium hydroxide anhydrous	MP Biomedicals
Span-80	Himedia
Toluidine Blue O, Hi-Cert™	Himedia
Triton X-100 (for molecular biology)	SRL Laboratories
Trypsin -EDTA solution 1X	Himedia
Xylene, AR	Himedia

Xylene, for histopathology	Himedia
----------------------------	---------

5.1.2. Cell lines and primary cells

Table 12. List of cell lines and primary cells

Name	Source
N-FLS primary cell	NISER, Bhubaneswar, India
RA-FLS primary cell	NISER, Bhubaneswar, India

IAEC number: NISER-IAEC/SBS-AH-222

5.1.3. Kits

Table 13. List of kits

Kit Name	Source
Albumin kit	Meril Diagnostics
Alkaline phosphatase (ALP) kit	Meril Diagnostics
Cholesterol kit	Meril Diagnostics
Creatinine kit	Meril Diagnostics
FITC annexin V apoptosis detection kit I	BD Biosciences
Glucose kit	Meril Diagnostics
Myeloperoxidase (MPO) activity assay kit	Elabscience
Nitrite/Nitrate assay kit	Sigma -Aldrich,
Rat IL-10 ELISA kit	Elabscience
Rat IL-17 ELISA kit	Elabscience
Rat IL-1 β ELISA kit	Elabscience
Rat IL-6 ELISA kit	Elabscience
Rat RAN κ L ELISA kit	Elabscience
SGOT kit	Meril Diagnostics
SGPT kit	Meril Diagnostics
TNF- α rat ELISA kit	Invitrogen, Thermo Scientific
Total protein (TP) kit	Meril Diagnostics

Urea kit	Meril Diagnostics
----------	-------------------

5.1.4. Monoclonal antibodies

Table 14. List of monoclonal antibodies

Antibody	Host	Source	Application
FITC mouse anti-rat CD90	Mouse	BD Pharmingen	Flow cytometry
PE mouse anti-rat CD106	Mouse	BD Pharmingen	Flow cytometry

5.1.5. Animals

Healthy SD rats (180-240 g b.w., both sexes) were used for all the *in vivo* experiments in this thesis. The animals were housed in pathogen-free controlled climatic conditions with artificial lighting (12:12 h of light: dark cycle). The rats were individually kept and acclimatized for seven days before the experiment. Clean drinking water and a commercially available standard pellet diet were provided *ad libitum*. All animal experiments complied with ARRIVE guidelines and were performed per the National Institutes of Health (NIH) guide for the care and use of Laboratory animals (NIH Publications No. 8023, revised 1978). The experimental protocols were performed by CPCSEA regulations (Registration No. 1634/GO/ReBi/S/12/CPCSEA, DoR- 29.03.2012). They were approved by the Institutional Animal Ethics Committee (IAEC) at the National Institute of Science Education and Research (NISER), Bhubaneswar, Odisha, India (Ethical Approval No: NISER/SBS/AH-148 and NISER/SBS/AH-222).

5.2. Methods

The methods are mainly divided into two parts

1. Part A- Methods related to Chapter 2

2. Part B - Methods related to Chapter 3

Part A

5.2.1. Preparation and characterization of PEITC-loaded hydrogels

5.2.1.1. Preparation of the PF-127/ CS hydrogel

The PF-127/CS hydrogel was prepared by physical mixing cold method in an aqueous acid solution following a procedure well-described to prepare pluronic-based hydrogels (Jung et al., 2017; Pelegrino et al., 2018; Zhang et al., 2018). Briefly, CS (1 % w/v) was completely dissolved in 0.01 M aqueous acetic acid by stirring in cold conditions (< 10 °C). This CS solution was then adjusted to pH – 6.0 and kept at 4 °C until further use. Initially, a varying amount of PF-127 10-40 (10, 15, 18, 20, 25, 30, 35, and 40) % w/v was gradually incorporated into the pH adjusted to CS solution while stirring. The mixture containing 20 % w/v of PF-127 and 1% w/v of CS mixture (**BH**) was finally considered for further studies.

5.2.1.2. Incorporation of PEITC into PF-127/ CS hydrogel

Different PEITC-loaded hydrogels were prepared by loading PEITC to varying amounts of 20 mg, 40 mg, and 60 mg into the BH for further studies, hereafter referred to as PH20, PH40, and PH60, respectively. Pure PEITC (20, 40, and 60 mg) was first suspended in 100 µL absolute ethanol with gentle mixing for 10-15 min. In light-protected conditions, the resultant ethanolic PEITC was finally added to the BH while stirring (at < 10 °C) for 24 h until a homogenous solution was obtained. The final concentration of all three PEITC-containing hydrogels was 20 mg/mL (PH20), 40 mg/mL (PH40), and 60 mg/mL (PH60) of PEITC, respectively. The concentration of absolute ethanol in the hydrogel solution was 2 % v/v. To remove the ethanol

fraction from the PEITC-containing hydrogel solutions, the solutions were kept at stirring (at < 10 °C) for 24 h. The final pH of the different hydrogel formulations BH and PEITC-loaded hydrogels (PH20, PH40, PH60) was measured in triplicates using a digital pH meter (Five Easy TM Plus, Mettler-Toledo AG, Switzerland) (Ahsan et al., 2020). All hydrogels (PEITC-loaded and Blank) were stored at 4 °C until further studies.

Drug encapsulation efficiency (EE %) was indirectly measured; for this purpose, the 1 mL swollen PEITC-loaded hydrogels (PH20, PH40, PH60) solution was incubated with 9 mL 1X PBS (37 °C, pH 7.4) for 2 h. The drug concentration in the solution was measured spectrophotometrically at 365 nm using the 1,2-benzene dithiol (BDT)-based cyclo-condensation assay (Cong et al., 2018; Zhang, 2012).

Table 15. Name and description of hydrogel preparations related to methods section –Part A

Name of hydrogel preparations	Description
BH	Blank hydrogel
PH20	PEITC-loaded hydrogel at conc. 20 mg/mL
PH40	PEITC-loaded hydrogel at conc. 40 mg/mL
PH60	PEITC-loaded hydrogel at conc. 60 mg/mL
PEITC20	Free PEITC at conc. 20 mg/mL
PEITC60	Free PEITC at conc. 60 mg/mL

5.2.1.3. Physicochemical characterization

5.2.1.3.1. Sol-gel-sol phase transition measurements ($T_{sol-gel}$) in PEITC-loaded hydrogels

Tube-tilting method was performed to study the hydrogel's phase transition, where the BH's thermo-sensitive behavior (1 % CS and 10-40 % PF-127) was determined as a function of gelation time (Ahmad et al., 2019; Jung et al., 2017). For this purpose, a glass vial (5 mL screw-capped) containing 1 mL of the polymer solution was dipped in water baths (Julabo ED, Germany) maintained at 25 °C and 37 °C. The fluidity of the hydrogel mixture was checked by tilting the immersed vial at different time points. At any given time, the mixture in the solution phase was considered a 'flowing liquid' and the gel phase as a 'non-flowing gel.' The time taken until no flow was observed in the solution was taken as gelation time. The samples were independently tested at 25 °C and 37 °C in triplicates and expressed as a mean \pm SD.

5.2.1.3.2. Injectability of hydrogels

The injectability of solutions of BH and PEITC-loaded hydrogels (PH20, PH40, PH60) was assessed by observing thread-like hydrogel formation when the solution (at 4 °C) in a syringe (24-gauge needle) was injected into a vial containing PBS solution at 37 °C (Fan et al., 2017).

5.2.1.3.3. FTIR characterization

FTIR studies for PH60, BH, and PEITC60 samples were conducted to check for PEITC incorporation or any chemical modifications (Nicolet iS5, Thermo Scientific, USA) (Xu et al., 2017). The freeze-dried hydrogel samples were powdered, thoroughly mixed with KBr by grinding with a mortar and pestle, compressed to a pellet using a die, and placed in the FTIR sample holder. For the PEITC60 spectrum, a sample drop was placed between two plates and mounted on the FTIR sample holder to record the spectrum. The FTIR spectrum was recorded from 24 scans for wave numbers ranging from 4000 to 400 cm^{-1} with 2 cm^{-1} resolution in

transmittance mode. The FTIR spectra were normalized, and major vibration bands were associated with its chemical groups.

5.2.1.3.4. Morphological characterization of the hydrogels

The morphology of the BH and PH60 was analyzed using FESEM. The samples were frozen at $-80\text{ }^{\circ}\text{C}$ for 12 h and kept in a freeze-dryer for 36 h (FreeZone 4.5, Labconco, USA) (Pankongadisak and Suwantong, 2019; Qian et al., 2019; Yu et al., 2017). The dried materials were uniformly spread on a silicon wafer and coated with gold under a vacuum. The gold-coated silicon wafer was then pasted on a metallic stub for analysis using a FESEM (ZEISS GeminiSEM 450, Carl Zeiss, Germany). The analysis was performed at an operating voltage of 5 kV under a high vacuum.

5.2.1.3.5. Evaluation of pH-responsiveness of hydrogel (swelling ratio)

Freeze-dried hydrogels (ranging from 100-180 mg) were used to study the swelling behavior of hydrogels (at $37\text{ }^{\circ}\text{C}$) in pH 5.4 and pH 7.4 buffered solutions. The dried hydrogel (W_0) was weighed and allowed to swell separately in 5 mL of buffer solutions (for 5 h, $37\text{ }^{\circ}\text{C}$) in glass vials (10 mL screw-capped). The excess solution was removed from the swollen gels at different intervals by blotting and weighing (W_t) using a digital analytical balance (Quintix 224 Analytical Balance, Sartorius, Germany). Later, a fresh volume of buffer solution (5 mL) was added to the respective gels to maintain the sink conditions and further swelling (Chatterjee et al., 2019; Davoodi et al., 2016; Montaser et al., 2019). The swelling ratio of the different hydrogel formulations was calculated from *equation (1)*:

$$\text{Swelling ratio (\%)} = \frac{W_t - W_0}{W_0} \times 100 \quad (1)$$

5.2.1.3.6. In vitro hydrogel degradation studies

The *in vitro* degradation profile of the BH and PEITC-loaded hydrogels (PH20, PH40, PH60) was performed *in situ* by observing the behavior of gels in their wet form for 14 days (Arunkumar et al., 2016; Chatterjee et al., 2019; Pankongadisak and Suwantong, 2019). Firstly, 1 mL of each sample in a tube was allowed to gel completely at 37 °C for 3 h. The final concentration of PEITC-loaded hydrogels was 20 mg/mL (PH20), 40 mg/mL (PH40), and 60 mg/mL (PH60) of PEITC, respectively. About 3 mL of PBS (0.1 M, pH 7.4) was then added to the gels and stirred (70 rpm, 37 °C) in a shaking incubator (New Brunswick™ Excella® E24 Shaker Series, Eppendorf AG, Germany). After every 24 h, the buffer solution was drained to weigh the hydrogels, followed by a fresh addition of PBS (3 mL) to the individual vials. The procedure was continued every 24 h for 14 days. The *in vitro* degradation of hydrogels in the swollen state was studied by determining the % weight remaining at a given time. The experiments were performed in triplicates, with the values presented as mean \pm SD. The % weight of the remaining gel was weighed and plotted against the time (days).

5.2.1.3.7. *In vitro* drug release studies

The release of encapsulated drugs from the hydrogel at different pH was studied in acidic (5.4) and physiological (7.4) conditions. *In vitro*, PEITC release studies from the PEITC-loaded hydrogels (PH20, PH40, PH60) were carried out using a dialysis membrane of MWCO 12,000-14,000 Da (Nie et al., 2011; Xu et al., 2017). A 1 mL freshly prepared hydrogel formulation was taken into the dialysis membrane and immersed in 10 mL of freshly prepared buffer at two different pH conditions, 5.4 and 7.4, respectively (Lin et al., 2020; Tran Vo et al., 2022; Wang et al., 2020). The samples were stirred at 100 rpm (37 °C) in a rotary shaker (New Brunswick™ Excella® E24 Shaker Series, Eppendorf AG, Germany). At pre-determined time intervals, 200 μ L of the medium was withdrawn, and a fresh 200 μ L dissolution medium was added. The

amount of PEITC released in the PBS was determined by a BDT assay. The sample absorbance was measured at 365 nm using a UV-vis spectrophotometer (BioSpectrometer® kinetic Eppendorf, Hamburg, Germany). All tests were conducted in triplicate. The following buffer composition of the release medium was used for the *in vitro* drug release study.

A. Buffer Composition of release medium at pH 5.4

1. Sodium acetate anhydrous (mw: 82.03 g/mol)
2. Glacial Acetic acid (mw : 60.05 g/mol)
3. Adjust the pH with Hydrochloric acid and Sodium hydroxide solution

B. Buffer Composition of release medium at pH 7.4

1. Sodium chloride (mw: 58.44 g/mol)
2. Potassium chloride (mw: 74.55 g/mol)
3. Disodium hydrogen phosphate (mw: 141.96 g/mol)
4. Potassium dihydrogen phosphate (mw: 136.08 g/mol)
5. Adjust the pH with Hydrochloric acid.

5.2.1.3.8. Determination of PEITC using BDT assay

A cyclo-condensation reaction between ITCs and BDT was performed to quantify the amount of PEITC present in the samples (Zhang, 2012). Briefly, 100 μ L of the sample was mixed thoroughly with potassium phosphate buffer (500 μ L in 1 % Triton X-100, pH 8.5), followed by 8 mM methanolic BDT (500 μ L). The BDT reaction was performed at 65 °C for 2 h in a dry bath (AccuBlock™ Digital Dry bath, Labnet International Inc, USA) and cooled to room temperature. The absorbance of the supernatant obtained following centrifugation (at 21000 x g for 10 min) was measured at 365 nm.

5.2.1.4. Hemocompatibility assessment

Fresh blood from healthy male SD rats was withdrawn by retro-orbital bleeding, and vials containing EDTA solution (anticoagulant) were collected. The vials were centrifuged at 2000 rpm for 15 min to collect the erythrocytes and then washed thrice with PBS (pH 7.4). The hemolysis assay was performed by incubating 50 μ L of the samples with 950 μ L of erythrocyte solution (5 % erythrocytes/PBS suspension) in a centrifuge tube (1.5 mL) for 3 h at 37 $^{\circ}$ C. Following incubation, the samples were centrifuged at 2000 rpm at 4 $^{\circ}$ C for 10 min. A 150 μ L of supernatant was transferred to the respective well of a 96-well plate (flat-bottomed, Eppendorf). The sample absorbance was measured at 540 nm in a multimode microplate reader (Thermo Scientific, Varioscan Flash, USA). The total hemolysis was achieved by incubating the erythrocytes with 1 % Triton X-100 (positive control) and PBS as a negative control for comparison (Hu et al., 2021; Pandit et al., 2019; Zhao et al., 2020). The following equation calculated the hemolysis rate for the different concentrations of hydrogels *equation (2)*:

$$\text{Hemolysis rate} = \frac{(\text{Sample } O.D - \text{Negative control } O.D)}{(\text{Positive Control } O.D - \text{Negative control } O.D)} \times 100 \quad (2)$$

5.2.1.5. *In vivo* gel formation and degradation studies

Male SD rats (180-220 g b.w.) were used for the *in vivo* gel formation and degradation studies. The animals were randomized into six groups (with six animals in each group): (i) the negative control, (ii) PEITC20, (iii) BH, (iv) PH20, (v) PH40, (vi) PH60 and anesthetized (inhalation, 3-5 % isoflurane) prior to injection or surgery. For the (i) *negative control group*, 400 μ L of sterile PBS was administered as an SC injection at the prominent vertebra (seventh cervical spine) of the animal. In the case of other groups (ii - vi), 400 μ L of the hydrogel solution was injected at the same anatomical site. The injected site was palpitated after 30 mins to

observe gel formation *in situ*. At pre-determined intervals, the anesthetized rats (CO₂ asphyxiation) were sacrificed, and the gel site was cut open for observation (Wu et al., 2017; Xu et al., 2019; Zhang et al., 2017; Zhao et al., 2015).

5.2.1.6. Biocompatibility assessment

The *in vivo* biocompatibility was microscopically evaluated by examining the histological samples stained with H&E (Xu et al., 2019; Zhang et al., 2017). The histology section was prepared by excising the skin surrounding the gel-implanted site. The paraffin-embedded blocks of skin samples were prepared by initially fixing them for 4 days in 10 % neutral buffered formalin, followed by a dehydration procedure in a graded series of ethanol. About 5.0 µm thick sections were sliced on a semi-automatic rotary microtome (Radical Scientific, India), followed by H&E staining. The stained samples were observed at different magnifications (4x and 10x) using a digital optical microscope (Meji, Japan) to evaluate the observations.

5.2.1.7. Sample preparation and conditions for HPLC

The samples to detect PEITC levels in plasma/tissues were prepared following a BDT reaction. The amount of PEITC present was assessed with respect to the amount of cyclocondensation adduct that was detected using Reverse phase (RP)-HPLC. The LC 20A HPLC system (Shimadzu, Maryland, USA) consisted of a degasser, a binary pump, a manual injector, a temperature oven, and a model SPD-20A photodiode array detector. The chromatographic analysis was performed using the Enable C18H column (4.6 × 150 mm i.d., Spinco Biotech, India) with a particle size of 5 µm and maintained at 60 °C. The mobile phase consisted of double-distilled water (solvent A) and ACN (solvent B) at a ratio (40:60, v/v) with a flow rate of 1 mL/min for 10 min (Qindeel et al., 2020). The samples for HPLC analysis were prepared as follows. Briefly, 25 µL of plasma/tissue was incubated with a reaction mixture containing 125

μL of 100 mM potassium phosphate buffer (pH 8.5) and 125 μL of 8 mM BDT in ACN at 65 °C for 2 h to allow PEITC and their metabolites (mainly N-acetylcysteine conjugates) to be converted into its adducts 1,3-benzodithiole-2-thione. The 1,3-benzodithiole-2-thione adduct formed was detected at 365 nm. About 10 μL of the sample was injected into the HPLC system. The amount of PEITC present in the plasma/tissues was deduced from the standard curve of PEITC obtained from a serial dilution of PEITC stock solution (from 0.1 to 10 $\mu\text{g}/\text{mL}$) with the blank plasma/tissue samples.

5.2.1.8. Pharmacokinetic analysis using HPLC

The pharmacokinetic studies were performed on healthy male SD rats randomly divided into three groups. Animals in group I and group II were treated as reference groups where the group I animals received a single oral dose of PEITC in 1 % DMSO (PEITC equivalent to 33.3 mg/kg b.w.) while group II animals received an SC injection of 500 μL of PEITC solution (20 mg/mL in 1 % DMSO). In group III animals, 500 μL of PH20 was injected with SC to form a gel at the injection site. The blood samples withdrawn at defined time points (0.5, 1, 1.5, 2, 2.5, 3, 4, 6, 8, 12, 16, 24, 36, and 48 h) were mixed with EDTA solution followed by centrifugation (3000 $\times g$ at 4 °C) to remove the plasma and stored in a -80 °C freezer until further analysis by HPLC. The samples for the HPLC analysis were prepared by mixing 200 μL plasma samples with 400 μL acetonitrile (ACN) and centrifuging the contents thoroughly at 16,600 $\times g$ at 4 °C for 5 min. The supernatant containing the PEITC was subjected to BDT following the methods **described in section 5.2.1.7.**(Chuang et al., 2019; Ye et al., 2002). A 10 μL of this clear supernatant was injected into the HPLC system (Ahmad et al., 2019; Jin et al., 2020). PK solver software (an add-in program in Microsoft Excel) was used to determine the different pharmacokinetic parameters (Qindeel et al., 2020).

5.2.1.9. *In vivo* biodistribution studies

A biodistribution study was performed on healthy SD rats. A single 500 μ L single administration of the different formulations [two concentrations of Free PEITC (PEITC20 and PEITC60) and PEITC-loaded hydrogels (PH20 and PH60)] was administered in the animals by SC route. The rats were euthanized at 2 h and 8 h post-injection with CO₂ asphyxiation for excision of major organs (kidney, liver, heart, spleen, and lungs). The isolated organs were thoroughly washed with ice-cold PBS and stored at -80 °C. Before the sample preparation, the excised tissue was thawed, rinsed well with saline (ice-cold), and blotted dry. The samples for HPLC were prepared by homogenizing the 100 mg of the tissue sample in 100 μ L of PBS and mixing it with 700 μ L of ACN in a clean tube and vortexed for 5 min. The homogenates were centrifuged (at $15,700 \times g$ for 15 min at 4 °C) to collect the supernatants. The amount of PEITC (following a BDT reaction) in the different tissue supernatant was determined by HPLC analysis (Kim et al., 2015).

5.2.1.10. *In vivo* safety studies

For the *in vivo* studies, twelve SD rats in four groups (n = 3) received a single SC injection of 500 μ L sterile PBS (standard control), a group I; PEITC60, group II; BH, Group III; PH60, and group IV respectively. The animal's general status was monitored daily, and their body weight was measured every 7th day using a digital balance. On the 14th day post-injection, the blood samples and other major organs (heart, liver, spleen, and kidneys) were removed from the euthanized rats. The serum samples were prepared to assess liver and kidney function as major indicators using a semi-automated biochemistry analyzer (Merilyzer Cliniquant, India). The complete blood panel data from healthy control and treated rats were also tested using a hematology analyzer (PE-6800, Prokan, China). Paraffin-embedded blocks of the major organs

were prepared following fixation with 10 % neutral buffered formalin for 4 days. A 5.0 μm section was stained using H&E, and a histological examination was performed under an optical microscope (Meji, Japan) (Yu et al., 2018).

5.2.1.11. Development of an advanced AIA rat model

FCA was used to induce arthritis in female SD (180-240 g b.w.) rats. Briefly, 250 μL of FCA was injected SC into the sub-plantar region of the left hind paw under deep isoflurane anesthesia except for the rats serving as control (administered 250 μL of sterile PBS). The animals were monitored for arthritis parameters for 12 days following FCA immunization to assess disease development (Deng et al., 2021; El-Sheikh et al., 2019; Helmy et al., 2017; Pandey et al., 2018; Zeb et al., 2017).

5.2.1.12. *In vitro* biocompatibility of PEITC-loaded hydrogel on isolated primary cells

5.2.1.12.1. Isolation and primary culture FLS cells

A single intradermal injection (250 μL) of FCA, a solution containing 1 mg/mL heat-killed *Mycobacterium tuberculosis* (Sigma-Aldrich, St. Louis, USA) in sterile paraffin oil, was administered into the sub plantar region of the left hind paw of the healthy SD rats to induce arthritis. By day 7, clinical symptoms such as swelling of the feet and an inability to bend the ankle had been noticed. FLS were isolated following the previously reported method with minor modifications (Ganesan & Rasool, 2017). On day 12 following arthritis induction, the synovial tissues with the synovial membrane were isolated from FCA-induced arthritis-induced rat knees under sterile conditions. For healthy rats, the isolation of fresh synovial tissues with the synovial membrane from rat knees was performed at day 0 under aseptic conditions. Initially, the rats were euthanized using CO₂ asphyxiation, and their knee joints were removed and then soaked in 75 % alcohol for 2 min. Muscle tissues were removed, and the hind limbs were separated at the

femur/fibula/tibia junction. The synovial layer tissues containing the synovial membrane were isolated in a sterile environment, soaked in sterile PBS for 5 min, rinsed with PBS, and placed in a petri dish. The synovial tissue was minced and digested by incubating it with 0.1 % (w/v) type IV collagenase (Sigma-Aldrich, St. Louis, USA) in DMEM supplemented with 5 % FBS and antibiotic solution 1X for 3 h at 37 °C under gently agitating tube every 15 min in a water bath. Following incubation, add fresh DMEM Media supplemented with 10% FBS and antibiotic solution 1X to the tube before centrifuging at 300 x g, RT for 10 min. Remove the supernatant with caution so as not to disrupt the pellet, then resuspend the pellet in a fresh DMEM medium. Transfer the cell-containing supernatant to a 60 mm x 15 mm tissue culture dish, and then incubate for 7 days at 37 °C with 5 % CO₂. The tissue suspension is filtered through a sterile 70-µm nylon mesh cell strainer (Himedia, India) to eliminate tissue debris to get a healthy cell population. The adhering cells were trypsinized at 80–90% confluence, passaged at a 1:2 ratio, and recultured in the same condition. At the 4th passage, the purity of isolated FLS cells was assessed by flow cytometry using FITC-coupled monoclonal antibodies to CD90.1 and PE-coupled monoclonal antibodies to VCAM1 (CD106) cell surface markers. A homogeneous population of FLS at passages ranging from 3 to 9 was used for the experiments. Healthy FLS is referred to as N-FLS, whereas arthritis-induced FLS is referred to as RA-FLS.

5.2.1.12.2. *In vitro* cytotoxicity test (MTT assay)

The MTT assay assessed the *in vitro* cytotoxicity of PEITC-loaded hydrogel against N-FLS and RA-FLS. The cells were seeded in 96-well plates at 10×10^3 cells/well density and cultured for 36 h at 37 °C with 5% CO₂ in a CO₂ incubator. BH and the various concentrations of PH50 were added to wells to maintain a final drug concentration over a range of 5–100 µM. The media was discarded 24 and 48 h after the incubation period. After adding fresh 30 µL of MTT

solution (5 mg/mL), the cells were incubated for an additional 4 h. Finally, 150 μ L of DMSO was added to each well to dissolve the formazan crystal that had formed, and an absorbance measurement at 570 nm was performed using a multimode microplate reader (Thermo Scientific, Varioskan Flash, USA). The untreated cells served as a control. The following *equation (3)* was employed to calculate cell viability:

$$\text{Cell viability (\%)} = \frac{\text{Absorbance of the tested sample}}{\text{Absorbance of the control sample}} \times 100 \quad (3)$$

5.2.1.13. *In vivo* therapeutic efficacy of PEITC-loaded hydrogel

5.2.1.13.1. *Induction of AIA in SD rats*

The AIA rat model was developed per the method described in **section 5.2.1.11**. The animals were monitored for arthritis parameters every 4th day up to the 36th day following FCA immunization (Deng et al., 2021; El-Sheikh et al., 2019; Helmy et al., 2017; Pandey et al., 2018; Zeb et al., 2017).

Following 12 days of the arthritis induction, macroscopical observations were made for uniform swelling and redness in the FCA-injected paws (Pandey et al., 2018; Zeb et al., 2017). The rats were randomly divided into five groups (n = 4), (i) regular healthy control group (standard), (ii) arthritis group (FCA-challenged and injected with sterile PBS, *model*), (iii) PH50 challenged with FCA, (iv) PEITC50 treated group challenged with FCA, and (v) BH treated group challenged with FCA. The hydrogel administration protocol was initiated after day 12 by locally injecting 50 μ L of PBS, PH50, PEITC50, and BH directly into the knee joints of arthritic rats on days 12, 18, 24, 30 after FCA immunization (Kim et al., 2019).

5.2.1.13.2. *Assessment of arthritis progression upon FCA administration*

The paw edema in each rat was periodically examined on the 14th, 21st, 28th, and 35th day after administration of different formulations (Gou et al., 2017; Vincenzi et al., 2013). Paw edema volume (expressed in *ml*) was measured by making a visible mark on each paw at the tibiotarsal joint and dipping the paw at the marked level. The displaced volumes were recorded using a digital plethysmometer (WBP01, Vihan Techno Services, India). The body weight of rats was measured using a standard digital weighing balance. From day 0 to 36, the body weight of each animal was recorded every 4 days and presented as (g) (Pan et al., 2017).

The arthritis score was determined by microscopically observing the degree of swelling and redness of joint edema of periarticular tissues in the FCA-injected and non-injected paw. The arthritis score was assigned based on the following observations: a). '0' for normal with no erythema and swelling; b). '1' for swollen digits with erythema; c). '2' for mild swelling of limbs and erythema, d). '3' for moderate swelling observed from the ankle extending to the metatarsophalangeal or metacarpophalangeal joints, and e). '4' for severe swelling observed extending from the ankle to the digits, culminating in ankylosis and loss of joint movement. The arthritis score for an individual rat was calculated as the sum of the four paw scores (a maximum score taken as 16 per rat). The severity of arthritis and therapeutic efficacy of the formulation was assessed based on the scores obtained by the rats from the treatment groups (on day 14, 21, 28, and 35) (Asenso et al., 2019; Qian et al., 2017; Wei et al., 2013).

5.2.1.13.3. Blood collection and serum separation

Blood was withdrawn from each animal by retro-orbital plexus bleeding under isoflurane anesthesia and sacrificed by CO₂ asphyxiation at the endpoint. The blood samples were collected in a sterile 1.5 mL tube and centrifuged at 3000 rpm for 10 min at 4 °C (Centrifuge 5424 R, Eppendorf AG, Germany). The serum samples thus obtained were used for assessing different

biochemical parameters and markers for oxidative stress and inflammation. (Hassan et al., 2019; Pandey et al., 2018; Yang et al., 2020; Yin et al., 2020b).

5.2.1.13.4. Determination of thymus and spleen index

On the final day (37th day) of immunization, the rats from the different treatment groups were sacrificed using CO₂ asphyxia to isolate the immune organs (thymus and spleen). The organs were weighed to determine the index of the spleen and thymus as follows in *equations (4 and 5)* (Jing et al., 2019; Wang et al., 2019; Yang et al., 2020):

$$\text{Spleen index (\%)} = \frac{\text{Spleen weight}}{\text{Bodyweight}} \times 100 \quad (4)$$

$$\text{Thymus index (\%)} = \frac{\text{Thymus weight}}{\text{Bodyweight}} \times 100 \quad (5)$$

5.2.1.13.5. Evaluation of oxidative stress

Oxidative stress in the animals was assessed by estimating the serum levels of different biochemical markers such as MDA, NO, GSH, and MPO. MDA is one of the thiobarbituric acid-reactive substances (TBARS) generally used for estimating lipid peroxidation. Lipid peroxidation in the serum was determined by following a standard protocol where the formation of malondialdehyde-thiobarbituric acid (MDA-TBA) adduct upon reacting MDA with TBA in acidic conditions at 100 °C. The absorbance of the reaction end product (TBARS) was determined at 532 nm using a spectrophotometer. 1,1,3,3-tetra methoxy propane was used as the standard, with the results expressed as µM of TBARS (Helmy et al., 2017; Mazumder et al., 2019; Uchiyama and Mihara, 1978; Yagi, 1998). Serum NO was measured by Griess assay using a commercial Nitrite/Nitrate Assay Kit (Sigma-Aldrich, USA) and performed per the manufacturer's instructions (Brizzolari et al., 2021; Helmy et al., 2017; Miranda et al., 2001). Estimation of GSH in the serum was performed by the standard Ellman and Moron

dithionitrobenzoic acid (DTNB) method (Ellman, 1959; Moron et al., 1979). Here, the sulfhydryl groups in the samples, when mixed with DTNB, formed a yellow color solution detected at 412 nm. The concentration of GSH (in μM) was calculated from the standard GSH curve. MPO activity in serum was detected following the protocol provided by the manufacturer (Elabscience, MD, USA).

5.2.1.13.6. Evaluation of cytokines levels in the serum

An ELISA was performed to determine the relative serum levels of representative pro-inflammatory cytokines, anti-inflammatory cytokines, and bone erosion markers (Helmy et al., 2017; Linghang et al., 2020; Wei et al., 2013; Yeo et al., 2019). Here, interleukins (IL-1 β , IL-17A, IL-6, and IL-10) and RANKL were measured using commercially available rat-specific ELISA kits from Elabscience, MD, USA, and Invitrogen, Thermo Fisher Scientific, MI, USA in case of TNF- α as per manufacturer's instruction. The serum (50 μL) obtained from the animals of the different treatment groups was used to detect cytokines. The procedures and data analyses provided by the manufacturer were followed. Absorbance at 450 nm was measured using a multimode microplate spectrophotometer (Thermo Scientific, Varioscan Flash, USA), and the concentrations of cytokines were calculated from a standard curve.

5.2.1.13.7. Biochemical test to assess liver and kidney function

The hepatotoxicity and nephrotoxicity in different treatment animal groups were evaluated by determining the levels of different biochemical markers following the 37-day study period. The serum levels of ALT, AST, BUN, and CRE were determined according to the manufacturer's instructions using commercially available kits (Meril Diagnostics). A Merilyzer Cliniquant, a semi-automated biochemical analyzer, was used to test these biochemical parameters (Wang et al., 2019; Yin et al., 2020b).

Part B

5.2.2. Preparation and therapeutic evaluation of dual-drug nanoparticles loaded hydrogel

5.2.2.1. Fabrication and characterization of drug-loaded nanosystems

5.2.2.1.1. Fabrication of blank NP and MTX NP

The nanoprecipitation technique was applied to fabricate MTX NP. In brief, different amounts (80-150 mg) of PLGA (**shown in Table 16**) were dissolved in a solvent mixture of acetone and DMSO (9:1), followed by the addition of MTX, and vortexed until a clear solution was obtained. The above organic phase was added drop-by-drop into an aqueous phase (20 mL) containing 0.1 % w/v PF-127 surfactant under continuous stirring (at 800 rpm) until complete removal of organic solvent. The obtained nanoparticles were dialyzed against 10 % DMSO to remove unloaded Free MTX, followed by dialysis against water to remove small residuals of DMSO. Finally, the obtained **MTX NP** was lyophilized using Mannitol (cryoprotectant) and stored at 4 °C.

Table 16. Different polymer compositions for the preparation of MTX NP

Batch no	PLGA polymer composition (mg)	Amount of MTX (mg)	Solvent mixture (Acetone: DMSO)	PF-127 % (w/v)
I	80	5.2	9:1	0.1
II	120	5.2	9:1	0.1
III	150	5.2	9:1	0.1

5.2.2.1.2. Preparation of PEITC NE

PEITC NE was prepared and optimized by varying the concentration of surfactants (Span-80: Tween-80) shown in **Table 17**. Different surfactant mixtures were selected based on

the hydrophilic-lipophilic balance (HLB) values between 4 and 15 and used for NE preparation. The procedure involved specific amounts of olive oil and surfactant mixture taken in a glass vial and subjected to stirring for 1 h at 1200 rpm. Subsequently, under constant stirring, the aqueous phase was added dropwise to the oil phase, and stirring was continued for another 3 h. The obtained blank NE was probe sonicated at 60 % amplitude (with a pulse of 5 s ON and 5s OFF) for 30 min (Li et al., 2015). Further optimized blank NE was used to prepare the **PEITC NE**, in which PEITC (40 mg) and specific amounts of olive oil were added in the oil phase. A similar procedure was employed as that of blank NE.

Table 17. Different surfactant concentrations for the preparation of PEITC NE

Batch no	Constants	PEITC Content (mg)	Variables	
			Surfactant 1 (% Span 80)	Surfactant 2 (% Tween 80)
1	Aqueous phase- 72% Oil phase- 18%	40	6	4
2			8	2
3			2	8
4			9	1
5			3	7
6			1	9
7			9.7	0.3
8			10	0

5.2.2.1.3. Determination of % EE and % DL of MTX NP

The prepared drug-loaded nanoparticles were placed in a dialysis bag (MWCO 10 kDa) and dialyzed against 10 % DMSO in a static condition for 4 h. Finally, the concentration of Free

MTX was determined using a UV-visible spectrophotometer (BioSpectrometer® kinetic Eppendorf, Hamburg, Germany) at 302 nm (Mohanty et al., 2020).

5.2.2.1.4. Drug content for the optimized PEITC NE

The PEITC content in the NE was determined by taking 10 µL of PEITC NE, diluting it to 100 µL with DMSO, and vortexing thoroughly until a clear solution. The obtained clear solution containing PEITC was analyzed using a UV-visible spectrophotometer (BioSpectrometer® kinetic Eppendorf, Hamburg, Germany) using BDT assay at 365 nm **described in section 5.2.1.2 with minor modification** (Aly et al., 2019).

5.2.2.1.5. PS, PDI, and ZP

PS, PDI, and ZP were determined by preparing different dilutions of samples using Milli Q water at a room temperature of 25 °C with a backscattered angle of 173° using Zetasizer Nano ZS (Malvern Instruments, Malvern, UK) (Danhier et al., 2018).

5.2.2.2. Fabrication and characterization of dual-drug nanoparticles loaded hydrogel

5.2.2.2.1. Fabrication of dual-drug nanoparticles loaded hydrogel

Pluronic F-127 (PF-127) and sodium alginate (SA) polymers were used to prepare the single and dual nanoparticles loaded thermosensitive hydrogels (BD NP HG, MTX NP HG, PEITC NE HG, and DD NP HG). All the hydrogel formulations were prepared according to the method previously described by Yin *et al.* 2020a (Yin et al. 2020a). Briefly, blank PLGA NP was uniformly dispersed in the o/w NE by sonication for 10-15 min. After the dispersion, 1 % SA was added and mixed uniformly at 600 rpm until homogenous dispersion. To the above nanoparticulate SA dispersion, different concentrations of PF-127 (shown in **Table 18**) were

added in cold conditions (4-10 °C) and stirred continuously at 1000 rpm for 24 h to obtain the **BD NP HG**. In the preliminary studies, different concentrations of PF -127 (11, 12, 13, and 15 % w/v) with 1% SA were used to optimize the preparation of **BD NP HG**. A similar procedure was followed to fabricate **MTX NP HG**, **PEITC NE HG**, and **DD NP HG**. For the preparation of **BD NP HG**, **PEITC NE HG**, and **DD NP HG**, 12 % w/v PF-127 was used, whereas for **MTX NP HG**, 19 % w/v PF-127 was selected. The different hydrogels obtained were stored at a refrigerated temperature (4 °C) (Qindeel et al., 2019; Vignesh et al., 2018; Yin et al., 2020a).

Table 18. Different compositions of SA and PF-127 for the preparation of *in-situ* hydrogels

Batch no.	Name of the hydrogel	SA composition (%) (w/v)	PF-127 composition (%) (w/v)
I	MTX NP HG	1	19
II	PEITC NE HG	1	12
III	DD NP HG	1	12

Table 19. Name and description of hydrogel preparations related to methods section –Part

B

Name of hydrogel preparations	Description
BD NP HG	Blank dual nanoparticles loaded hydrogel.
MTX NP HG	MTX-PLGA nanoparticle-loaded hydrogel
PEITC NE HG	PEITC nanoemulsion-loaded hydrogel
DD NP HG	Dual-drug nanoparticles loaded with hydrogel.
BL HG	Blank hydrogel

BL HG was prepared by 1% (w/v) SA and 19 % (w/v) PF-127. The name and description of hydrogel preparations are mentioned in **Table 19**.

5.2.2.2.2. FTIR study

FTIR studies for Free MTX, Free PEITC, BD NP HG, MTX NP HG, PEITC NE HG, and DD NP HG were analyzed to investigate the incorporation of drug or chemical interactions between the drug and excipients using FTIR spectrophotometer (Nicolet iS5, Thermo Scientific, USA) in which each sample was mixed with KBr and compressed into a pellet using a die. Each sample pellet was further scanned individually at an average of 16 scans at a resolution of 4 cm⁻¹ over a wavelength of 4000-500 cm⁻¹.

5.2.2.2.3. Determination of drug content

The amounts of drug loaded into the different hydrogels were estimated using centrifugation. Briefly, 100 µL of the gel was taken, and the contents were dissolved entirely in 1 mL DMSO. Later, it was centrifuged at 10,000 rpm for 15 min, and the obtained clear supernatant was subjected to different dilutions using DMSO and measured by a UV-visible spectrophotometer. MTX was determined at 302 nm, and PEITC was analyzed using BDT assay at 365 nm.

5.2.2.2.4. Solubility studies

Using the shaking method, the aqueous solubility studies were carried out between the free MTX, free PEITC, and the optimized DD NP HG. The specified amount of hydrogel was taken, equivalent to the unprocessed free drugs, and then dispersed in the water. Further, the shaking was done at 100 rpm for 1 h, and the dispersions were centrifuged at 10,000 rpm for 15 min. Finally, the amount of drug in the supernatant was examined using a UV-visible

spectrophotometer at 302 nm for MTX and 365 nm for BDT-conjugated PEITC (Aly et al., 2019).

5.2.2.2.5. Determination of gelation time

The determination of gelation time for all the hydrogel formulations was measured as per the **method described in section 5.2.1.3.1.**

5.2.2.2.6. In vitro degradation studies

The *in vitro* degradation profile of different hydrogel formulations was performed by observing the behavior of gels in their wet form using the shaking method. Initially, 1 mL of hydrogel formulation (in sol form) was taken in a 5 mL glass vial and left undisturbed for 30 min at 37 °C to form a gel. About 3 mL of PBS (0.1 M, pH 7.4) was added to the gels and gently stirred (50 rpm, 37 °C) in a shaking incubator (New Brunswick™ Excella® E24 Shaker Series, Eppendorf AG, Germany). After every 24 h, the buffer solution was removed to weigh the hydrogels, followed by a fresh addition of PBS (3 mL) to the individual vials. A similar procedure was continued until > 80 % degradation of the hydrogel. The process was continued every 24 h for 6 days. All the experiments were performed in triplicates, and the results were presented as mean ± SD. A graph was plotted between the % weight of the gel remaining versus time in days (Mao et al., 2016; Qu et al., 2019). The *in vitro* degradation rate of the hydrogels was estimated by using *equation 6*:

$$\text{In vitro biodegradation} = \frac{(W_i - W_d)}{W_i} \times 100 \quad (6)$$

W_i represents the initial weight of the hydrogel

W_d represents the weight of the degraded hydrogel

5.2.2.2.7. Injectability of hydrogels

The injectability of BD NP HG, MTX NP HG, PEITC NE HG, and DD NP HG was performed per the method **described in section 5.2.1.3.2.**

5.2.2.2.8. Morphological characterization of the dual-drug nanoparticles loaded hydrogel

The morphology of the BL HG and DD NP HG was analyzed using FESEM as per the method **described in section 5.2.1.3.4.**

5.2.2.2.9. Rheological properties of the dual-drug nanoparticles loaded hydrogel

The rheological properties of the hydrogels were performed using an HR-30 rheometer (TA instruments). The storage modulus (G') and loss modulus (G'') were recorded during a temperature ramp from 25 °C to 45 °C, with a rate of 3 °C/min. The complex viscosity (η^*) measurements were also performed at 25 °C and 37 °C, with a range of angular frequencies (ω : 0.1-100 rad/s) for the injectable application. For G' and G'' of frequency dependencies, the data were collected for the modulus with a frequency range of a range of angular frequencies (ω : 0.1-100 rad/s) at 37 °C (Ke et al., 2020; Monteiro do Nascimento et al., 2021).

5.2.2.2.10. In-vitro drug release and kinetics studies

The MTX and PEITC release profiles from different formulations were evaluated *in vitro* at pH 7.4 in PBS with 0.5 % Tween-80 (Yin et al., 2020a). Briefly, 250 μ L of the different samples (MTX NP HG, PEITC NE HG, and DD NP HG) containing 1 mg MTX and 10 mg PEITC were placed into a dialysis membrane (MWCO 10 kDa) and allowed to form a gel (at 37 °C). The dialysis bag with the sample gel was suspended in a beaker containing 50 mL dissolution medium (PBS with 0.5 % tween-80) and placed in a shaker incubator with constant shaking at 100 rpm maintained at physiological body conditions (37 °C, pH-7.4). Samples were

withdrawn at different time intervals: 0, 1, 2, 4, 6, 8, 12, 24, 36, 48, 72, 96, and 120 h. The specific amount of drug released at different time points was analyzed using a UV-visible spectrophotometer at 302 nm for MTX and 365 nm for PEITC using BDT assay.

The results were plotted in various kinetic models, including Zero-order, first-order, Higuchi, Hixon-Crowell, and Korsmeyer Peppas, to determine the drug release kinetics from the hydrogels models.

5.2.2.2.11. Stability studies

The physical stability of the drug-loaded hydrogels (MTX NP HG, PEITC NE HG, and DD NP HG) was investigated by storing the nanoparticular hydrogels at 4 °C for 60 days. The samples were withdrawn at predetermined intervals and estimated for percentage drug loading (% DC). The stability of the hydrogel was assessed by studying the variations in the final drug content (Mura et al., 2018).

5.2.2.3. Cell-based studies

5.2.2.3.1. In vitro cytotoxicity test (MTT assay)

The MTT assay was used to assess the *in vitro* cytotoxicity of DD NP HG against N-FLS and RA-FLS as per the **method described in section 5.2.1.12.2**. The cells were treated with **BD NP HG, PEITC NE HG** (PEITC at final concentration: 25 50,100 μM), **MTX NP HG** (MTX at final concentration: 0.375, 0.75, 1.5 μM) & **DD NP HG** (PEITC – 25 50,100 μM & MTX – 0.375, 0.75, 1.5 μM) for 24 h and 48 h; respectively. All experiments were conducted in six replicates (mean ± SD, n = 6).

5.2.2.3.2. Apoptosis detection assay

RA-FLS cells' apoptosis rate was assessed using a flow cytometer (FACS Calibur BD LSRFortessa TM, USA). The cells (5×10^5) were treated with BD NP HG, PEITC NE HG

(PEITC at final concentration: **100 µM**), MTX NP HG (MTX at final concentration: **1.5 µM**) & DD NP HG (**PEITC: 100 µM & MTX: 1.5 µM**) for 24 h (Chen et al., 2017). A FITC annexin v apoptosis detection kit I (BD Biosciences, San Diego, CA, USA) was used to quantify the apoptotic cells of cultured RA-FLS, according to the manufacturer's protocol. After 24 h of treatment, the cells were collected and stained for 15 minutes at 4°C in the dark with Annexin V-fluorescein isothiocyanate (FITC) and propidium iodide (PI). The BD FACSDiva™ Software determined the apoptotic rate (Chen et al., 2021). The assay was performed in three replicates.

5.2.2.3.3. *ELISA assay*

To evaluate the anti-inflammatory effect of DD NP HG, the RA-FLS cells were cultured in a 6-well plate. The six groups were assigned as **control** (untreated RA-FLS, Group I), **model** (LPS stimulated RA-FLS, Group II), **BD NP HG** (LPS + blank dual nanoparticles loaded hydrogel treated RA-FLS, Group III), **MTX NP HG** (LPS + MTX-PLGA nanoparticle loaded hydrogel RA-FLS, Group IV), **PEITC NE HG** (LPS + PEITC nanoemulsion loaded hydrogel treated RA-FLS, Group V), and **DD NP HG** (LPS+ Dual-drug nanoparticles loaded hydrogel treated RA-FLS, Group VI). The concentration of the PEITC NE HG (PEITC at final concentration: **100 µM**), MTX NP HG (MTX at final concentration: **1.5 µM**) & DD NP HG (**PEITC: 100 µM & MTX: 1.5 µM**) were maintained. Except for the control group, LPS with medium concentration was controlled at 1 µg/mL in all groups and then incubated for 4 h. Further, the cells were treated with different formulations and incubated for another 24 h at 37 °C and 5 % CO₂. The levels of various cytokines (TNF-α, IL-17A, and IL-6) in the supernatant were determined using ELISA kits (Invitrogen, USA) (Yu et al., 2022). The samples were prepared by carefully collecting the supernatant in each well into individual microfuge tubes centrifuged at 3000 rpm for 10 min. The required volume of the samples was then transferred

into a 96-well plate to determine the OD value at 450 nm on the enzyme scale instrument, and the concentration of inflammatory factors was calculated according to the standard curve.

5.2.2.3.4. Quantitative RT-PCR analysis

The RA-FLS cells were plated in 6-well flat bottom tissue culture plates with a 5×10^5 cells/well density. The cells were then divided into six treatment groups: **control** (untreated RA-FLS, Group I), **model** (LPS stimulated RA-FLS, Group II), **BD NP HG** (LPS + blank dual nanoparticles loaded hydrogel treated RA-FLS, Group III), **MTX NP HG** (LPS + MTX-PLGA nanoparticle loaded hydrogel treated RA-FLS, Group IV), **PEITC NE HG** (LPS + PEITC nanoemulsion loaded hydrogel treated RA-FLS, Group V), and **DD NP HG** (LPS+ Dual-drug nanoparticles loaded hydrogel treated RA-FLS, Group VI). The concentration of the PEITC NE HG (PEITC at final concentration: **100 μM**), MTX NP HG (MTX at final concentration: **1.5 μM**) & DD NP HG (PEITC: **100 μM** & MTX: **1.5 μM**) were maintained. Except for the control group, LPS with medium concentration was controlled at 1 $\mu\text{g}/\text{mL}$ in all groups and then incubated for 4 h. Further, the cells were incubated by these materials for 24 h under bacteria-free conditions of 37 °C and 5 % CO_2 (Yu et al., 2022).

After 28 h, the total RNA was extracted from RA-FLS using an RNA isolation kit (PureLink™ RNA Mini Kit, Thermo Fischer Scientific) according to the manufacturer's instructions. The RNA quantity and integrity were estimated using NanoDrop (ONE^C, Thermo Fisher Scientific) and verified by electrophoresis using 1 % agarose gel. RNA with good quality having A_{260}/A_{280} ratio = 1.9 – 2.0 with a visible band corresponding to 16S and 28S were selected for cDNA synthesis. Further, about 2 μg of total RNA was used for reverse transcription using a Reverse Transcription Kit (Maxima First Strand cDNA kit, Thermo Fischer Scientific) in

a Thermal Cycler (Veriti[®], Applied Biosystems) following the manufacturer's instructions. Real-time PCR was performed to measure the mRNA expression levels of *IL-1 β* , *OPG*, *RANKL*, *DKK1*, *NFATc1*, and the *GAPDH* (housekeeping gene), using an SYBR Green PCR Master mix (iTaq Universal SYBR[®] Green reaction mix, BioRad) in a QuantStudio5 (Applied Biosystems). PCR reactions consisted of 0.25 μ M of forward and reverse primers (Sigma-Aldrich), 1X SYBR Green reaction mix (BioRad), and a dilution series of cDNA with a total volume of 10 μ L. Reaction condition was performed at 95°C for 3 min followed by 40 cycles of 95°C for 15 s; 60°C for 1 min. Finally, the relative gene expression of the genes was analyzed from the $2^{-\Delta\Delta C_t}$ values (Schmittgen and Livak, 2008). For comparison, the control (**group I**) and LPS-stimulated RA-FLS as a *model* (**group II**) were used as untreated. Details of primers used in real-time PCR are listed in **Table 20**.

Table 20. Sequences of the primers used for real-time PCR

Sl. No.	Gene	Primer sequence		Amplicon size (bp)	Tm (°C)	Reference
1	<i>IL-1β</i>	FP	5'-GCTGTGGAGAAGCTGTGGCA-3'	153	62.5	(Jeong et al., 2020)
		RP	5'-GGGAACGTCACACACCAGCA-3'		62.5	
2	<i>OPG</i>	FP	5'-GAGTGTGCGAATGTGAGGAA-3'	215	58.4	(Courbon et al., 2018)
		RP	5'-AATTAGCAGGAGGCCAAGTG-3'		58.4	
3	<i>RANKL</i>	FP	5'-CCGAGACTACGGCAAGTACC-3'	208	62.5	(Neog et al., 2017)
		RP	5'-CTGCGCTCGAAAGTACAGGA-3'		60.5	
4	<i>DKK1</i>	FP	5'-CAACGCGATCAAGAACCTGC-3'	138	60.5	-
		RP	5'-CAAGGGTAGGGCTGGTAGTT-3'		60.5	
5	<i>NFATc1</i>	FP	5'-ATACATGAGCCCATCCCTGC-3'	155	60.5	-
		RP	5'-GTCCTCCAGCAGAAGCCTTC-3'		62.5	
6	<i>GAPDH</i>	FP	5'-GTGATGGGTGTGAACCACGA-3'	141	60.5	-
		RP	5'-GACTGTGGTCATGAGCCCTT-3'		60.5	

5.2.2.4. *In vivo* therapeutic efficacy of dual-drug nanoparticles loaded hydrogel

5.2.2.4.1. *AA induction and monitoring*

The AIA rat model was established by injecting FCA in female SD rats, **as described in section 5.2.1.11**. The animals were regularly monitored, and the arthritis parameters were measured from day 4 to day 33 following FCA immunization (Deng et al., 2021; El-Sheikh et al., 2019; Helmy et al., 2017; Pandey et al., 2018; Zeb et al., 2017). After 12 days of the arthritis induction, the rats with uniform swelling and redness in the FCA-injected paws were selected for the study (Pandey et al., 2018; Zeb et al., 2017). The rats were randomly divided into seven groups (n = 4), (i) regular healthy control group (standard control), (ii) arthritis group (FCA-challenged and injected with sterile PBS, arthritis control), (iii) PEITC NE HG challenged with FCA, (iv) MTX NP HG challenged with FCA, (v) Free PEITC and Free MTX (Free PEITC + Free MTX) treated group challenged with FCA, (vi) DD NP HG group challenged with FCA, and (vii) BD NP HG treated group challenged with FCA. The treatments were started from day 12 by IA injecting 50 μ L of the test substances directly into the knee joint area of arthritic rats on days 12, 17, 22, and 27 after FCA immunization (Kim et al., 2019).

5.2.2.4.2. *Assessment of arthritis progression upon FCA administration*

The paw edema in each rat was examined at specific time points on the 12th, 15th, 20th, 25th, 30th, and 33rd day after administration of different formulations (Gou et al., 2017; Vincenzi et al., 2013). Paw edema volume (expressed in *ml*) was measured by making a visible mark on each paw at the tibiotarsal joint and dipping the paw at the marked level. The displaced volumes were recorded using a digital plethysmometer (WBP01, Vihan Techno Services, India). The paw thickness (expressed in *mm*) was measured using a digital micrometer (Mitutoyo, Japan) at defined time points. The body weight of rats was measured using a standard digital weighing

balance. Every four days, from day 0 to day 32, the body weight of each animal was recorded and shown as (g) (Pan et al., 2017). The arthritis score was calculated by microscopically observing the swelling and redness of joint edema of periarticular tissues in the FCA-injected and non-injected hind paws as per the **method described in section 5.2.1.13.2**. The severity of arthritis and therapeutic efficacy of the formulation was assessed based on the scores obtained by the rats from the treatment groups (on day 12, 15, 20, 25, 30, and 33) (Asenso et al., 2019; Qian et al., 2017; Wei et al., 2013).

5.2.2.4.3. Blood collection and serum separation

Blood was withdrawn from each animal by retro-orbital plexus bleeding under isoflurane anesthesia and sacrificed by CO₂ asphyxiation at the endpoint (33rd day). The serum separation protocol was followed per the **method described in section 5.2.1.13.3**.

5.2.2.4.4. Determination of thymus and spleen index

The rats from the various treatment groups were sacrificed using CO₂ asphyxia on the final day (33rd day) to isolate the immune organs (thymus and spleen) as per the **method described in section 5.2.1.13.4**.

5.2.2.4.5. Evaluation of oxidative stress

The biochemical markers such as MDA, NO, GSH, and MPO to assess the oxidative stress were measured per **protocols described in section 5.2.1.13.5**.

5.2.2.4.6. Evaluation of cytokines levels in the serum

The mean serum levels of representative pro-inflammatory cytokines ((TNF- α , IL-1 β , IL-17A, IL-6), anti-inflammatory cytokine (IL-10), and bone erosion marker (RANKL) were estimated using the ELISA assays. The protocols and ELISA kits were used for this study, as **described in section 5.2.1.13.6**.

5.2.2.4.7. Biochemical test to assess liver and kidney function

The serum levels of different biochemical markers in different treatment animal groups at the endpoint (33rd day) were performed per the methods and kits **described in section 5.2.1.13.7.**

5.2.2.4.8. Histopathological assessment

At the end of the studies (on day 37: Part A and day 33: Part B), the rats were sacrificed to dissect the hind limbs of each group. The excised hind limbs were preserved in 10 % neutral buffered formalin and later decalcified with 14 % neutral EDTA solution. The decalcified tissue embedded in paraffin blocks was sliced using an automated Rotary Microtome (HistoCore AUTOCUT, Leica Biosystems, Germany). On the sliced sections, H&E, SO-FG, and T&B staining were performed according to standard protocols for microscopical observations (Deng et al., 2021; Ren et al., 2021).

5.2.2.5. Statistical analysis

All quantitative parameters are presented as the mean \pm SD. GraphPad Prism 8.0 (GraphPad Software, La Jolla, CA, USA) was used for statistical analysis. Comparative analysis between multiple groups (more than 2 groups) was carried out by one-way analysis of variance (ANOVA) followed by Dunnett's multiple comparisons tests. A two-tailed paired Student's t-test was used to compare the difference between the two groups. The difference with p values: * $p < 0.05$, ** $p < 0.01$, *** $p < 0.001$ was considered statistically significant.

Chapter 6

Bibliography

- A.M. Bendele, 2001. Animal models of rheumatoid arthritis. *J. Musculoskelet. Neuronal Interact.* 1, 377–385.
- Abdel Jaleel, G.A., Azab, S.S., el-Bakly, W.M., Hassan, A., 2021. 'Methyl palmitate attenuates adjuvant induced arthritis in rats by decrease of CD68 synovial macrophages. *Biomed. Pharmacother.* 137, 111347. <https://doi.org/10.1016/j.biopha.2021.111347>
- Abdeltawab, H., Svirskis, D., Sharma, M., 2020. Formulation strategies to modulate drug release from poloxamer based in situ gelling systems. *Expert Opin. Drug Deliv.* 17, 495–509. <https://doi.org/10.1080/17425247.2020.1731469>
- Aborehab, N.M., El Bishbishy, M.H., Refaiy, A., Waly, N.E., 2017. A putative Chondroprotective role for IL-1 β and MPO in herbal treatment of experimental osteoarthritis. *BMC Complement. Altern. Med.* 17, 495. <https://doi.org/10.1186/s12906-017-2002-y>
- Ahmad, U., Sohail, M., Ahmad, M., Minhas, M.U., Khan, S., Hussain, Z., Kousar, M., Mohsin, S., Abbasi, M., Shah, S.A., Rashid, H., 2019. Chitosan based thermosensitive injectable hydrogels for controlled delivery of loxoprofen: development, characterization and in-vivo evaluation. *Int. J. Biol. Macromol.* 129, 233–245. <https://doi.org/10.1016/j.ijbiomac.2019.02.031>
- Ahsan, A., Farooq, M.A., Parveen, A., 2020. Thermosensitive chitosan-based injectable hydrogel as an efficient anticancer drug carrier. *ACS Omega* 5, 20450–20460. <https://doi.org/10.1021/acsomega.0c02548>
- Alivernini, S., Firestein, G.S., McInnes, I.B., 2011. The pathogenesis of rheumatoid arthritis.

Immunity 55, 2255–2270. <https://doi.org/10.1016/j.immuni.2022.11.009>

Alonso, J.M., Del Olmo, J.A., Gonzalez, R.P., Saez-martinez, V., 2021. Injectable hydrogels: From laboratory to industrialization. *Polymers (Basel)*. 13, 650. <https://doi.org/10.3390/polym13040650>

Alpízar-Rodríguez, D., Pluchino, N., Canny, G., Gabay, C., Finckh, A., 2017. The role of female hormonal factors in the development of rheumatoid arthritis. *Rheumatol. (United Kingdom)* 56, 1254–1263. <https://doi.org/10.1093/rheumatology/kew318>

Alunno, A., Carubbi, F., Giacomelli, R., Gerli, R., 2017. Cytokines in the pathogenesis of rheumatoid arthritis: New players and therapeutic targets. *BMC Rheumatol.* 1, 3. <https://doi.org/10.1186/s41927-017-0001-8>

Aly, U.F., Abou-Taleb, H.A., Abdellatif, Ah.A.H., Tolba, N.S., 2019. Formulation and evaluation of simvastatin polymeric nanoparticles loaded in hydrogel for optimum wound healing purpose. *Drug Des. Devel. Ther.* 13, 1567–1580. <https://doi.org/10.2147/DDDT.S198413>

Arunkumar, P., Indulekha, S., Vijayalakshmi, S., Srivastava, R., 2016. Poly (caprolactone) microparticles and chitosan thermogels based injectable formulation of etoricoxib for the potential treatment of osteoarthritis. *Mater. Sci. Eng. C* 61, 534–544. <https://doi.org/10.1016/j.msec.2015.12.039>

Asagiri, M., Sato, K., Usami, T., Ochi, S., Nishina, H., Yoshida, H., Morita, I., Wagner, E.F., Mak, T.W., Serfling, E., Takayanagi, H., 2005. Autoamplification of NFATc1 expression determines its essential role in bone homeostasis. *J. Exp. Med.* 202, 1261–1269.

<https://doi.org/10.1084/jem.20051150>

Asenso, J., Yu, J., Xiao, F., Zhao, M., Wang, J., Wu, Y., Wang, C., Wei, W., 2019. Methotrexate improves the anti-arthritic effects of Paeoniflorin-6'-O-benzene sulfonate by enhancing its pharmacokinetic properties in adjuvant-induced arthritis rats. *Biomed. Pharmacother.* 112, 108644. <https://doi.org/10.1016/j.biopha.2019.108644>

Bailly, A.L., Correard, F., Popov, A., Tselikov, G., Chaspoul, F., Appay, R., Al-Kattan, A., Kabashin, A. V., Braguer, D., Esteve, M.A., 2019. In vivo evaluation of safety, biodistribution and pharmacokinetics of laser-synthesized gold nanoparticles. *Sci. Rep.* 9, 12890. <https://doi.org/10.1038/s41598-019-48748-3>

Barra, L., Pope, J., Bessette, L., Haraoui, B., Bykerk, V., 2011. Lack of seroconversion of rheumatoid factor and anti-cyclic citrullinated peptide in patients with early inflammatory arthritis: A systematic literature review. *Rheumatology* 50, 311–316. <https://doi.org/10.1093/rheumatology/keq190>

Bartok, B., Firestein, G.S., 2010. Fibroblast-like synoviocytes: Key effector cells in rheumatoid arthritis. *Immunol. Rev.* 233, 233–255. <https://doi.org/10.1111/j.0105-2896.2009.00859.x>

Ben Mrid, R., Bouchmaa, N., Ainani, H., El Fatimy, R., Malka, G., Mazini, L., 2022. Anti-rheumatoid drugs advancements: New insights into the molecular treatment of rheumatoid arthritis. *Biomed. Pharmacother.* 151, 113126. <https://doi.org/10.1016/j.biopha.2022.113126>

Bergholt, N.L., Lysdahl, H., Lind, M., Foldager, C.B., 2019. A Standardized Method of Applying Toluidine Blue Metachromatic Staining for Assessment of Chondrogenesis.

Cartilage 10, 370–374. <https://doi.org/10.1177/1947603518764262>

Brizzolari, A., Dei Cas, M., Cialoni, D., Marroni, A., Morano, C., Samaja, M., Paroni, R., Rubino, F.M., 2021. High-Throughput Griess Assay of Nitrite and Nitrate in Plasma and Red Blood Cells for Human Physiology Studies under Extreme Conditions. *Molecules* 26, 4569. <https://doi.org/10.3390/molecules26154569>

Cang, S., Ma, Y., Chiao, J. wei, Liu, D., 2014. Phenethyl isothiocyanate and paclitaxel synergistically enhanced apoptosis and alpha-tubulin hyperacetylation in breast cancer cells. *Exp. Hematol. Oncol.* 3, 5. <https://doi.org/10.1186/2162-3619-3-5>

Carbinatto, F.M., de Castro, A.D., Evangelista, R.C., Cury, B.S.F., 2014. Insights into the swelling process and drug release mechanisms from cross-linked pectin/high amylose starch matrices. *Asian J. Pharm. Sci.* 9, 27–34. <https://doi.org/10.1016/j.ajps.2013.12.002>

Catrina, A.I., Joshua, V., Klareskog, L., Malmström, V., 2016. Mechanisms involved in triggering rheumatoid arthritis. *Immunol. Rev.* 269, 162–174. <https://doi.org/10.1111/imr.12379>

Chang, J.Y., Oh, Y.K., Choi, H. gon, Kim, Y.B., Kim, C.K., 2002. Rheological evaluation of thermosensitive and mucoadhesive vaginal gels in physiological conditions. *Int. J. Pharm.* 241, 155–163. [https://doi.org/10.1016/S0378-5173\(02\)00232-6](https://doi.org/10.1016/S0378-5173(02)00232-6)

Chatterjee, S., Hui, P.C. leung, Kan, C. wai, Wang, W., 2019. Dual-responsive (pH/temperature) Pluronic F-127 hydrogel drug delivery system for textile-based transdermal therapy. *Sci. Rep.* 9, 11658. <https://doi.org/10.1038/s41598-019-48254-6>

Chen, J., Wang, H., Long, W., Shen, X., Wu, D., Song, S.S., Sun, Y.M., Liu, P.X., Fan, S., Fan,

- F., Zhang, X.D., 2013. Sex differences in the toxicity of polyethylene glycol-coated gold nanoparticles in mice. *Int. J. Nanomedicine* 8, 2409–2419. <https://doi.org/10.2147/IJN.S46376>
- Chen, J., Wright, K., Davis, J.M., Jeraldo, P., Marietta, E. V., Murray, J., Nelson, H., Matteson, E.L., Taneja, V., 2016. An expansion of rare lineage intestinal microbes characterizes rheumatoid arthritis. *Genome Med.* 8, 43. <https://doi.org/10.1186/s13073-016-0299-7>
- Chen, Jingqin, Qi, J., Chen, C., Chen, Jianhai, Liu, L., Gao, R., Zhang, T., Song, L., Ding, D., Zhang, P., Liu, C., 2020. Tocilizumab–Conjugated Polymer Nanoparticles for NIR-II Photoacoustic-Imaging-Guided Therapy of Rheumatoid Arthritis. *Adv. Mater.* 32, e2003399. <https://doi.org/10.1002/adma.202003399>
- Chen, X., Lin, H., Chen, J., Wu, L., Zhu, J., Ye, Y., Chen, S., Du, H., Li, J., 2021. Paclitaxel Inhibits Synoviocyte Migration and Inflammatory Mediator Production in Rheumatoid Arthritis. *Front. Pharmacol.* 12, 714566. <https://doi.org/10.3389/fphar.2021.714566>
- Chen, Z., Xing, L., Fan, Q., Cheetham, A.G., Lin, R., Holt, B., Chen, L., Xiao, Y., Cui, H., 2017. Drug-bearing supramolecular filament hydrogels as anti-inflammatory agents. *Theranostics* 7, 2003–2014. <https://doi.org/10.7150/thno.19404>
- Choudhary, N., Bhatt, L.K., Prabhavalkar, K.S., 2018. Experimental animal models for rheumatoid arthritis. *Immunopharmacol. Immunotoxicol.* 40, 193–200. <https://doi.org/10.1080/08923973.2018.1434793>
- Choudhary, N., Gupta, R., Bhatt, L.K., 2020. Anti-rheumatic activity of Phenethyl isothiocyanate via inhibition of histone deacetylase-1. *Chem. Biol. Interact.* 324, 109095.

<https://doi.org/10.1016/j.cbi.2020.109095>

Chuang, W.T., Liu, Y.T., Huang, C.S., Lo, C.W., Yao, H.T., Chen, H.W., Lii, C.K., 2019. Benzyl Isothiocyanate and Phenethyl Isothiocyanate Inhibit Adipogenesis and Hepatosteatosis in Mice with Obesity Induced by a High-Fat Diet. *J. Agric. Food Chem.* 67, 7136–7146. <https://doi.org/10.1021/acs.jafc.9b02668>

Chung, C.K., Fransen, M.F., van der Maaden, K., Campos, Y., García-Couce, J., Kralisch, D., Chan, A., Ossendorp, F., Cruz, L.J., 2020. Thermosensitive hydrogels as sustained drug delivery system for CTLA-4 checkpoint blocking antibodies. *J. Control. Release* 323, 1–11. <https://doi.org/10.1016/j.jconrel.2020.03.050>

Cohen, S., Emery, P., 2010. The American College of Rheumatology/European League Against Rheumatism criteria for the classification of rheumatoid arthritis: A game changer. *Arthritis Rheum.* 62, 2592–2594. <https://doi.org/10.1002/art.27583>

Cong, Z., Shi, Y., Wang, Yang, Wang, Yanhong, Niu, J., Chen, N., Xue, H., 2018. A novel controlled drug delivery system based on alginate hydrogel/chitosan micelle composites. *Int. J. Biol. Macromol.* 107, 855–864. <https://doi.org/10.1016/j.ijbiomac.2017.09.065>

Coscueta, E.R., Sousa, A.S., Reis, C.A., Pintado, M., 2021. Chitosan-olive oil microparticles for phenylethyl isothiocyanate delivery: Optimal formulation. *PLoS One* 16, e0248257. <https://doi.org/10.1371/journal.pone.0248257>

Courbon, G., Lamarque, R., Gerbaix, M., Caire, R., Linossier, M.T., Laroche, N., Thomas, M., Thomas, T., Vico, L., Marotte, H., 2018. Early sclerostin expression explains bone formation inhibition before arthritis onset in the rat adjuvant-induced arthritis model. *Sci.*

Rep. 8, 3492. <https://doi.org/10.1038/s41598-018-21886-w>

Cronstein, B.N., Aune, T.M., 2020. Methotrexate and its mechanisms of action in inflammatory arthritis. *Nat. Rev. Rheumatol.* 16, 145–154. <https://doi.org/10.1038/s41584-020-0373-9>

Crowson, C.S., Matteson, E.L., Myasoedova, E., Michet, C.J., Ernste, F.C., Warrington, K.J., Davis, J.M., Hunder, G.G., Thorneau, T.M., Gabriel, S.E., 2011. The lifetime risk of adult-onset rheumatoid arthritis and other inflammatory autoimmune rheumatic diseases. *Arthritis Rheum.* 63, 633–639. <https://doi.org/10.1002/art.30155>

Dalal, S.R., Hussein, M.H., El-Naggar, N.E.A., Mostafa, S.I., Shaaban-Dessuuki, S.A., 2021. Characterization of alginate extracted from *Sargassum latifolium* and its use in *Chlorella vulgaris* growth promotion and riboflavin drug delivery. *Sci. Rep.* 11, 16741. <https://doi.org/10.1038/s41598-021-96202-0>

Danaei, M., Dehghankhold, M., Ataei, S., Hasanzadeh Davarani, F., Javanmard, R., Dokhani, A., Khorasani, S., Mozafari, M.R., 2018. Impact of particle size and polydispersity index on the clinical applications of lipidic nanocarrier systems. *Pharmaceutics* 10, 57. <https://doi.org/10.3390/pharmaceutics10020057>

Danhier, F., Danhier, P., Schleich, N., Po, C., Laurent, S., Sibret, P., Jérôme, C., Poucelle, V., Gallez, B., Pr at, V., 2018. Tumor Targeting by RGD-Grafted PLGA-Based Nanotheranostics Loaded with Paclitaxel and Superparamagnetic Iron Oxides, in: *Methods in Pharmacology and Toxicology*. https://doi.org/10.1007/7653_2015_43

Dar, W.R., Mir, I.A., Siddiq, S., Nadeem, M., Singh, G., 2022. The Assessment of Fatigue in Rheumatoid Arthritis Patients and Its Impact on Their Quality of Life. *Clin. Pract.* 12, 591–

598. <https://doi.org/10.3390/clinpract12040062>

Davoodi, P., Ng, W.C., Yan, W.C., Srinivasan, M.P., Wang, C.H., 2016. Double-walled microparticles-embedded self-cross-linked, injectable, and antibacterial hydrogel for controlled and sustained release of chemotherapeutic agents. *ACS Appl. Mater. Interfaces* 8, 22785–22800. <https://doi.org/10.1021/acsami.6b03041>

Dayalan Naidu, S., Suzuki, T., Yamamoto, M., Fahey, J.W., Dinkova-Kostova, A.T., 2018. Phenethyl Isothiocyanate, a Dual Activator of Transcription Factors NRF2 and HSF1. *Mol. Nutr. Food Res.* 62, e1700908. <https://doi.org/10.1002/mnfr.201700908>

Deane, K.D., 2013. Can rheumatoid arthritis be prevented? *Best Pract. Res. Clin. Rheumatol.* 27, 467–485. <https://doi.org/10.1016/j.berh.2013.09.002>

Deng, C., Zhang, Q., He, P., Zhou, B., He, K., Sun, X., Lei, G., Gong, T., Zhang, Z., 2021. Targeted apoptosis of macrophages and osteoclasts in arthritic joints is effective against advanced inflammatory arthritis. *Nat. Commun.* 12, 2174. <https://doi.org/10.1038/s41467-021-22454-z>

Diaz-Rodriguez, P., Mariño, C., Vázquez, J.A., Caeiro-Rey, J.R., Landin, M., 2021. Targeting joint inflammation for osteoarthritis management through stimulus-sensitive hyaluronic acid based intra-articular hydrogels. *Mater. Sci. Eng. C Mater. Biol. Appl.* 128, 112254. <https://doi.org/10.1016/j.msec.2021.112254>

Edwards, J.C., 1994. The nature and origins of synovium: experimental approaches to the study of synoviocyte differentiation. *J. Anat.* 184 (Pt 3), 493–501.

El-Husseiny, H.M., Mady, E.A., Hamabe, L., Abugomaa, A., Shimada, K., Yoshida, T., Tanaka,

- T., Yokoi, A., Elbadawy, M., Tanaka, R., 2022. Smart/stimuli-responsive hydrogels: Cutting-edge platforms for tissue engineering and other biomedical applications. *Mater. Today Bio* 13, 100186. <https://doi.org/10.1016/j.mtbio.2021.100186>
- El-Sheikh, S.M.A., Abd El-Alim, A.E.A.F., Galal, A.A.A., El-Sayed, R.G., El-naseery, N.I., 2019. Anti-arthritic effect of β -caryophyllene and its ameliorative role on methotrexate and/or leflunomide-induced side effects in arthritic rats. *Life Sci.* 233, 116750. <https://doi.org/10.1016/j.lfs.2019.116750>
- Ellman, G.L., 1959. Tissue sulfhydryl groups. *Arch. Biochem. Biophys.* 82, 70–77. [https://doi.org/10.1016/0003-9861\(59\)90090-6](https://doi.org/10.1016/0003-9861(59)90090-6)
- Essien, E.N., Revi, N., Khatri, V., Liu, S., Van Thiel, G., Bijukumar, D., 2023. Methotrexate and sulfuraphane loaded PBA-G5-PAMAM dendrimers as a combination therapy for anti-inflammatory response in an intra-articular joint arthritic animal model. *Int. J. Pharm.* 642, 123150. <https://doi.org/10.1016/j.ijpharm.2023.123150>
- Fan, Z., Fu, M., Xu, Z., Zhang, B., Li, Z., Li, H., Zhou, X., Liu, X., Duan, Y., Lin, P.H., Duann, P., Xie, X., Ma, J., Liu, Z., Guan, J., 2017. Sustained Release of a Peptide-Based Matrix Metalloproteinase-2 Inhibitor to Attenuate Adverse Cardiac Remodeling and Improve Cardiac Function Following Myocardial Infarction. *Biomacromolecules* 18, 2820–2829. <https://doi.org/10.1021/acs.biomac.7b00760>
- Finckh, A., Gilbert, B., Hodkinson, B., Bae, S.C., Thomas, R., Deane, K.D., Alpizar-Rodriguez, D., Lauper, K., 2022. Global epidemiology of rheumatoid arthritis. *Nat. Rev. Rheumatol.* 18, 591–602. <https://doi.org/10.1038/s41584-022-00827-y>

- Firestein, G.S., 2003. Evolving concepts of rheumatoid arthritis. *Nature* 423, 356–361.
<https://doi.org/10.1038/nature01661>
- Frank-Bertoncelj, M., Trenkmann, M., Klein, K., Karouzakis, E., Rehrauer, H., Bratus, A., Kolling, C., Armaka, M., Filer, A., Michel, B.A., Gay, R.E., Buckley, C.D., Kollias, G., Gay, S., Ospelt, C., 2017. Epigenetically-driven anatomical diversity of synovial fibroblasts guides joint-specific fibroblast functions. *Nat. Commun.* 8, 14852.
<https://doi.org/10.1038/ncomms14852>
- Gan, N., Wu, Y.C., Brunet, M., Garrido, C., Chung, F.L., Dai, C., Mi, L., 2010. Sulforaphane activates heat shock response and enhances proteasome activity through up-regulation of Hsp27. *J. Biol. Chem.* 285, 35528–35536. <https://doi.org/10.1074/jbc.M110.152686>
- Gao, L., Xia, L., Zhang, R., Duan, D., Liu, X., Xu, J., Luo, L., 2017. Enhanced antitumor efficacy of poly (D , L-lactide- on sarcoma 180 tumor-bearing mice. *Drug Des. Devel. Ther.* 11, 3065–3075. DOI: 10.2147/DDDT.S143942
- Giknis, M L A., Clifford, C.B., 2008. Clinical laboratory parameters for crl: WI(Han) rats. Charles River Lab. 1–14.
- Gou, K.J., Zeng, R., Dong, Y., Hu, Q.Q., Hu, H.W.Y., Maffucci, K.G., Dou, Q.L., Yang, Q.B., Qin, X.H., Qu, Y., 2017. Anti-inflammatory and analgesic effects of Polygonum orientale L. extracts. *Front. Pharmacol.* 8, 562. <https://doi.org/10.3389/fphar.2017.00562>
- Gravallese, E.M., 2002. Bone destruction in arthritis. *Ann. Rheum. Dis.* 61, 84–86.
https://doi.org/10.1136/ard.61.suppl_2.ii84
- Gregersen, P.K., Silver, J., Winchester, R.J., 1987. The shared epitope hypothesis. An approach

- to understanding the molecular genetics of susceptibility to rheumatoid arthritis. *Arthritis Rheum.* 30, 1205–1213. DOI: 10.1002/art.1780301102
- Guo, Q., Wang, Y., Xu, D., Nossent, J., Pavlos, N.J., Xu, J., 2018. Rheumatoid arthritis: Pathological mechanisms and modern pharmacologic therapies. *Bone Res.* 6, 15. <https://doi.org/10.1038/s41413-018-0016-9>
- Hajishengallis, G., 2015. Periodontitis: From microbial immune subversion to systemic inflammation. *Nat. Rev. Immunol.* 15, 30–44. <https://doi.org/10.1038/nri3785>
- Haloi, P., Chawla, S., Konkimalla, V.B., 2023a. Thermosensitive smart hydrogel of PEITC ameliorates the therapeutic efficacy in rheumatoid arthritis. *Eur. J. Pharm. Sci.* 181, 106367. <https://doi.org/10.1016/j.ejps.2022.106367>
- Haloi, P., Lokesh, B.S., Chawla, S., Konkimalla, V.B., 2023b. Formulation of a dual drug-loaded nanoparticulate co-delivery hydrogel system and its validation in rheumatoid arthritis animal model. *Drug Deliv.* 30, 2184307. <https://doi.org/10.1080/10717544.2023.2184307>
- Hashemnejad, S.M., Badruddoza, A.Z.M., Zarket, B., Ricardo Castaneda, C., Doyle, P.S., 2019. Thermoresponsive nanoemulsion-based gel synthesized through a low-energy process. *Nat. Commun.* 10, 2749. <https://doi.org/10.1038/s41467-019-10749-1>
- Hassan, U.H., Alamgeer, Shahzad, M., Shabbir, A., Jahan, S., Saleem, M., Bukhari, I.A., Assiri, A.M., 2019. Amelioration of adjuvant induced arthritis in Sprague Dawley rats through modulation of inflammatory mediators by *Ribes alpestre* Decne. *J. Ethnopharmacol.* 235, 460–471. <https://doi.org/10.1016/j.jep.2019.02.025>
- He, Q., Su, G., Liu, K., Zhang, F., Jiang, Y., Gao, J., Liu, L., Jiang, Z., Jin, M., Xie, H., 2017.

Sex-specific reference intervals of hematologic and biochemical analytes in Sprague-Dawley rats using the nonparametric rank percentile method. *PLoS One* 12, e0189837. <https://doi.org/10.1371/journal.pone.0189837>

Helmy, H.S., El-Sahar, A.E., Sayed, R.H., Shamma, R.N., Salama, A.H., Elbaz, E.M., 2017. Therapeutic effects of lornoxicam-loaded nanomicellar formula in experimental models of rheumatoid arthritis. *Int. J. Nanomedicine* 12, 7015–7023. <https://doi.org/10.2147/IJN.S147738>

Hemelryck, S. Van, Dewulf, J., Niekus, H., van Heerden, M., Ingelse, B., Holm, R., Mannaert, E., Langguth, P., 2019. In vitro evaluation of poloxamer in situ forming gels for bedaquiline fumarate salt and pharmacokinetics following intramuscular injection in rats. *Int. J. Pharm.* X 1, 100016. <https://doi.org/10.1016/j.ijpx.2019.100016>

Holers, V.M., 2013. Autoimmunity to citrullinated proteins and the initiation of rheumatoid arthritis. *Curr. Opin. Immunol.* 25, 728–735. <https://doi.org/10.1016/j.coi.2013.09.018>

Hu, B., Gao, M., Boakye-Yiadom, K.O., Ho, W., Yu, W., Xu, X., Zhang, X.Q., 2021. An intrinsically bioactive hydrogel with on-demand drug release behaviors for diabetic wound healing. *Bioact. Mater.* 6, 4592–4606. <https://doi.org/10.1016/j.bioactmat.2021.04.040>

Hu, J., Straub, J., Xiao, D., Singh, S. V., Yang, H.S., Sonenberg, N., Vatsyayan, J., 2007. Phenethyl isothiocyanate, a cancer chemopreventive constituent of cruciferous vegetables, inhibits cap-dependent translation by regulating the level and phosphorylation of 4E-BP1. *Cancer Res.* 67, 3569–3573. <https://doi.org/10.1158/0008-5472.CAN-07-0392>

Huang, J., Fu, X., Chen, X., Li, Z., Huang, Y., Liang, C., 2021. Promising Therapeutic Targets

- for Treatment of Rheumatoid Arthritis. *Front. Immunol.* 12, 686155.
<https://doi.org/10.3389/fimmu.2021.686155>
- Jang, C.H., Koo, Y.W., Kim, G.H., 2020. ASC/chondrocyte-laden alginate hydrogel/PCL hybrid scaffold fabricated using 3D printing for auricle regeneration. *Carbohydr. Polym.* 248, 116776. <https://doi.org/10.1016/j.carbpol.2020.116776>
- Jang, J.H., Jeong, S.H., Lee, Y.B., 2019. Preparation and in vitro/in vivo characterization of polymeric nanoparticles containing methotrexate to improve lymphatic delivery. *Int. J. Mol. Sci.* 20, 3312. <https://doi.org/10.3390/ijms20133312>
- Jay, G.D., 1992. Characterization of a bovine synovial fluid lubricating factor. I. Chemical, surface activity and lubricating properties. *Connect. Tissue Res.* 28, 71–88.
<https://doi.org/10.3109/03008209209014228>
- Jay, G.D., Torres, J.R., Warman, M.L., Laderer, M.C., Breuer, K.S., 2007. The role of lubricin in the mechanical behavior of synovial fluid. *Proc. Natl. Acad. Sci. U. S. A.* 104, 6194–6199.
<https://doi.org/10.1073/pnas.0608558104>
- Jeong, M., Park, J.H., 2021. Nanomedicine for the Treatment of Rheumatoid Arthritis. *Mol. Pharm.* 18, 539–549. <https://doi.org/10.1021/acs.molpharmaceut.0c00295>
- Jeong, S., Kim, B.W., Park, M., Ban, E., Lee, S.H., Kim, A., 2020. Improved diabetic wound healing by EGF encapsulation in gelatin-alginate coacervates. *Pharmaceutics* 12, 334.
<https://doi.org/10.3390/pharmaceutics12040334>
- Jin, I.S., Jo, M.J., Park, C.W., Chung, Y.B., Kim, J.S., Shin, D.H., 2020. Physicochemical, pharmacokinetic, and toxicity evaluation of soluplus® polymeric micelles encapsulating

fenbendazole. *Pharmaceutics* 12, 1000. <https://doi.org/10.3390/pharmaceutics12101000>

Jing, R., Ban, Y., Xu, W., Nian, H., Guo, Y., Geng, Y., Zang, Y., Zheng, C., 2019. Therapeutic effects of the total lignans from *Vitex negundo* seeds on collagen-induced arthritis in rats. *Phytomedicine* 58, 152825. <https://doi.org/10.1016/j.phymed.2019.152825>

Joshi, N., Yan, J., Levy, S., Bhagchandani, S., Slaughter, K. V., Sherman, N.E., Amirault, J., Wang, Y., Riegel, L., He, X., Rui, T.S., Valic, M., Vemula, P.K., Miranda, O.R., Levy, O., Gravallesse, E.M., Aliprantis, A.O., Ermann, J., Karp, J.M., 2018. Towards an arthritis flare-responsive drug delivery system. *Nat. Commun.* 9, 1275. <https://doi.org/10.1038/s41467-018-03691-1>

Juarez, M., McGettrick, H.M., Scheel-Toellner, D., Yeo, L., Spengler, J., de Paz, B., Hardy, R., Cooper, M., Raza, K., Buckley, C.D., Filer, A., 2016. DKK1 expression by synovial fibroblasts in very early rheumatoid arthritis associates with lymphocyte adhesion in an in vitro flow co-culture system. *Arthritis Res. Ther.* 18, 14. <https://doi.org/10.1186/s13075-016-0915-3>

Jung, Y. seok, Park, W., Park, H., Lee, D.K., Na, K., 2017. Thermo-sensitive injectable hydrogel based on the physical mixing of hyaluronic acid and Pluronic F-127 for sustained NSAID delivery. *Carbohydr. Polym.* 156, 403–408. <https://doi.org/10.1016/j.carbpol.2016.08.068>

Kalinina, E. V., Chernov, N.N., Novichkova, M.D., 2014. Role of glutathione, glutathione transferase, and glutaredoxin in regulation of redox-dependent processes. *Biochem.* 79, 1562–1583. <https://doi.org/10.1134/S0006297914130082>

Karolewicz, B., Gajda, M., Górniak, A., Owczarek, A., Mucha, I., 2017. Pluronic F127 as a

suitable carrier for preparing the imatinib base solid dispersions and its potential in development of a modified release dosage forms: Thermal, spectroscopic, microscopic, and dissolution studies. *J. Therm. Anal. Calorim.* 130, 383–390. <https://doi.org/10.1007/s10973-017-6139-1>

Ke, X., Li, M., Wang, Xiaoqing, Liang, J., Wang, Xing, Wu, S., Long, M., Hu, C., 2020. An injectable chitosan/dextran/ β -glycerophosphate hydrogel as cell delivery carrier for therapy of myocardial infarction. *Carbohydr. Polym.* 229, 115516. <https://doi.org/10.1016/j.carbpol.2019.115516>

Kharlamova, N., Jiang, X., Sherina, N., Potempa, B., Israelsson, L., Quirke, A.M., Eriksson, K., Yucel-Lindberg, T., Venables, P.J., Potempa, J., Alfredsson, L., Lundberg, K., 2016. Antibodies to Porphyromonas gingivalis Indicate Interaction between Oral Infection, Smoking, and Risk Genes in Rheumatoid Arthritis Etiology. *Arthritis Rheumatol.* 68, 604–613. <https://doi.org/10.1002/art.39491>

Kim, J., Kim, H.Y., Song, S.Y., Go, S.H., Sohn, H.S., Baik, S., Soh, M., Kim, K., Kim, D., Kim, H.C., Lee, N., Kim, B.S., Hyeon, T., 2019. Synergistic Oxygen Generation and Reactive Oxygen Species Scavenging by Manganese Ferrite/Ceria Co-decorated Nanoparticles for Rheumatoid Arthritis Treatment. *ACS Nano* 13, 3206–3217. <https://doi.org/10.1021/acsnano.8b08785>

Kim, Y.J., Lee, D.H., Ahn, J., Chung, W.J., Jang, Y.J., Seong, K.S., Moon, J.H., Ha, T.Y., Jung, C.H., 2015. Pharmacokinetics, tissue distribution, and anti-lipogenic/adipogenic effects of allyl-isothiocyanate metabolites. *PLoS One* 10, e0132151. <https://doi.org/10.1371/journal.pone.0132151>

- Klouda, L., Mikos, A.G., 2008. Thermoresponsive hydrogels in biomedical applications. *Eur. J. Pharm. Biopharm.* 68, 34–45. <https://doi.org/10.1016/j.ejpb.2007.02.025>
- Ko, J.Y., Choi, Y.J., Jeong, G.J., Im, G. Il, 2013. Sulforaphane-PLGA microspheres for the intra-articular treatment of osteoarthritis. *Biomaterials* 34, 5359–5368. <https://doi.org/10.1016/j.biomaterials.2013.03.066>
- Ko, S., Park, J.Y., Oh, Y.K., 2019. A microbial siderophore-inspired self-gelling hydrogel for noninvasive anticancer phototherapy. *Cancer Res.* 79, 6178–6189. <https://doi.org/10.1158/0008-5472.CAN-19-0975>
- Koland, M., Narayanan Vadakkepushpakath, A., John, A., Tharamelvelyil Rajendran, A., Raghunath, I., 2022. Thermosensitive In Situ Gels for Joint Disorders: Pharmaceutical Considerations in Intra-Articular Delivery. *Gels* 8, 723. <https://doi.org/10.3390/gels8110723>
- Konig, M.F., Abusleme, L., Reinholdt, J., Palmer, R.J., Teles, R.P., Sampson, K., Rosen, A., Nigrovic, P.A., Sokolove, J., Giles, J.T., Moutsopoulos, N.M., Andrade, F., 2016. *Aggregatibacter actinomycetemcomitans*-induced hypercitrullination links periodontal infection to autoimmunity in rheumatoid arthritis. *Sci. Transl. Med.* 8, 369ra176. <https://doi.org/10.1126/scitranslmed.aaj1921>
- Krishnamurthy, A., Joshua, V., Hensvold, A.H., Jin, T., Sun, M., Vivar, N., Ytterberg, A.J., Engström, M., Fernandes-Cerqueira, C., Amara, K., Magnusson, M., Wigerblad, G., Kato, J., Jiménez-Andrade, J.M., Tyson, K., Rapecki, S., Lundberg, K., Catrina, S.B., Jakobsson, P.J., Svensson, C., Malmström, V., Klareskog, L., Wähämaa, H., Catrina, A.I., 2016. Identification of a novel chemokine-dependent molecular mechanism underlying Rheumatoid arthritis-associated autoantibody-mediated bone loss. *Ann. Rheum. Dis.* 75,

721–729. <https://doi.org/10.1136/annrheumdis-2015-208093>

Kumar, H., Kim, I.S., More, S.V., Kim, B.W., Choi, D.K., 2014. Natural product-derived pharmacological modulators of Nrf2/ARE pathway for chronic diseases. *Nat. Prod. Rep.* 31, 109–139. <https://doi.org/10.1039/c3np70065h>

Laurent, L., Anquetil, F., Clavel, C., Ndong-Thiam, N., Offer, G., Miossec, P., Pasquali, J.L., Sebbag, M., Serre, G., 2015. IgM rheumatoid factor amplifies the inflammatory response of macrophages induced by the rheumatoid arthritis-specific immune complexes containing anticitrullinated protein antibodies. *Ann. Rheum. Dis.* 74, 1425–1431. <https://doi.org/10.1136/annrheumdis-2013-204543>

Lenz, T.L., Deutsch, A.J., Han, B., Hu, X., Okada, Y., Eyre, S., Knapp, M., Zhernakova, A., Huizinga, T.W.J., Abecasis, G., Becker, J., Boeckxstaens, G.E., Chen, W.M., Franke, A., Gladman, D.D., Gockel, I., Gutierrez-Achury, J., Martin, J., Nair, R.P., Nöthen, M.M., Onengut-Gumuscu, S., Rahman, P., Rantapää-Dahlqvist, S., Stuart, P.E., Tsoi, L.C., Van Heel, D.A., Worthington, J., Wouters, M.M., Klareskog, L., Elder, J.T., Gregersen, P.K., Schumacher, J., Rich, S.S., Wijmenga, C., Sunyaev, S.R., De Bakker, P.I.W., Raychaudhuri, S., 2015. Widespread non-additive and interaction effects within HLA loci modulate the risk of autoimmune diseases. *Nat. Genet.* 47, 1085–1090. <https://doi.org/10.1038/ng.3379>

Leyva-Gómez, G., Santillan-Reyes, E., Lima, E., Madrid-Martínez, A., Kröttsch, E., Quintanar-Guerrero, D., Garcíadiego-Cázares, D., Martínez-Jiménez, A., Hernández Morales, M., Ortega-Peña, S., Contreras-Figueroa, M.E., Cortina-Ramírez, G.E., Abarca-Buis, R.F., 2017. A novel hydrogel of poloxamer 407 and chitosan obtained by gamma irradiation

- exhibits physicochemical properties for wound management. *Mater. Sci. Eng. C Mater. Biol. Appl.* 74, 36–46. <https://doi.org/10.1016/j.msec.2016.12.127>
- Li, C., Li, H., Wang, Q., Zhou, M., Li, M., Gong, T., Zhang, Z., Sun, X., 2017. pH-sensitive polymeric micelles for targeted delivery to inflamed joints. *J. Control. Release* 246, 133–141. <https://doi.org/10.1016/j.jconrel.2016.12.027>
- Li, X., Wang, H., Zou, X., Su, H., Li, C., 2022. Methotrexate-loaded folic acid of solid-phase synthesis conjugated gold nanoparticles targeted treatment for rheumatoid arthritis. *Eur. J. Pharm. Sci.* 170, 106101. <https://doi.org/10.1016/j.ejps.2021.106101>
- Li, X., Yuan, K., Zhu, Q., Lu, Q., Jiang, H., Zhu, M., Huang, G., Xu, A., 2019. Andrographolide ameliorates rheumatoid arthritis by regulating the apoptosis–NETosis balance of neutrophils. *Int. J. Mol. Sci.* 20, 5035. <https://doi.org/10.3390/ijms20205035>
- Li, Y., Teng, Z., Chen, P., Song, Y., Luo, Y., Wang, Q., 2015. Enhancement of aqueous stability of allyl isothiocyanate using nanoemulsions prepared by an emulsion inversion point method. *J. Colloid Interface Sci.* 438, 130–137. <https://doi.org/10.1016/j.jcis.2014.09.055>
- Li, Z., Zhou, Y., Li, T., Zhang, J., Tian, H., 2021. Stimuli-responsive hydrogels: Fabrication and biomedical applications. *View* 3, 20200112. <https://doi.org/10.1002/viw.20200112>
- Lieber, E., Rao, C.N.R., Ramachandran, J., 1959. The infrared spectra of organic thiocyanates and isothiocyanates. *Spectrochim. Acta* 13, 296–299. [https://doi.org/10.1016/0371-1951\(59\)80030-8](https://doi.org/10.1016/0371-1951(59)80030-8)
- Lillian A. Mundt , Kristy Shanahan, 2011. Synovial fluid. in Graff's textbook of routine urinalysis and body fluids. Lippincott Williams & Wilkins: Philadelphia.

- Lin, J., He, Z., Liu, F., Feng, J., Huang, C., Sun, X., Deng, H., Wang, Y., Xi, L., Zhang, B., Zhu, Q., Su, F., Jelonek, K., Orchel, A., Kasperczyk, J., Li, S., Tran Vo, T.M., Piroonpan, T., Preuksarattanawut, C., Kobayashi, T., Potiyaraj, P., 2020. Hybrid hydrogels for synergistic periodontal antibacterial treatment with sustained drug release and NIR-responsive photothermal effect. *Int. J. Nanomedicine* 28, 290–299. <https://doi.org/10.2147/IJN.S248538>
- Linghang, Q., Yiyi, X., Guosheng, C., Kang, X., Jiyuan, T., Xiong, L., Guangzhong, W., Shuiqing, L., Yanju, L., 2020. Effects of Atractylodes Oil on Inflammatory Response and Serum Metabolites in Adjuvant Arthritis Rats. *Biomed. Pharmacother.* 127, 110130. <https://doi.org/10.1016/j.biopha.2020.110130>
- Liu, J., Fang, Q., Lin, H., Yu, X., Zheng, H., Wan, Y., 2020. Alginate-poloxamer/silk fibroin hydrogels with covalently and physically cross-linked networks for cartilage tissue engineering. *Carbohydr. Polym.* 247,116593. <https://doi.org/10.1016/j.carbpol.2020.116593>
- Liu, Y., Aryee, M.J., Padyukov, L., Fallin, M.D., Hesselberg, E., Runarsson, A., Reinius, L., Acevedo, N., Taub, M., Ronninger, M., Shchetynsky, K., Scheynius, A., Kere, J., Alfredsson, L., Klareskog, L., Ekström, T.J., Feinberg, A.P., 2013. Epigenome-wide association data implicate DNA methylation as an intermediary of genetic risk in rheumatoid arthritis. *Nat. Biotechnol.* 31, 142–147. <https://doi.org/10.1038/nbt.2487>
- Lyu, J., Wang, L., Bai, X., Du, X., Wei, J., Wang, J., Lin, Y., Chen, Z., Liu, Z., Wu, J., Zhong, Z., 2021. Treatment of Rheumatoid Arthritis by Serum Albumin Nanoparticles Coated with Mannose to Target Neutrophils. *ACS Appl. Mater. Interfaces* 13, 266–276. <https://doi.org/10.1021/acsami.0c19468>

- Ma, S., Gu, S., Zhang, J., Qi, W., Lin, Z., Zhai, W., Zhan, J., Li, Q., Cai, Y., Lu, Y., 2022. Robust drug bioavailability and safety for rheumatoid arthritis therapy using D-amino acids-based supramolecular hydrogels. *Mater. Today Bio* 15, 100296. <https://doi.org/10.1016/j.mtbio.2022.100296>
- MacGregor, A.J., Snieder, H., Rigby, A.S., Koskenvuo, M., Kaprio, J., Aho, K., Silman, A.J., 2000. Characterizing the quantitative genetic contribution to rheumatoid arthritis using data from twins. *Arthritis Rheum.* 43, 30–37. [https://doi.org/10.1002/1529-0131\(200001\)43:1<30::AID-ANR5>3.0.CO;2-B](https://doi.org/10.1002/1529-0131(200001)43:1<30::AID-ANR5>3.0.CO;2-B)
- Makrygiannakis, D., Hermansson, M., Ulfgren, A.K., Nicholas, A.P., Zendman, A.J.W., Eklund, A., Gmnewald, J., Skold, C.M., Klareskog, L., Catrina, A.I., 2008. Smoking increases peptidylarginine deiminase 2 enzyme expression in human lungs and increases citrullination in BAL cells. *Ann. Rheum. Dis.* 67, 1488–1492. <https://doi.org/10.1136/ard.2007.075192>
- Mao, Y., Li, X., Chen, G., Wang, S., 2016. Thermosensitive Hydrogel System with Paclitaxel Liposomes Used in Localized Drug Delivery System for in Situ Treatment of Tumor: Better Antitumor Efficacy and Lower Toxicity. *J. Pharm. Sci.* 105, 194–204. <https://doi.org/10.1002/jps.24693>
- Marc Feldmann and, Maini, S.R.N., 2008. Role of cytokines in rheumatoid arthritis: an education in pathophysiology and therapeutics. *Immunol. Rev.* 49–68. <https://doi.org/10.2165/00002512-199812050-00004>
- Martel-Pelletier, J., Welsch, D.J., Pelletier, J.P., 2001. Metalloproteases and inhibitors in arthritic diseases. *Best Pract. Res. Clin. Rheumatol.* 15, 805–829. <https://doi.org/10.1053/berh.2001.0195>

- Masi, A.T., 1983. Articular patterns in the early course of rheumatoid arthritis. *Am. J. Med.* 75, 16–26. [https://doi.org/10.1016/0002-9343\(83\)90471-0](https://doi.org/10.1016/0002-9343(83)90471-0)
- Mazumder, M.K., Paul, R., Bhattacharya, P., Borah, A., 2019. Neurological sequel of chronic kidney disease: From diminished Acetylcholinesterase activity to mitochondrial dysfunctions, oxidative stress and inflammation in mice brain. *Sci. Rep.* 9, 3097. <https://doi.org/10.1038/s41598-018-37935-3>
- McHugh, J., 2020. Targeting FLS signalling in RA. *Nat. Rev. Rheumatol.* 16, 351. <https://doi.org/10.1038/s41584-020-0444-y>
- McInnes, I.B., Schett, G., 2017. Pathogenetic insights from the treatment of rheumatoid arthritis. *Lancet* 389, 2328–2337. [https://doi.org/10.1016/S0140-6736\(17\)31472-1](https://doi.org/10.1016/S0140-6736(17)31472-1)
- Miranda, K.M., Espey, M.G., Wink, D.A., 2001. A rapid, simple spectrophotometric method for simultaneous detection of nitrate and nitrite. *Nitric Oxide* 5, 62–71. <https://doi.org/10.1006/niox.2000.0319>
- Mizoguchi, F., Slowikowski, K., Wei, K., Marshall, J.L., Rao, D.A., Chang, S.K., Nguyen, H.N., Noss, E.H., Turner, J.D., Earp, B.E., Blazar, P.E., Wright, J., Simmons, B.P., Donlin, L.T., Kalliolias, G.D., Goodman, S.M., Bykerk, V.P., Ivashkiv, L.B., Lederer, J.A., Hacohen, N., Nigrovic, P.A., Filer, A., Buckley, C.D., Raychaudhuri, S., Brenner, M.B., 2018. Functionally distinct disease-associated fibroblast subsets in rheumatoid arthritis. *Nat. Commun.* 9, 789. <https://doi.org/10.1038/s41467-018-02892-y>
- Mohanty, S., Sahoo, A.K., Konkimalla, V.B., Pal, A., Si, S.C., 2020. Naringin in combination with isothiocyanates as liposomal formulations potentiates the anti-inflammatory activity in

different acute and chronic animal models of rheumatoid arthritis. *ACS Omega* 5, 28319–28332. <https://doi.org/10.1021/acsomega.0c04300>

Montaser, A.S., Rehan, M., El-Naggar, M.E., 2019. pH-Thermosensitive hydrogel based on polyvinyl alcohol/sodium alginate/N-isopropyl acrylamide composite for treating re-infected wounds. *Int. J. Biol. Macromol.* 124, 1016–1024. <https://doi.org/10.1016/j.ijbiomac.2018.11.252>

Monteiro do Nascimento, M.H., Ambrosio, F.N., Ferraraz, D.C., Windisch-Neto, H., Querobino, S.M., Nascimento-Sales, M., Alberto-Silva, C., Christoffolete, M.A., Franco, M.K.K.D., Kent, B., Yokaichiya, F., Lombello, C.B., de Araujo, D.R., 2021. Sulforaphane-loaded hyaluronic acid-poloxamer hybrid hydrogel enhances cartilage protection in osteoarthritis models. *Mater. Sci. Eng. C Mater. Biol. Appl.* 128, 112345. <https://doi.org/10.1016/j.msec.2021.112345>

Moron, M.S., Depierre, J.W., Mannervik, B., 1979. Levels of glutathione, glutathione reductase and glutathione S-transferase activities in rat lung and liver. *Biochim. Biophys. Acta.* 582, 67–78. [https://doi.org/10.1016/0304-4165\(79\)90289-7](https://doi.org/10.1016/0304-4165(79)90289-7)

Movahedi, M., Beauchamp, M., Abrahamowicz, M., 2015. Risk of Incident Diabetes Associated with Dose and Duration of Oral Glucocorticoid Therapy in Patients with Rheumatoid Arthritis. *Arthritis Rheumatol.* 68, 1089–98. <https://doi.org/DOI: 10.1002/art.39537>

Muller, S., Radic, M., 2015. Citrullinated Autoantigens: From Diagnostic Markers to Pathogenetic Mechanisms. *Clin. Rev. Allergy Immunol.* 49, 232–239. <https://doi.org/10.1007/s12016-014-8459-2>

- Mura, P., Mennini, N., Nativi, C., Richichi, B., 2018. In situ mucoadhesive-thermosensitive liposomal gel as a novel vehicle for nasal extended delivery of opiorphin. *Eur. J. Pharm. Biopharm.* 122, 54–61. <https://doi.org/10.1016/j.ejpb.2017.10.008>
- Murakami, A., Song, M., Ohigashi, H., 2007. Phenethyl isothiocyanate suppresses receptor activator of NF-kappaB ligand (RANKL)-induced osteoclastogenesis by blocking activation of ERK1/2 and p38 MAPK in RAW264.7 macrophages. *BioFactors* 30, 1–11. <https://doi.org/10.1002/biof.5520300101>
- Nasra, S., Bhatia, D., Kumar, A., 2022. Recent advances in nanoparticle-based drug delivery systems for rheumatoid arthritis treatment. *Nanoscale Adv.* 4, 3479–3494. <https://doi.org/10.1039/d2na00229a>
- Nell-Duxneuner, V., Machold, K., Stamm, T., Eberl, G., Heinzl, H., Hoefler, E., Smolen, J.S., Steiner, G., 2010. Autoantibody profiling in patients with very early rheumatoid arthritis: A follow-up study. *Ann. Rheum. Dis.* 69, 169–174. <https://doi.org/10.1136/ard.2008.100677>
- Neog, M.K., Joshua Pragasam, S., Krishnan, M., Rasool, M., 2017. p-Coumaric acid, a dietary polyphenol ameliorates inflammation and curtails cartilage and bone erosion in the rheumatoid arthritis rat model. *BioFactors* 43, 698–717. <https://doi.org/10.1002/biof.1377>
- Ngo, S.T., Steyn, F.J., McCombe, P.A., 2014. Gender differences in autoimmune disease. *Front. Neuroendocrinol.* 35, 347–369. <https://doi.org/10.1016/j.yfrne.2014.04.004>
- Nie, S., Hsiao, W.W., Pan, W., Yang, Z., 2011. Thermoreversible pluronic® F127-based hydrogel containing liposomes for the controlled delivery of paclitaxel: In vitro drug release, cell cytotoxicity, and uptake studies. *Int. J. Nanomedicine* 6, 151–166.

<https://doi.org/10.2147/IJN.S15057>

- Nygaard, G., Firestein, G.S., 2020. Restoring synovial homeostasis in rheumatoid arthritis by targeting fibroblast-like synoviocytes. *Nat. Rev. Rheumatol.* 16, 316–333. <https://doi.org/10.1038/s41584-020-0413-5>
- Pan, T., Cheng, T. fang, Jia, Y. ran, Li, P., Li, F., 2017. Anti-rheumatoid arthritis effects of traditional Chinese herb couple in adjuvant-induced arthritis in rats. *J. Ethnopharmacol.* 205, 1–7. <https://doi.org/10.1016/j.jep.2017.04.020>
- Pandey, S., Kumar, V., Leekha, A., Rai, N., Ahmad, F.J., Verma, A.K., 2018. Co-Delivery of Teriflunomide and Methotrexate from Hydroxyapatite Nanoparticles for the Treatment of Rheumatoid Arthritis: In Vitro Characterization, Pharmacodynamic and Biochemical Investigations. *Pharm. Res.* 35, 201. doi: 10.1007/s11095-018-2478-2.
- Pandit, A.H., Mazumdar, N., Imtiyaz, K., Rizvi, M.M.A., Ahmad, S., 2019. Periodate-Modified Gum Arabic Cross-linked PVA Hydrogels: A Promising Approach toward Photoprotection and Sustained Delivery of Folic Acid. *ACS Omega* 4, 16026–16036. <https://doi.org/10.1021/acsomega.9b02137>
- Pankongadisak, P., Suwantong, O., 2019. Enhanced properties of injectable chitosan-based thermogelling hydrogels by silk fibroin and longan seed extract for bone tissue engineering. *Int. J. Biol. Macromol.* 138, 412–424. <https://doi.org/10.1016/j.ijbiomac.2019.07.100>
- Parish, L.C., 1963. An historical approach to the nomenclature of rheumatoid arthritis. *Arthritis Rheumatol.* 6, 138–58. <https://doi.org/10.1002/art.1780060206>.
- Park, K.M., Lee, S.Y., Joung, Y.K., Na, J.S., Lee, M.C., Park, K.D., 2009. Thermosensitive

- chitosan-Pluronic hydrogel as an injectable cell delivery carrier for cartilage regeneration. *Acta Biomater.* 5, 1956–1965. <https://doi.org/10.1016/j.actbio.2009.01.040>
- Pearson, C.M., 1956. Development of Arthritis, Periarthritis and Periostitis in Rats Given Adjuvants. *Proc. Soc. Exp. Biol. Med.* 91, 95–101. <https://doi.org/10.3181/00379727-91-22179>
- Pelegriño, M.T., Lima, B. de A., do Nascimento, M.H.M., Lombello, C.B., Brocchi, M., Seabra, A.B., 2018. Biocompatible and Antibacterial Nitric Oxide-Releasing Pluronic F-127/Chitosan Hydrogel for Topical Applications. *Polymers (Basel)*. 10, 452. <https://doi.org/10.3390/polym10040452>
- Pettit, A.R., Ji, H., Von Stechow, D., Müller, R., Goldring, S.R., Choi, Y., Benoist, C., Gravallese, E.M., 2001. TRANCE/RANKL knockout mice are protected from bone erosion in a serum transfer model of arthritis. *Am. J. Pathol.* 159, 1689–1699. [https://doi.org/10.1016/S0002-9440\(10\)63016-7](https://doi.org/10.1016/S0002-9440(10)63016-7)
- Pettit, A.R., Walsh, N.C., Manning, C., Goldring, S.R., Gravallese, E.M., 2006. RANKL protein is expressed at the pannus-bone interface at sites of articular bone erosion in rheumatoid arthritis. *Rheumatology* 45, 1068–1076. <https://doi.org/10.1093/rheumatology/ke1045>
- Phillips, D.C., Dias, H.K.I., Kitas, G.D., Griffiths, H.R., 2010. Aberrant reactive oxygen and nitrogen species generation in rheumatoid arthritis (RA): Causes and consequences for immune function, cell survival, and therapeutic intervention. *Antioxidants Redox Signal.* 12, 743–785. <https://doi.org/10.1089/ars.2009.2607>
- Pulliero, A., Wu, Y., Fenoglio, D., Parodi, A., Romani, M., Soares, C.P., Filaci, G., Lee, J.L.,

- Sinkam, P.N., Izzotti, A., 2014. Nanoparticles increase the efficacy of cancer chemopreventive agents in cells exposed to cigarette smoke condensate. *Carcinogenesis* 36, 368–377. <https://doi.org/10.1093/carcin/bgv008>
- Qian, C., Kuang, M., Wang, Y., 2017. Effect of Qianghuo Erhuang Decoction on T Regulatory and T Helper 17 Cells in Treatment of Adjuvant-induced Arthritis in Rats. *Sci. Rep.* 7, 17198. <https://doi.org/10.1038/s41598-017-17566-w>
- Qian, C., Zhang, T., Gravesande, J., Baysah, C., Song, X., Xing, J., 2019. Injectable and self-healing polysaccharide-based hydrogel for pH-responsive drug release. *Int. J. Biol. Macromol.* 123, 140–148. <https://doi.org/10.1016/j.ijbiomac.2018.11.048>
- Qindeel, M., Ahmed, N., Sabir, F., Khan, S., Ur-Rehman, A., 2019. Development of novel pH-sensitive nanoparticles loaded hydrogel for transdermal drug delivery. *Drug Dev. Ind. Pharm.* 45, 629–641. <https://doi.org/10.1080/03639045.2019.1569031>
- Qindeel, M., Khan, D., Ahmed, N., Khan, S., Asim Ur Rehman, 2020. Surfactant-Free, Self-Assembled Nanomicelles-Based Transdermal Hydrogel for Safe and Targeted Delivery of Methotrexate against Rheumatoid Arthritis. *ACS Nano* 14, 4662–4681. <https://doi.org/10.1021/acsnano.0c00364>
- Qu, Y., Tang, J., Liu, L., Song, L.L., Chen, S., Gao, Y., 2019. α -Tocopherol liposome loaded chitosan hydrogel to suppress oxidative stress injury in cardiomyocytes. *Int. J. Biol. Macromol.* 125, 1192–1202. <https://doi.org/10.1016/j.ijbiomac.2018.09.092>
- Rao, K., Roome, T., Aziz, S., Razzak, A., Abbas, G., Imran, M., Jabri, T., Gul, J., Hussain, M., Sikandar, B., Sharafat, S., Shah, M.R., 2018. Bergenin loaded gum xanthan stabilized silver

nanoparticles suppress synovial inflammation through modulation of the immune response and oxidative stress in adjuvant induced arthritic rats. *J. Mater. Chem. B* 6, 4486–4501. <https://doi.org/10.1039/c8tb00672e>

Ray, S., Mishra, A., Mandal, T.K., Sa, B., Chakraborty, J., 2015. Optimization of the process parameters for the fabrication of a polymer coated layered double hydroxide-methotrexate nanohybrid for the possible treatment of osteosarcoma. *RSC Adv.* 5, 102574–102592. <https://doi.org/10.1039/c5ra15859a>

Redlich, K., Smolen, J.S., 2012. Inflammatory bone loss: Pathogenesis and therapeutic intervention. *Nat. Rev. Drug Discov.* 11, 234–250. <https://doi.org/10.1038/nrd3669>

Redlich, K., Wagner, E.F., Schett, G., Redlich, K., Hayer, S., Ricci, R., David, J., Tohidastakrad, M., Kollias, G., Steiner, G., Smolen, J.S., Wagner, E.F., Schett, G., 2002. Osteoclasts are essential for TNF- α mediated joint destruction Find the latest version: joint destruction. *J. Clin. Invest.* 110, 1419–1427. <https://doi.org/10.1172/JCI200215582.Introduction>

Ren, S., Liu, H., Wang, X., Bi, J., Lu, S., Zhu, C., Li, H., Kong, W., Chen, R., Chen, Z., 2021. Acupoint nanocomposite hydrogel for simulation of acupuncture and targeted delivery of triptolide against rheumatoid arthritis. *J. Nanobiotechnology* 19, 409. <https://doi.org/10.1186/s12951-021-01157-z>

Ren, Y., Zhao, X., Liang, X., Ma, P.X., Guo, B., 2017. Injectable hydrogel based on quaternized chitosan, gelatin and dopamine as localized drug delivery system to treat Parkinson's disease. *Int. J. Biol. Macromol.* 105, 1079–1087. <https://doi.org/10.1016/j.ijbiomac.2017.07.130>

- Reum Son, A., Kim, D.Y., Hun Park, S., Yong Jang, J., Kim, K., Ju Kim, B., Yun Yin, X., Ho Kim, J., Hyun Min, B., Keun Han, D., Suk Kim, M., 2015. Direct chemotherapeutic dual drug delivery through intra-articular injection for synergistic enhancement of rheumatoid arthritis treatment. *Sci. Rep.* 5, 14713. <https://doi.org/10.1038/srep14713>
- Sarwan, T., Kumar, P., Choonara, Y.E., Pillay, V., 2020. Hybrid Thermo-Responsive Polymer Systems and Their Biomedical Applications. *Front. Mater.* 7, 73. <https://doi.org/10.3389/fmats.2020.00073>
- Sawhney, S., Aggarwal, A., 2016. Human Joint Anatomy and Physiology. In: Sawhney, S., Aggarwal, A. (eds) *Pediatric Rheumatology*. Springer, Singapore. https://doi.org/https://doi.org/10.1007/978-981-10-1750-6_4
- Schmittgen, T.D., Livak, K.J., 2008. Analyzing real-time PCR data by the comparative CT method. *Nat. Protoc.* 3, 1101–1108. <https://doi.org/10.1038/nprot.2008.73>
- Shi, K., Wang, Y.L., Qu, Y., Liao, J.F., Chu, B.Y., Zhang, H.P., Luo, F., Qian, Z.Y., 2016. Synthesis, characterization, and application of reversible PDLLA-PEG-PDLLA copolymer thermogels in vitro and in vivo. *Sci. Rep.* 6, 19077. <https://doi.org/10.1038/srep19077>
- Shoaib, S., Tufail, S., Sherwani, M.A., Yusuf, N., Islam, N., 2021. Phenethyl Isothiocyanate Induces Apoptosis Through ROS Generation and Caspase-3 Activation in Cervical Cancer Cells. *Front. Pharmacol.* 12, 673103. <https://doi.org/10.3389/fphar.2021.673103>
- Sikdar, P., Uddin, M.M., Dip, T.M., Islam, S., Hoque, M.S., Dhar, A.K., Wu, S., 2021. Recent advances in the synthesis of smart hydrogels. *Mater. Adv.* 2, 4532–4573. <https://doi.org/10.1039/d1ma00193k>

- Smolen, J.S., Aletaha, D., Barton, A., Burmester, G.R., Emery, P., Firestein, G.S., Kavanaugh, A., McInnes, I.B., Solomon, D.H., Strand, V., Yamamoto, K., 2018. Rheumatoid arthritis. *Nat. Rev. Dis. Prim.* 4, 18001. <https://doi.org/10.1038/nrdp.2018.1>
- Smolen, J.S., Aletaha, D., Koeller, M., Weisman, M.H., Emery, P., 2007. New therapies for treatment of rheumatoid arthritis. *Lancet* 370, 1861–1874. [https://doi.org/10.1016/S0140-6736\(07\)60784-3](https://doi.org/10.1016/S0140-6736(07)60784-3)
- Smolen, J.S., Steiner, G., 2003. Therapeutic strategies for rheumatoid arthritis. *Nat. Rev. Drug Discov.* 2, 473–488. <https://doi.org/10.1038/nrd1109>
- Sokolove, J., Johnson, D.S., Lahey, L.J., Wagner, C.A., Cheng, D., Thiele, G.M., Michaud, K., Sayles, H., Reimold, A.M., Caplan, L., Cannon, G.W., Kerr, G., Mikuls, T.R., Robinson, W.H., 2014. Rheumatoid factor as a potentiator of anti-citrullinated protein antibody-mediated inflammation in rheumatoid arthritis. *Arthritis Rheumatol.* 66, 813–821. <https://doi.org/10.1002/art.38307>
- Sokolove, J., Wagner, C.A., Lahey, L.J., Sayles, H., Duryee, M.J., Reimold, A.M., Kerr, G., Robinson, W.H., Cannon, G.W., Thiele, G.M., Mikuls, T.R., 2016. Increased inflammation and disease activity among current cigarette smokers with rheumatoid arthritis: A cross-sectional analysis of US veterans. *Rheumatol. (United Kingdom)* 55, 1969–1977. <https://doi.org/10.1093/rheumatology/kew285>
- Song, Y., Cai, H., Yin, T., Huo, M., Ma, P., Zhou, J., Lai, W., 2018. Paclitaxel-loaded redox-sensitive nanoparticles based on hyaluronic acid-vitamin E succinate conjugates for improved lung cancer treatment. *Int. J. Nanomedicine* 13, 1585–1600. <https://doi.org/10.2147/IJN.S155383>

Stahl, E.A., Raychaudhuri, S., Remmers, E.F., Xie, G., Eyre, S., Thomson, B.P., Li, Y., Kurreeman, F.A.S., Zhernakova, A., Hinks, A., Guiducci, C., Chen, R., Alfredsson, L., Amos, C.I., Ardlie, K.G., Barton, A., Bowes, J., Brouwer, E., Burtt, N.P., Catanese, J.J., Coblyn, J., Coenen, M.J.H., Costenbader, K.H., Criswell, L.A., Crusius, J.B.A., Cui, J., De Bakker, P.I.W., De Jager, P.L., Ding, B., Emery, P., Flynn, E., Harrison, P., Hocking, L.J., Huizinga, T.W.J., Kastner, D.L., Ke, X., Lee, A.T., Liu, X., Martin, P., Morgan, A.W., Padyukov, L., Posthumus, M.D., Radstake, T.R.D.J., Reid, D.M., Seielstad, M., Seldin, M.F., Shadick, N.A., Steer, S., Tak, P.P., Thomson, W., Van Der Helm-Van Mil, A.H.M., Van Der Horst-Bruinsma, I.E., Van Der Schoot, C.E., Van Riel, P.L.C.M., Weinblatt, M.E., Wilson, A.G., Wolbink, G.J., Wordsworth, B.P., Wijmenga, C., Karlson, E.W., Toes, R.E.M., De Vries, N., Begovich, A.B., Worthington, J., Siminovitch, K.A., Gregersen, P.K., Klareskog, L., Plenge, R.M., 2010. Genome-wide association study meta-analysis identifies seven new rheumatoid arthritis risk loci. *Nat. Genet.* 42, 508–514. <https://doi.org/10.1038/ng.582>

Stamp, L.K., Khalilova, I., Tarr, J.M., Senthilmohan, R., Turner, R., Haigh, R.C., Winyard, P.G., Kettle, A.J., 2012. Myeloperoxidase and oxidative stress in rheumatoid arthritis. *Rheumatol. (United Kingdom)* 51, 1796–1803. <https://doi.org/10.1093/rheumatology/kes193>

Steiner, G., 2007. Auto-antibodies and autoreactive T-cells in rheumatoid arthritis: Pathogenetic players and diagnostic tools. *Clin. Rev. Allergy Immunol.* 32, 23–35. <https://doi.org/10.1007/BF02686079>

Stolina, M., Adamu, S., Ominsky, M., Dwyer, D., Asuncion, F., Geng, Z., Middleton, S., Brown, H., Pretorius, J., Schett, G., Bolon, B., Feige, U., Zack, D., Kostenuik, P.J., 2005. RANKL

is a marker and mediator of local and systemic bone loss in two rat models of inflammatory arthritis. *J. Bone Miner. Res.* 20, 1756–1765. <https://doi.org/10.1359/JBMR.050601>

Stolina, M., Schett, G., Dwyer, D., Vonderfecht, S., Middleton, S., Duryea, D., Pacheco, E., Van, G., Bolon, B., Feige, U., Zack, D., Kostenuik, P., 2009. RANKL inhibition by osteoprotegerin prevents bone loss without affecting local or systemic inflammation parameters in two rat arthritis models: Comparison with anti-TNF α or anti-IL-1 therapies. *Arthritis Res. Ther.* 11, R187. <https://doi.org/10.1186/ar2879>

Stolt, P., Källberg, H., Lundberg, I., Sjögren, B., Klareskog, L., Alfredsson, L., 2005. Silica exposure is associated with increased risk of developing rheumatoid arthritis: Results from the Swedish EIRA study. *Ann. Rheum. Dis.* 64, 582–586. <https://doi.org/10.1136/ard.2004.022053>

Sugiyama, D., Nishimura, K., Tamaki, K., Tsuji, G., Nakazawa, T., Morinobu, A., Kumagai, S., 2010. Impact of smoking as a risk factor for developing rheumatoid arthritis: A meta-analysis of observational studies. *Ann. Rheum. Dis.* 69, 70–81. <https://doi.org/10.1136/ard.2008.096487>

Sundaram, V., Mohammed, S., Srinivasan, M.R., Johnson, J., Suepaul, R., Pargass, I., John, C., Ramdhanie, D., Lallack, S., Daniel, E., Gilkes, L., 2021. Acute and subacute toxicity evaluation of hydroalcoholic extract from the stem bark of Bois Bande (*Parinari campestris* Aubl.1772) in rats. *BMC Pharmacol. Toxicol.* 22, 51. <https://doi.org/10.1186/s40360-021-00522-w>

Svendsen, A.J., Gervin, K., Lyle, R., Christiansen, L., Kyvik, K., Junker, P., Nielsen, C., Houen, G., Tan, Q., 2016. Differentially methylated DNA regions in monozygotic twin pairs

discordant for rheumatoid arthritis: An epigenome-wide study. *Front. Immunol.* 7, 510.
<https://doi.org/10.3389/fimmu.2016.00510>

Swann, D.A., Sotman, S., Dixon, M., Brooks, C., 1977. The isolation and partial characterization of the major glycoprotein (LGP-I) from the articular lubricating fraction from bovine synovial fluid. *Biochem. J.* 161, 473–485. <https://doi.org/10.1042/bj1610473>

Szymańska, E., Winnicka, K., 2015. Stability of chitosan - A challenge for pharmaceutical and biomedical applications. *Mar. Drugs* 13, 1819–1846. <https://doi.org/10.3390/md13041819>

Takayanagi, H., Kim, S., Koga, T., Nishina, H., Isshiki, M., Yoshida, H., Saiura, A., Isobe, M., Yokochi, T., Inoue, J.I., Wagner, E.F., Mak, T.W., Kodama, T., Taniguchi, T., 2002. Induction and activation of the transcription factor NFATc1 (NFAT2) integrate RANKL signaling in terminal differentiation of osteoclasts. *Dev. Cell* 3, 889–901.
[https://doi.org/10.1016/S1534-5807\(02\)00369-6](https://doi.org/10.1016/S1534-5807(02)00369-6)

Too, C.L., Muhamad, N.A., Ilar, A., Padyukov, L., Alfredsson, L., Klareskog, L., Murad, S., Bengtsson, C., 2016. Occupational exposure to textile dust increases the risk of rheumatoid arthritis: Results from a Malaysian population-based case-control study. *Ann. Rheum. Dis.* 75, 997–1002. <https://doi.org/10.1136/annrheumdis-2015-208278>

Tran Vo, T.M., Piroonpan, T., Preuksarattanawut, C., Kobayashi, T., Potiyaraj, P., 2022. Characterization of pH-responsive high molecular-weight chitosan/poly (vinyl alcohol) hydrogel prepared by gamma irradiation for localizing drug release. *Bioresour. Bioprocess.* 9,89. <https://doi.org/10.1186/s40643-022-00576-6>

Trujillo-Nolasco, R.M., Morales-Avila, E., Ocampo-García, B.E., Ferro-Flores, G., Gibbens-

- Bandala, B. V., Escudero-Castellanos, A., Isaac-Olive, K., 2019. Preparation and in vitro evaluation of radiolabeled HA-PLGA nanoparticles as novel MTX delivery system for local treatment of rheumatoid arthritis. *Mater. Sci. Eng. C Mater. Biol. Appl.* 103, 109766. <https://doi.org/10.1016/j.msec.2019.109766>
- Turabee, M.H., Jeong, T.H., Ramalingam, P., Kang, J.H., Ko, Y.T., 2019. N,N,N-trimethyl chitosan embedded in situ Pluronic F127 hydrogel for the treatment of brain tumor. *Carbohydr. Polym.* 203, 302–309. <https://doi.org/10.1016/j.carbpol.2018.09.065>
- Uchiyama, M., Mihara, M., 1978. Determination of malonaldehyde precursor in tissues by thiobarbituric acid test. *Anal. Biochem.* 86, 271–278. [https://doi.org/10.1016/0003-2697\(78\)90342-1](https://doi.org/10.1016/0003-2697(78)90342-1)
- Ur-Rehman, T., Tavelin, S., Gröbner, G., 2011. Chitosan in situ gelation for improved drug loading and retention in poloxamer 407 gels. *Int. J. Pharm.* 409, 19–29. <https://doi.org/10.1016/j.ijpharm.2011.02.017>
- van Eden, W., Wagenaar-Hilbers, J.P.A., Wauben, M.H.M., 2001. Adjuvant Arthritis in the Rat. *Curr. Protoc. Immunol.* Chapter 15, 15.4.1-15.4.8. <https://doi.org/10.1002/0471142735.im1504s19>
- Vesperini, V., Lukas, C., Fautrel, B., Le Loet, X., Rincheval, N., Combe, B., 2013. Association of tobacco exposure and reduction of radiographic progression in early rheumatoid arthritis: Results from a French multicenter cohort. *Arthritis Care Res.* 65, 1899–1906. <https://doi.org/10.1002/acr.22057>
- Viatte, S., Massey, J., Bowes, J., Duffus, K., Eyre, S., Barton, A., Worthington, J., Loughlin, J.,

- Arden, N., Birrell, F., Carr, A., Deloukas, P., Doherty, M., McCaskie, A.W., Ollier, W.E.R., Rai, A., Ralston, S.H., Spector, T.D., Valdes, A.M., Wallis, G.A., Wilkinson, J.M., Zeggini, E., 2016. Replication of Associations of Genetic Loci Outside the HLA Region With Susceptibility to Anti-Cyclic Citrullinated Peptide–Negative Rheumatoid Arthritis. *Arthritis Rheumatol.* 68, 1603–1613. <https://doi.org/10.1002/art.39619>
- Viatte, S., Plant, D., Bowes, J., Lunt, M., Eyre, S., Barton, A., Worthington, J., 2012. Genetic markers of rheumatoid arthritis susceptibility in anti-citrullinated peptide antibody negative patients. *Ann. Rheum. Dis.* 71, 1984–1990. <https://doi.org/10.1136/annrheumdis-2011-201225>
- Viatte, S., Plant, D., Han, B., Fu, B., Yarwood, A., Thomson, W., Symmons, D.P.M., Worthington, J., Young, A., Hyrich, K.L., Morgan, A.W., Wilson, A.G., Isaacs, J.D., Raychaudhuri, S., Barton, A., 2015. Association of HLA-DRB1 haplotypes with rheumatoid arthritis severity, mortality, and treatment response. *JAMA - J. Am. Med. Assoc.* 313, 1645–1656. <https://doi.org/10.1001/jama.2015.3435>
- Vignesh, S., Sivashanmugam, A., Annapoorna, M., Janarthanan, R., Subramania, I., Shantikumar V., N., Jayakumar, R., 2018. Injectable deferoxamine nanoparticles loaded chitosan-hyaluronic acid coacervate hydrogel for therapeutic angiogenesis. *Colloids Surfaces B Biointerfaces* 161, 129–138. <https://doi.org/10.1016/j.colsurfb.2017.10.033>
- Vincenzi, F., Padovan, M., Targa, M., Corciulo, C., Giacuzzo, S., Merighi, S., Gessi, S., Govoni, M., Borea, P.A., Varani, K., 2013. A2A Adenosine Receptors Are Differentially Modulated by Pharmacological Treatments in Rheumatoid Arthritis Patients and Their Stimulation Ameliorates Adjuvant-Induced Arthritis in Rats. *PLoS One* 8, e54195.

<https://doi.org/10.1371/journal.pone.0054195>

- Wang, Q., Bao, Y., 2021. Nanodelivery of natural isothiocyanates as a cancer therapeutic. *Free Radic. Biol. Med.* 167, 125–140. <https://doi.org/10.1016/j.freeradbiomed.2021.02.044>
- Wang, Q., Wei, H., Deng, C., Xie, C., Huang, M., 2020. Improving Stability and Accessibility of Quercetin in Olive Oil-in-Soy Protein Isolate/Pectin Stabilized O/W Emulsion. *Foods* 9,123. doi: 10.3390/foods9020123.
- Wang, W., Wat, E., Hui, P.C.L., Chan, B., Ng, F.S.F., Kan, C.W., Wang, X., Hu, H., Wong, E.C.W., Lau, C.B.S., Leung, P.C., 2016. Dual-functional transdermal drug delivery system with controllable drug loading based on thermosensitive poloxamer hydrogel for atopic dermatitis treatment. *Sci. Rep.* 6, 24112. <https://doi.org/10.1038/srep24112>
- Wang, X., Shen, Y., Zhuang, X., Wang, N., Zhang, Qi, Zhu, L., Liu, Y., Lu, X., Qin, L., Zhang, Qiaoyan, 2021. Jintiange Capsule Alleviates Rheumatoid Arthritis and Reverses Changes of Serum Metabolic Profile in Collagen-Induced Arthritic Rats. *J. Inflamm. Res.* 14, 6685–6706. <https://doi.org/10.2147/JIR.S338107>
- Wang, Y., Liu, Z., Li, T., Chen, L., Lyu, J., Li, C., Lin, Y., Hao, N., Zhou, M., Zhong, Z., 2019. Enhanced therapeutic effect of RGD-modified polymeric micelles loaded with low-dose methotrexate and nimesulide on rheumatoid arthritis. *Theranostics* 9, 708–720. <https://doi.org/10.7150/thno.30418>
- Wang, Y., Xi, L., Zhang, B., Zhu, Q., Su, F., Jelonek, K., Orchel, A., Kasperczyk, J., Li, S., 2020. Bioresorbable hydrogels prepared by photo-initiated crosslinking of diacrylated PTMC-PEG-PTMC triblock copolymers as potential carrier of antitumor drugs. *Saudi*

Pharm. J. 28, 290–299. <https://doi.org/10.1016/j.jsps.2020.01.008>

Webber, M.P., Moir, W., Zeig-Owens, R., Glaser, M.S., Jaber, N., Hall, C., Berman, J., Qayyum, B., Loupasakis, K., Kelly, K., Prezant, D.J., 2015. Nested case-control study of selected systemic autoimmune diseases in world trade center rescue/recovery workers. *Arthritis Rheumatol.* 67, 1369–1376. <https://doi.org/10.1002/art.39059>

Wei, Z.F., Jiao, X.L., Wang, T., Lu, Q., Xia, Y.F., Wang, Z.T., Guo, Q.L., Chou, G.X., Dai, Y., 2013. Norisoboldine alleviates joint destruction in rats with adjuvant-induced arthritis by reducing RANKL, IL-6, PGE 2, and MMP-13 expression. *Acta Pharmacol. Sin.* 34, 403–413. <https://doi.org/10.1038/aps.2012.187>

Wruck, C.J., Fragoulis, A., Gurzynski, A., Brandenburg, L.O., Kan, Y.W., Chan, K., Hassenpflug, J., Freitag-Wolf, S., Varoga, D., Lippross, S., Pufe, T., 2011. Role of oxidative stress in rheumatoid arthritis: Insights from the Nrf2-knockout mice. *Ann. Rheum. Dis.* 70, 844–850. <https://doi.org/10.1136/ard.2010.132720>

Wu, C., Cheng, J., Li, W., Yang, L., Dong, H., Zhang, X., 2021. Programmable Polymeric Microneedles for Combined Chemotherapy and Antioxidative Treatment of Rheumatoid Arthritis. *ACS Appl. Mater. Interfaces* 13, 55559–55568. <https://doi.org/10.1021/acsami.1c17375>

Wu, F., Zhang, M., Chu, X., Zhang, Q., Su, Y., Sun, B., Lu, T., Zhou, N., Zhang, J., Wang, J., Yi, X., 2019. Black phosphorus nanosheets-based nanocarriers for enhancing chemotherapy drug sensitiveness via depleting mutant p53 and resistant cancer multimodal therapy. *Chem. Eng. J.* 370, 387–399. <https://doi.org/10.1016/j.cej.2019.03.228>

- Wu, X., Wu, Y., Ye, H., Yu, S., He, C., Chen, X., 2017. Interleukin-15 and cisplatin co-encapsulated thermosensitive polypeptide hydrogels for combined immuno-chemotherapy. *J. Control. Release* 255, 81–93. <https://doi.org/10.1016/j.jconrel.2017.04.011>
- Xiao, Y., Gu, Y., Qin, L., Chen, L., Chen, X., Cui, W., Li, F., Xiang, N., He, X., 2021. Injectable thermosensitive hydrogel-based drug delivery system for local cancer therapy. *Colloids Surf. B Biointerfaces* 200, 111581. <https://doi.org/10.1016/j.colsurfb.2021.111581>
- Xu, G., Li, B., Wang, T., Wan, J., Zhang, Y., Huang, J., Shen, Y., 2018. Enhancing the anti-ovarian cancer activity of quercetin using a self-assembling micelle and thermosensitive hydrogel drug delivery system. *RSC Adv.* 8, 21229–21242. <https://doi.org/10.1039/c8ra03274b>
- Xu, X., Gu, Z., Chen, X., Shi, C., Liu, C., Liu, M., Wang, L., Sun, M., Zhang, K., Liu, Q., Shen, Y., Lin, C., Yang, B., Sun, H., 2019. An injectable and thermosensitive hydrogel: Promoting periodontal regeneration by controlled-release of aspirin and erythropoietin. *Acta Biomater.* 86, 235–246. <https://doi.org/10.1016/j.actbio.2019.01.001>
- Xu, X., Huang, Ziyuan, Huang, Zeqian, Zhang, X., He, S., Sun, X., Shen, Y., Yan, M., Zhao, C., 2017. Injectable, NIR/pH-Responsive Nanocomposite Hydrogel as Long-Acting Implant for Chemophothermal Synergistic Cancer Therapy. *ACS Appl. Mater. Interfaces* 9, 20361–20375. <https://doi.org/10.1021/acsami.7b02307>
- Yagi, K., 1998. Simple assay for the level of total lipid peroxides in serum or plasma. *Methods Mol. Biol.* 108, 101–106. <https://doi.org/10.1385/0-89603-472-0:101>
- Yang, J., Fu, X., Liao, X., Li, Y., 2020. Nrf2 Activators as Dietary Phytochemicals Against

- Oxidative Stress, Inflammation, and Mitochondrial Dysfunction in Autism Spectrum Disorders: A Systematic Review. *Front. Psychiatry* 11, 561998. <https://doi.org/10.3389/fpsy.2020.561998>
- Yang, L., Liu, R., Fan, A., Zhao, J., Zhang, Y., He, J., 2020. Chemical Composition of *Pterospermum heterophyllum* Root and its Anti-Arthritis Effect on Adjuvant-Induced Arthritis in Rats via Modulation of Inflammatory Responses. *Front. Pharmacol.* 11, 584849. <https://doi.org/10.3389/fphar.2020.584849>
- Ye, L., Dinkova-Kostova, A.T., Wade, K.L., Zhang, Y., Shapiro, T.A., Talalay, P., 2002. Quantitative determination of dithiocarbamates in human plasma, serum, erythrocytes and urine: Pharmacokinetics of broccoli sprout isothiocyanates in humans. *Clin. Chim. Acta* 316, 43–53. [https://doi.org/10.1016/S0009-8981\(01\)00727-6](https://doi.org/10.1016/S0009-8981(01)00727-6)
- Yeo, J., Lee, Y.M., Lee, J., Park, D., Kim, K., Kim, J., Park, J., Kim, W.J., 2019. Nitric Oxide-Scavenging Nanogel for Treating Rheumatoid Arthritis. *Nano Lett.* 19, 6716–6724. <https://doi.org/10.1021/acs.nanolett.9b00496>
- Yin, N., Guo, X., Sun, R., Liu, H., Tang, L., Gou, J., Yin, T., He, H., Zhang, Y., Tang, X., 2020a. Intra-articular injection of indomethacin-methotrexate: In situ hydrogel for the synergistic treatment of rheumatoid arthritis. *J. Mater. Chem. B* 8, 993–1007. <https://doi.org/10.1039/c9tb01795j>
- Yin, N., Guo, X., Sun, R., Liu, H., Tang, L., Gou, J., Yin, T., He, H., Zhang, Y., Tang, X., 2020b. Intra-articular injection of indomethacin-methotrexate: In situ hydrogel for the synergistic treatment of rheumatoid arthritis. *J. Mater. Chem. B* 8, 993–1007. <https://doi.org/10.1039/c9tb01795j>

- Yin, N., Tan, X., Liu, H., He, F., Ding, N., Gou, J., Yin, T., He, H., Zhang, Y., Tang, X., 2020c. A novel indomethacin/methotrexate/MMP-9 siRNA: In situ hydrogel with dual effects of anti-inflammatory activity and reversal of cartilage disruption for the synergistic treatment of rheumatoid arthritis. *Nanoscale* 12, 8546–8562. <https://doi.org/10.1039/d0nr00454e>
- Yu, G.T., Rao, L., Wu, H., Yang, L.L., Bu, L.L., Deng, W.W., Wu, L., Nan, X., Zhang, W.F., Zhao, X.Z., Liu, W., Sun, Z.J., 2018. Myeloid-Derived Suppressor Cell Membrane-Coated Magnetic Nanoparticles for Cancer Theranostics by Inducing Macrophage Polarization and Synergizing Immunogenic Cell Death. *Adv. Funct. Mater.* 28, 1801389. <https://doi.org/10.1002/adfm.201801389>
- Yu, H., Fan, J., Shehla, N., Qiu, Y., Lin, Y., Wang, Z., Cao, L., Li, B., Daniyal, M., Qin, Y., Peng, C., Cai, X., Liu, B., Wang, W., 2022. Biomimetic Hybrid Membrane-Coated Xuetongsu Assisted with Laser Irradiation for Efficient Rheumatoid Arthritis Therapy. *ACS Nano* 16, 502–521. <https://doi.org/10.1021/acsnano.1c07556>
- Yu, S., Zhang, X., Tan, G., Tian, L., Liu, D., Liu, Y., Yang, X., Pan, W., 2017. A novel pH-induced thermosensitive hydrogel composed of carboxymethyl chitosan and poloxamer cross-linked by glutaraldehyde for ophthalmic drug delivery. *Carbohydr. Polym.* 155, 208–217. <https://doi.org/10.1016/j.carbpol.2016.08.073>
- Yu, W.J., Huang, D.X., Liu, S., Sha, Y.L., Gao, F.H., Liu, H., 2020. Polymeric Nanoscale Drug Carriers Mediate the Delivery of Methotrexate for Developing Therapeutic Interventions Against Cancer and Rheumatoid Arthritis. *Front. Oncol.* 10, 1734. <https://doi.org/10.3389/fonc.2020.01734>
- Zarrintaj, P., Ramsey, J.D., Samadi, A., Atoufi, Z., Yazdi, M.K., Ganjali, M.R., Amirabad, L.M.,

- Zangene, E., Farokhi, M., Formela, K., Saeb, M.R., Mozafari, M., Thomas, S., 2020. Poloxamer: A versatile tri-block copolymer for biomedical applications. *Acta Biomater.* 110, 37–67. <https://doi.org/10.1016/j.actbio.2020.04.028>
- Zeb, A., Qureshi, O.S., Yu, C.H., Akram, M., Kim, H.S., Kim, M.S., Kang, J.H., Majid, A., Chang, S.Y., Bae, O.N., Kim, J.K., 2017. Enhanced anti-rheumatic activity of methotrexate-entrapped ultradeformable liposomal gel in adjuvant-induced arthritis rat model. *Int. J. Pharm.* 525, 92–100. <https://doi.org/10.1016/j.ijpharm.2017.04.032>
- Zhang, E., Li, J., Zhou, Y., Che, P., Ren, B., Qin, Z., Ma, L., Cui, J., Sun, H., Yao, F., 2017. Biodegradable and injectable thermoreversible xyloglucan based hydrogel for prevention of postoperative adhesion. *Acta Biomater.* 55, 420–433. <https://doi.org/10.1016/j.actbio.2017.04.003>
- Zhang, Q., Dehaini, D., Zhang, Y., Zhou, J., Chen, X., Zhang, Lifan, Fang, R.H., Gao, W., Zhang, Liangfang, 2018. Neutrophil membrane-coated nanoparticles inhibit synovial inflammation and alleviate joint damage in inflammatory arthritis. *Nat. Nanotechnol.* 13, 1182–1190. <https://doi.org/10.1038/s41565-018-0254-4>
- Zhang, W., Jin, X., Li, H., Zhang, R. run, Wu, C. wei, 2018. Injectable and body temperature sensitive hydrogels based on chitosan and hyaluronic acid for pH sensitive drug release. *Carbohydr. Polym.* 186, 82–90. <https://doi.org/10.1016/j.carbpol.2018.01.008>
- Zhang, Y., 2012. The 1,2-Benzenedithiole-Based Cyclocondensation Assay: A Valuable Tool for the Measurement of Chemopreventive Isothiocyanates. *Crit. Rev. Food Sci. Nutr.* 52, 525–532. <https://doi.org/10.1080/10408398.2010.503288>

- Zhang, Y., Wang, F., Li, M., Yu, Z., Qi, R., Ding, J., Zhang, Z., Chen, X., 2018. Self-Stabilized Hyaluronate Nanogel for Intracellular Codelivery of Doxorubicin and Cisplatin to Osteosarcoma. *Adv.Sci. (Weinh)* 5, 1700821. <https://doi.org/10.1002/advs.201700821>
- Zhao, X., Li, P., Guo, B., Ma, P.X., 2015. Antibacterial and conductive injectable hydrogels based on quaternized chitosan-graft-polyaniline/oxidized dextran for tissue engineering. *Acta Biomater.* 26, 236–248. <https://doi.org/10.1016/j.actbio.2015.08.006>
- Zhao, X., Zhang, H., Gao, Y., Lin, Y., Hu, J., 2020. A Simple Injectable Moldable Hydrogel Assembled from Natural Glycyrrhizic Acid with Inherent Antibacterial Activity. *ACS Appl. Bio Mater.* 3, 648–653. <https://doi.org/10.1021/acsabm.9b01007>
- Zhao, Z., Zhang, Y., Wang, C., Wang, X., Wang, Y., Zhang, H., 2021. Angiotensin II upregulates RANKL/NFATC1 expression in synovial cells from patients with rheumatoid arthritis through the ERK1/2 and JNK pathways. *J. Orthop. Surg. Res.* 16, 297. <https://doi.org/10.1186/s13018-021-02451-0>
- Zheng, Y., Cheng, Y., Chen, J., Ding, J., Li, M., Li, C., Wang, J.C., Chen, X., 2017. Injectable hydrogel-microsphere construct with sequential degradation for locally synergistic chemotherapy. *ACS Appl. Mater. Interfaces* 9, 3487–3496. <https://doi.org/10.1021/acsami.6b15245>
- Ziff, M., 1974. Relation of cellular infiltration of rheumatoid synovial membrane to its immune response. *Arthritis Rheum.* 17, 313–319. <https://doi.org/10.1002/art.1780170317>
- Zimmerman, M.C., Clemens, D.L., Duryee, M.J., Sarmiento, C., Chiou, A., Hunter, C.D., Tian, J., Klassen, L.W., O'Dell, J.R., Thiele, G.M., Mikuls, T.R., Anderson, D.R., 2017. Direct

antioxidant properties of methotrexate: Inhibition of malondialdehyde-acetaldehyde-protein adduct formation and superoxide scavenging. *Redox Biol.* 13, 588–593.
<https://doi.org/10.1016/j.redox.2017.07.018>